Effect of Compressive Force on Aeroelastic Stability of a Strut-Braced Wing

Erwin Sulaeman

Dissertation submitted to the Faculty of the
Virginia Polytechnic Institute and State University
in partial fulfillment of the requirements for the degree of

Doctor of Philosophy
in
Aerospace Engineering

Rakesh K. Kapania, Chair
Bernard Grossman
Eric R. Johnson
Liviu Libresu
William H. Mason
Joseph A. Schetz

November 26, 2001
Blacksburg, Virginia

Keywords: Aeroelasticity, Strut-Braced Wing, Unsteady Aerodynamics,
Non-uniform Beam Finite Element, Buckling

Copyright ©2001, Erwin Sulaeman

Effect of Compressive Force on Aeroelastic Stability of a Strut-Braced Wing

by

Erwin Sulaeman

Committee Chairman: Rakesh K. Kapania

Aerospace Engineering

(ABSTRACT)

Recent investigations of a strut-braced wing (SBW) aircraft show that, at high positive load factors, a large tensile force in the strut leads to a considerable compressive axial force in the inner wing, resulting in a reduced bending stiffness and even buckling of the wing. Studying the influence of this compressive force on the structural response of SBW is thus of paramount importance in the early stage of SBW design.

The purpose of the this research is to investigate the effect of compressive force on aeroelastic stability of the SBW using efficient structural finite element and aerodynamic lifting surface methods. A procedure is developed to generate wing stiffness distribution for detailed and simplified wing models and to include the compressive force effect in the SBW aeroelastic analysis. A sensitivity study is performed to generate response surface equations for the wing flutter speed as functions of several design variables. These aeroelastic procedures and response surface equations provide a valuable tool and trend data to study the unconventional nature of SBW.

In order to estimate the effect of the compressive force, the inner part of the wing structure is modeled as a beam-column. A structural finite element method is developed based on an analytical stiffness matrix formulation of a non-uniform beam element with

arbitrary polynomial variations in the cross section. By using this formulation, the number of elements to model the wing structure can be reduced without degrading the accuracy.

The unsteady aerodynamic prediction is based on a discrete element lifting surface method. The present formulation improves the accuracy of existing lifting surface methods by implementing a more rigorous treatment on the aerodynamic kernel integration. The singularity of the kernel function is isolated by implementing an exact expansion series to solve an incomplete cylindrical function problem. A hybrid doublet lattice/doublet point scheme is devised to reduce the computational time.

SBW aircraft selected for the present study is the fuselage-mounted engine configuration. The results indicate that the detrimental effect of the compressive force to the wing buckling and flutter speed is significant if the wing-strut junction is placed near the wing tip.

Dedication

This work is dedicated to the memories of
my mother, Amanah
and my father, Ma’mun

Acknowledgement

I would like to express my sincere gratitude and appreciation to the chairman of my committee, Prof. Rakesh Kapania, for his guidance and advice during the course of this research. I am grateful for his support and giving me the opportunity to involve in many important projects: the truss-braced wing, UCAV and ZONA aeroelastic projects. His encouragement, thoughtfulness, and supervision are deeply acknowledge. He will always be my guru.

I would like to thank Profs. Bernard Grossman, William Mason, and Joseph Schetz for their valuable guidance, constructive ideas, and generosity in sharing their experiences. I have been very fortunate to receive invaluable lessons especially during the weekly meeting of the truss-braced wing project. I am very grateful to Prof. Eric Johnson for his important advice. I learned a lot on wing structure models from his thin-wall structure class notes. I would like to thank Prof. Liviu Librescu who introduced me the beauty of aeroelasticity in his excellent lectures. I must also express my gratitude to Prof. Raphael Haftka of University of Florida for his useful guidance. I wish to acknowledge my sincere thanks to Profs. Daniel Inman and Harry Robertshaw of CIMMS, Virginia Tech, who provided me with a valuable opportunity when I worked for a short duration on the UCAV project. I owe a lot to Prof. Danny Liu of Arizona State University and P.C. Chen of ZONA Tech for their valuable support and assistance. ZONA Tech has been very kind to let me use their facilities during the final stage of the present work.

I would like to thank my friends in TBW and UCAV projects, especially to Amir, Anand, Andy, Frank, Jay, Joel, and Philippe for their support and encouragement. I would like to thank Goyal, Iridiastadi and Rildova for their readiness when I needed their help.

I would like to acknowledge that the financial support received during the first three years of my graduate study was provided from the science and technology for industrial development (STAID) project of the Indonesian Agency for the Assessment and Application of Technology. The truss-braced wing project was sponsored by NASA Langley Research Center, Grant No. NAG1-1852.

Finally, I would like to express my deep appreciation to my beloved wife, Dwityastuti, for her unconditional help, sacrifice and patience. I am forever grateful to my family for their love.

Contents

Abstract ii

Dedications iv

Acknowledgements v

List of Figures xii

List of Tables xvi

List of Symbols xviii

1 Introduction 1

1.1 Literature Review 3

1.1.1 Strut-Braced Wing Aircraft 3

1.1.2 Structural Wing Modeling 5

1.1.3 Non-Uniform Beam Finite Element Formulation 8

1.1.4 Unsteady Aerodynamic Load Formulation 11

1.1.5 Strut-Braced Wing Aeroelasticity 21

1.2 Dissertation Outline 23

1.3 Contribution to the Field 24

2 Strut Braced Wing Aeroelasticity Without Geometric Stiffness Effect 26

2.1 Introduction 26
2.2 Wing Cross Section Model 32
2.2.1 Double Plate Model 32
2.2.2 Basic Hexagonal Wing Section Model 34
2.2.3 Equivalent Hexagonal Wing Section Model 36
2.3 Finite Element Model 41
2.4 Flutter Analysis Using NASTRAN 43
2.5 Sensitivity Analysis 52

3 Nonuniform Beam Element Formulation 61

3.1 Introduction 61
3.2 Axial Stiffness Matrix of Non-uniform Beam Elements 64
3.2.1 Deformation of the Cantilever Beam Problem 65
3.2.2 Flexibility Matrix 67
3.2.3 Stiffness Matrix 68
3.3 Torsional Stiffness Matrix of Non-uniform Beam Elements 68
3.4 Flexural Stiffness Matrix of Non-uniform Beam Elements 69
3.4.1 Displacement of a Cantilever Beam Problem 70
3.4.2 Flexibilty Matrix of the Cantilever Beam 74
3.4.3 Stiffness Matrix 74
3.5 Non-uniform Load 75
3.6 Non-symmetric Beam Cross Section 78
3.7 Geometric Stiffness Matrix Formulation 80
3.8 Validation 84
3.9 Buckling Analysis of the Strut-Braced Wing 88

4 Aerodynamic Load Formulation 92

4.1 Introduction 92
4.2 Theoretical Background 93
4.2.1 Assumptions 93
4.2.2 Basic Concept 93
4.2.3 Boundary Conditions 98
4.2.4 Evaluation of the Kernel Function 98
4.2.5 Evaluation of the Aerodynamic Operator 101
4.2.6 Discrete Element Lifting Surface Methods 103
4.2.7 Doublet Lattice Method of Rodden et al 104
4.2.8 Doublet Point Method of Ueda and Dowell 110
4.2.9 Doublet Hybrid Method of Eversman and Pitt 115
4.3 Contribution of the Present Work 115
4.3.1 The Doublet Lattice Method (DLM) 116
4.3.2 The Doublet Point Method (DPM) 117
4.3.3 The Doublet Hybrid Method (DHM) 117
4.4 Alternate Expansion Series for the Incomplete Cylindrical Function 120
4.5 Present Vortex Lattice Method 123
4.6 Present Doublet Point Method 127
4.6.1 Present DPM for Planar Lifting Surfaces 127
4.6.2 Present DPM for Non-planar Lifting Surfaces 130
4.7 Present Doublet Lattice Method 136
4.7.1 Present DLM for Planar Lifting Surfaces 137
4.7.2 Present DLM for Non-planar Lifting Surfaces 139
4.8 Present Doublet Hybrid Method 141
4.9 Unsteady Aerodynamic Load in Laplace Domain 144
4.8.1 Kernel Function Formulation 145

4.8.2 Incomplete Cylindrical Function 147
4.8.3 Application to the Strut-Based Wing Aeroelastic Analysis 149
4.10 Validation 150
4.9.1 Delta Wing with AR = 2 151
4.9.2 Double-Delta Wing 153
4.9.3 Sweptback Wing with Partial Flap 154
4.9.4 AGARD Wing—Horizontal Tail 156
4.9.5 Strut-Based Wing with Camber and Twist Angle 158
4.11 Unsteady Transonic Aerodynamic 161

5 Strut Braced Wing Aeroelasticity With Geometric Stiffness Effect 167

5.1 Introduction 167
5.2 The Flutter K-Method 169
5.2.1 Theoretical Background 169
5.2.2 Validation of the Present Flutter Procedure 173
5.3 The Compressive Force Effect 176
5.4 Trim Analysis of the Strut-Braced Wing 178
5.5 Modal Analysis 182
5.6 Flutter Calculation at Reference Condition 186
5.7 Sensitivity Analysis 190

6 Conclusion 195

7 Further Work 198

References 200

Appendices

A Detailed Derivation of the Kernel Function Integration A.1

B Sample Input and Output B.1

C Minimum Denominator Rational Function C.1

D Translation of Axis Procedure D.1

Vita V.1

List of Figures

1.1	The strut-braced wing aircraft with fuselage-mounted engine configuration.	2
1.2	The rectangular wing box models for the joined-wing structure model.	6
1.3	The double-plate and the hexagonal box models for the strut-braced wing structure model.	7
1.4	The strut-braced wing model of the Keldysh problem.	22
1.5	The present aeroelastic computational module of the strut-braced wing.	25
2.1	The SBW model of the Keldysh problem.	28
2.2	A space frame model of the present strut-braced wing.	30
2.3	Front view of the present strut-braced wing.	30
2.4	The double plate model to represent the wing bending box.	32
2.5	The hexagonal wing section model.	35
2.6	EI_{xx} distribution (G lb ft2) of the double plate model and three hexagonal models based on the procedures 1, 2, and 3.	38
2.7	(a) The double plate model, (b) The equivalent hexagonal model 1, (c) The equivalent hexagonal model 2.	39
2.8	The strut braced wing frame generated using *ehexa.f*.	43
2.9a	Mode1: First vertical bending(2.33 Hz).	44
2.9b	Mode 2: Second vertical bending (2.97 Hz).	45
2.9c	Mode3: Third vertical bending(3.74 Hz).	45

2.9d	Mode 4: First aft bending (4.37 Hz).	46
2.9e	Mode 5: Fourth vertical bending (6.76 Hz).	46
2.9f	Mode 6: Second aft bending (7.71 Hz).	47
2.9g	Mode 7: First Torsion (9.09 Hz).	47
2.10	The flutter *V-g* and *V-f* plots.	50
2.11	The *V-g* plot of the strut braced wing at the reference condition.	51
2.12	Flutter speed as a function of the strut junction position at the fuselage in the *x* (longitudinal) direction. V_{ref} = 902 fps.	54
2.13	Flutter speed as a function of the spanwise position of the strut junction at the wing. V_{ref} = 902 fps.	55
2.14	Flutter speed as a function of the chordwise and spanwise position of the wing-strut junction. V_{ref} = 902 fps.	57
2.15	Flutter speed, at sea level, as a function of the length of the offset beam connecting the wing and strut. V_{ref} = 902 fps, $h_{offset\text{-}Ref}$ = 3.17 ft.	58
2.16	Flutter speed, at sea level, as a function of the length of the offset beam connecting the wing and strut. V_{ref} = 902 fps, $h_{offset\text{-}Ref}$ = 3.17 ft.	60
3.1	Geometry and sign convention of a tapered axial bar element.	61
3.2	A cantilever beam model to derive the flexibility matrix.	64
3.3	Geometry and sign convention of a tapered beam element.	66
3.4	A cantilever beam model to derive the flexibility matrix.	71
3.5	A non-uniform beam element under a non-uniform distributed load.	77
3.6	Convergence of the error of the tip displacement of the cantilever non-prismatic beam under a concentrated moment load M at the tip.	86
3.7	A space frame geometry consisted of uniform and tapered beam elements.	85

3.8	Convergence of the displacement of Point 1 of the space frame structure.	87
3.9	A non-prismatic beam with several supports.	88
3.10	A space frame model of the wing-strut configuration.	89
3.11	Buckling load versus spanwise location of the strut junction.	90
3.12	Buckling load versus the offset beam length and stiffness.	91
4.1	The induced velocity at point P (x,y,z) due to pressure loading on an infinitesimal area $dx\ dh$ concentrated at point (x, h, z).	95
4.2	Lifting surface idealization in the doublet lattice method.	104
4.3	The lifting surface idealization in the doublet point method.	111
4.4	Lifting surface idealization in the vortex lattice method.	124
4.5	Vortex segment geometry.	125
4.6	Lifting surface discritezation in the present doublet lattice method.	136
4.7	Spanwise lift distribution of a delta wing with AR=2 and M=0.13.	152
4.8	A double delta wing planform with AR=1.7.	153
4.9	A sweptback wing with partial flap.	155
4.10	Pressure distribution at y = 1.95 of the swept-back wing with flap.	155
4.11a	Schematic of AGARD coplanar wing-horizontal tail configuration.	156
4.11b	The lift curve slope C_{La} of AGARD wing-horizontal tail as a function of the vertical gap between the wing and horizontal tail.	157
4.12	Strut-braced wing camber and twist angle for y < 0.4.	159
4.13	Lift distribution of the strut-braced wing with camber and twist angle distribution.	160
4.14	Typical transonic dip plots near the sonic Mach number.	162

5.1	The AGARD Standard 445.6 wing planform.	175
5.2	The *V-g* plot of the AGARD 445.6 wing at M = 0.90.	175
5.3	The *V-f* plot of the AGARD 445.6 wing at M = 0.90.	176
5.4	Flowchart for the flutter analysis of the strut braced wing.	178
5.5	A bilinear stress-strain relationship of the strut for calculation of wing response under aerodynamic loading.	181
5.6	Flow chart for the trim analysis of the SBW wing under aerodynamic loads	182
5.7a	Mode 1 (2.23 Hz).	183
5.7b	Mode 2 (3.07 Hz).	184
5.7c	Mode 3 (3.72 Hz).	184
5.7d	Mode 4 (4.78 Hz).	185
5.7e	Mode 5 (6.65 Hz).	185
5.7f	Mode 6 (8.54 Hz).	185
5.7g	Mode 7 (9.17 Hz).	186
5.8	The *V-g* and *V-f* plots of the strut braced wing at the reference condition.	189
5.9	Flutter speed as a function of the spanwise position of the strut junction at the wing. V_{ref} = 834.6 fps.	191
5.10	Flutter speed as function of the length of the offset beam at wing strut junction. V_{ref} = 834.6 fps.	192
5.11	Flutter speed boundary of the strut braced wing. V_{ref} = 834.6 fps.	194

List of Tables

1.1	Non-uniform beam stiffness and load functions.	10
1.2	Unsteady planar lifting surface formulation.	12
1.3	Kernel function formulation for unsteady lifting surface aerodynamics.	13
1.4	Solution to the incomplete cylindrical function occurring in the kernel function of the unsteady lifting surface theory.	15
2.1	Strut-braced wing aircraft parameters.	31
2.2	Natural frequencies of the strut-braced wing.	44
4.1	The coefficients a_I in Laschka approximation series.	107
4.2	The number of Gauss integration points N.	138
4.3	List of procedures used in the doublet hybrid method.	142
4.4	Lift coefficient CL of a delta wing with AR=2 and α= 4.3°.	154
4.5	The lift coefficient of a double delta wing with AR=1.7 and α=1°.	153
4.6	The lift coefficient CL of the wing with partial flap. AR=2.94, α = 0°, δ = 0.66°, k = 0.372.	154
4.7	The lift coefficient C_{LH} / ik of AGARD wing-horizontal tail harmonically plunging with k= 1.5 and M = 0.8.	156
5.1	Comparison of flutter speed and frequency of the AGARD 445.6 flexible wing.	174

5.2 Strut-braced wing aircraft parameters. 162

5.3 Natural frequencies of the strut-braced wing. 169

5.4 Comparison of the flutter speed and frequency of the strut braced wing. 174

List of Symbols

A	Cross-section area of a beam element
AR	Aspect ratio of a lifting surface
b	Semichord length of a root chord, or reference length
B_n	The incomplete cylindrical function
c	Chord length
C_L	Complex lift coefficient
C_{La}	Complex lift-curve slope
C_m	Complex moment coefficient
C_n	Complex normal force coefficient
C_{Na}	Complex normal-curve slope
E	Modulus of elasticity
e	Element/panel semiwidth
f_{ij}	Flexibility matrix coefficient
G	Shear modulus
g	Structural damping, also flight load factor
h	Vertical displacement amplitude of a lifting surface
I	Moment of inertia
I_n	B_n / r^2
$\boldsymbol{I_n}$	The modified Bessel function of the first kind and order n
$\mathfrak{I}$	Aerodynamic operator

J	Torsional constant
K	Kernel function, also stiffness matrix
K_1	The planar part of the kernel function
K_1^*	K_1 / r^2
K_2	The nonplanar part of the kernel
K_2^*	K_2 / r^4
K_{10}	Planar part of the kernel function for steady case
K_{20}	Nonplanar part of the kernel function for steady case
K_g	Geometric stiffness matrix
$\boldsymbol{K_n}$	The modified Bessel function of the second kind and order n
k	Non-dimensional reduced frequency
L	Lift force, also length of beam element
$\boldsymbol{L_n}$	The modified Struve function of the order n
M	Mach number, also bending moment
P	Axial force
q	Dynamic pressure
R	$\sqrt{x_0^2 + \beta^2 r^2}$
r	$\sqrt{y_0^2 + z_0^2}$
r_a	$\sqrt{y^2 + \hat{z}^2}$
r_b	$\sqrt{y^2 + \hat{z}^2}$
r_m	$\sqrt{\hat{y}^2 + \hat{z}^2}$
S	Total area of a lifting surface
s_{ij}	Stiffness matrix coefficient
t	Wing skin thickness, also time
U_∞	Uniform flow velocity

U_n	The n term of the Ueda's series defined in Equation (3.27)
u, v, w	The backwash, sidewash and downwash velocities
u_1	$-X/r$
V	Lateral force
v	Lateral displacement
W_n	The weighting function in the Gaussian quadrature formula.
X	$(x_0 - M R)/\beta^2$
X_1	$\sqrt{X^2 + r^2}$
x, y, z	Global coordinates of a receiving point
$\hat{x}, \hat{y}, \hat{z}$	Local coordinates of a receiving point defined in Equation (3.27)
x_0, y_0, z_0	$(x-\xi), (y-\eta), (z-\zeta)$
x_m, y_m, z_m	$(\hat{x}-\hat{\xi}), (\hat{y}-\hat{\eta}), (\hat{z}-\hat{\zeta})$
y_a, y_b	$\hat{y}-e, \hat{y}+e$
Γ	Gamma Function
α	Angle of attack
β	$\sqrt{1-M^2}$
γ	Euler's constant = 0.57721566490153286060651 2…
γ_r, γ_s	Dihedral angles of receiving and sending elements respectively
$\hat{\gamma}$	$\gamma_r - \gamma_s$
ξ, η, ζ	Global coordinates of a sending point
ξ_c, η_c, ζ_c	Global coordinates of the doublet point of sending element
$\hat{\xi}, \hat{\eta}, \hat{\zeta}$	Local coordinates of a sending point defined in Equation (3.27b)
ω	Frequency
ρ_∞	Uniform flow density

Λ	Sweep angle of a quarter chord line of each element
φ	Velocity potential
ρ	Air density
∇	The Lagrange operator

Subscripts and Superscripts

c	The distance form the doublet point, also spar caps
h	Heaving motion
i	Imaginary part
L, l	Lift force
m	The distance from the middle of a doublet lifting line
N, n	Normal force
r	Real parts
reg	Regular or non-singular functions
sing	Singular functions
s	Sending point, also stringer
x	In a chordwise or *x* direction
y	In a spanwise or *y* direction
0	The distance from the middle of a doublet lifting line in a global coordinates
1	Planar parts, also the first term of a series
2	Nonplanar parts, also the second term of a series
-	Amplitude of a sinusoidal motion
^	The position based on a local coordinate of each element

Abbreviations

AIAA	American Institute of Aeronautics and Astronautics
AGARD	Advisory Group for Aerospace Research and Development
CIMMS	Center for Intelligent Material Systems and Structures (CIMSS)
FAA	Federal Aviation Administration
FAR	Federal Aviation Regulation
MDO	Multidisciplinary Design Optimization
MAD Center	Multidisciplinary Analysis and Design Center
NACA	National Advisory Committee for Aeronautics
NASA	National Aeronautics and Space Administration
SBW	Strut-Braced Wing
UCAV	Unmanned Combat Air Vehicle

Chapter 1

Introduction

For the last half-century, the design of large transonic transport aircraft throughout the world is dominated by a cantilever wing configuration. Many improvements have been made to increase the aircraft performance, but very few diverted from the cantilever wing based design. It is unlikely that a big jump in performance will be possible without a significant departure in vehicle configuration.

In recent years, however, numerous aircraft configuration concepts have been introduced to find a better alternative to the conventional cantilever wing design. A strut-braced wing (SBW) aircraft, Fig. 1, is one such candidate that has the potential for both a higher aerodynamic efficiency and a lower structural weight than a cantilever wing aircraft. Recent research suggests that the major contribution to the improvement of the strut braced wing is due to favorable interactions between structures, aerodynamics and propulsion [1-7] and the use of Multidisciplinary Design Optimization (MDO) to fully exploit the most desirable synergism among these fields[8-22].

Due to the unconventional nature of the strut-braced wing, specific researches on different fields related to its design have been conducted. An important innovation in the form of a telescoping sleeve mechanism for the strut has been proposed by the Multidisciplinary Analysis and Design Center (MAD) of Virginia Tech to prevent strut buckling in a negative-g load maneuver[8-10]. Investigation of the wing-strut interference drag

has been conducted in Refs. 11 and 12. Comprehensive study of the MDO aspects of the strut braced wing were presented in Refs. 8-10 and 17-21.

In the present work, the aeroelastic aspect of the strut braced wing was investigated, and an in-house code, to perform the aeroelastic analysis in an MDO environment, was developed. The code takes into account the influence of the compressive force effect on the aeroelastic analysis. Structural and aerodynamic aspects of the aeroelasticity, including wing modeling, non-uniform beam formulation, unsteady lifting surface aerodynamic formulation and flutter solution, are incorporated in the code.

In the present chapter, a review of the literatures related to the present work will be presented first, including a survey on strut braced wing research, wing modeling, non-uniform finite element beam formulation, unsteady aerodynamics, and wing aeroelasticity. The last section of this chapter presents the contribution of the present work to the field.



Figure 1.1. The strut-braced wing aircraft with fuselage-mounted engine configuration

1.1 Literature Review

1.1.1 Strut Braced Wing Aircraft

A strut-braced wing (SBW) aircraft is a transport aircraft configuration with a strut connected between the wing and the fuselage, as shown in Fig. 1. The strut-braced wing configuration, actually, have been used both in the early days of aviation and is being used in today's small airplane. In the early days, the strut was needed to give additional support to the wing with thin airfoil section or to the double wing. However, the presence of the strut, without a proper strut shape design and arrangement, resulted in a significant drag penalty. On the other hand, improvement on a cantilever wing structure, with appropriate wing-box reinforcement and advancement of composite material, makes it less attractive to use the external strut to support the wing of a large transport aircraft[21].

However, the idea of the strut-braced wing has continued in the aerospace research and industry. In 1954 Pfenninger of Northorp[1] introduced the SBW concept as a means to reduce the induced drag through an increase of the wing aspect ratio for a long range transport. In the 1960s, Lockheed investigated the use of the strut-braced wing on a C-5A fuselage for a long range military transport[2]. In 1978, Kulfan and Vachal[3] of Boeing showed the advantage of the SBW performance over a cantilever wing in a preliminary design study of a large subsonic military plane. Turriziani *et al.*[5] addressed fuel efficiency advantage of the SBW of aspect ratio 25. Gradually, through these efforts, it was understood that the bending moment of the wing can be reduced by employing the strut appropriately. Therefore it becomes possible to reduce wing weight, to reduce airfoil thickness or to increase the wing aspect ratio. The increase of wing span may decrease the induced drag. Also, a lower wing thickness allows a reduction in transonic wave drag and, hence, allows a reduction in wing sweep angle. Reduced wing swept angle and increased wing aspect ratio provide a possibility for a region of laminar flow, and hence less skin friction drag on the wing's

surface. The reduction in the weight and an enhanced aerodynamic efficiency results in both a smaller engine and less fuel consumption.

Consequently, because of the tight coupling between aerodynamics, structures and propulsion, an MDO approach is needed to fully exploit the synergism of these fields. Previous implementations of the MDO approach in aircraft design, showed that the overall performance can be improved significantly.[14-16] In 1996, Dennis Bushnell, chief scientist of NASA Langley Research Center, challenged the Multidisciplinary Analysis and Design (MAD) Center of Virginia Tech to apply MDO methodology to the design of the strut-braced wing aircraft concept[7,8]. The strut braced wing was designed to have a range of 7,500 nautical miles, 325 passengers, and a cruise Mach number of 0.85. Three configurations were investigated including the SBW configurations with under-wing engine, wing-tip mounted engine and fuselage-mounted engine [9-12]. The multidisciplinary teams of graduate students and faculty members worked on aerodynamics, structure and the integration of the fields in an MDO framework. Contributions of the Virginia Tech team to the SBW design have been published in Refs. 7 – 12, and 16 - 22.

Earlier studies on a strut-braced wing have shown that, without any special treatment, the strut may exhibit a large deformation or even buckle under a negative-g load maneuver. Park in Ref. 4 reported that, a significant increase in the strut size was needed to avoid the strut buckling. To answer this major design issue, the Virginia Tech team proposed an important contribution: a telescoping sleeve mechanism for the strut that permits the strut to be inactive during a negative-g flight maneuver[7,9]. For a typical single strut design this means that the strut would first engage in tension at some positive load factor. This can be achieved by providing a slack in the wing strut mechanism. To prevent the strut from engaging and disengaging during cruise due to wind gust loads, the strut was designed to initially engage at the load factor of 0.8 g.

Another major challenge in the SBW design is the interference drag between the wing, strut and fuselage. To address the problem, a computationally intense investigation has been conducted using CFD tools to predict the interference drag of a streamlined strut

intersecting a surface in transonic flow[11,12]. The investigation is for a generic case employed to simulate the flowfield in the vicinity of wing-strut, wing-pylon, and wing-body junctions. Several parameters influencing the interference drag are investigated including the strut-wall angle, strut thickness to chord ratio and cruise Reynolds number. By constructing a response surface function of the interference drag with respect to these parameters, the MDO module of the strut braced wing can exploit the influence of the interference drag to the global design.

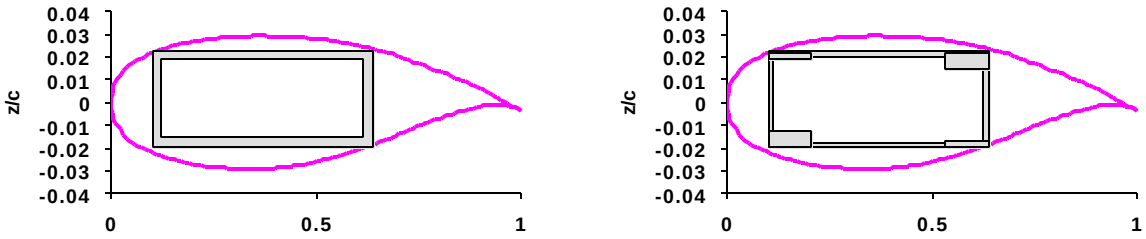
A detailed investigation of the effect of the MDO design constraints on the three different SBW configurations and one cantilever wing aircraft has been performed in Refs. 17 and 18. The three SBW aircraft investigated include the fuselage-mounted engine, the under-wing engine, and wing-tip mounted engine configurations. The study revealed that in all the design configurations, the aircraft range is the most crucial constraint in the design. The results showed also that all three SBW design were less sensitive to constraints than the cantilever wing aircraft.

1.1.2 Structural Wing Modeling

For a conventional cantilever wing aircraft, a common approach to estimate the aircraft weight is by using the weight estimation routine from NASA Langley's Flight Optimization System (FLOPS)[23]. For unconventional aircraft designs, however, some modifications to the FLOPS routine are needed to include the influence of the unique characteristics of such designs. For a structural investigation of the so-called joined-wing aircraft, Kroo *et al.*[24] proposed to use two rectangular box models for their wing structure as shown in Figs. 1.2.a and b. Initially, their wing model used a symmetrical box with caps and webs of uniform thickness (Fig. 1.2a). However, another study [24, 25] on the joined wing design indicated that the most desirable arrangement for the joined-wing spars is asymmetric, with most of the material stiffness concentrated in opposite corners of the rectangular box as shown in Fig 1.2b. The total design variables of their latest wing box model are four, including the cross-sectional areas of the stringers (where diagonally opposite stringers have

the same area) for the bending weight, and the web and skin thickness for the shear and torsional weight prediction.

In the strut-braced wing design investigated in MAD Center of Virginia Tech, the bending weight of the structural wing box was calculated initially based on the so-called double plate model as shown in Fig. 1.3a[9, 12]. This model is made of upper and lower skin panels to carry the wing bending moment The design variable needed for each wing box section is only one since the upper and lower plate thicknesses are identical. Because of the simplicity of the model, the double plate formulation offers the possibility to extract the wing bending weight distribution by a closed form solution. The accuracy of the model to a cantilever wing design has been demonstrated in Ref. 12.



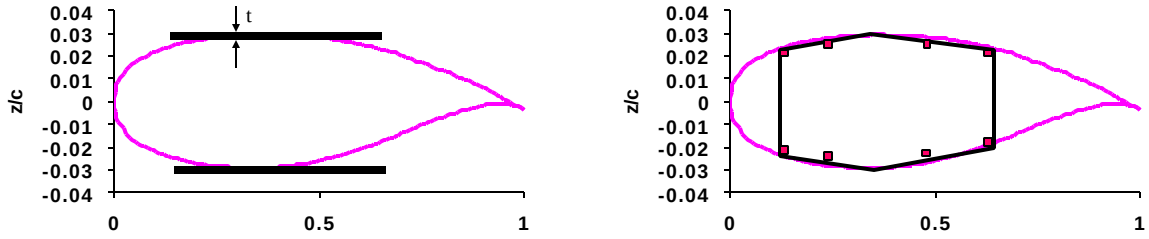
(a) (b)

Figure 1.2. The rectangular wing box models for the joined-wing structure model

The drawback of the double plate approach is its inability to predict the wing-box torsional stiffness. This torsional stiffness becomes essential for calculating wing twist and flexible wing spanload, as well as for predicting flutter speed. Therefore, in the present work, a hexagonal wing-box model (Figure 1.3b) was proposed. The basic form of the model was provided by Lockheed Martin Aeronautical Systems (LMAS) in Marietta, Georgia[26]. As shown in Figure 1.3b, the wing section consists of four skin panels covering the upper and lower part of the airfoil, two shear webs at the front and rear, four spar caps and four stringers at the middle of each skin panels web. Therefore in each section there are 14 different

variables representing wing section sub component stiffness. Compared to the double plate model that needs only one variable, the hexagonal model has more complicated geometry to better simulate the shape of the airfoil and is consequently more difficult to find its optimum stiffness directly.

To simplify the problem, Olliffe of LMAS[26] suggested setting only one sub-component as the independent variable and the other 13 sub-components as dependent variables. For example, if the dimension of the lower-rear part of the skin is given, than the other dimensions of the skins, shear webs, stringers and spar caps can be calculated directly. Such direct calculation can be performed provided the aspect ratio between the sectional area of each part of the element is known. In the present work, the use of the optimized aspect ratio among wing section elements suggested by LMAS was employed in such a way that the total bending weight of the double plate model is the same as the present hexagonal wing box model. More detail description of the hexagonal wing box model will be presented in Chapter 2.



(a) (b)

Figure 1.3. The double-plate model (a) and the hexagonal box model (b) for the strut-braced wing structure model

The present hexagonal wing box was employed to generate two wing models: the detailed wing model and the simplified non-uniform beam model. Both wing models were

used to predict the strut-braced wing flutter speed. The detailed wing model consists of various structural wing sub-components such as the wing skins, shear web, spars, and caps modeled as plate and rod finite elements. The aeroelastic analysis of the detailed model was performed using NASTRAN[34], a commercially available finite element code. The detailed model gives an accurate result for the aeroelastic analysis of the strut-braced wing. However, the results are restricted to the case where the compressive force effect is not included. This restriction is due to the fact that the current NASTRAN module does not include the evaluation of the geometric stiffness matrix for the aeroelastic analysis. In addition, a direct application of the detailed model for aeroelastic analysis in the MDO environment is computationally expensive.

On the other hand, the simplified wing model offers a much faster calculation since the number of element are reduced significantly. The simplified model consists of non-uniform beam elements distributed along the elastic axis of the wing. Typical size of the global stiffness matrix in the detailed model is 4000 x 4000, whereas that of the simplified model is only 400 x 400. The accuracy of the simplified model is improved by employing an exact formulation for the non-uniform beam element and by using a hexagonal wing box model to calculate the flexural, torsional and extensional stiffness distribution of the simplified beam. In addition, the effect of the compressive force can be included in the aeroelastic analysis of the simplified beam. More detailed results of the aeroelastic analysis for the detailed and simplified wings are presented in Chapters 2 and 5 respectively.

1.1.3 Non-uniform Beam Finite Element Formulation

Non-uniform cross-section beams, ranging from small frame components to large bridge girder beams, are widely used as structural elements in many engineering fields. They are used to improve the structural strength, to reduce structural weight, or to satisfy architectural or aesthetical requirements. Important characteristic of non-uniform beam-

colums have been investigated since 1773 when Lagrange[31,32] introduced an optimum non-uniform shape of a column subject to an axial load. In aeroelasticity, non-uniform beam models are often used to represent a wing[33,34]. NASA Langley[35] investigated dynamic and buckling characteristics of numerous non-uniform beam geometries for the construction of a large structure platform in space, where, in this critical weight saving case, the use of non-uniform members may prove worthwile[35, 36].

A large number of investigations on the non-uniform beam can be classified into three groups: (i) the study of the element static stiffness matrix[36-46] and geometric stiffness matrix[46-50]; (ii) the study of the dynamic stiffness matrices[46,48,152-156]; and (iii) the study of the shape optimization of the beam-columns[32,157-165].

The formulation of the static stiffness matrix for non-uniform beams has been studied by many researchers[36-46]. Several different techniques have been adopted, including finite element formulations[36-43], finite difference methods[47], and recurrence series methods[44]. Gallagher and Lee[48] and others proposed to use a variational principle to develop the element stiffness matrix. Their development is based on a cubic displacement function, which is the same as the formulation for a uniform beam. The formulation is simple yet it proved to be superior to a piecewise stepped uniform element representation. This method is adopted and extended in many finite element codes such as NASTRAN[186] and ASTROS[187].

Another approach to study beams using the finite element method is based on the flexibility method. Weaver and Gere[36] describe a procedure to construct the stiffness matrix based on the flexibility method for a tapered beam with a linear variation of the bending stiffness *EI*. The flexibility matrix is constructed first based on the tip deflection and rotation of a cantilever beam. A direct integration of the Euler-Bernoulli differential equation is performed to find the deflection or rotation for each concentrated force or moment unit load at the tip of the beam. Karabalis and Beskos[46] present the solution for beams with constant width and linear depth variation. Banerjee and Williams[36] follow the same procedure and present the solution for a non uniform beam with a stiffness variation in the form shown in Table 1.1.

Reference 36 deals with the formulation of a beam element for m = 1, 3, and 4; corresponding to many beam sectional profiles such as circular, rectangular, triangular and other regular geometric sections. Baker[42] solves a more general form of the *EI(x)* function as shown in Table 1.1.

Previous analytical solutions for the non-uniform are restricted only to symmetric cross-sections, i.e the cross coupling moment of inertia E_{yz} is assumed to be zero. There are at least three cases that can not be solved by using the previous analytical solutions:

Table 1.1 Non-uniform beam stiffness and load functions

Method	Beam stiffness distribution function	Load distribution
Karabalis and Beskos[46]	$EI(x) = EI_0\{1+r\ (x/L)\}^m$ $EI_{yz} = 0$	N/A
Banerjee and Williams[36]	$EI(x) = EI_0\{1+r\ (x/L)\}^m$ $EI_{yz} = 0$	N/A
Baker[42]	$EI\ (x)\ =\ EI\ _0\{1+\ r\ \ (x\ /\ L\ )^{m_p}\}^{m_q}$ $EI_{yz} = 0$	$p(x) = \sum_{i=1}^{N_p} s_i x^i$ $0\ <\ x\ <\ L$ (full span)
Present	$EI(x) = \sum_{i=1}^{N_k} p_i\ x^i = EI_c \prod_{j=1}^{N} (x - c_j)^{m_j}$ $EI_{yz}(x) = \sum_{i=1}^{M_k} q_i\ x^i = EI_{yz0} \prod_{j=1}^{M} (x - d_j)^{n_j}$	$p(x) = \sum_{i=1}^{N_p} s_i x^i$ $0\ <\ x_1\ <\ x\ <\ x_2\ <\ L$

M, M_i , m, m_p, m_q, m_j, N, N_i, Np, nj = arbitrary integer number

(1) The first case is related to optimum shapes of columns, such as the one investigated in Refs. 157 – 165, where *EI(x)* can be arbitrary. To accommodate the shape of such optimum column, the polynomial function of the *EI(x)* should have arbitrary multiple roots. In the present work, a more general stiffness distribution along the beam element is shown in Table 1.1

(2) The second case is related to non-uniform loads applied to the beam. Baker[42] solves the static deflection problem of the non-uniform beam under a non-uniform distributed load. However, the non-uniform load considered in Ref. 42 is applicable only for a full span of the beam. For a more general case, where the load can be partially applied to the beam span, the solution given in Ref. 42 can not be applied directly. In the present work, the analytical solution for the general partially distributed load to the non-uniform beam was developed in Chapter 3.

(3) The third case is related to the basic assumption adopted in the previous analytical solution where the beam cross sections should be symmetric, i.e. the cross-coupling moment of inertia term is zero. A treatment for a more general class of the problem, i.e. for non-uniform beam with asymmetric cross section where the cross-coupling moment of inertia distribution is also non-uniform, is developed in Chapter 3 of the present work.

1.1.4 Unsteady Aerodynamic Load Formulation

The Lifting Surface Equation

Accurate prediction of unsteady aerodynamics loads is an essential part of solving aeroelasticity problems. This accurate estimation is required in aircraft design as it is related directly to predicting maximum structural stresses, deflections, flight speed and flight envelope among other quantities of interest. Significant research has been performed in the past in analytical, numerical and experimental aspects of the problem in subsonic, transonic and supersonic flows[51-131]. Such investigations are still going on in an effort to improve the accuracy and efficiency of the prediction methods for more complicated aerodynamic

configurations ranging from two dimensional thin airfoils to full aircraft configurations. In the present work, a numerical approach is proposed for predicting the aerodynamic load for multiple lifting surfaces in steady and unsteady subsonic flows.

Based on a linearized potential aerodynamic equation, or the Laplace equation, several basic theoretical procedures have been developed to evaluate aerodynamic loads on unsteady thin wings or the so-called lifting surfaces[51, 52] as shown in Table 1.2. All of the approaches make use of the Green integral equation to form the working equation. The most widely used version in aeroelasticity is the pressure – normal wash formulation[52, 55] since one deals directly with the pressure difference distribution and the velocity on the surface without any evaluation in the wake region. This formulation was first proposed in 1935 by Kussner[51] in the form shown in Table 1.2. His formulation however did not describe the detailed form of the kernel function *K* that relates the pressure difference with the downwash velocity.

Table 1.2. Unsteady planar lifting surface formulation

Formulation	The Integral Equation*	References
Pressure - normal wash equation	$w = \int_S \Delta p \; K_p \, dA$	Kussner, Laschka, Watkins *et al.*, Giesing *et al.*
Velocity potential formulation	$w = \int_{S+W} \Delta\phi \; K_\phi \, dA$	Jones, Stark, Houbolt, Haviland, Singh, Liu *et al.*
Acceleration potential formulation	$\varphi_z = \int_S \Delta p \; K_\phi \, dA$	Van Spiegel
Integrated acceleration formulation	$\psi_z = \int_{S+W} \Delta\psi \; K_\phi \, dA$	Stark

*S = surface region, W = wake region, Δp = pressure difference, w = downwash velocity, f = velocity potential, j = acceleration potential, $y = \int \varphi \, dx$

Formulation of The Kernel Function

In 1955 Watkins *et al.*[60] published the kernel function K as a function of the oscillating frequency of the lifting surface and Mach number. This first formulation has been widely used to calculate unsteady subsonic loads on planar wing - horizontal tail configurations[52,56]. However, for nonplanar arrangements, such as wings with dihedral, non-planar wing-tail configurations, T or V- tails and wings in ground-effect, a more general approach should be performed. In light of this need, significant development in the formulation of the kernel for nonplanar configurations have been contributed by Laschka[65], Yates[63], Rodemich[64], Landahl[64], and Berman, Shyprykevich and Smedfjeld[105]. Table 1.3 shows a summary of this formulation. Laschka[65] formulated the kernel function for non-planar configurations in terms of the x, y and z components of the induced velocity vector. Yates[63] proposed the kernel function in a slightly different form for the non-planar configurations. The most widely used formula is the one proposed by Landahl[52, 62, 66, 70 – 87, 91 – 93] since it is less complicated than the other formulas mentioned above[64]. The Landahl's formulation is also used in the present work.

Table 1.3. Kernel function formulation for unsteady lifting surface aerodynamic

Contributor	The kernel function form	Publication
Watkins *et al.* (NACA)[60]	Planar configuration, K_w	NACA R 1234 (1955)
Laschka (Germany)[65]	Non planar config. K_u, K_v and K_w	Z. Angew. Math. Mech. (1963)
Yates (NASA)[63]	Non planar config. K_u, K_v and K_w	AIAA Journal (1966)
Landahl (MIT)[52]	Non planar config. K (unified)	AIAA Journal (1967)
Berman *et al.* (Grumman)[55]	Non planar config. K inclined to the free stream	J. Aircraft (1970)
Lan (Univ. Kansas)[88]	Non planar config. K of oscillating horseshoe vortices	NASA SP-405 (1976)

The Incomplete Cylindrical Function

All of the kernel functions formulation for the pressure-normalwash equation summarized in Table 1.3 contains the so-called *incomplete* cylindrical function where the integral limit of the function is ranging from a finite point x on the lifting surface to the infinite point $+\infty$. Before 1981, no exact mathematical solution to the incomplete cylindrical function was available. The only available closed form solution was for a *complete* cylindrical function where the integral limit of the kernel function is ranging from 0 to $+\infty$. The closed form solution for the complete cylindrical function is available in the form of modified Bessel and modified Struve functions of the first and second kinds. More description on the incomplete cylindrical function will be given in Chapter 4 and Appendix A of the present work.

An attempt to approximate the incomplete cylindrical function has been first conducted by Watkins *et al.* in Ref. 51 (1955). In their approximation, the integrand of the kernel function is approximated by four term series in a form that is easily integrated. More accurate approximations were presented by Laschka (1963)[102] , Dat-Malfois (1970)[103], Desmarais (1982), and a more recent publication by Epstein and Bliss (1995)[151]. A summary of these approximation was presented in Table 1.4.

The exact solution to the incomplete cylindrical function was first proposed by Ueda in 1981 by using an expansion series approach[78]. The proof of the Ueda's solution has been presented by the present author in Ref. 135. Another exact solution was presented by Bismarck-Nasr (1991)[70] by using a differential equation approach resulting in the solution in the form of modified Bessel, modified Struve, and sine integral functions. Both Ueda's and Bismarck-Nasr's analytical solutions are converged to the solution of the complete cylindrical function when the finite point on the surface x is set to 0. The only drawback of those solutions is that the strong singularity terms are not easily evaluated since the singularity terms are hidden in the series. A technique to separate the singular and regular

parts of the kernel function has been presented by the present author in Ref. 135 using a modified Bessel function. In the present work, a different approach will be conducted to analytically separate the singular and regular functions. The present approach uses an expansion series to the complex exponential function embedded in the incomplete cylindrical function. A new series in the form of regular term series without the modified Bessel function term will be presented. This effort does not destroy the accuracy of the analytical solution since the separation is performed analytically.

Table 1.4. Solution to the incomplete cylindrical function occurring in the kernel function of the unsteady lifting surface theory

Method	Solution
Watkins *et al.* (1955)	Four term approximation series
Laschka (1963)	11 term approximation series
Dat and Malfois (1970)	Seven term approximation series
Desmarais (1982)	12 term approximation series
Epstein and Bliss (1995)	Three and Four term series
Ueda (1981)	Analytical solution using an expansion series
Bismarck-Nasr (1991)	Analytical solution using differential equation approach
Present	Analytical solution using an expansion series and separation of the singular and regular functions

The Lifting Surface Method

After the kernel function has been well formulated, the next challenge for predicting the unsteady aerodynamic load was the method to solve the integration of the kernel function. This integration should be performed in a rather careful way since the kernel function contains a strong singularity function when its argument is near zero. Vast literature on the

methods shows a gradual improvement on the accuracy, capability and efficiency of the integration technique, as is pointed out in the survey papers in References 52, 55, 68, and 69.

The integration solution methods can be divided into two broad categories, the mode function method (or the kernel function method) and the discrete element method[66]. The mode function methods use an assumption that the pressure distribution may be approximated by a series of orthogonal polynomial functions with unknown coefficients which are determined by satisfying the flow tangency boundary conditions at a collocation point.[52,69]. For wing with control surfaces or other complex configurations, a careful treatment for pressure discontinuity is needed and therefore make this first method sensitive to the manner of representing the additional singularities associated with such geometry.

The usual procedure for the second method is to divide the lifting surfaces into infinitesimal trapezoidal panel elements which permit the assumption that the pressure load is constant within one element. The integral equation of the pressure-normal wash equation is represented in a discrete set of linear equations with the pressure load at each element as the unknown. The linear equation is solved by imposing the flow tangency boundary condition at each element. This approach, which is used in the present work, is more suitable for a complicated lifting surface planform since a similar treatment to discritize the planform can be performed.

Several variations of the discrete element method have been proposed. For the steady subsonic flow, one of the well known discrete element methods is the vortex lattice method (VLM), such as the method of Weissinger[121], Falkner[141], Campbell[142], Hedman[137], Belotserkovskii[140], Rubbert[189], Dulmovits[190], Margason and Lamar[90], Lan[88,100] and Mook *et al.*[186] For unsteady subsonic flow, these include the doublet lattice method (DLM) of Stark[52], Albano *et al.*[70], Jordan[71], and Giesing *et al.*[62, 67, 72], Rodden *et al.*[143-145], and van Zyl [146-148], the doublet point method (DPM) of Houbolt[73], and Ueda and Dowell[66], the doublet strip method of Ichikawa *et al.*[74], and the hybrid doublet-lattice/doublet point (DHM) of Eversman and Pitt[75].

In the present work, a scheme to improve the numerical procedure of the doublet lattice method, doublet point method and doublet hybrid method will be proposed. A brief introduction to the existing DLM, DPM, and DHM methods is discussed and the new approach is described in subsequent sections.

The Doublet Lattice Method

For a subsonic aeroelasticity analysis, the most widely-used version of the unsteady aerodynamics method is the doublet lattice method of Rodden *et al.*[80] because of its ready applicability to complex nonplanar configurations. NASTRAN[53, 80] uses the DLM version developed in Refs. 12, 17 and 22 where a quadratic approximation (DLM-quadratic) is used for integrating the kernel function. Despite the wide acceptance of the method, however, the DLM-quadratic version is sensitive to the element aspect ratio and the number of chordwise boxes per wavelength. To obtain acceptably accurate results for DLM-quadratic version, NASTRAN User's Manual[80] suggests using the element aspect ratios less than 3 and at least 25 boxes per wavelength. Van Zyl[146, 147] pointed out that the DLM-quadratic version contains an inaccuracy in the integration of the elemental kernel function. He proposed to improve the accuracy by using a piecewise cubic spline approximation to replace the quadratic function in each element[146] and reported improvement in the convergence rate[147]. However, van Zyl's DLM version required a considerable amount of calculation since for each element the method would need a large number of interpolation points. Reference 146 shows that the interpolation points needed for convergence can be as many as 129 points per element as compared to only 3 points per element needed for the DLM-quadratic version.

Recently, Rodden *et al.* [143-145] attempted to improve the accuracy of the DLM by proposing a DLM-quartic version, a new scheme for the integration of the kernel function by increasing the order of the polynomial approximation from a quadratic function to a quartic function. The DLM-quartic version[143, 144] allows the use of the element aspect ratio of up to 10, a considerable improvement compared to the maximum aspect ratio of 3 for the DLM-quadratic. The DLM-quartic version, however, still requires a large number of chordwise

boxes per wavelength. Reference 144 suggested a minimum number of 50 chordwise boxes per wavelength, which is significantly higher than that for the DLM-quadratic version. A numerical study devoted to investigate the convergence of the DLM was conducted in Ref. 147 and concluded that the limitation of the DLM-quartic version is as a result of the integration error introduced by the approximations to the kernel numerators.

Another limitation of the DLM-quadratic version was pointed in Ref. 72. In their analysis, Rodden *et al.*[72] mentioned that the near-coplanar configuration problem is not completely solved. The procedure fails, for example, if the vertical separation between two lifting surfacess is very small. For such a case, the DLM-quadratic version automatically sets the vertical separation to be zero. For practical cases, it may be acceptable to assume the two lifting surfaces to be coplanar if the vertical separation is very small. However, from theoretical point of view, this indicates that an effort to improve and optimize the method is still needed.

An effort to improve the accuracy of the method has been proposed by Jordan in Ref. 71. In his DLM version, an exact integration of the kernel at a quarter chord of the element has been completed. However, this technique is limited to rectangular planar surfaces in incompressible flow ($M = 0$). It should be noted that, if the Prandtl-Glauert compressibility correction is taken into account, the mathematical form of the kernel function becomes very complicated. An exact integration of the kernel function is still a challenge. In the present work, only the singular part of the kernel function can be integrated analytically. The regular part is integrated numerically using Gauss-Legendre quadrature technique.

One possible source of the inaccuracy in the previous DLM is the integration to the improper cylindrical function occurring in the kernel function. The incomplete cylindrical function in the DLM-quadratic version is solved using Laschka's series to approximate the integrand of the integral as described in Table 1.4. There are two disadvantages to this scheme. *First*, the accuracy of Laschka's series is limited to the order of three digits. *Second*, the series approximates the integrand, and not the integral itself. Gazzini *et al.*[82] showed that an approach to performing the integration by approximating the integrand may

not be equivalent to the approach to performing the integral itself. Therefore, it is believed that the application of the exact solution to performing the improper integral directly, which is conducted in the present work, will increase the accuracy of the previous works.

The kernel function in the DLM of NASTRAN contains regular and singular functions as the values of r approaches zero and $X > 0$. There is no separation between these functions in the DLM. Therefore the Mangler procedure is also applied to the regular function, which is not a proper way to solve the problem. In the present work, the regular and singular functions will be identified and treated separately.

The DLM uses a quadratic or a quartic approximation for the numerator of the kernel to simplify the integration procedure. This procedure may be improved if one uses Gaussian quadrature technique as is suggested by some authors [83-86]. The Gaussian technique does not need a fixed number of integration points. Less than three points may be used if the sending/receiving panel pairs are distant or if the reduced frequency is low. If the reduced frequency is high, or if the distance between sending and receiving panels is close such that the kernel function may vary rapidly, one may use more than three integration points. The improvements outlined above will be implemented in the present work.

The Doublet Point Method

The idea of the DPM was first proposed by Houbolt[81] based on the pressure-velocity potential concept, and independently by Ueda and Dowell[66] based on the pressure-normal wash concept. Houbolt (1969)[81], however, did not give numerical results for three-dimensional flows since a direct evaluation of the incomplete cylindrical function was not available at that time. The exact solution of this type integral was given in 1981, and the first version of the DPM was developed in 1982 for planar surfaces[66].

There are two basic assumptions used in the original DPM[66]. First, the lifting pressure is assumed to be concentrated at a single point located at the one-quarter chord along the center line of each element. The point is called a doublet point. Similar to the DLM, the control point is placed at the three-quarter chord along the mid-span of each panel.

Second, if the receiving point is located on the wake of the sending element, i.e. $X > 0$ and $r = 0$, then the singularity problem occurs and the finite part of the Mangler integration procedure should be used by utilizing an average value of the modified Bessel function to treat the singularity problem.

Although the formulation is very simple, the DPM gives a reasonable accuracy for various planar lifting surfaces[66]. However, for a lifting surface with a large swept angle, the accuracy of the DPM can be less than that of the DLM. Rodden commented in Ref. 66 that the DPM does not have the *local* sweep angle effect in their formulation. In the present DPM formulation, it will be shown that the local sweep angle effect is incorporated in the formulation based on a proper integration of the kernel function.

Improvements to the DPM proposed in the present study also include a treatment for nonplanar configurations which is not considered in the original DPM[66]. The idea to separate the singular and regular parts of the kernel functions is also applied to the nonplanar surface formulation. It will be shown that some singular parts of the planar term will cancel the other singular parts of the nonplanar term in the present formulation. This treatment clearly will improve the accuracy of the nonplanar DPM.

Doublet Hybrid Method of Eversman and Pitt

An extension of the DPM for nonplanar interfering surfaces has been made by Eversman and Pitt[75] based on the nonplanar kernel function of Landahl. In their work, a treatment for the singular term of the kernel nonplanar part was not well established. The results have been reported to be less accurate than the DLM results. For this reason, they concluded that the best approach is to utilize the nonplanar DPM only for sending/receiving pairs which are distant. If the distance between sending and receiving points are close, they suggest using the nonplanar DLM. This combined technique is the basis of their doublet hybrid method (DHM). No further treatment for the limitation of DPM and DLM was conducted, therefore some singularity problems associated with the DPM and DLM may be found in their DHM.

In the present DHM, the singularity problem is identified and solved in each of the present DPM and DLM procedures. The present DHM also unifies the present DLM and DPM procedures such that the present DPM becomes a special case of the present DLM.

1.1.5 Strut-Braced Wing Aeroelasticity

Aeroelasticity is one important factor in the strut braced wing design. Aeroelasticity takes into account the flexibility of the aircraft structure and its static or dynamic interaction with the aerodynamic loads. Aeroelasticity may constraint the flight envelope, structural weight and aircraft performance which are closely related to design variables of the MDO tool used in the present strut braced wing design.

Most previous publications on the strut braced wing aeroelasticity deal with the static aeroelastic response of the structure under a given aerodynamic loading. The main concern has been usually to take advantage of the strut support for reducing wing bending moment. Few publications have investigated the aeroelastic behavior, such as flutter and divergence, of the strut braced wing. Reference 28 introduced the so-called "the Keldysh problem" to analyze the aeroelastic stability of a simple wing model with a strut as shown in Figure 1.4. The wing planform is rectangular, straight and has no dihedral. The wing aspect ratio of the considered wing is high and the flow is assumed to be incompressible to allow the use of simple strip theory for the unsteady aerodynamic calculation.

The bending and torsional stiffness along the wing span is assumed to be constant in the Keldysh problem. The strut is a perfectly rigid rod connecting the wing-strut junction to the fuselage-strut junction (Figure 1.4). Based on the Bubnov-Galerkin one term approximation, Keldysh concluded that the wing is stable if the wing-strut junction location y_s is greater than 0.47 of the half span L. In a more recent article, Mailybaev and Seiranyan[27] corrected the Keldysh's solution by using a more rigorous approach and adding a divergence related instability as the solution to the problem. One of their conclusions for the Keldysh problem is that, for $y_s > 0.47$ L, the wing will experience divergence, rather than be stable as concluded by Keldysh. The divergence speed is twice the critical speed of a cantilever wing

of the same size but without a strut. Hence, for the Keldysh problem, the best location for the wing-strut junction is between 47% of the half span and the wing tip.

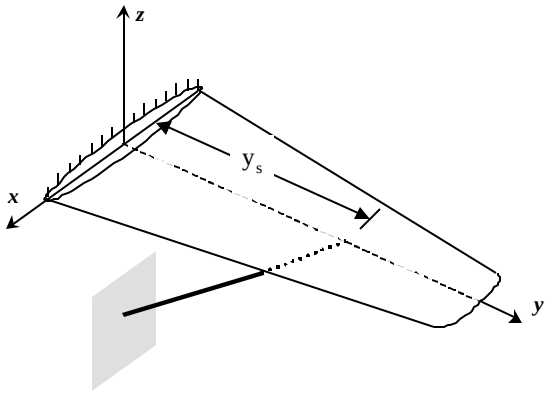


Figure 1.4 The strut braced wing model of the Keldysh problem

The Keldysh problem above demonstrates the importance of the location of the wing strut junction. In the present work, a broader problem is considered. The wing is swept back and tapered. The wing taper ratio is 0.21, the quarter chord swept angle is 29.9° and the aspect ratio is 12.17. The unsteady aerodynamic load is predicted using the doublet lattice lifting surface method which is better than the simple strip theory approach used in Ref. 22. The strut stiffness in the present work is not infinite and the angle between the wing and strut is very shallow (Fig. 1.1) which will impose a more flexible support at the wing-strut junction point. Figure 1.1 also shows that the wing and strut are not in the same plane and therefore the wing strut junction point moves elastically in the six degrees-of-freedom deformations.

The aeroelastic analysis of the present strut-braced wing problem will be conducted with two different wing models: detailed and simplified wing models. The analysis of the detailed wing model will be performed using NASTRAN software. The analysis of the simplified model will be performed using the aeroelastic analysis code developed in the

present work. The aeroelastic analysis results of the detailed and simplified wing model are presented in Chapters 2 and 5, respectively.

1.2 Dissertation Outline

The present work will be organized as follows:

- Chapter 2 presents the aeroelastic analysis of the detailed model of the strut-braced wing. The calculation is performed using NASTRAN. No compressive force effect is included in the calculation.
- Chapter 3 describes the formulation and validation of the structural stiffness of the present non-uniform beam finite element.
- Chapter 4 describes the formulation and validation of the present unsteady lifting surface methods.
- Chapter 5 presents the aeroelastic analysis of the simplified model of the strut braced wing. The calculation is performed using the present code. The compressive force effect is included in the calculation.
- Chapters 6 and 7 present the concluding remarks and recommendation for future work, respectively.
- Appendix A describes the detailed derivation of the present kernel function integration related to the formulation of the unsteady lifting surface methods in Chapter 4.
- Appendix B presents a brief description of the aeroelastic stability envelope.
- Appendices C and D describe detailed derivation of the rational function and translation of axis needed for the FEM formulation of the non-uniform beam in Chapter 3.

1.3 Contribution to the Field

The following are the original contributions contained in this dissertations:

1. An analytical formulation of the non-uniform beam stiffness is introduced to reduce the number of elements used in the wing finite element model, and, hence, to reduce the computational time.

   The beam element stiffness distribution is an arbitrary polynomial function. The stiffness distribution of the element includes the variation in the cross sectional area A, the moment of inertia I_{yy}, I_{zz} and I_{yz}, and the torsional stiffness J.
2. An iteration procedure to improve the buckling calculation of the beam is introduced based on a Taylor expansion series.

   The iteration scheme is qudratically convergent. The result gives the same result as the standard buckling calculation if only a single iteration is performed and the initial buckling load is zero.
3. A numerical scheme to unify the doublet-lattice and doublet point methods is introduced to improve the accuracy and reduce the computational time. The present formulation is derived based on analytical separation of the regular and singular functions embedded in the lifting surface kernel function.
4. A strut-braced wing model is developed for static and dynamic aeroelastic stability analysis. Two models were generated, including a detailed wing model and a simplified beam model. The detailed wing model consists of 14 wing section sub-components such as wing skins, spars, caps, and webs. The simplified beam model include the compressive force effect in the aeroelastic calculation.
5. A procedure to include the compressive force effect in aeroelastic stability of the strut-braced wing is developed. The developed code modules are as follows:
   - *ehexa.f* : to generate the detailed wing model as well as the simplified model based on the equivalent hexagonal wing box approach.
   - *fem.f* : to generate the FEM stiffness, geometric stiffness and mass matrices of the structural beam model.
   - *vlm.f* : to generate the steady aerodynamic load.
   - *dhm.f* : to generate the unsteady aerodynamic load.

- *trim.f* : to calculate the wing aerodynamic load, structural displacement, and structural (compressive) forces for the wing under given flight load condition. The wing flexibility and strut slack load factor are included in the analysis.
- *Mode.f*: to calculate the frequencies and mode shapes of the strut braced wing including the compressive force effect.

The relationship between these modules are shown in Fig. 1.5.

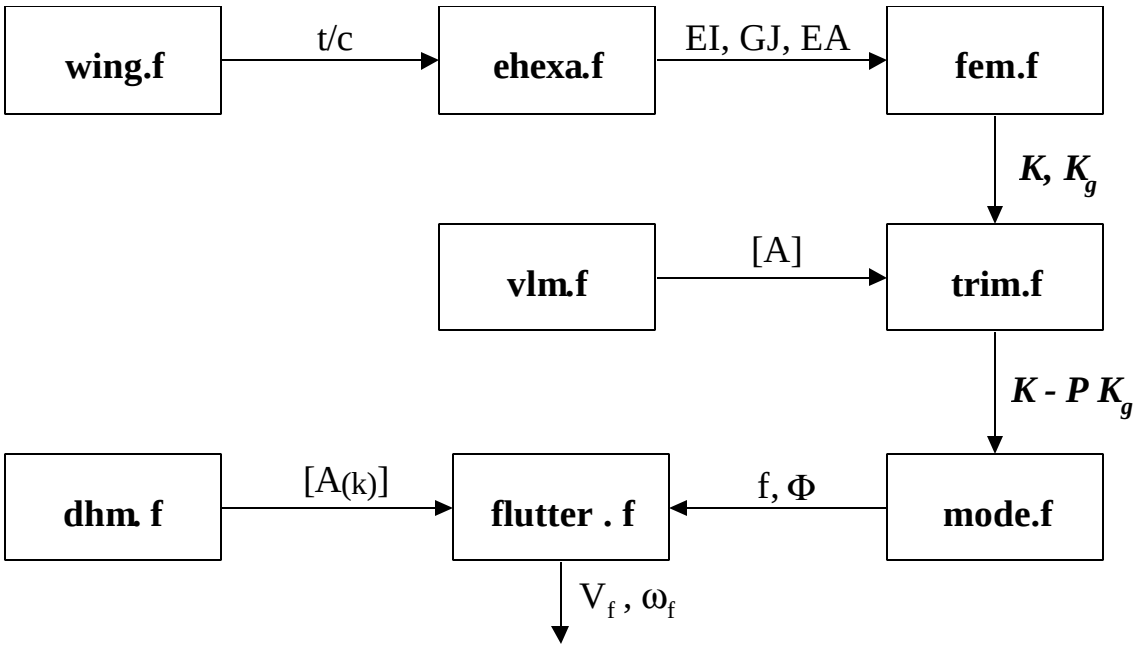


Figure 1.5. The present aeroelastic computational module of the strut-braced wing

Chapter 2
Strut-Braced Wing Aeroelasticity Without Geometric Stiffness Effect

2.1 Introduction

Aeroelasticity is one important factor in aircraft design. Aeroelasticity takes into account the flexibility of the aircraft structure and its static or dynamic interaction with the aerodynamic load. Aeroelasticity may provide a constraint on the flight envelope, structural weight and aircraft performance. For the strut braced wing aircraft design, aeroelasticity has a more significant role due to the unconventional nature of the aircraft as described in the previous chapter. From the aeroelastic point of view, the strut-braced wing aircraft has at least three important characteristics which make the aeroelastic behavior of a strut-braced wing different from the conventional aircraft. First, the strut gives additional support to the wing that changes the aerodynamic load distribution pattern on the wing. This aerodynamic load redistribution further affects the wing weight and structural stiffness distribution. Second, as a further result of multi-disciplinary optimization of various fields involved in the design of the strut-braced wing aircraft, the wing thickness becomes thinner and the wing aspect ratio becomes larger. With a more flexible structure, aeroelastic considerations become even more important. Third, the presence of the compressive axial force in the inner

wing due to the strut force adds a geometric stiffness term to the aeroelastic set of equations. This additional geometric stiffness term increases the complexity of the stability problem since an eigen problem related to the wing buckling is added to the conventional aeroelastic problem. In the present Chapter, the aeroelastic analysis of the strut braced wing is performed by focusing on the first two aforementioned effects. The third effect, related to the effect of compressive force on the strut braced wing aeroelastic response, is described in Chapter 5.

Most previous publications on the strut braced wing aeroelasticity usually with the static aeroelastic response of the structure under aerodynamic loading. The main concern is usually to take advantage of the strut support for reducing the wing bending moment. References 9 and 13 describe a simple approach to predicting the strut-braced wing weight based on a double plate model for the wing section. The double plate model gives an accurate prediction for the wing bending weight, however it is not suitable for predicting the torsional stiffness of the wing. For this reason, Refs. 9 and 19 introduced an alternate hexagonal section model of the wing that allows a more accurate prediction of both the wing bending and torsional stiffness. A detailed description of the hexagonal section model used in the present work is described in Section 2.2.

Few publications have investigated the aeroelastic behavior, such as flutter and divergence, of the strut braced wing. Reference 28 introduced the so-called “the Keldysh problem” to analyze the aeroelastic stability of a simple wing model with a strut as shown in Figure 2.1. The wing planform is rectangular, straight and has no dihedral. The wing aspect ratio is considerably high and the flow is assumed to be incompressible to allow a simple strip theory for unsteady aerodynamic calculation.

The bending and torsional stiffness along the wing span is assumed to be constant in the Keldysh problem. The strut is a perfectly rigid rod connecting the wing-strut junction to the fuselage-strut junction (Figure 2.1). The wing strut junction point is on the wing elastic axis. The rigid strut assumption imposes a pin-type support boundary condition at the wing-strut junction point, i.e. the wing is continuous at the junction point, is free to rotate but is

restrained from transverse displacement. The Keldysh problem also ignores the geometric stiffness effect.

Based on the Bobuno*v*-*G*alerkin one term approximation, Keldysh concluded that the wing is stable if the wing-strut junction location y_s is beyond 0.47 of the half span L. In a subsequent article, Mailybaev and Seiranyan[27] improved the Keldysh's solution by using a more rigorous approach and adding a divergence related instability as a possible solution to the problem. Their conclusions for the Keldysh problem are as follows:

(a) For $y_s > 0.47\ L$, the divergence instability is more critical than the flutter. It is found also that the divergence speed is constant, i.e. the strut support does not improve the stability performance if the junction point is moved further outboard.

(b) For $y_s = 0.47\ L$, the flutter speed becomes the same as the divergence speed.

(c) for $y_s < 0.47\ L$, the flutter instability is more critical than the divergence. The flutter speed varies as the junction point moves inboard, but the flutter speed is less than the speed at $y_s = 0.47\ L$.

(d) Therefore, the optimum location of the strut is located in the region $y_s > 0.47\ L$. The minimum divergence speed is 60.3 m/s which is higher than the critical speed of a cantilever wing, the same size but without strut, 30.3 m/s. Hence, for the Keldysh problem, the strut increases the critical speed more than 100%.

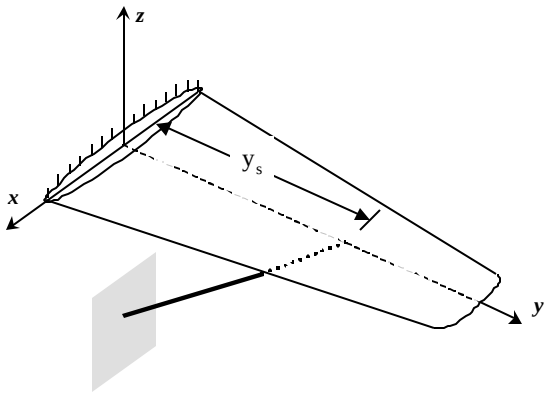


Figure 2.1 The strut braced wing model of the Keldysh problem

The Keldysh problem above demonstrates the effectiveness of the strut to increase the critical speed and the importance of the location of the wing strut junction. In the present work, a broader problem is considered. The wing is aft-swept and tapered. The wing taper ratio is 0.21, the quarter chord swept angle is 29.9° and the aspect ratio is 12.17. The unsteady aerodynamic load is predicted using the doublet lattice lifting surface method which is better than the simple strip theory approach used in Refs. 27 and 28. The compressibility of the aerodynamic load is taken into account by employing the Prandtl-Glauert transformation in the unsteady aerodynamic governing equations.

The strut stiffness in the present work is not infinite and the angle between the wing and strut is very shallow (Figures 2.2 and 2.3) which will impose a more flexible support at the wing-strut junction point. Figure 2.2 also shows that the wing and strut are not in the same plane and therefore the wing strut junction point moves elastically in the six degrees of freedom deformations. The wing bending and torsional stiffness is not constant. A more detailed data of the aircraft is given in Table 1.1.

The present strut-braced wing problem is solved using the MSC/NASTRAN finite element code. The effect of the wing-strut junction position in spanwise and chordwise directions is investigated, as well as the fuselage-strut junction point. The wing bending stiffness is obtained based on the double plate model. In order to estimate the wing torsional stiffness, a hexagonal wing section approach is used to model the structural wing box. A more detailed description of the hexagonal wing section approach is described in Section 2.2. The flutter and divergence of the strut-braced wing and the sensitivity of the wing-strut junction location are described in Section 2.3 and 2.4 respectively.

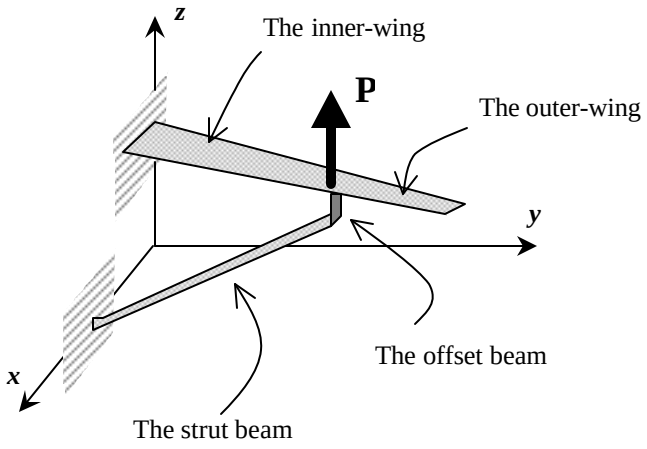


Figure 2.2. A space frame model of the present strut-braced wing-strut

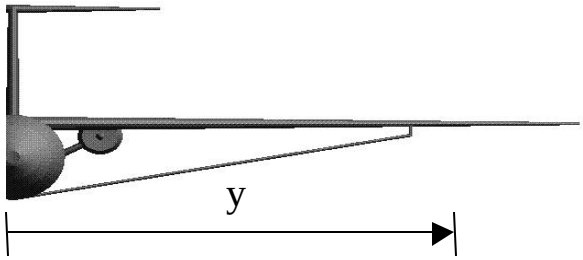


Figure 2.3. Front view of the present strut-braced wing

Table 2.1. Strut-braced wing aircraft parameters

Wing half-span	108.44 ft
Wing - strut junction point	74.52 ft
Wing sweep (3/4 chord)	25.98°
Strut sweep (3/4 chord)	19.01°
Strut offset length	2.74 ft
Wing root chord	32.31 ft
Wing tip chord	6.77 ft
Strut force at 1 g load	215 387 lb
Strut chord (constant)	6.62 ft
Wing root t/c	13.75%
Wing tip t/c	6.44%
Strut t/c	8.0%
Fuselage diameter	20.33 ft
Wing flap area	1411.02 ft^2
Wing reference area	4237.30 ft^2
Take-off gross weight	504833 lb

2.2 Wing Section Model

2.2.1 Double Plate Model

A common approach to estimating the preliminary bending weight of a conventional wing is usually by using a semi-empirical equation such as the NASA Langley developed Flight Optimization System FLOPS[23]. Application of this procedure to a strut braced wing, however, may give inaccurate results due to the unconventional nature of the structure. For this reason, several bending weight calculation procedures, by taking into account the influence of the strut upon the structural wing design, were developed in the MAD Center of Virginia Tech. The earliest work is based on a double plate assumption of the wing box structure as reported in Refs. 13, 19, and 21.

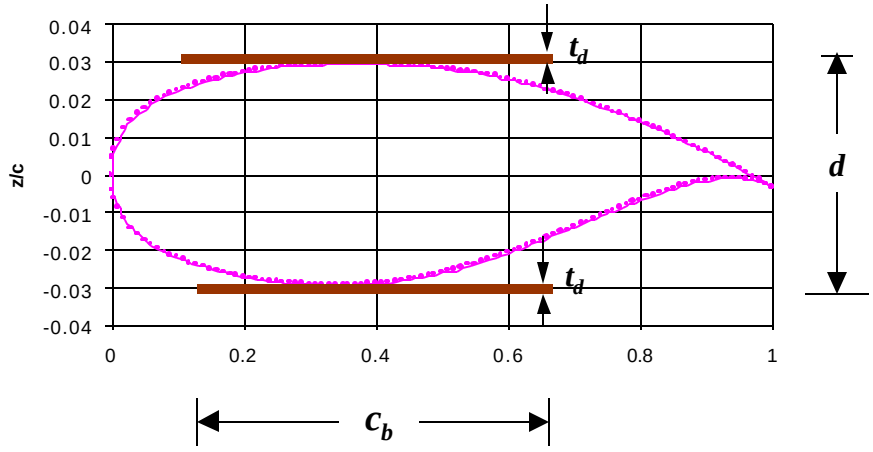


Figure 2.4. The double plate model to represent the wing bending box

To calculate the wing-bending weight of single strut configuration, a piecewise linear beam model, representing the wing structure as an idealized double plate model, was used first. This model is made up of upper and lower skin panels (Figure 2.4), which are assumed to carry the bending moment. The double-plate model offers the possibility to extract the

material thickness distribution by a closed-form equation. The cross-sectional moment of inertia of the wing box can be expressed as:

$$I(y) = \frac{t_d(y)\, c_b(y)\, d^2(y)}{2} \tag{2.1}$$

where $t_d(y)$ is the wing skin thickness, $c_b(y)$ is the wing box chord, and $d(y)$ is the wing airfoil thickness. Note that the upper and lower wing skin thickness are equal. To obtain the bending material weight, the corresponding bending stress in the wing is calculated from:

$$s_{\max} = \frac{M(y)d(y)}{2I(y)} \tag{2.2}$$

where $s_{\max}$ denotes the maximum stress, $M(y)$ is the bending moment of the wing, and $I(y)$ denotes the cross-sectional moment of inertia.

If the wing is designed according to the fully-stressed criterion, the allowable stress s_{all} can be substituted into Eq. (2.2) for $s_{\max}$. Substituting $I(y)$ into Eq. (2.2), the wing panel thickness can be specified as:

$$t_d(y) = \frac{|M(y)|}{c_b(y)d(y)\sigma_{all}} \tag{2.3}$$

The chord length c_b and the maximum airfoil thickness d along the wing span are given from the wing geometry data for each iteration in the MDO optimization loop. The bending moment $M(y)$ is obtained by considering three critical loading cases including the –2.0 g taxi bump, the 2.5 g pull-up, and the –1.0 g push-over maneuvers. The loading is simplified by assuming a piecewise linear distribution along the wing span. In addition to fulfilling the strength requirement in Eq. (2.3), this loading is also employed to calculate the wing tip displacement constraint. The final panel thickness along the wing span is obtained as a minimum thickness curve envelope that satisfies the structural strength and displacement constraints for all of the loading maneuvers specified above.

Three of the most important features of the double plate approach are as follows:

- In each section of the wing box, only one independent variable, which is the panel thickness $t_d(y)$, is needed to represent the bending stiffness and weight.
- Since the model is simple, a closed form solution for the panel thickness can be obtained based on the fully stressed design concept.
- The numerical procedure to approximate the wing bending weight, because of its simple formulation, is very fast. Therefore the method is suitable for an MDO calculation module.

The accuracy of the double plate method to approximate the wing bending weight has been demonstrated in Refs. 12 and 17. A more detailed description of the method is described in Ref. 12.

2.2.2 Basic Hexagonal Wing Section Model

Although the double plate model renders very accurate estimates for the wing bending material weight, it is not suitable for calculation of the wing-box torsional stiffness. This torsional stiffness becomes essential when calculating wing twist and flexible wing spanload, as well as for the incorporation of aeroelastic constraints into the MDO optimization.

Therefore, a hexagonal wing-box model (Figure 2.5) was proposed for the wing weight calculation module. The basic form of the model was provided by Lockheed Martin Aeronautical Systems (LMAS) in Marietta, Georgia[26]. As shown in Figure 2.5, the wing section consists of the following elements:

- Four skin panels covering the upper and lower part of the airfoil. Each panel has different thickness. The skin thickness of each part is t_1, t_2, t_4, and t_5 respectively.
- Two shear web at the front and rear spars with the skin thickness t_3 and t_6 respectively.

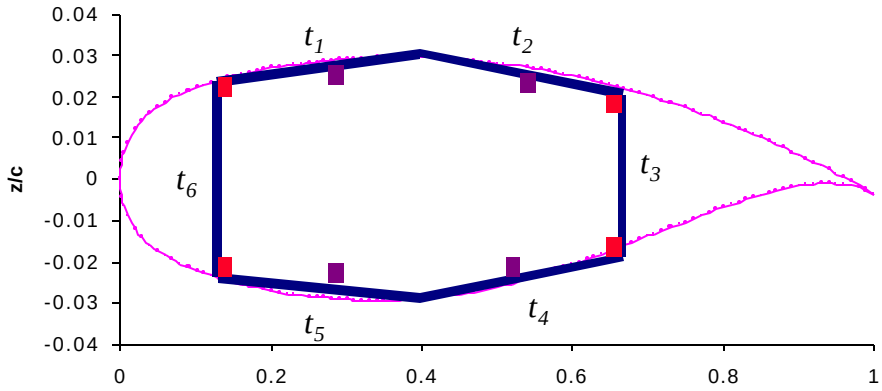


Figure 2.5. The hexagonal wing section model

- Four spar caps at each tip of the shear web with the cross section area A_{c1}, A_{c2}, A_{c3}, and A_{c4}, respectively. The numbering of the cap is started from the upper front spar cap and rotated in clockwise direction.
- Four stringers at the middle of each skin panels web with the cross section area A_{s1}, A_{s2}, A_{s3}, and A_{s4}, respectively. The numbering of the stringer is started from the middle of upper front skin t_1 and rotated in clockwise direction.

Therefore in each section there are 14 different variables representing wing section sub component stiffness. Compared to the double plate model that needs only one variable, the hexagonal model has more complicated geometry to better simulate the shape of the airfoil and is consequently difficult to find its optimum stiffness directly.

To simplify the problem, Bob Olliffe of LMAS[26] suggested setting only one sub-component as the independent variable and the other 13 sub-components as dependent variables. For example, if the dimension of t_4 is given, than the other dimensions of the skins, shear webs, stringers and spar caps can be calculated directly. Such direct calculation can be performed provided the ratio between the sectional area of each part of the element is known. In the present work, t_4 is selected as the independent variable and the other 13 sub-

components are calculated based on an optimized ratio among hexagonal wing box elements suggested by LMAS[26]. The ratio of each element is given in five spanwise wing sections. The ratio of each elements in other wing sections is interpolated by using a cubic spline approach.

The remaining part to be solved in the hexagonal box model is to find the independent variable t_4. For the strut braced wing, there are two approaches developed in the MAD Center of Virginia Tech. The earliest approach is the equivalent hexagonal box model developed by the present author mainly for the SBW aeroelastic analysis. The latest approach was developed by Gern[29] for predicting the SBW wing bending weight as well as aeroelastic analysis. In Section 2.2.3, only the first method is described. A more detailed description of the second method is given in Ref. 29.

2.2.3 Equivalent Hexagonal Wing Section Model

The equivalent hexagonal model was developed as the first attempt to find the wing torsional stiffness distribution for aeroelastic analysis of the strut braced wing. The wing torsional stiffness, as well as bending stiffness, was needed for flutter and divergence speed calculations. At that time, the only available data was the wing bending stiffness distribution calculated by using the double plate model. Since the double plate module, called *wing.f*, has been validated and was well-established as part of the MDO code of the strut-braced wing, the first idea was just to find an equivalent hexagonal model. The equivalent hexagonal model (EHM) should have equal bending weight and bending stiffness with that of the double plate model as shown in the following equations:

$$A_{eq}(y) = A_{dpm} = 2\, t_d(y)\, c_b(y) \tag{2.4a}$$

$$I_{eq}(y) = I_{dpm} = \frac{t_d(y)\, c_b(y)\, d^2(y)}{2} \tag{2.4b}$$

To fulfill this goal, three procedures are investigated. Each procedure has different assumption on the hexagonal bending weight.

2.2.3.1 Equivalent Hexagonal Model (EHM) Procedure 1

The first procedure is based on the assumption that the whole cross sectional area of the hexagonal box is the same as the bending weight calculated using the double plate model, or

$$A_{eq1} = 2\, t_d(y)\, c_b(y) \tag{2.5}$$

where the bending weight of the EHM Procedure 1 is

$$A_{eq1} = \sum_{i=1}^{14} \frac{\rho_i A_i}{\rho_{ref}} \tag{2.6}$$

Equation (2.6) shows that all of the 14 sub-components of the hexagonal model contribute to the bending weight. The density ρ_{ref} is the same as the density of the double plate model. If the ratio of each sub-component area with respect to the area of the fourth skin is defined as

$$r_i(y) = \frac{A_i}{t_4 L_4} \tag{2.7}$$

then the dimension of the fourth skin can be obtained as

$$t_4(y) = \frac{2\, t_d(y)\, c_b(y)}{L_4 \sum_{i=1}^{14} r_i(y)} \tag{2.8}$$

The centroid of the hexagonal box is calculated as

$$x_c = \frac{\sum_{i=1}^{14} A_i x_i E_i}{\sum_{i=1}^{14} A_i E_i} \quad ; \quad z_c = \frac{\sum_{i=1}^{14} A_i z_i E_i}{\sum_{i=1}^{14} A_i E_i} \tag{2.9}$$

Therefore, the moment of inertia I_{xx} of the hexagonal box can be calculated as

$$I_{eq1} = I_{xx} = \sum_{i=1}^{14} \frac{E_i}{E_{ref}} \left(I_{xx,o_i} + A_i (z_i - z_c)^2 \right) \tag{2.10}$$

where the referenced Young modulus E_{ref} is the same as the Young modulus of the double plate model. The result of this approximation is compare to the double plate result as shown in Fig. 2.6. The result indicates that I_{eq1} is less than I_{dpm}. Indeed, I_{eq1} is always less than I_{dpm} because the moment arm of the EHM 1 is less than that of the double plate model. This short coming led us to develop a second approach for the EHM. This approach is described in the following section.

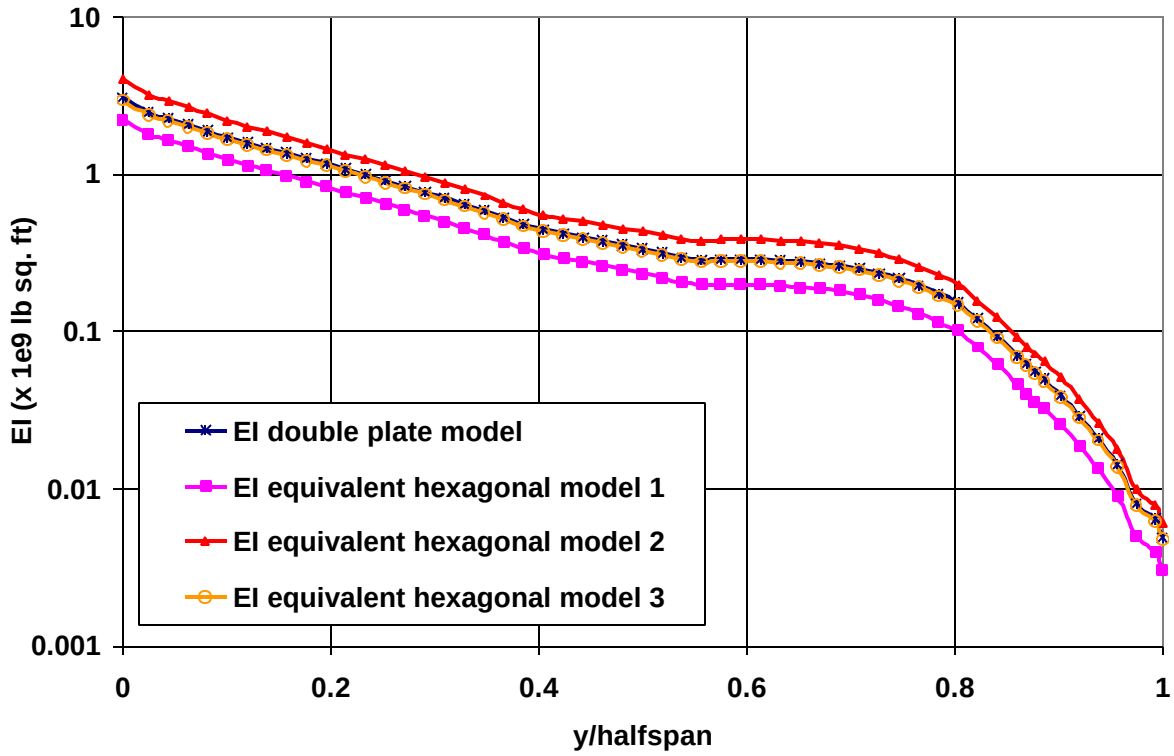


Figure 2.6. EI_{xx} distribution (G lb ft2) of the double plate model and three hexagonal models Based on the procedures 1,2, and 3

2.2.3.2 Equivalent Hexagonal Model (EHM) Procedure 2

The second approach is based on the assumption that the *bending* weight of the hexagonal model does not include the skins and webs t_1 until t_6 (Figure 2.7). Therefore, the bending weight of EHM 2 includes only the spars and stringers as follows:

$$A_{eq2} = \sum_{i=1}^{4} \frac{\rho_{c,i} A_{c,i}}{\rho_{ref}} + \sum_{i=1}^{4} \frac{\rho_{s,i} A_{s,i}}{\rho_{ref}} = \sum_{i=7}^{14} \frac{\rho_i A_i}{\rho_{ref}} \tag{2.11}$$

such that the bending weight of the EHM 2 is the same as that of the double plate model, or

$$A_{eq2} = 2\, t_d(y)\, c_b(y) \tag{2.12}$$

Note that the assumption to ignore the skin and web for the bending weight calculation is commonly used in some references[176].

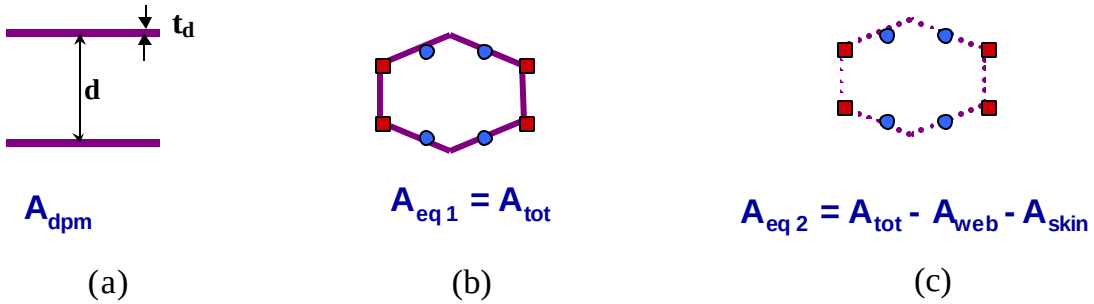


Figure 2.7. (a) Double plate model, (b) the equivalent hexagonal model 1, (c) the equivalent hexagonal model 2

The thickness t_4 is calculated by substituting of Eq. (2.11) into Eq. (2.12) and applying the same aspect ratio of each sub-component to give

$$t_4(y) = \frac{2\, t_d(y)\, c_b(y)}{L_4 \sum_{i=7}^{14} r_i(y)} \tag{2.13}$$

Note that the index of summation in Eqs. (2.11) and (2.13) is started from $i = 7$ since the first six indices belong to the skins and webs. After t_4 is calculated, the dimensions of the hexagonal sub components can be calculated based on Eq. (2.7). The sectional centroid is calculated as:

$$x_c = \frac{\sum_{i=7}^{14} A_i x_i E_i}{\sum_{i=7}^{14} A_i E_i} \quad ; \quad z_c = \frac{\sum_{i=7}^{14} A_i z_i E_i}{\sum_{i=7}^{14} A_i E_i} \tag{2.14}$$

The bending moment of inertia is calculated as

$$I_{xx} = \sum_{i=7}^{14} \frac{E_i}{E_{ref}} \left(I_{xx,\,o_i} + A_i (z_i - z_c)^2 \right) \tag{2.15}$$

The moment of inertia I_{xx} calculated by Eq. (2.15) is still less than I_{dpm} since the moment arm is smaller. However, it is possible to increase the total moment inertia if we take into account the skin and web contribution as follows:

$$I_{eq2} = I_{xx} + I_{skin} + I_{web} = \sum_{i=1}^{14} \frac{E_i}{E_{ref}} \left(I_{xx,\,o_i} + A_i (z_i - z_c)^2 \right) \tag{2.16}$$

Comparison between $I_{eq\,2}$ and I_{dpm} and $I_{eq\,1}$ is given in Fig. 2.7. The second approach clearly overpredicts the double plate model, or $I_{eq\,1} < I_{dpm} < I_{eq\,2}$.

2.2.3.3 Equivalent Hexagonal Model (EHM) Procedure 3

The third approach is based on the combination of the previous two approaches. The bending weight of the third approach can be calculated as

$$A_{eq3} = a_1 A_{eq1} + a_2 A_{eq\,2} = A_{dpm} \tag{2.17}$$

Since $A_{eq\,1} = A_{eq\,2} = A_{dpm}$, then the coefficients a_1 and a_2 in Eq. (2.17) are related by

$$a_1 + a_2 = 1 \tag{2.18}$$

The moment of inertia of the third approach is calculated as

$$I_{eq3} = a_1 I_{eq1} + a_2 I_{eq2} \approx I_{dpm} \tag{2.19}$$

The last two equations, i.e. Eqs. (2.18) and (2.19), are sufficient to find the coefficients a_1 and a_2. The next step is to obtain the sub component area of the hexagonal model by multiplying a_1 and a_2 to A_i calculated in Procedure 1 and 2 respectively. It should be noted that there is no iteration needed in this procedure, and the Procedures 1 and 2 can be calculated simultaneously. Therefore the computational time for this procedure is very small and is still suitable as part of an MDO module.

Comparison between I_{eq3} and other approaches are shown in Fig. 2.6. As expected, the third approach gives a very close approximation to the double plate result. This approach is used in the present work to provide the bending and torsional stiffness distribution for the aeroelastic analysis.

2.3 Finite Element Model

To implement the equivalent hexagonal model procedures described in Section 2.2, a FORTRAN computer code called *ehexa.f* was developed. The input data to *ehexa.f* is the thickness distribution resulted from *wing.f* (the double plate model code) and the wing geometry data including airfoil thickness. The output is the wing finite element model automatically generated in a NASTRAN format. The finite element output is arranged such that it can be used directly for static, structural dynamics and aeroelastic analyses of the strut braced wing using NASTRAN.

There are two finite element models that can be generated by the *ehexa.f*. The first model is a piecewise non-uniform beam element. The beam stiffness distributions in terms

of EI_{xx}, EI_{zz}, EI_{xz}, EA, and GJ for each wing section are generated by the equivalent hexagonal model procedure. The number of beam elements used are 62 elements connecting 63 structural grid points along the wing elastic axis. The finite element formulation for the non uniform beam element is presented in Chapter 3. The aeroelastic analysis for the non-uniform beam element is described in Chapter 5. Further description of the model is presented in Chapters 3 and 5.

The second model is a detailed wing model consisting of the wing skins, webs, spars and stringers. The model is used in Section 2.4 as an off-design aeroelastic analysis. The two dimensional element such as skins and webs are modeled as quadrilateral QUAD4 or triangular TRIA3 shells in a NASTRAN format. The one-dimensional elements, such as spars and stringers, are modeled as ROD elements. Figure 2.8 shows the wing box structure of this model. The number of QUAD4, TRIA3 and ROD elements are 862, 3 and 1112, respectively. The number of nodes connected by these elements are 630. Assuming that each node has six degrees-of-freedom, the total number of degrees-of-freedom is 3780. Obviously, the model is not suitable to be used in the MDO since a structural analysis with such a detailed model will need a large computational time. For this reason, the second hexagonal model is used to verify the final MDO result. If the aeroelastic analysis module is required as part of the MDO code, then the first hexagonal model is more suitable than the second model.

It should be noted that each sub-component of the hexagonal wing box model may have different material properties, *i.e.* different modulus of elasticity, shear modulus and density. For the detailed model, the wing skin can be modeled as composite layers with various fly angles. Each layer may have different transverse shear factor. The structural stiffness of the composite is included directly in the wing structure stiffness, such that there is no need to use the so-called ‘technology’ factor to consider the effect of composite materials. Note that the ‘technology’ factor for the composite material is used in Ref. 13 to simplify the prediction of the wing bending weight.

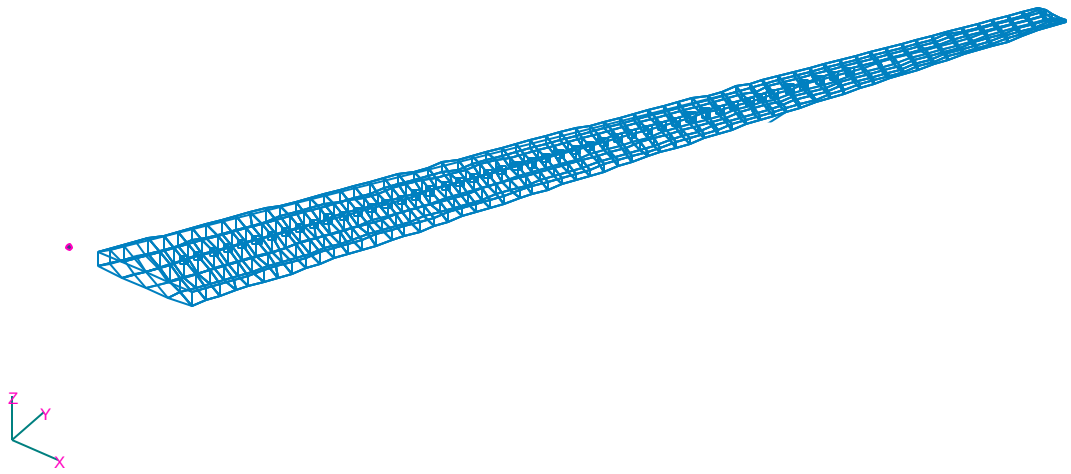


Figure 2.8. The strut braced wing frame generated using *ehexa.f*

2.4 Flutter Analysis Using Nastran

Based on the finite element data generated by *ehexa.*f, a structural dynamics analysis was performed using the SOL 103 module of NASTRAN[34] to calculate the natural frequencies and modes of the strut-braced wing. For all the cases considered in the present work, the connection between the fuselage and wing strut and between the fuselage and strut are assumed to be rigid, i.e. there are no relative displacements and rotations at the wing-fuselage and strut-fuselage junctions. The free-vibration analysis was performed for a half wing model using the Lanczos eigen solution[34]. The natural frequencies for the first ten

modes are presented in Table 2.2. The mode shapes for the first 6 modes are shown in Fig. 2.9a – 2.9e.

Table 2.2.

Natural frequencies of the strut-braced wing

Mode Shape	Frequency (Hz)	Mode Shape	Frequency (Hz)
1	2.33	6	7.71
2	2.97	7	9.09
3	3.74	8	10.79
4	4.37	9	12.24
5	6.76	10	15.30

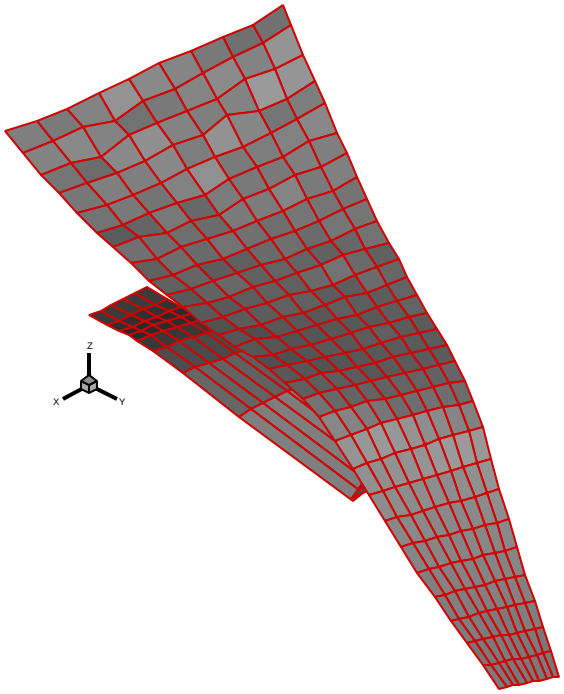


Figure 2.9a. Mode 1: First vertical bending(2.33 Hz)

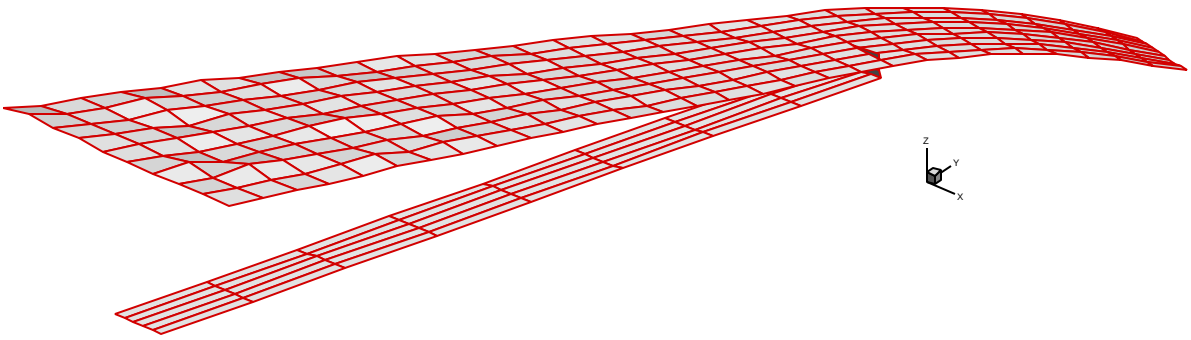


Figure 2.9b. Mode 2: Second vertical bending (2.97 Hz)

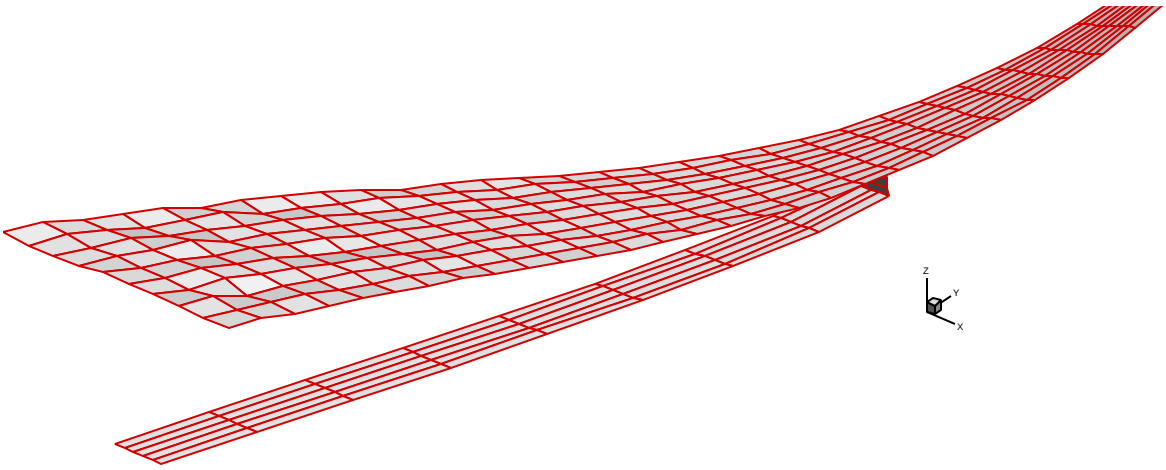


Figure 2.9c. Mode 3: Third vertical bending (3.74 Hz)

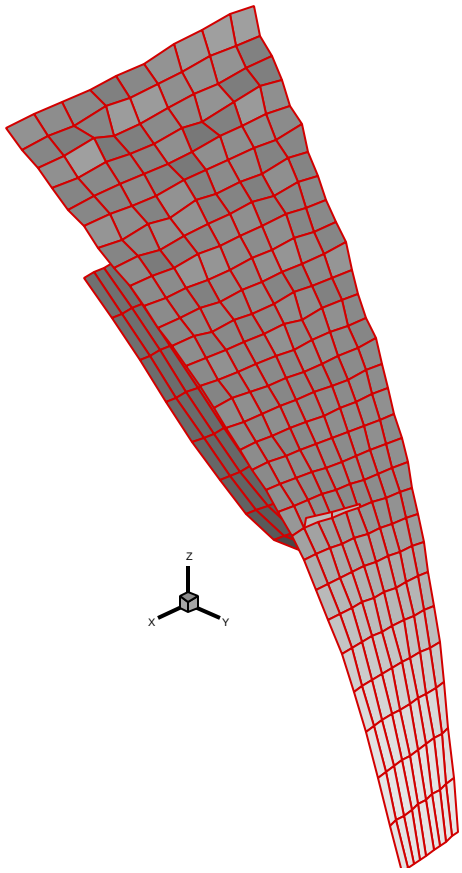


Figure 2.9d. Mode 4: First aft bending (4.37 Hz)

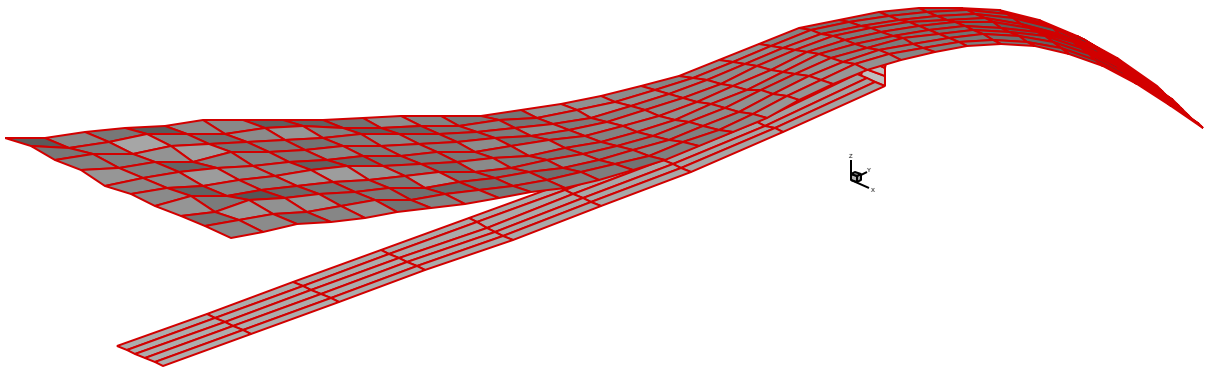


Figure 2.9e. Mode 5: Fourth vertical bending (6.76 Hz)

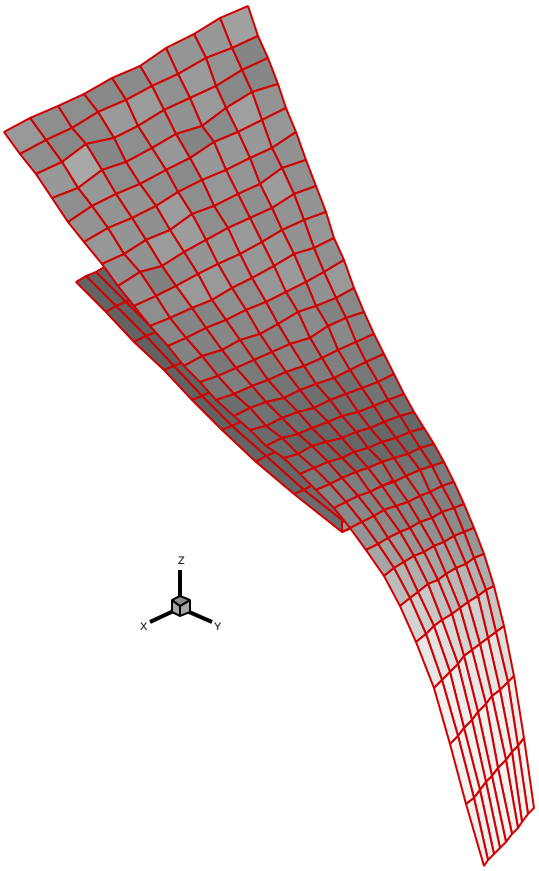


Figure 2.9f. Mode 6: Second aft bending (7.71 Hz)

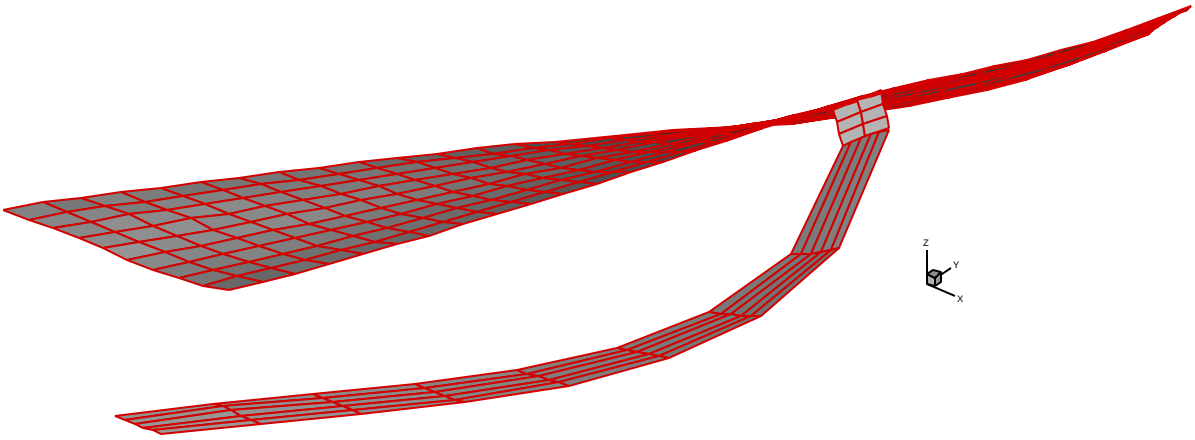


Figure 2.9g. Mode 7: First Torsion (9.09 Hz)

The flutter analysis was performed for the half wing model using the PK method option in NASTRAN[34]. The basic equation for the PK method is

$$\left[M\, p^2 + \left(B - \frac{\rho c V}{4k} Q_B \right) p + \left(K - \frac{\rho V^2}{2} Q_K \right) \right] \left\{ u \right\} = 0 \qquad (2.20)$$

where

M = modal structural mass matrix

B = modal structural damping matrix

K = modal structural stiffness matrix

Q_B = modal aerodynamic damping matrix

Q_K = modal aerodynamic stiffness matrix

u = modal amplitude

p = eigenvalue = $w\,(g/2 \pm i)$

g = (artificial) structural damping

k = reduced frequency = $w\,c\,/\,2V$

c = reference length = average wing chord

V = air speed

w = circular frequency

r = air density

The structural modal matrices K, B and M are generated using the finite element method. The aerodynamic modal matrices Q_K and Q_B are generated using the aerodynamic lifting surface theory. For subsonic flow, the lifting surface method is based on the doublet lattice method of Giesing, Rodden and Kalman[34]. For supersonic flow, the lifting surface method is based on the harmonic gradient method of Chen and Liu[177]. It should be noted that

the aerodynamic modal matrices Q_K and Q_B are functions of the reduced frequency k and mach number M. A more detailed description of the doublet lattice method is presented in Chapter 4 of the present work.

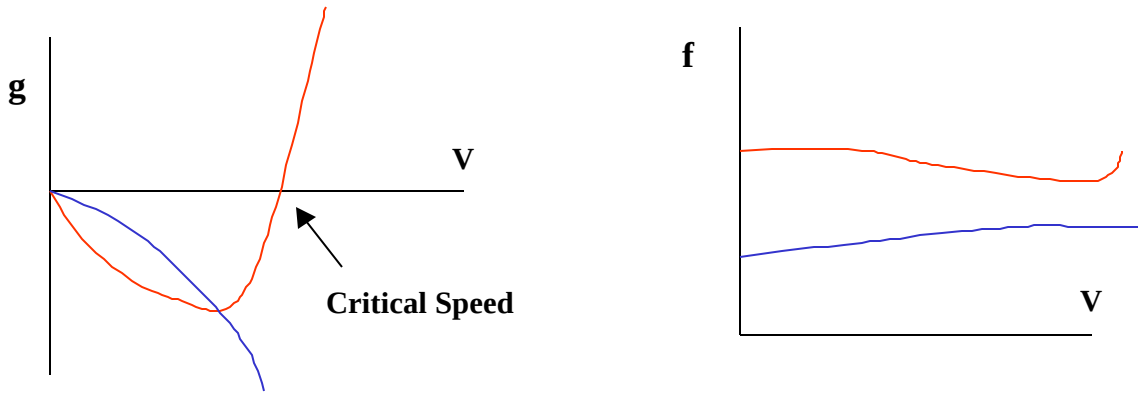
Equation (2.20) is solved in a state space form as follows:

$$[\, A - p\, I \,] \left\{ \begin{array}{c} \\ u \\ \\ \end{array} \right\} = 0 \tag{2.21}$$

where A is the real matrix

$$A = \left[\begin{array}{cc} 0 & I \\ -M^{-1}\left(K - \dfrac{\rho V^2}{2} Q_K \right) & -M^{-1}\left(B - \dfrac{\rho c V}{4k} Q_B \right) \end{array} \right] \tag{2.22}$$

The eigenvalue and eigenvector solution of Eq. (2.21) are calculated in NASTRAN using the upper Hessenberg method described by Komzsik[178]. In general, the eigensolutions are complex conjugate pairs. The eigenvalues are calculated for each air speed V, and the results are presented in the form of the well-known V-g and V-f plots as shown in Figure 2.10. The V-g plot shows the structural damping g of each mode as a function of the air speed V. The V-f plot shows the frequency f of each mode as a function of the air speed V. The flutter or divergence critical speed is obtained from the V-g plot as the lowest velocity V at which the g curve crosses the V axis from negative structural damping g (stable region) to positive g (unstable region) as shown in Fig. 2.10. The V-f plot is useful to differentiate if the critical speed is flutter or divergence speed. If, at the critical speed, the frequency of the related mode is zero, the critical speed is a divergence speed. The critical speed is a flutter speed if the related frequency at the critical speed is greater than zero.



(a) *V-g* plot **(b) *V-f* plot**

Figure 2.10. The flutter *V-g* and *V-f* plots

In the present work, the flutter speed is calculated first for the reference condition, and then followed by flutter calculations for a number of parameter variations including altitude, strut locations, strut stiffness etc. The reference condition is defined as follows:

- The wing and strut geometric and structural data are based on the final iteration result of the MDO study
- The wing strut junction location is at 69 % of the wing semi-span.
- The length of the offset beam between the wing and strut is 3.17 ft.
- The fuselage-strut junction location is at x = 29.01 ft from the leading edge of the wing root.
- The computation is performed for sea level condition.
- The structural damping is set at g = 0%.

In the present flutter analysis, all of the first ten vibration modes are used. The *V-g* and *V-f* plots of the flutter results for the reference condition are shown in Figures 2.11a and 2.11b, respectively. The flutter speed is found at V_f = 902 fps with the frequency f = 3.93 Hz. It will be shown in the next section that this flutter speed is beyond the flight speed envelope of the strut-braced wing design.

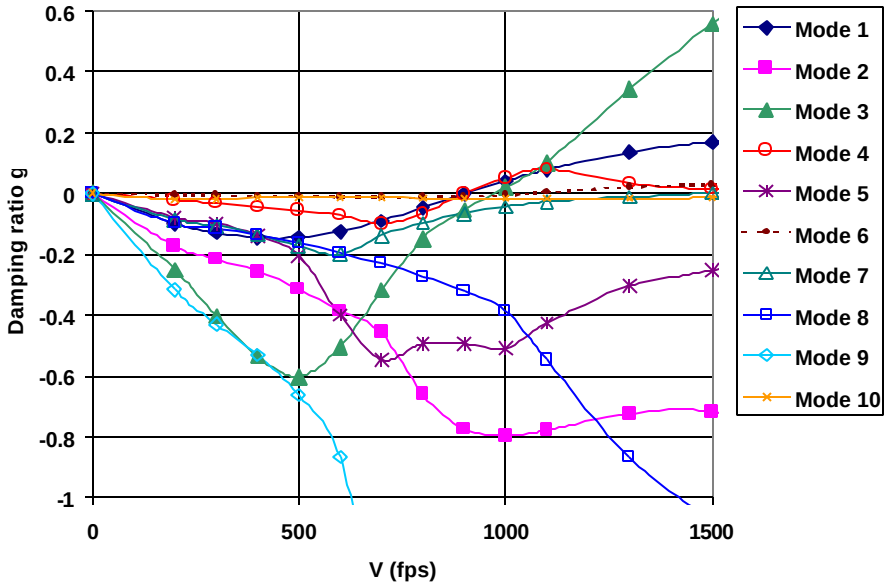


Figure 2.11a. The *V-g* plot of the strut braced wing at the reference condition

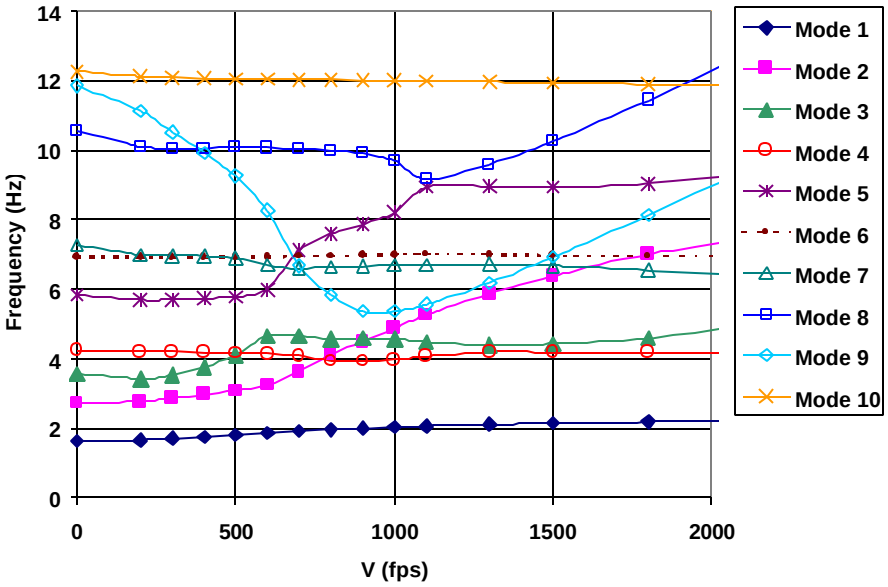


Figure 2.11b. The *V-f* plot of the strut braced wing at the reference condition

2.5 Sensitivity Analysis

A sensitivity study was performed to study the behavior of the aeroelastic response near the reference condition described in the previous section. Variation of several parameters are selected including the changes in:

- longitudinal/axial position of the the fuselage-strut junction
- spanwise position of the wing-strut junction
- chordwise position of the wing strut junction
- length of the offset beam connecting the wing and strut
- fuel loading on the wing
- altitude

For convenience, the reference condition is rewritten as follows:

- The wing and strut geometric and structural data are based on the final iteration result of the MDO.
- The wing strut junction location is at 69 % of the wing semi-span.
- The length of the offset beam between the wing and strut is 3.17 ft.
- The fuselage-strut junction location is at x = 29.01 ft from the leading edge of the wing root.
- The computation is performed for the sea level condition.
- The structural damping is set at g = 0%.
- The flutter speed for this reference condition is 902 fps. This flutter speed is set as a reference velocity for the strut-braced wing detailed model, i.e. V_{ref} = 902 fps.

It is assumed that the stiffness and dimension of the wing and strut are fixed at the reference condition as the aforementioned parameters are made to vary.

The first variation is to investigate the flutter and divergence speeds if the strut position at the fuselage changes in the longitudinal or x direction. The distance x is measured from the leading edge of the wing root parallel to the flow direction. Figure 2.12 shows that the flutter speed increases as the strut-fuselage junction moves forward along the fuselage axis. This trend can be related to the so called mass-balance effect, where the flutter speed is higher if the center of gravity of the system moves forward. Reference 54 shows that for a two-dimensional aeroelastic problem, frequently no flutter occurs if the center of gravity is ahead of the elastic axis. For the under-wing mounted engine configuration, the flutter speed usually increases if the center of gravity of the engine moves forward. Note that, in the present sensitivity study, the cross sectional area of strut is kept constant as the strut junction moves forward. Therefore, the strut weight increases and the center of gravity moves forward as the strut-fuselage junction moves forward.

No divergence speed was found within this range. This result is expected since for a swept back wing the divergence speed is usually very high. For this reason, only flutter results are investigated in the remaining part of this work. Note that the reference speed V_{ref} is the flutter speed at the reference condition as defined in Section 2.4, i.e. in the present work, $V_{ref} = 902$ fps.

The second sensitivity study is related to investigating the variation of the flutter speed if the wing-strut junction position changes along the spanwise direction. Figure 2.13 shows that the flutter speed decreases significantly as the junction location moves outboard from $y = 0.8\,L$ to the wing tip. For $0 < y < 0.70\,L$, the flutter speed decreases gradually. The trend of the present result is relatively the same as the analysis result of Mailybaev and Seiranyan[27] for the Keldysh wing. In their result, the flutter speed also decreases if the junction moves outboard, except that the divergence speed is more critical than flutter speed for $0.40\,L < y < 1.0\,L$. In the present analysis, no divergence speed was predicted.

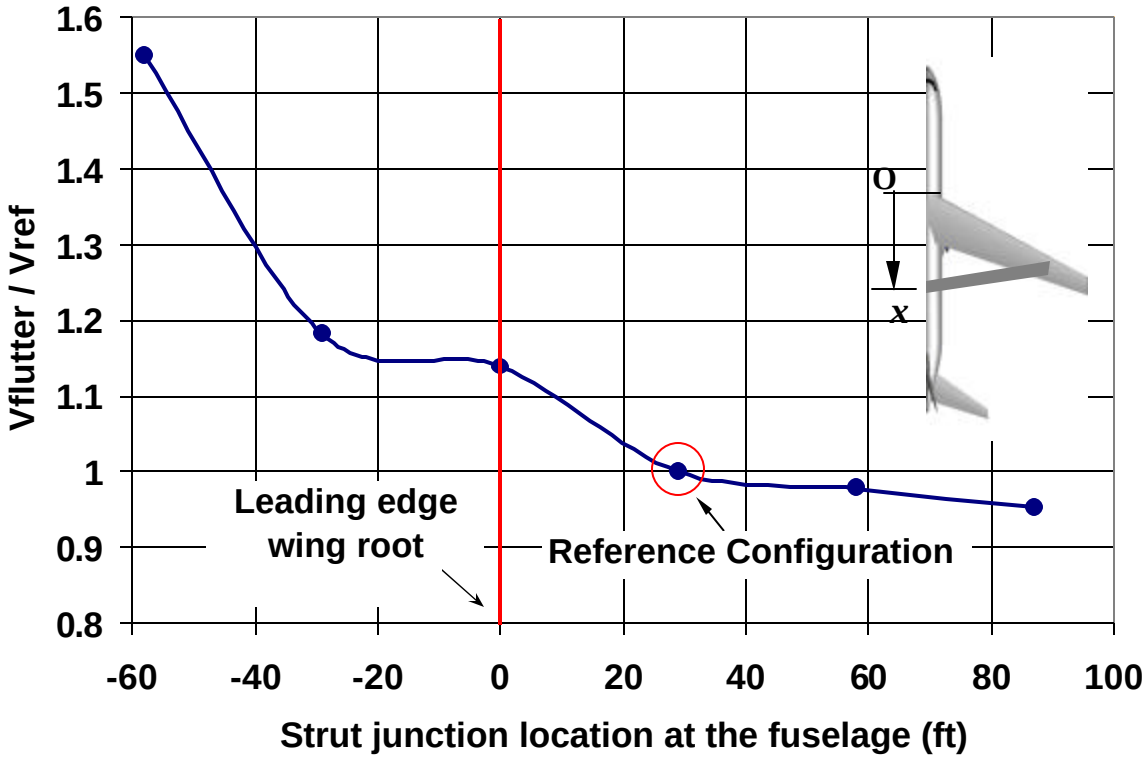


Figure 2.12. Flutter speeds as function of the strut junction position at the fuselage in x (longitudinal) direction. V_{ref} = 902 fps.

The trend of the SBW flutter speed that decreases when the strut support moves outboard can be related to the reduction of the strut stiffness as the length of the strut increases. Note that the axial, flexural and torsional stiffness of a beam is proportional to (EA / L), (EI / L^3) and (GJ / L), respectively. In the present sensitivity study, the strut material properties E and G, and the sectional area A and moment of inertia I are kept constant as the length of the strut L increases.

An interesting behavior is the increase of the flutter speed in the region $0.7 < y_s < 0.8$ when the strut support moves outboard. The increase is related to the fact that the flutter mode switches from a torsional mode outside this region to a bending mode inside this

region. This trend may indicate that the aeroelastic stability system of the strut-braced wing is not dominated by the lower order modes. For the aeroelastic stability system where higher order modes is also important, it is possible for the flutter mode to switch.

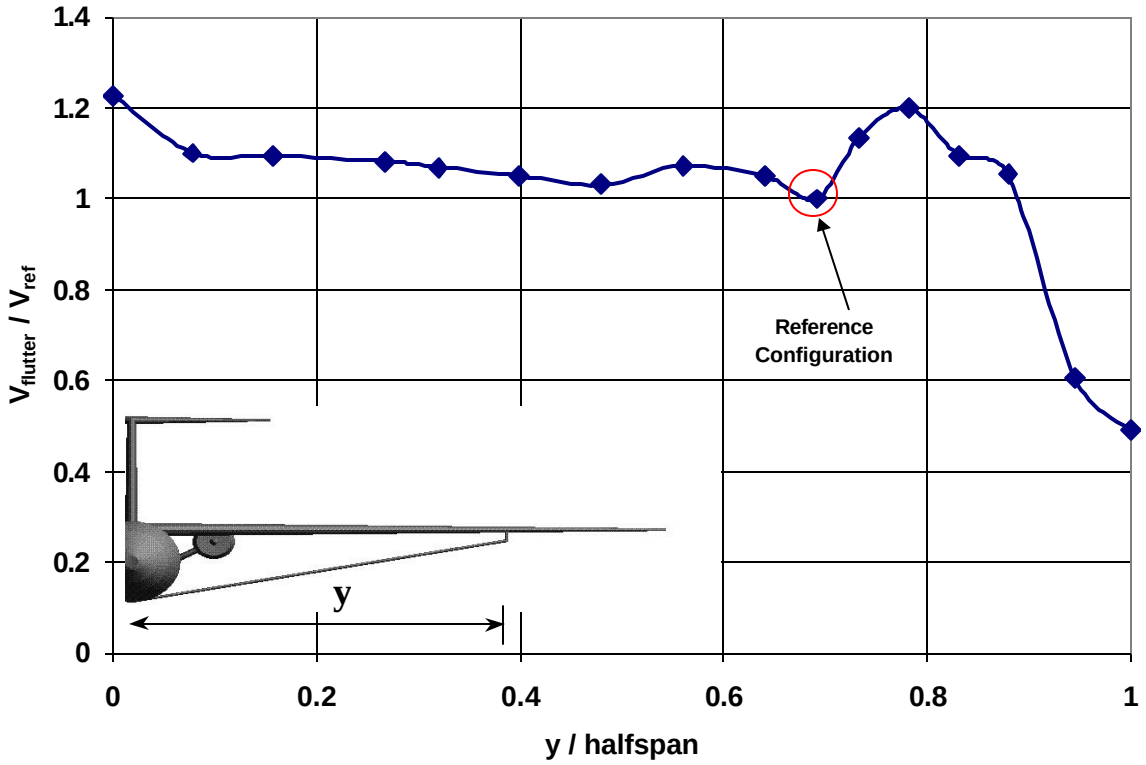


Figure 2.13. Flutter speed as a function of the spanwise position of the strut junction at the wing. V_{ref} = 902 fps.

The third sensitivity study is performed to investigate the variation of the flutter speed if the location of the wing-strut junction changes along the chord wise direction. Figure 2.14 shows the results for three possible positions of the strut supports: at the wing elastic axis, the front spar, and the rear spar. For each of these three chordwise positions, the flutter calculation was performed as function of the strut support along the spanwise direction. The results (Fig. 2.14) indicate that the strut support at the rear spar gives the lowest flutter speed

among other chordwise locations. The strut support at the front spar gives the highest flutter speed, or at least the same as the result for the strut support at the elastic axis.

Note that the strut support at the front spar was also selected by Gern *et al*.[21] as the best support positions for the SBW flexible wing to have aerodynamic load alleviation during positive load maneuver. Reference 21 described that, if the strut is attached to the wing front spar, the strut twists the leading edge downward, thus decreasing the sectional angle of attack on the outboard (wash-out effect). As a result, the lift load is shifted inboard, producing a decrease in the spanwise wing bending moment. This passive load alleviation, that works for a steady aerodynamic distribution, contributes to the increase of the flutter speed. Possible reasons for this behavior are as follows:

- It has been shown in Ref. 70 that the unsteady aerodynamic load can be divided into two parts: the steady aerodynamic and the incremental unsteady aerodynamic parts. If the steady aerodynamic load is shifted inboard, the total unsteady aerodynamic load is also shifted inboard.
- The unsteady aerodynamic load is shifted inboard to satisfy the surface boundary condition as the sectional angle of attack of the outboard surface decreases.
- The flutter speed becomes higher if the spanwise center of pressure is shifted inboard, since the load center is shifted to the place where the wing stiffness is higher.

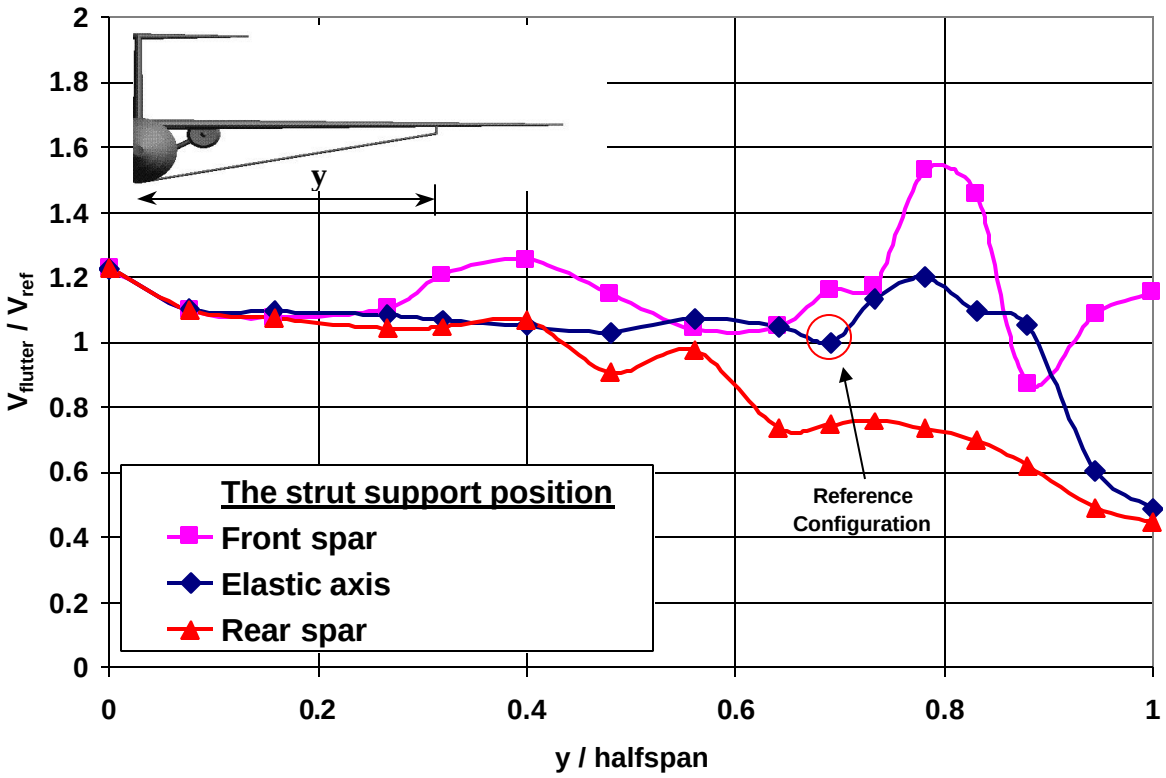


Figure 2.14. Flutter speed as a function of the chordwise and spanwise position of the wing-strut junction. V_{ref} = 902 fps.

A further study is performed to investigate the influence of the different length of the offset beam connecting the wing and strut (see Fig. 2.15). Note that the reference condition is for the condition where the offset beam length is equal to 3.17 ft. The result (Fig. 2.15) reveals that the flutter speed decreases by increasing the offset beam length. This trend is related to the fact that the stiffness of the SBW structure decreases as the length of the offset beam increases.

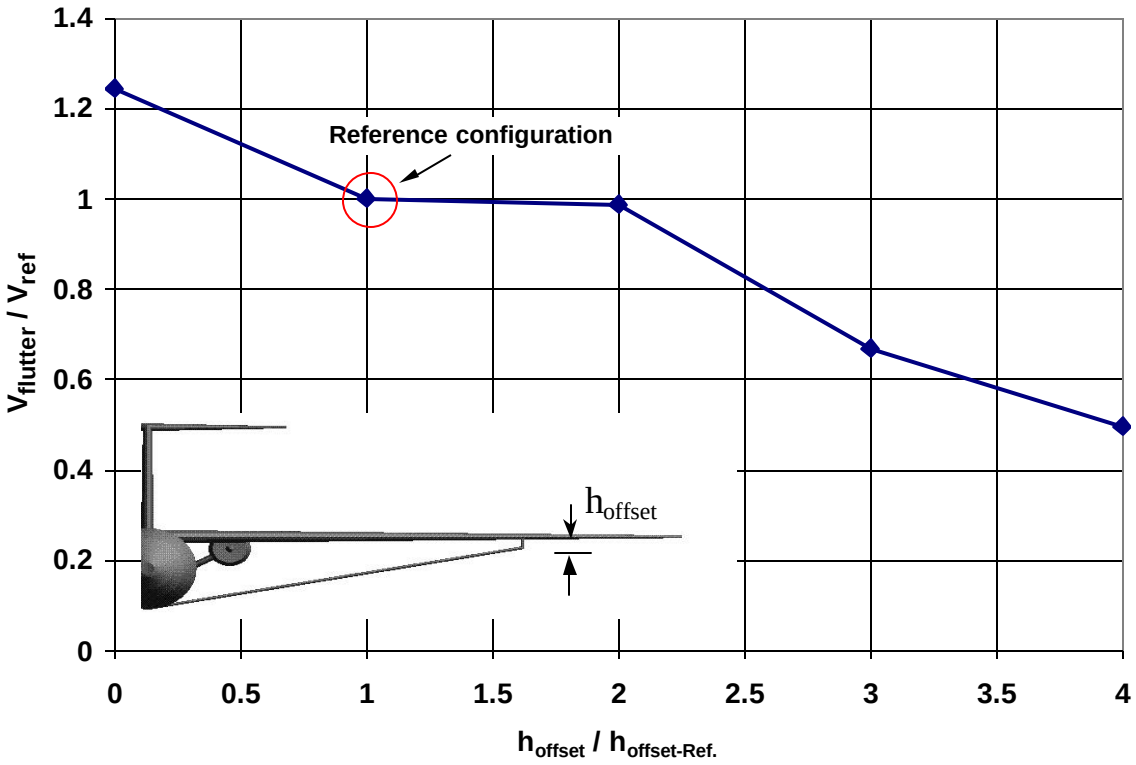


Figure 2.15. Flutter speed at sea level as function of the length of the offset beam connecting the wing and strut. V_{ref} = 902 fps, $h_{offset-Ref}$ = 3.17 ft.

The influence of fuel load and flight altitude on the flutter speed is shown in Fig. 2.16. The flutter speed was calculated for every altitude for the strut-braced wing with and without the fuel to comply with the relevant FAA regulation[25]. Note that the reference condition is the SBW aircraft at sea level with zero fuel load. Figure 2.16 shows that in most altitude the strut braced wing without fuel is more critical than the one with fuel. This trend may be related also to the static unbalance effect. In the present case, the increase of fuel weight may shift the center of gravity of the wing structural and non-structural mass toward the leading edge.

It should be noted that most of the flutter modes shown in Fig 2.16 are the first torsional mode. However, for the full fuel case at sea level and at 42,000 ft, the flutter mode switches to the bending mode. This trend again indicates that higher order modes of the strut-braced wing may couple with the lower modes such that the switching modes are possible.

Comparison between the strut braced wing flutter analysis and the flight envelope is also shown in Fig. 2.16. The results show that the present design of the strut-braced wing aircraft is free from flutter within its flight envelope. This important conclusion is in agreement with the finding by LMAS in Ref. 26. The strut braced wing aircraft version of LMAS is derived from the present configuration with a more refined aerodynamic and structural design of the wing. After performing a flutter analysis using a more detailed aircraft structure, LMAS concluded, in their final report to NASA-Langley, that their strut-braced wing is free from flutter.

The investigated flutter sensitivity with respect to several design parameters, such as the strut location and stiffness, fuel distribution, and flight altitude, are useful to better understand the effect of these parameters on the aeroelastic stability. The results can be arranged to form a response surface describing the flutter sensitivity near a reference condition for these parameters. It is possible to further include this flutter response surface as part of any MDO code for a strut-braced wing optimization.

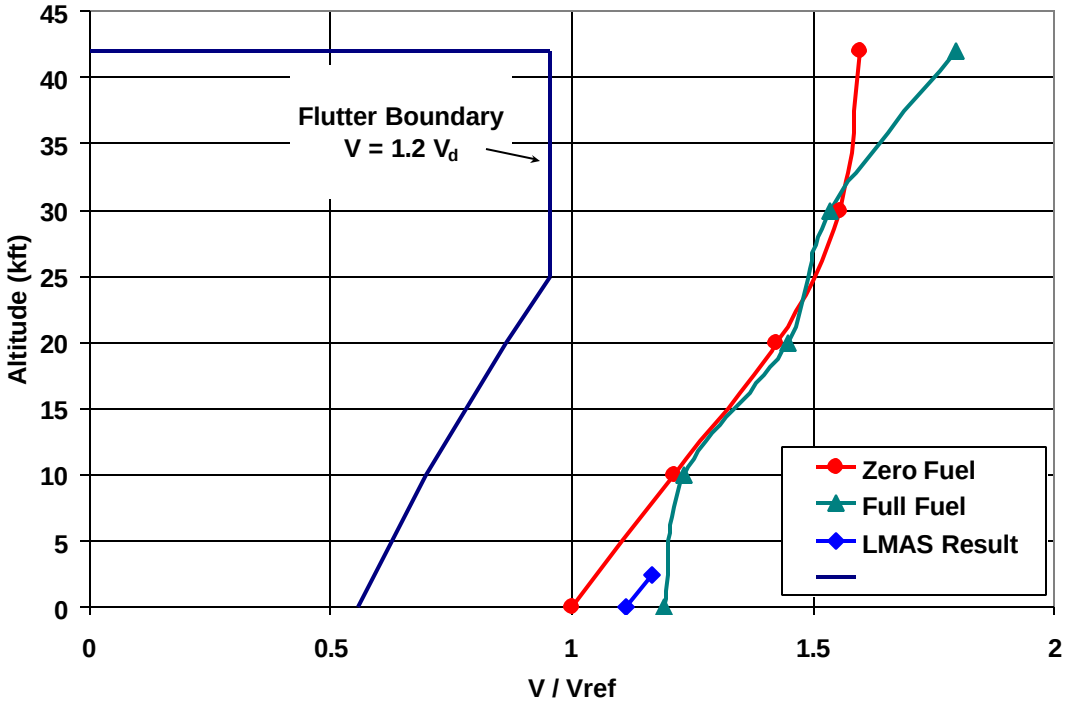


Figure 2.16. Flutter speed as a function of the altitude for the wing with or without fuel load. V_{ref} = 902 fps.

Chapter 3

Nonuniform Beam Element Formulation

3.1 Introduction

Non-uniform cross-section beams, ranging from small frame components to large bridge girder beams, are widely used as structural elements in many engineering fields. They are used to improve the structural strength, to reduce structural weight, or to satisfy architectural or aesthetical requirements. Important characteristic of non-uniform beam-colums have been investigated since 1773 when Lagrange[31,32] introduced an optimum non-uniform shape of a column subject to an axial load. In aeroelasticity, non-uniform beam models are often used to represent a wing[33,34]. NASA Langley[35] investigated dynamic and buckling characteristics of numerous non-uniform beam geometries for the construction of a large structure platform in space, where, in this critical weight saving case, the use of non-uniform members may prove worthwile[6].

A large number of investigations on the non-uniform beam can be classified into three groups: (i) the study of the element static stiffness matrix[36-46] and geometric stiffness matrix[46-50]; (ii) the study of the dynamic stiffness matrices[46,48,152-156]; and (iii) the study of the shape optimization of the beam-columns[32,157-165].

The formulation of the static stiffness matrix for non-uniform beams has been studied by many researchers[36-46]. Several different techniques have been adopted, including finite

element formulations[36-43], finite difference method[47], and recurrence series methods[44]. Gallagher and Lee[48] and others proposed to use a variational principle to develop the element stiffness matrix. Their development is based on a cubic displacement function, which is the same as the formulation for a uniform beam. The formulation is simple yet it proved to be superior to a piecewise stepped uniform element representation. This method is adopted and extended in many finite element codes such as NASTRAN[186] and ASTROS[187].

Another approach to study beams using the finite element method is based on the flexibility method. Weaver and Gere[36] describe a procedure to construct the stiffness matrix based on the flexibility method for a tapered beam with a linear variation of the bending stiffness *EI*. The flexibility matrix is constructed first based on the tip deflection and rotation of a cantilever beam. A direct integration of the Euler-Bernoulli differential equation is performed to find the deflection or rotation for each concentrated force or moment unit load at the tip of the beam. The stiffness matrix is obtained by inverting the flexibility matrix. Karabalis and Beskos[46] present the solution for beams with constant width and linear depth variation. Banerjee and Williams[36] follow the same procedure and present the solution for a non uniform beam with a stiffness variation in the form:

$$EI(x) = EI_0\left\{1 + r\ (x/L)\right\}^m \tag{3.1}$$

where L is the length of the element. Reference 36 deals with the formulation of a beam element for m = 1, 3, and 4; corresponding to many beam sectional profiles such as circular, rectangular, triangular and other regular geometric sections. The resulting formulation is exact if the beam stiffness distribution function follows Eq. (3.1). Baker[42] solves a more general form of the *EI(x)* function given as

$$EI(x) = EI_0\left\{1 + r\ (x/L)^{m_p}\right\}^{m_q} \tag{3.2}$$

where m_p and m_q are arbitrary integer numbers. Friedman and Kosmatka[40] give an explicit stiffness matrix expression for m_p=2 and m_q=3. It should be noted that to have a physical

meaning, the stiffness function *EI(x)* in Eqs. (3.1) and (3.2), and elsewhere in the present work, should be greater than 0 for the whole span of the beam:

$$EI(x) > 0 \qquad for \qquad 0 \leq x \leq L \tag{3.3}$$

Previous analytical solutions for the beam with a stiffness variation in the form of Eqs. (3.1) and (3.2) are, however, restricted only to symmetric generic cross-sections. There are at least three cases that can not be solved by using the previous analytical solutions:

(1) The first case is related to optimum shapes of columns, such as the one investigated in Refs. 177 – 185, where the *EI(x)* does not always follows Eqs. (3.1) and (3.2). To accommodate the shape of such optimum column, the polynomial function of the *EI(x)* should have arbitrary multiple roots. In the present work, a more general stiffness distribution, given as follows, is used:

$$EI(x) = \sum_{i=1}^{N_k} d_i \, x^i \tag{3.4}$$

Or, an alternate form of Eq. (3.3) in terms of the polynomial roots, which is suitable for the present method, can be written as:

$$EI(x) = EI_c \prod_{j=1}^{N} \left(x - c_j\right)^{m_j} \tag{3.5}$$

where N, m_i and c_i are arbitrary constant parameters that fit the stiffness distributions along the element. The parameter c_j are the roots of the polynomial function *EI(x)* and m_j is the multiplicity number of the root c_j. The formulations for bending, axial and torsional stiffness matrices of the general non uniform beam are presented in the next three sections of this Chapter.

(2) The second case is related to non-uniform loads applied to the beam. Baker[42] solves the static deflection problem of the non-uniform beam under a non-uniform distributed load. However, the non-uniform load considered in by Baker[42] is applicable only for a full span of the beam. For a more general case, where the load can be partially applied to the

beam span, the solution given in that reference can not be applied directly. In the present work, the analytical solution for the general partially distributed load to the non-uniform beam is presented in Section 3.5.

(3) The third case is related to the basic assumption adopted in the previous analytical solution where the beam cross sections should be symmetric, i.e. the cross-coupling moment of inertia term is zero. A treatment for a more general class of the problem, i.e. for non-uniform beam with asymmetric cross section where the cross-coupling moment of inertia distribution is also non-uniform, is presented in Section 3.6 of this Chapter. Validation is included by comparing the results from the present study with those given by NASTRAN or available exact solutions for several cases.

3.2 Axial Stiffness Matrix of Non-uniform Axial Bar Elements

Consider a tapered axial bar element of length L made of an isotropic elastic material of modulus E as shown in Fig. 3.1. In the present section, we assume that the cross-section area $A = A(x)$ about the x axis varies as an arbitrary polynomial function in x as follow:

$$A(x) = A_c \prod_{j=1}^{N} \left(x - c_j\right)^{m_j} \tag{3.5}$$

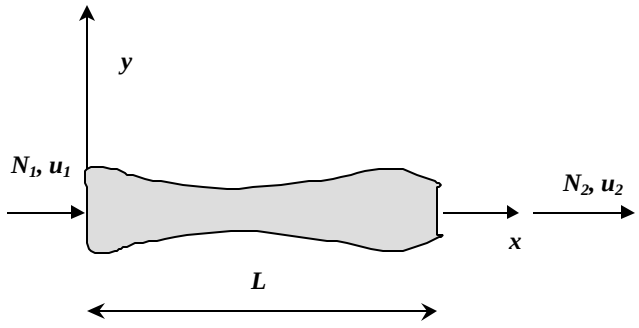


Figure 3.1. Geometry and sign convention of a tapered axial bar element

Based on the sign convention of Fig. 3.1, one can write the nodal force-displacement relation for the axial deformation of the element in the form:

$$\begin{Bmatrix} N_1 \\ N_2 \end{Bmatrix} = \begin{bmatrix} s_{11} & s_{12} \\ s_{21} & s_{22} \end{bmatrix} \begin{Bmatrix} u_1 \\ u_2 \end{Bmatrix} \tag{3.6}$$

The purpose of this section is to formulate the stiffness matrix coefficients s_{ij} in Eq. (3.6) in terms of the geometric parameters EA_j, c_j , m_j , N and L. The formulation includes the following three steps: deformation of the cantilever bar, the flexibility matrix, and the stiffness matrix.

3.2.1 Deformation of the cantilever bar problem

Consider a cantilever bar with a fixed support at $x = L$ as shown in Fig. 3.2. The bar stiffness $EA(x)$ varies according to Eq. (3.5). The Euler-Lagrange differential equation for the Bernoulli-beam with a small deflection assumption can be written as

$$\frac{d}{dx}\left(EA(x)\frac{du}{dx}\right) = p(x) \tag{3.7}$$

where $p(x)$ is a distributed axial load along the element span. A treatment for $p(x) \neq 0$ is given in Section 3.5. In the present section, assume $p(x) = 0$ and solve Eq. (3.7) to give

$$EA(x)\frac{du}{dx} = N \tag{3.8}$$

where N is a constant internal axial force at $0 < x < L$. The internal force N is related to the concentrated axial load N_0 at the free end of the cantilever beam (Fig. 3.2) as follows:
where

$$e_0 = \frac{N_0}{EA_c} \tag{3.10}$$

To solve Eq. (3.8), the boundary condition at the cantilever support is needed as follows:

$$u\,\big|_{x=L} = 0 \tag{3.11}$$

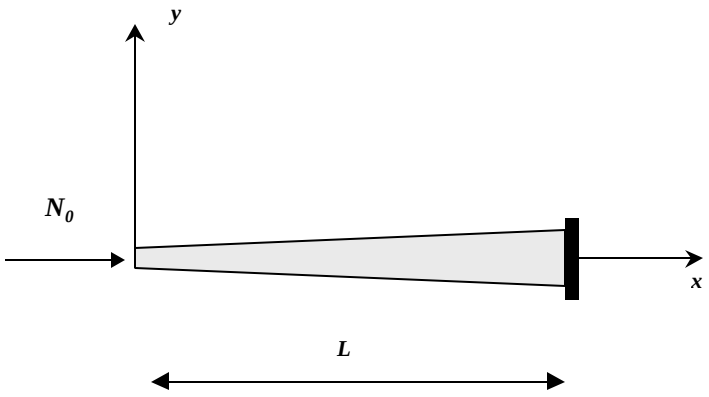


Figure 3.2. A cantilever beam model to derive the flexibility matrix

To find a deformation at the free end due to N_0, substitute Eqs. (3.5) and (3.9) into Eq. (3.8) and simplify the result by eliminating EA_c from the left and right sides of the equation to give:

$$\frac{du}{dx} = \frac{e_0}{\prod_{j=1}^{N}\left(x-c_j\right)^{m_j}} \tag{3.12}$$

A systematic way to solve Eq. (3.12) for u is by rewriting the rational function in the right-hand side of Eq. (3.12) as a sum of terms with minimal denominators such as the procedure explained in Appendix C. By referring to Eq. (C11), the right-hand side of Eq. (3.12) becomes

$$\frac{du}{dx} = \frac{e_0}{\prod_{j=1}^{N}\left(x-c_j\right)^{m_j}} = \sum_{j=1}^{N}\frac{a_j}{\left(x-c_j\right)^{m_j}} + \sum_{j=1}^{N}\sum_{k=1}^{m_j-1}\frac{d_{jk}}{\left(x-c_j\right)^{k}} \tag{3.13}$$

where the coefficients a_a *and* d_{ab} have been solved in Eq. (C12) and (C17) respectively as follow

$$a_a = \frac{e_0}{\prod_{\substack{k=1 \\ k \neq a}}^{N} (c_a - c_k)} \tag{3.14}$$

$$d_{ab} = \frac{1}{(m_a - ß)!} \frac{d^{m_a - b}}{d x^{m_a - b}} \left(\frac{e_0}{\prod_{\substack{j=1 \\ j \neq a}}^{N} (x - c_j)^{m_j}} \right) \Bigg|_{x = c_a} \tag{3.15}$$

It should be noted that Eq. (3.15) is used when a symbolic package package solver such as *Mathematica*[184] is available. As an alternate formula suitable for FORTRAN or C computer programming languages, the coefficient d_{jk} can be computed as a vector from Eqs. (C18 - C23) given in Appendix C.

The axial deformation can be obtained by a direct integration of Eq. (3.13) to give:

$$u(x, N_0) = f(x, N_0) - f(L, N_0) \tag{3.16}$$

where

$$f(x, N_0) = \sum_{j=1}^{N} a_j \, A(j, m_j) + \sum_{j=1}^{N} \sum_{k=1}^{m_j - 1} d_{jk} \, A(j, m_j) \tag{3.17}$$

$$A(j,k) = \begin{cases} \ln (x - c_j) & \text{for} \quad k = 1 \\ \dfrac{(x - c_j)^{1-k}}{(1-k)} & \text{for} \quad k > 1 \end{cases} \tag{3.18}$$

3.2.2 Flexibility Matrix of the Cantilever Bar

Based on the sign convention of Fig. 3.1, one can write the flexibility matrix of the cantilever bar in the form:

$$u_1 = f_{11} N_1 \tag{3.19}$$

The coefficient f_{11} is a deformation at Point 1 due to a unit axial force $N_1 = 1$ at Point 1. Referring to Eq. (3.16), we can write f_{11} as

$$f_{11} = u(0,1) = f(0,1) - f(L,1) \tag{3.20}$$

3.2.3 Stiffness Matrix

By following the steps given in Appendix D, the stiffness matrix coefficient s_{11} can be obtained as:

$$s_{11} = \frac{1}{f_{11}} \tag{3.21a}$$

Since the transformation matrix T_{jk} is equal to 1, the other stiffness matrix coefficients can be obtained as:

$$s_{22} = -s_{12} = -s_{21} = s_{11} = \frac{1}{f_{11}} \tag{3.21b}$$

Therefore Eq. (3.6) now can be written with the final form of the axial stiffness matrix as follow

$$\begin{Bmatrix} N_1 \\ N_2 \end{Bmatrix} = \frac{1}{f_{11}} \begin{bmatrix} 1 & -1 \\ -1 & 1 \end{bmatrix} \begin{Bmatrix} u_1 \\ u_2 \end{Bmatrix} \tag{3.22}$$

where Eqs. (3.14) – (3.20) are needed to calculate f_{11}.

3.3 Torsional Stiffness Matrix of Non-uniform Beam Elements

Similar to the formulation of the axial stiffness matrix, the formulation of the torsional stiffness matrix of a non-uniform beam can be developed by following the derivation in Section 3.2. The twist angle f, the torque T and the torsional stiffness GJ are

used in the torsional stiffness formulation to replace the elongation u, the axial force N and the axial stiffness EA, respectively. Therefore the torque moment – twist deformation relation with the final form of the torsional stiffness matrix can be written as follow

$$\begin{Bmatrix} T_1 \\ T_2 \end{Bmatrix} = \frac{1}{f_{11}} \begin{bmatrix} 1 & -1 \\ -1 & 1 \end{bmatrix} \begin{Bmatrix} f_1 \\ f_2 \end{Bmatrix} \tag{3.23}$$

where f_{11} is calculated from Eqs. (3.14) – (3.20). For the formulation of the torsional stiffness matrix, the axial stiffness variables defined in Eqs. (3.5) and (3.11) are replaced by the following forms:

$$J(x) = J_c \prod_{j=1}^{N} \left(x - c_j\right)^{m_j}$$
$$e_0 = \frac{T_0}{GJ_c} \tag{3.24}$$

3.4 Flexural Stiffness Matrix of Non-uniform Beam Elements

Stiffness matrix formulation for a beam bending problem is more involved than the formulation for axial and torsional problems. Consider a tapered beam element of length L made of an isotropic elastic material of modulus E as shown in Fig. 3.3. Similar to the assumption adopted by Gallagher and Lee in Ref. 48, shear deflections and rotatory inertia effects are neglected for the present model. In the present section, we assume that the cross-coupling moment of inertia $I_{yz} = 0$. The treatment for $I_{yz} \neq 0$ is presented in Section 3.6. The moment of inertia $I = I(x)$ about the z axis varies as an arbitrary polynomial function in x as follow:

$$I(x) = I_c \prod_{j=1}^{N} \left(x - c_j\right)^{m_j} \tag{3.25}$$

Based on the sign convention of Fig. 3.3, one can write the nodal force-displacement relation for the flexural deformation of the element in the form:

$$\begin{pmatrix} V_1 \\ M_1 \\ V_2 \\ M_2 \end{pmatrix} = \begin{bmatrix} s_{11} & s_{12} & s_{13} & s_{14} \\ & s_{22} & s_{23} & s_{24} \\ & & s_{33} & s_{34} \\ Symm. & & & s_{44} \end{bmatrix} \begin{pmatrix} v_1 \\ \theta_1 \\ v_2 \\ \theta_2 \end{pmatrix} \tag{3.26}$$

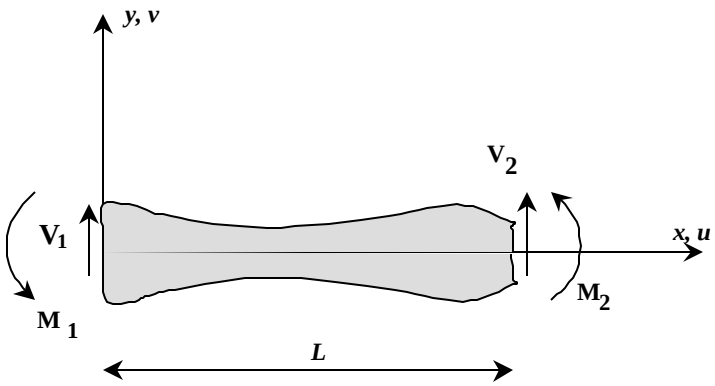


Figure 3.3. Geometry and sign convention of a tapered beam element

The purpose of this section is to formulate the stiffness matrix coefficients s_{ij} in Eq. (3.26) in terms of the geometric parameters EI_j, c_j , m_j , N and L. The formulation includes the following three steps: Displacement of a cantilever beam problem, the flexibility matrix, and the stiffness matrix.

3.4.1 Displacement of a cantilever beam problem

Consider a cantilever beam with a fixed support at $x = L$ as shown in Fig. 3.4. The beam stiffness $EI(x)$ varies according to Eq. (3.25). The Euler-Lagrange differential equation for the Euler-Bernoulli-beam with a small deflection assumption can be written as

$$\frac{d^2}{dx^2}\left(EI(x)\frac{d^2 v}{dx^2} \right) = q(x) \tag{3.27}$$

where $q(x)$ is the transverse distributed load. A treatment for $q(x) \neq 0$ is given in Section 3.5. In the present section, assume $q(x) = 0$ and solve Eq. (3.27) to give

$$\frac{d}{dx}\left(EI(x)\frac{d^2 v}{dx^2} \right) = Q \tag{3.28}$$

$$EI(x)\frac{d^2 v}{dx^2} = M(x) \tag{3.29}$$

where Q is a constant shear force and $M(x)$ is a bending moment for $0 < x < L$.

To solve Eq. (3.29), two boundary conditions at the cantilever beam support (Fig. 3.4) are needed as follows:

$$\begin{aligned} v\big|_{x=L} &= 0 \\ \left.\frac{dv}{dx}\right|_{x=L} &= 0 \end{aligned} \tag{3.30}$$

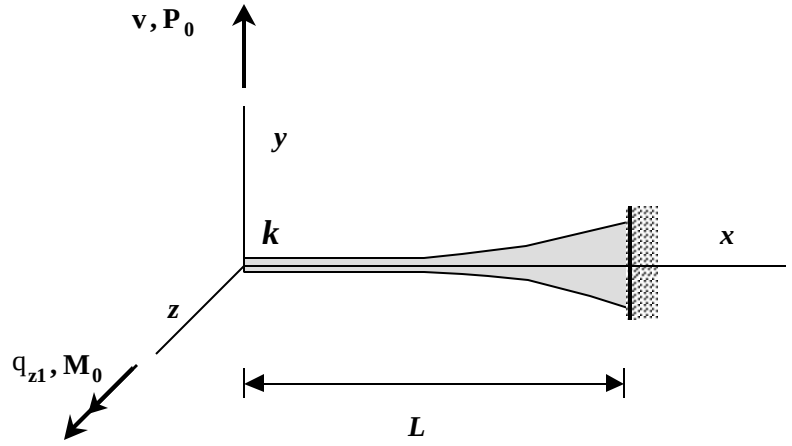


Figure 3.4. A cantilever beam model to derive the flexibility matrix

If concentrated force and moment P_0 and M_0 are loaded at the free end of the beam, the bending moment $M(x)$ in Eq. (3.29) can be written as:

$$M(x) = M_0 - P_0\, x \tag{3.31}$$

To simplify the solution, Equation (3.31) is simplified by introducing the following variable e_I such that Eq. (3.31) becomes

$$M(x) = EI_c\left(e_0 + e_1\, x\right) \tag{3.32}$$

where

$$e_0 = \frac{M_0}{EI_c} \tag{3.33a}$$

$$e_1 = \frac{-P_0}{EI_c} \tag{3.33b}$$

To find a deflection at the free end due to P_0 and M_0, substitute Eqs. (3.27) and (3.32) into Eq. (3.29) and simplify the result by eliminating EI_c from the left and right sides of the equation to give:

$$\frac{d^2 v}{d x^2} = \frac{e_0 + e_1 x}{\prod_{j=1}^{N}\left(x - c_j\right)^{m_j}} \tag{3.34}$$

Similar to the treatment for the axial stiffness problem, Eq. (3.34) is solved for v and dv/dx is by rewriting the rational function in the right-hand side of Eq. (3.34) as a sum of terms with minimal denominators such as the procedure proposed in Appendix C. By referring to Eq. (C.11), the right-hand side of Eq. (3.34) becomes:

$$\frac{d^2 v}{d x^2} = \frac{e_0}{\prod_{j=1}^{N}\left(x - c_j\right)^{m_j}} = \sum_{j=1}^{N}\frac{a_j}{\left(x - c_j\right)^{m_j}} + \sum_{j=1}^{N}\sum_{k=1}^{m_j - 1}\frac{d_{jk}}{\left(x - c_j\right)^{k}} \tag{3.35}$$

where the coefficients a_a *and* d_{ab} have been solved in Eq. (C12) and (C17) respectively as follow

$$a_a = \frac{e_0}{\prod_{\substack{k=1 \\ k \neq a}}^{N} (c_a - c_k)} \tag{3.36}$$

$$d_{ab} = \frac{1}{(m_a - ß)!} \frac{d^{m_a - b}}{d x^{m_a - b}} \left(\frac{e_0}{\prod_{\substack{j=1 \\ j \neq a}}^{N} (x - c_j)^{m_j}} \right) \Bigg|_{x = c_a} \tag{3.37}$$

It should be noted that Eq. (3.37) is used when a symbolic package solver such as *Mathematica*[184] is available. As an alternate formula suitable for FORTRAN or C computer programming languages, the coefficient d_{jk} can be computed as a vector from Eqs. C(18-23) in Appendix C.

The tip rotation and deflection can be obtained now by a direct integration of Eq. (3.35) to give:

$$\begin{aligned} v'(x, P_0, M_0) &= f(x, P_0, M_0) - f(L, P_0, M_0) \\ v(x, P_0, M_0) &= F(x, P_0, M_0) - F(L, P_0, M_0) - x f(x, P_0, M_0) + L f(L, P_0, M_0) \end{aligned} \tag{3.38}$$

where

$$\begin{aligned} f(x, P_0, M_0) &= \sum_{j=1}^{N} a_j A(j, m_j) + \sum_{j=1}^{N} \sum_{k=1}^{m_j - 1} d_{jk} A(j, m_j) \\ F(x, P_0, M_0) &= \sum_{j=1}^{N} a_j B(j, m_j) + \sum_{j=1}^{N} \sum_{k=1}^{m_j - 1} d_{jk} B(j, m_j) \end{aligned} \tag{3.39}$$

$$A(j,k) = \begin{cases} \ln(x - c_j) & \text{for} \quad k = 1 \\ \dfrac{(x - c_j)^{1-k}}{(1-k)} & \text{for} \quad k > 1 \end{cases} \tag{3.40}$$

$$B(j,k) = \begin{cases} -x + (x-c_j)\ln(x-c_j) & for \quad k=1 \\ -\ln(x-c_j) & for \quad k=2 \\ \dfrac{(x-c_j)^{2-k}}{(1-k)(2-k)} & for \quad k>2 \end{cases} \tag{3.41}$$

3.4.2 Flexibility Matrix of the Cantilever Beam

Based on the sign convention of Fig. 3.3, one can write the flexibility matrix of the cantilever beam in the form:

$$\begin{Bmatrix} v_1 \\ \theta_1 \end{Bmatrix} = \begin{bmatrix} f_{11} & f_{12} \\ f_{21} & f_{22} \end{bmatrix} \begin{Bmatrix} M_1 \\ M_1 \end{Bmatrix} \tag{3.42}$$

where

$$f_{21} = f_{12}$$

The flexibility matrix given in Eq. (3.42) is important to form the stiffness matrix given in Eq. (3.28). In the present work, the stiffness matrix is obtained based on a translation of axis procedure described in Appendix D. The procedure is useful to reduce the computational time since a direct inversion is avoided and only three independent coefficients f_{ij} of the flexibility matrix are needed. The easiest way to select the three coefficients f_{ij} in Eq. (3.42) is the one that is related to the beam deformations given by Eq. (3.38); i.e. the three coefficients are f_{11}, f_{12} and f_{22}. By referring to Fig. 3.4, the first coefficient f_{11} is a deflection at Point 1 due to a unit force P_0 =1, the second coefficient f_{12} is a rotation due to a unit force P_0 =1, and the third coefficient f_{22} is a rotation due to a unit moment M_0 =1. These deformations can be obtained from Eq. (3.38) as follow:

$$\begin{aligned} f_{11} &= v\,(x=0, P_0=1, M_0=0) \\ f_{12} &= v'(x=0, P_0=1, M_0=0) \\ f_{22} &= v'(x=0, P_0=0, M_0=1) \end{aligned} \tag{3.43}$$

3.4.3 Stiffness Matrix

By following the steps given in Appendix D, the stiffness matrix coefficient s_{ij} can be obtained as:

$$
\begin{aligned}
s_{11} &= s_{33} = -s_{13} = f_{22} / D_a \\
s_{12} &= -s_{23} = -f_{12} / D_a \\
s_{22} &= f_{11} / D_a \\
s_{14} &= s_{11}\, L - s_{12} \\
s_{24} &= s_{12}\, L - s_{22} \\
s_{44} &= s_{14}\, L - s_{24} \\
D_a &= f_{11}\, f_{22} - f_{12}^2
\end{aligned}
\tag{3.44}
$$

3.5 Non-uniform Load

Consider a tapered beam element subjected to concentrated and distributed loads as shown in Fig. 3.5a. The beam geometric data are similar to the beam described in the previous sections, i.e. shear deflections and rotatory inertia effects are neglected, I_{yz} = 0 and the moment of inertia $I = I(x)$ about the z axis varies as an arbitrary polynomial function in x as given in Eq. (3.25). The loads can be distributed in any 6 degrees-of-freedom (DOF) directions, i.e. they can be axial and lateral forces, and torque and flexural moment loads, or their combinations. The load can be partially loaded. The load distribution function is a general polynomial function in x with arbitrary order as follows:

$$
q(x) = \sum_{j=1}^{N_q} q_j\, x^j \qquad 0 \le x_a \le x \le x_b \le L \tag{3.45}
$$

The purpose of this section is to formulate the so-called fixed-end reactions, *i.e.* the reaction forces and moments at both ends of the element to balance the loading where the supports at both ends of the element are fixed. The fixed-end reactions are used in the global finite element calculation as external concentrated loads at each end of the element.

The fixed-end reactions at both supports of the beam subjected to the load shown in Fig. 3.5a are calculated based on the method of superposition. In this method, the support at the left-end of the beam is released first such that the structure becomes statically determinate as shown in Figs. 3.5b and 3.5c. If the total deformations at the tip of the cantilever beam due to the superposition of the non-uniform load and the reaction forces and moments at the left-end of the beam are set equal to zero, then the reaction forces and moments can be calculated.

Therefore, the necessary steps to generate the fixed-end reactions are as follows:

(1) Calculation of tip deformations of a cantilever beam under unit loads at the tip.

The 6 DOF deformations at the tip of the cantilever beam under each of the unit loads at the tip as shown in Fig. 3.5c are calculated first. Since there are 6 unit loads, the number of the tip deformations that can be generated are 36. If g_{ij} is defined as the tip deformation in the i direction due to the unit load in the j direction, then we can construct a 6-by-6 matrix of the tip deformation as follows

$$[g_{ij}] = \begin{bmatrix} g_{11} & g_{12} & g_{13} & g_{14} & g_{15} & g_{16} \\ & g_{22} & g_{23} & g_{24} & g_{25} & g_{26} \\ & & g_{33} & g_{34} & g_{35} & g_{36} \\ & & & g_{44} & g_{45} & g_{46} \\ & & & & g_{55} & g_{56} \\ \textit{Symm.} & & & & & g_{66} \end{bmatrix} \tag{3.46}$$

(2) Calculation of tip deformations of a cantilever beam under the non-uniform load.

The 6 DOF deformations of the cantilever beam under the non-uniform load (Fig. 3.5b) are next calculated. If h_j is defined as the deformation at the tip in the j direction, then we can construct the tip deformation vector as follows:

$$\{h_j\} = \begin{Bmatrix} h_1 \\ h_2 \\ \cdots \\ h_6 \end{Bmatrix} \tag{3.47}$$

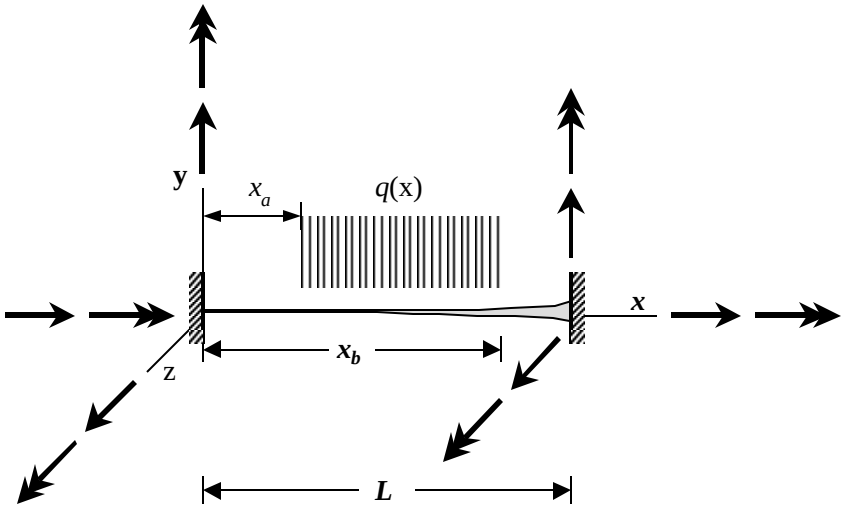


Fig. 3.5a

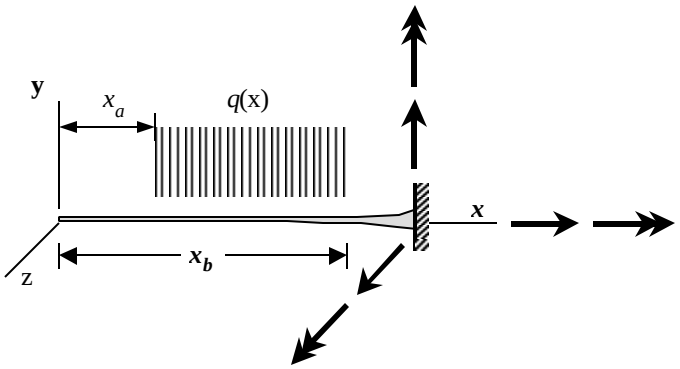


Fig. 3.5b

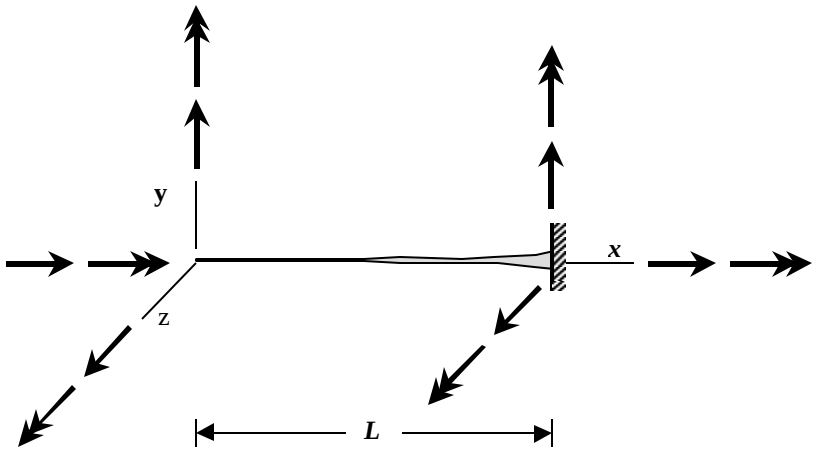


Fig. 3.5c

Figure 3.5. A non-uniform beam element under a non-uniform distributed load
(a) Fixed-end forces and moments of a non-uniform beam subjected to the distributed load $q(x)$
(b) A cantilever beam under the distributed load $q(x)$
(c) The cantilever beam under the concentrated forces and moments at the tip

(3) Calculation of the fixed end reactions

The fixed-end reactions at the left-end of the beam shown in Fig. 3.5a are calculated based on the following equation:

$$\{F_i\} = -\left[\ g_{ij}\ \right]^{-1} \{h_j\} \tag{3.48}$$

where F_i is defined as the reaction force or moment in the i direction. The fixed-end reactions at the right-end of the beam shown in Fig. 3.5a are calculated based on the force and moment equilibriums.

It should be noted that, to calculate the tip deformations in Steps (1) and (2) of the procedure above, the method developed in Sections 3.2 - 3.4 can be used. For the distributed lateral load, the distributed load $M(x)$ in Eq. (3.32) can be written as:

$$M(x) = EI_c \sum_{i=1}^{N_M} e_i\ x^i \tag{3.49}$$

where the coefficients e_i is functions of the external load coefficients q_j given in Eq. (3.45). The same procedure can be employed to calculate the fixed-end reaction forces and moments for the beam subjected to axial and torsional distributed loads.

3.6 Non-Symmetric Cross Section Beam

The procedure to formulate the flexural stiffness matrix derived in Section 3.4 is applicable only for a beam having a symmetric cross section, *i.e.* the cross coupling moment of inertia I_{yz} is equal to zero. For a non-symmetric cross-section beam, deformations of the beam in the x-y plane are coupled to the deformations in the x-z plane as follows:

$$\begin{aligned} EI_{zz}(x)\frac{d^2v}{dx^2} + EI_{yz}(x)\frac{d^2w}{dx^2} &= M_z(x) \\ EI_{yz}(x)\frac{d^2v}{dx^2} + EI_{yy}(x)\frac{d^2w}{dx^2} &= -M_y(x) \end{aligned} \tag{3.50}$$

or,

$$\begin{bmatrix} EI_{zz}(x) & EI_{yz}(x) \\ EI_{yz}(x) & EI_{yy}(x) \end{bmatrix} \begin{Bmatrix} \frac{d^2 v}{d x^2} \\ \frac{d^2 w}{d x^2} \end{Bmatrix} = \begin{Bmatrix} M_z(x) \\ -M_y(x) \end{Bmatrix} \tag{3.51}$$

Equation (3.51) can be solved for the second derivatives of the deformations as follows:

$$\begin{aligned} \frac{d^2 v}{d x^2} &= \frac{M_z(x)\, EI_{yz}(x) + M_y(x)\, EI_{zz}(x)}{EI_{zz}(x)\, EI_{yy}(x) - EI_{yz}^2(x)} \\ \frac{d^2 w}{d x^2} &= -\frac{M_z(x)\, EI_{yy}(x) + M_y(x)\, EI_{yz}(x)}{EI_{zz}(x)\, EI_{yy}(x) - EI_{yz}^2(x)} \end{aligned} \tag{3.52}$$

Based on Eq. (3.52), the deformations v and w can be evaluated separately by following the same procedure given in Section 3.4 except that the bending moment distribution M(x) in Eq. (3.32) and the stiffness distribution I(x) in Eq. (3.25) should be replaced by the followings:

For the deformation in the $x - y$ plane:

$$I(x) = I_{zz}(x)\, I_{yy}(x) - I_{yz}^2(x) \tag{3.53}$$

$$M(x) = M_z(x)\, EI_{yz}(x) + M_y(x)\, EI_{zz}(x) \tag{3.54}$$

For the deformation in the $x - z$ plane:

$$I(x) = I_{zz}(x)\, I_{yy}(x) - I_{yz}^2(x) \tag{3.55}$$

$$M(x) = -M_z(x)\, EI_{yy}(x) - M_y(x)\, EI_{yz}(x) \tag{3.56}$$

It should be noted that the procedure given in Section 3.4 is applicable for arbitrary polynomial function of the bending rigidity. Therefore, new polynomial functions of the

stiffness such as shown in Eqs. (3.53) and (3.55), may not introduce any difficulty in the application of the present procedure in the stiffness matrix formulation of the non-symmetric cross-section beam.

3.7 Geometric Stiffness Matrix Formulation

Gallagher and Lee[48] derived an approximation to the bending stiffness and geometric stiffness matrix [K_g] shown in Eq. (3.57) based on a cubic function displacement. It has been known that based on this assumption, the buckling load result given by the standard geometric stiffness matrix [K_g] is not exact even for a uniform beam. For a uniform beam, the number of elements should be increased to achieve an accurate result. Nevertheless, the assumption gives a simple formula for non-uniform beams and the accuracy can be increased consistently by increasing the number of elements[48].

$$\left[[K] - P\,[K_g] \right] \{ u \} = \{ 0 \} \tag{3.57}$$

On the other hand, an exact solution to the buckling problem of the uniform beam can be derived if an appropriate sinusoidal function is used for the displacement function. The result as given in Ref. 37 is shown in the following equation

$$[K_e\,(P)] \{ u \} = \{ 0 \} \tag{3.58}$$

where the modified stiffness matrix [K_e] is given as

$$[K_e] = \frac{EI}{L^3 D_b} \begin{bmatrix} s_1 & s_2 & -s_1 & s_2 \\ & s_3 & -s_2 & s_4 \\ & & s_1 & -s_2 \\ Symm. & & & s_3 \end{bmatrix} \tag{3.59}$$

$$D_b = 2 - 2\cos\lambda - \lambda\sin\lambda$$
$$\lambda = L\sqrt{\frac{P}{EI}} \tag{3.60}$$

$$s_1 = \lambda^3 \sin\lambda$$
$$s_2 = \lambda^2 \left(1 - \cos\lambda\right) L$$
$$s_3 = \lambda^2 \left(\sin\lambda - \lambda\cos\lambda\right) L^2 \tag{3.61}$$
$$s_4 = s_2\, L - s_3$$

Since the formulation of $[K_e]$ involves a non-linear function in terms of P, the eigen solution to Eq. (3.58) needs a special numerical scheme especially when the structure is modeled using a large number of elements. Standard matrix solution packages such as LAPACK and IMSL solve the eigenvalue problem given by Eq. (3.57) rather than Eq. (3.58). It appears desirable, therefore, to solve the buckling problem in the form of Eq. (3.57) but with improving the accuracy of the formulation without the need to increase the number of elements. In the present work, this idea can be accomplished by revisiting Eq. (3.57) based on a Taylor series expansion of Eq. (3.59) in terms of P

$$[K_e(P)] = \sum_{k=0}^{\infty} \frac{\partial^{(k)}}{\partial x^{(k)}} [K_e(P)] \Big|_{P=0} \frac{P^k}{k!} \tag{3.62}$$

If we retain only the linear term and perform an appropriate L'Hopital rule, the result is

$$[K_e(P)] = [K_e]\Big|_{P=0} + P \left[\frac{\partial}{\partial x} K_e\right]\Big|_{P=0} + O(P^2) \tag{3.63}$$

where

$$[K_e]\Big|_{P=0} = \frac{EI}{L^3}\begin{bmatrix} 12 & 6L & -12 & 6L \\ & 4L^2 & -6L & L^2 \\ & & 12 & -6L \\ & & & 4L^2 \end{bmatrix} \tag{3.64}$$

$$\left[\frac{\partial}{\partial x}K_e\right]\Big|_{P=0} = -\frac{1}{30\,L}\begin{bmatrix} 36 & 3L & -36 & 3L \\ & 40L^2 & -3L & -10L^2 \\ & & 36 & -3L \\ Sym. & & & 40L^2 \end{bmatrix} \tag{3.65}$$

Equations (3.64) and (3.65) yield respectively to the flexural stiffness matrix [K] and geometric stiffness matrix [K_g] of Eq. (3.57) for a uniform beam element. Therefore, Eq. (3.57) can be regarded as a linearization of Eq. (3.62) where only linear terms of P are considered.

If we further extend the idea by expanding the exact stiffness matrix [K_e] of Eq. (3.59) in terms of $(P - P_0)$, Eq. (3.62) becomes,

$$[K_e(P)] = \sum_{k=0}^{\infty} \frac{\partial^{(k)}}{\partial x^{(k)}} [K_e(P)] \Big|_{P=P_0} \frac{(P-P_0)^k}{k!} \tag{3.66}$$

By considering only the linear terms, Eq. (3.66) can be rearranged as

$$\begin{aligned} [K_e(P)] &= [K_e]\Big|_{P=P_0} + (P - P_0)\left[\frac{\partial}{\partial x}K_e\right]\Big|_{P=P_0} + O(P^2) \\ &= [K_0] + P[K_{g_0}] + O(P^2) \end{aligned} \tag{3.67}$$

where

$$[K_0] = \frac{EI}{L^3}\begin{bmatrix} s_1 & s_2 & -s_1 & s_2 \\ & s_3 & -s_2 & s_4 \\ & & s_1 & -s_2 \\ Symm. & & & s_3 \end{bmatrix} \tag{3.68}$$

$$[K_{g_0}] = \begin{bmatrix} n_1 & n_2 & -n_1 & n_2 \\ & n_3 & -n_2 & n_4 \\ & & n_1 & -n_2 \\ Symm. & & & n_3 \end{bmatrix} \tag{3.69}$$

$$s_1 = \frac{t^3}{2\,D_1}\left(\,t - \sin t\,\right)$$
$$s_2 = \frac{L}{2}\,s_1$$
$$s_3 = \frac{L^2\,t^2}{4D_2}\left(4t\left(\,t\ - \sin t\right)^2 + D_3\,\right) \tag{3.70}$$
$$s_4 = \ s_2\ L - s_3$$

$$n_1 = -\frac{t}{2\,L\,D_1}\left(\,t\,Cos\,t - 3\,Sin\,t + 2\,t\,\right)$$
$$n_2 = -\frac{1}{4\,D_1}\left(\,t\,Sin\,t + 4\,Cos\,t + t^2 - 4\,\right) \tag{3.71}$$
$$n_3 = \frac{L}{4\ D_2}\,D_3$$
$$n_4 = \ n_2\ L - n_3$$

$$D_1 = \left(\ \ t\ \ Cos\frac{t}{2}\ - 2\ \ Sin\frac{t}{2}\ \right)^2$$
$$D_2 = t\left(\,t\,Sin\,t\ +\ 2\ Cos\,t - 2\ \right)^2 \tag{3.72}$$

$$D_3 = -\,2\,t^3 - 4\,t\,Cos\,t + 4\,t\,Cos\,2t\ +\ 4\left(\,t^2 + 1\right)\,Sin\,t\ + \left(\,t^2 - 2\,\right)Sin\,2t$$

The non-dimensional parameter t is defined as

$$t\ =\ \sqrt{\frac{P_0\,L^2}{EI}} \tag{3.73}$$

where P_0 is the estimated axial force. If $P_0 = 0$ and the buckling load P is calculated only in one iteration, the result would be the same as that of Gallagher and Lee[48]. By using the present approach, the buckling load can be improved by updating P_0 with P calculated from the previous iteration for the same structural element, i.e. without the need to increase the number of elements. To accelerate the iteration, the initial estimation of P_0 can be started with a value that is greater than 0. In the present work, the default for the initial estimation of

P_0 is $p^2EI/4L^2$ which is the lowest possible buckling load for a cantilever uniform beam element of length L.

It should be noted that the geometric stiffness matrix given in Eqs. (3.69)-(3.73) is applicable for a flexural buckling problem. For a coupled torsional-flexural buckling problem, the approach proposed by Barsoum and Gallagher in Ref. 187 is used in the present work to formulate the geometric stiffness matrix. A detailed description of the approach for the coupled torsional-flexural buckling problem is given in Refs. 187 and 188.

3.8 Validation

The present procedure has been validated by comparison with NASTRAN for a number of different structural models. Three of these models are presented in the following. The first model, shown in Fig. 3.6, is a cantilever beam with a linear variation in $EI(x)$ with a concentrated moment load M_o acting at the tip. The flexural stiffness $EI(x)$ follows Eq. (3.1) with r = 8 and m=1. For this example, an exact result can be obtained by direct integration of the governing equation. Using NASTRAN, the tip deflections with 1, 2, 4, 8 and 16 tapered CBEAM beam elements are -1.601298, -1.647316, -1.655132, -1.655830, and -1.655861 $M_o L^2/EI_o$, respectively, as shown also in Fig. 3.6. The present method gives, with a single element, the exact deflection -1.65586235569 $M_o L^2/EI_o$.

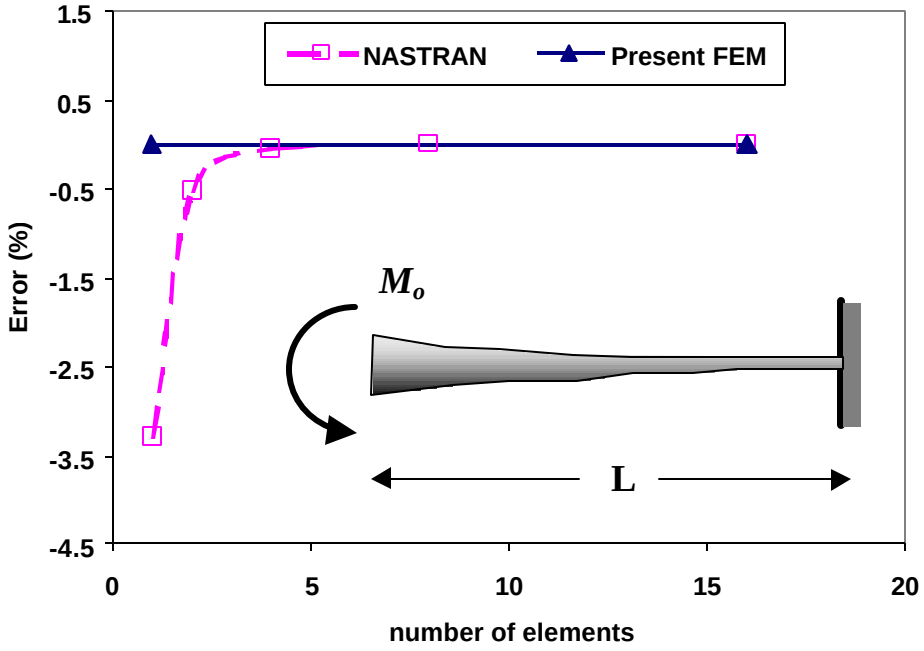


Figure 3.6. Convergence of the error of the tip displacement of the cantilever non-prismatic beam under a concentrated moment load M at the tip

The second model is a space frame structure consisting of seven identical uniform beams and one linearly tapered beam as shown in Fig. 3.7. A linearly distributed force load is applied to the tapered beam in the positive x direction. The stiffness variation of the tapered beam is the same as the first problem. The stiffness of the uniform beams is equal to EI_0. The exact solution is not available for this example. For each of the uniform beams, we can accurately use one beam element. The focus is on determining the accuracy of the tapered beam modeling. Using 1, 2, 4, and 8 tapered beam elements, NASTRAN solution for the deflection of Point 1 in the positive x-axis direction is -0.3083, 0.7394, 0.9161, and 0.9318 $q_0 L^3 / EI_0$ respectively. Figure 3.8 shows the convergence of the results with respect to the number of elements. The parameter $T_{reference}$ in Fig. 3.8 is the deflection of Point 1 calculated by the present method, and is equal to 0.9326 $q_0 L^3 / EI_0$ using one beam element to represent each frame members. The present method is more accurate since the stiffness

matrix of the tapered beam is formulated based on exact displacement function, whereas the CBEAM element of NASTRAN is based on a cubic displacement approximation.

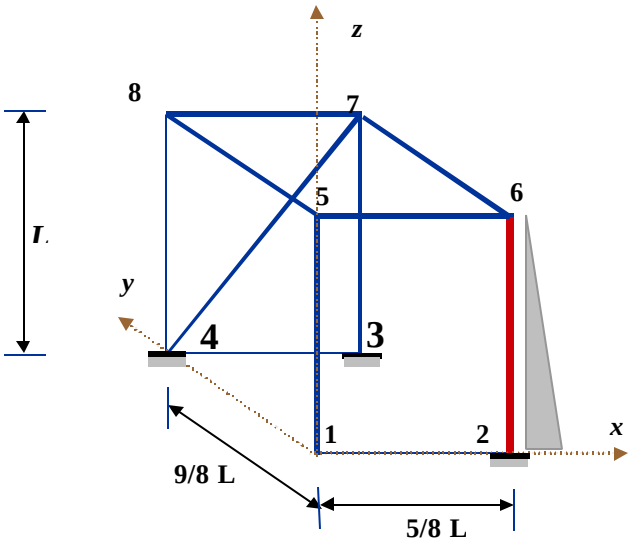


Figure 3.7. A space frame geometry consisted of uniform and tapered beam elements

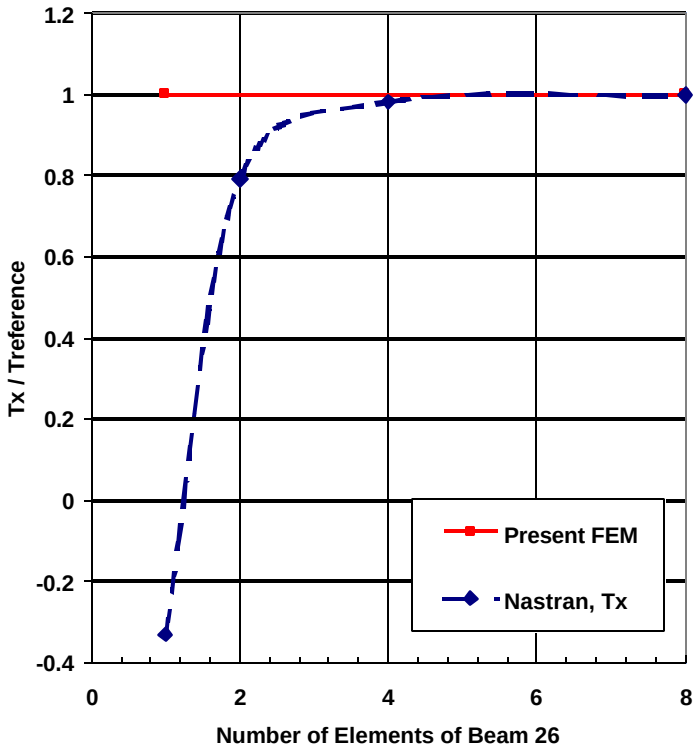


Figure 3.8. Convergence of the displacement of Point 1 of the space frame structure

The third example checks the accuracy for a buckling problem. A tapered beam with various supports and an axial concentrated force acting at the tip (see Fig. 3.9) is used. The stiffness variation of the beam is the same as for the first example. The linear and rotational spring constants k_a and k_b are EI_0 / L^3 and EI_0 / L^2, respectively. Since there are four supports on the span of the beam, at least three elements are needed. The beam is divided into several elements of equal length, except for the model with three elements. The NASTRAN solution for the first buckling load is 21.42748, 21.41838, 21.40572, and 21.40494 EI_0 / L^2 if the tapered beam is modeled using 3, 4, 8, and 16 tapered beam elements, respectively. By using three tapered elements, the present method gives the buckling load 21.40495 EI_0 / L^2.

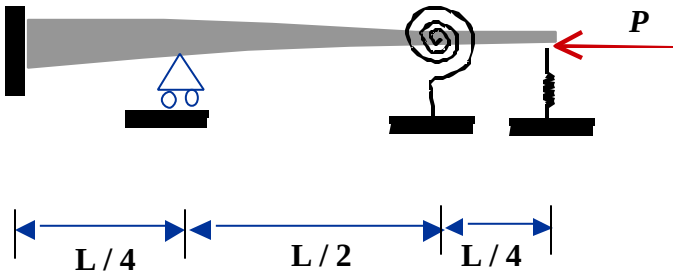


Figure 3.9. A non-prismatic beam with several supports

3.9 Buckling Analysis of Strut-Braced Wing

Buckling analysis in a strut-braced wing structure is not a new undertaking as it has been investigated for early biplane aircraft[185]. Von Karman and Biot in Ref. 185 showed that, in addition to aerodynamic loading, the biplane wing spar is subjected to an axial compression load exerted from horizontal component of the strut (connecting the two wings) forces. According to their formulation, the wing bending moment and deflection will increase infinitely when the axial load approaches the critical buckling load of the wing. In their treatment, however, the influence of the strut geometric stiffness is not included since the wing is simplified as a simply supported beam with hinged supports at the wing root and tip.

In the present work, a more rigorous model is used to predict the wing buckling limit. The wing-strut system is idealized as a space frame structure composed of tapered beams as shown in Fig. 3.10**.** The wing is clamped at the root and connected rigidly to the vertical offset beam at the wing strut junction. The strut junction location is at a distance $y_s\ b$ from the root where b is the wing semi-span. The geometric stiffness effect of the wing, strut and the offset beam is included in the buckling analysis by using the tapered beam finite element developed here. As a first approximation, the lift is approximated as a concentrated load. This wing-strut model simulates the wing deformation during a positive 2.5g maneuver

where the wing is bent upward, the wing inner part is in compression, and the strut is in tension. By using this model we can estimate the wing buckling capacity by finding the value of P that buckles the inner part of the wing.

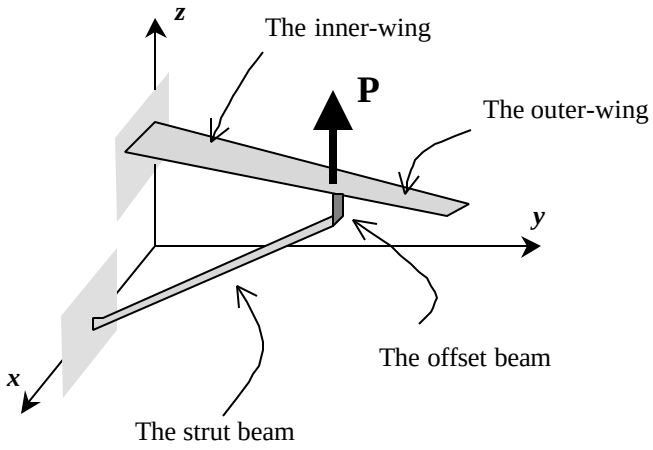


Figure 3.10. A space frame model of the wing-strut configuration

Assuming that the wing stiffness parameters do not change when the strut junction location is moved in spanwise direction, the wing buckling load for various positions y_s of the strut junction is shown in Fig. 3.11. The non-dimensional wing buckling load is the wing buckling capacity calculated by using the present method divided by $P_{referenced}$ which is the strut force P_s estimated by the MDO code. For the present configuration where y_s is 0.68, the safety factor is 2.52. It can be easily seen that as y_s decreases, *i.e.* the strut moves toward the wing root, the wing buckling capacity increases rapidly. This rapid increase of the buckling load is not surprising since in general the buckling load is inversely proportional to the square of the beam length $(y_s\, b)^2$. Figure 3.11 also presents the buckling load for a cantilever wing without strut subjected to an axial compressive load P at various position of y_s in the direction of the wing elastic axis. The significant increase in the wing buckling capacity for the wing with strut in comparison with respect to the wing without strut is shown in Fig. 3.11.

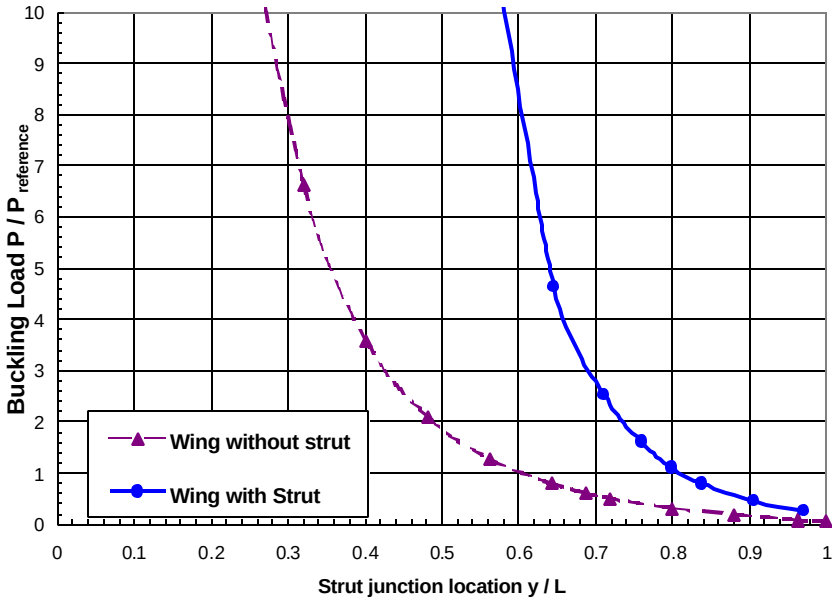


Figure 3.11. Buckling load versus spanwise location of the strut junction. $P_{reference}$ is the strut load calculated by the MDO code. For the wing without strut, P is an axial compression load in the direction of the wing elastic axis.

Previous investigation[22] conducted to increase the wing buckling load capacity revealed that the length of the offset beam between wing and strut may play an important role[22]. The dependence of the wing buckling load on the offset beam length and stiffness was calculated, and the result is shown in Fig. 3.12. The increase of the buckling load for this case is related to the slope of the strut axis, *i.e.* the buckling load increases as the slope of the strut axis decreases. However, the buckling load also decreases if the offset length increases since the increase of the offset length will reduce the rigidity of the wing-strut structure. For this reason Fig. 3.12 shows a peak curve for the buckling load. It is found that the optimum height for the offset beam is 2.5 times the original height given in Table 3.1.

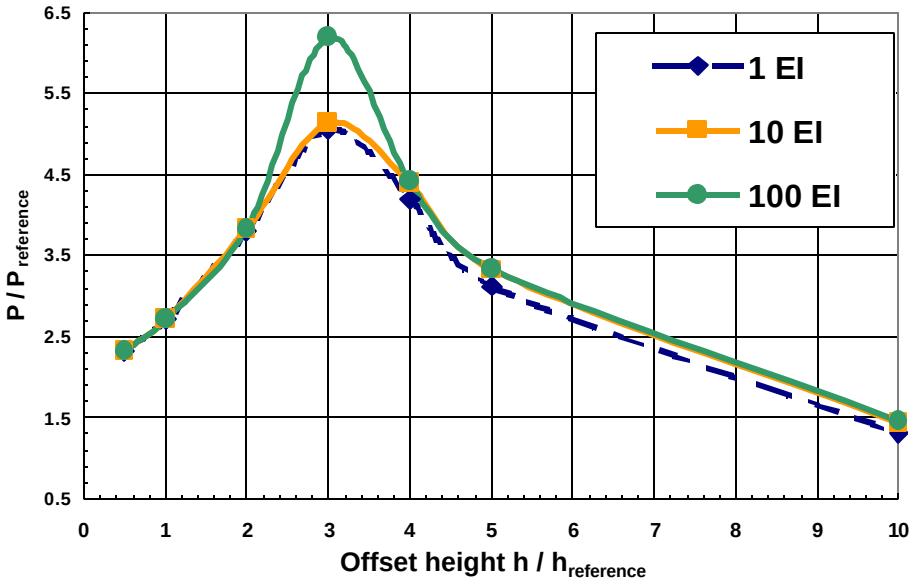


Figure 3.12. Buckling load versus the offset beam length and stiffness. $P_{reference}$ is the strut load predicted by the MDO code, $h_{reference}$ is the offset beam length given in Tabel 2.1.

Chapter 4
Unsteady Aerodynamic Load Prediction

4.1 Introduction

Accurate prediction of unsteady aerodynamic loads is an essential part of solving aeroelasticity problems. This accurate estimation is required for aircraft design as it is related directly to predicting maximum structural stresses, deflection, flight speed and flight envelope among other quantities of interest. Significant research has been performed in the past to study analytical, numerical and experimental aspects of the problem in all flight regimes[51-131]. Such investigations are still going on in an effort to improve the accuracy and efficiency of the prediction methods for more complicated aerodynamic configurations. Review of these development will be presented subsequently in this Chapter. Some of the review and theoretical background has been given in an earlier work of the present author in Ref. 135. They are presented, for completeness, in Sections 4.2 of the present work with additional new progress in lifting surface methods.

Several basic theoretical procedures have been developed to evaluate aerodynamic loads on thin wings or the so-called lifting surfaces[51, 52]. The most widely used version in aeroelasticity is the pressure – normal wash formulation[52, 55] since one deals directly with

the pressure difference distribution and the velocity on the surface without any evaluation in the wake region. This basic formulation will be used in the present work and described in the next sections of this chapter. A survey of various numerical solutions is presented and followed by the improvement of the solutions proposed in the present work. The present methodology consists of three different methods: the vortex lattice method (VLM), the doublet lattice method (DLM), and the doublet point method (DPM) which are described in Sections 4.5, 4.6 and 4.7 respectively. A detailed derivation of the present method will be addressed in Appendix A. Various wing planforms and configurations described in Section 4.10 are used to verify the applicability of the proposed methods, and the results are compared with experimental data or other lifting surface methods.

4.2 Theoretical Background

4.2.1 Assumptions

The basic lifting surface theory assumes that the flow is inviscid, isentropic, subsonic, and has no flow separation. The thickness of the surface is neglected and the angle of attack is small such that the small-disturbance potential flow approach may be used to linearize the mixed boundary value problem. The compressibility effect is taken into account in the aerodynamic governing equation using the Prandtl-Glauert transformation.

4.2.2 Basic Concept

The basic differential equations governing the velocity potential φ in Cartesian coordinates is [57, 58]

$$\nabla^2\varphi = \frac{1}{a^2}\left\{\frac{\partial}{\partial t}(\nabla\varphi \bullet \nabla\varphi) + \frac{\partial^2\varphi}{\partial t^2} + \nabla\varphi \bullet \nabla\left(\frac{\nabla\varphi \bullet \nabla\varphi}{2}\right)\right\} \tag{4.1}$$

where the vector operator ∇ is given as

$$\nabla = \vec{i}\,\frac{\partial}{\partial x} + \vec{j}\,\frac{\partial}{\partial y} + \vec{k}\,\frac{\partial}{\partial z} \tag{4.2}$$

If the lifting surface moves in the x direction and oscillates harmonically with frequency ω (radian/second) and with a small perturbation about its equilibrium, Eq. (4.1) becomes [54,59,60]

$$\nabla^2\,\varphi = \frac{1}{a^2}\left(i\,\omega + U\,\frac{\partial}{\partial x}\right)^2 \varphi \tag{4.3}$$

where

$$j\,(t) = j\;e^{iwt} \tag{4.4}$$

The velocity potential j is related to the harmonically varying pressure difference Δp by the Bernoulli equation :

$$\Delta\,p = -\rho_\infty\left(\frac{\partial\varphi}{\partial t} + U_\infty\,\frac{\partial\varphi}{\partial x}\right) \tag{4.5}$$

where

$$\Delta\,p = \Delta\,\overline{p}\,e^{i\omega t} \tag{4.6}$$

and the normal velocity or downwash is

$$\vec{w} = \frac{\partial\vec{J}}{\partial z} \tag{4.7}$$

Note that the z-direction is normal to the lifting surface as shown in Fig. 4.1.

To solve this boundary value problem, Kussner[61] proposed a general integral equation that relates the normal-wash $\overline{w}$ at a point (x, y, z) due to a pulsating pressure $\Delta\,\overline{p}$ on an infinitesimal area $d\xi\,d\eta$ centered at a point (x, h, z) as shown in Fig. 4.1. Kussner's integral equation can be written as:

$$\overline{w} = \frac{1}{8\pi} \iint_S \Delta \bar{p}\, K(x_o, y_o, z_0, k, M)\, d\xi\, d\eta \tag{4.8}$$

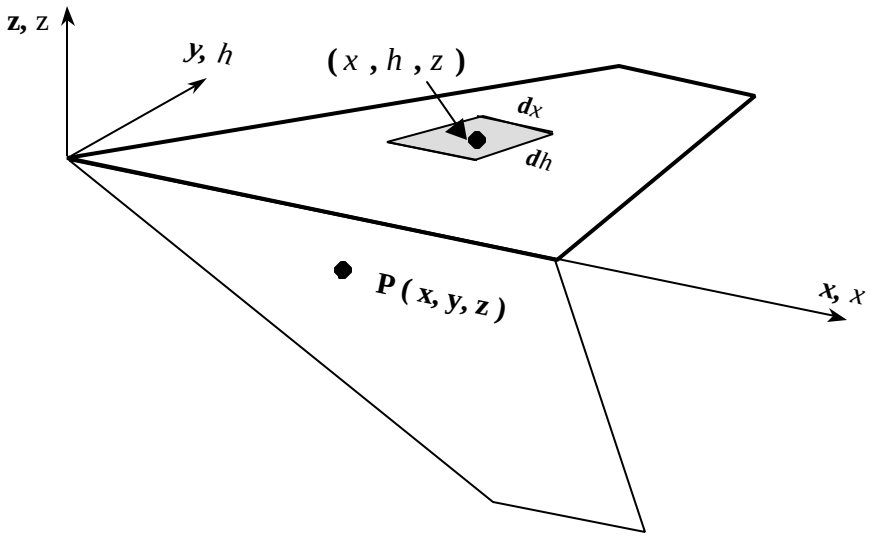


Figure 4.1. The induced velocity at point P (*x*,*y*,*z*) due to pressure loading on an infinitesimal area *dx dh* centered at point (*x*, *h*, *z*)

where the function $K(x_o, y_0, z_o, k, M)$ represents the kernel function of the integral equation. No detailed form of the kernel function was given in Ref. 61.

The first attempt to formulate the kernel function K for planar lifting surfaces has been accomplished by Watkins, Runyan and Woolston (1955)[60] in the following form:

$$K = \lim_{z_0 \to 0} e^{-ikxo} \frac{\partial^2}{\partial z_0^2} \int_{-\infty}^{x_0} \frac{e^{ik(u - M R_1)/(1-M^2)}}{\sqrt{u^2 + (1-M^2)(y_0^2 - z_0^2)}}\, du \tag{4.9}$$

$$k = \frac{\omega b}{U_\infty} = \text{reduced frequency}$$

$$x_o = x - \xi$$
$$y_o = y - \eta \tag{4.10}$$
$$z_o = z - \zeta$$

Equation (4.9), which is derived at length in Ref. 60, was obtained by employing the Prandtl acceleration potential theory. Another approach that can be used to obtain Eq. (4.9) is the second Green's theorem[59] which has been applied by Giesing *et al.*[62] and Dowell[54] to give the same result. Detailed derivation of Eq. (4.9) may be found in references 54, 60, and 62.

The kernel function in Equation (4.8) can be converted to a more useful form given by[54] :

$$K = e^{-ikxo}\left(\frac{M}{\sqrt{R\,X_1}}e^{ikx} + \int_{-X/r}^{\infty}\frac{e^{iku}}{\left(r^2 + u^2\right)^{n+1/2}}du\right) \tag{4.11}$$

where M is the upstream Mach number and

$$r = \sqrt{y_o^{\,2} + z_o^{\,2}}$$
$$R = \sqrt{x^2 + \beta^2 r^2}$$
$$X = \left(x_o - M R\right)\beta^{-2} \tag{4.12}$$
$$X_1 = \sqrt{X^2 + r^2}$$
$$b = \sqrt{1 - M^2}$$
$$M < 1 \quad \text{(subsonic)}$$

Equation (4.11) has been widely used to calculate unsteady subsonic loads on planar wing - horizontal tail configurations[52,56]. However, for nonplanar arrangements, such as wings with dihedral, non-planar wing-tail configurations, T or V- tails and wings in ground-effect, a more general approach should be performed. In light of this need,

significant development in the formulation of the kernel for nonplanar configurations have been contributed by Laschka[65]. Yates[63], Rodemich[64], Landahl[64], and Berman, Shyprykevich and Smedfjeld[105]. Appendix A in the present work gives details of these formulations. The most widely used formula is the one proposed by Landahl[52, 62, 66, 70 – 87, 91 – 93] since it is less complicated than other formulas mentioned above[64]. Landahl's formulation is also used in the present work, which can be written as follows:

$$K = e^{-ikx_o}\left(\frac{K_1 T_1 + K_2 T_2}{r^2}\right) \tag{4.13a}$$

where

$$K_1 = \frac{M r^2}{R X_1} e^{ikx} + I_1$$

$$K_2 = -\frac{M r^4 e^{ikx}}{R^2 X_1}\left(ikM + \frac{b^2}{R} + \frac{2R - MX}{X_1}\right) - 3 I_2 \tag{4.13b}$$

$$I_n = \int_{-X/r}^{\infty} \frac{e^{iku}}{(1+u^2)^{n+1/2}}\, du$$

$$T_1 = \cos(g_s - g_r)$$

$$T_2 = \frac{(z_o \cos\gamma_s - y_o \sin\gamma_s)(z_o \cos\gamma_r - y_0 \sin\gamma_r)}{r^2}$$

and γ_r and γ_s are dihedral angles at the points (x, y, z) and (x, h, z), respectively. The other parameters, such as r, X, and (x_0, y_0, z_0) are defined in Eq. (4.12).

Landahl proposed Eq. (4.12) in 1967 and it is used in many unsteady aerodynamic codes such as the doublet lattice method of NASTRAN[53]. To the best of the present author's knowledge, no publication on the derivation was available until 1994, when Blair[138] published a comprehensive mathematical proof of the formula. This derivation is thus not described in the present work.

4.2.3 Boundary Conditions

The pressure distribution on the lifting surface may be obtained by substitution of Equations (4.7) or (4.8) into Equation (4.5) with the requirement that the solutions should satisfy two boundary conditions, the so-called Kutta condition and the flow tangency condition. The Kutta condition states that the pressure difference at the trailing edge of a thin lifting surface must be zero. The flow tangency condition states that for an inviscid flow the velocity vector must be tangent to the surface of the streamlined body.

4.2.4 Evaluation of the Kernel Function

The most critical part of calculating the kernel function in Equation (4.8) is the evaluation of the so-called incomplete cylindrical function I_1 and I_2 occurring in Eq. (4.13). Research, world wide, has been devoted to this problem during the last six decades. Some of the formulas are listed in Table 1.4 of Chapter 1. The formulas may be classified into two types:

Type-A
$$B_n = \frac{I_n}{r^{2n}} = \frac{1}{r^{2n}} \int_{-X/r}^{\infty} \frac{e^{iku}}{\left(1+u^2\right)^{n+1/2}}\, du \tag{4.14a}$$

Type-B
$$B_n = \int_{-\infty}^{X} \frac{e^{iku}}{\left(r^2+u^2\right)^{n+1/2}}\, du \tag{4.14b}$$

where r and X are defined in Eq. (4.12).

The difference between the two types of the integrals may easily be seen for $r = 0$ and $X < 0$ where a direct calculation of I_n / r^{2n} by using the type A integral may give an infinite result. The type-A integral was used earlier than the type-B in the formulation of unsteady aerodynamic lifting surface methods. There are two reasons that motivated the earlier usage of the type-A integral. The first reason is to simplify the evaluation of the kernel function. It is shown in Eq. (4.13) that the parameter r^2 is set as the denominator and

the incomplete cylindrical function I_n as the numerator. The usual approach in the past, such as in the formulation of the doublet lattice method, was to assume that the numerator can be approximated as a quadratic function. Or, in other words, the type-A integral form is more suitable since the parameter r^2 has already been extracted from the integral form. A more detailed derivation of the doublet lattice method is given in Section 4.2.7 of the present work. The second reason is because the analytical solution for the type-B was not available before 1981. Therefore it was difficult to analytically separate the regular and singular parts of the kernel function. In the present work, the type B integral is selected for the formulation of the present lifting surface discrete element method.

Solutions to both type-A and type-B integrals have been reported using approximation approach[51, 102, 103, 151] and analytical approach[78, 79]. A summary of these solutions is given in Table 1.4 of Chapter 1. The first attempt to perform analytical integration of the incomplete cylindrical function was conducted by Laschka using a Taylor expansion series[102]. However, he did not use his expansion series in his kernel function method[102] since he performed the integration only in the sub-interval [0, X] where the singularities occurred in the real and imaginary parts of the series. Ueda in Refs. 77 and 78 performed analytical solution of the type *B* form by conducted the integration completely in the sub-intervals [0, *X*] and [-∞, 0]. In his solution, the singularities occurring in the sub-interval [0, X] and [-∞, 0] cancel out each other if *X* is negative. His solution coincide exactly with the modified Bessel and Struve functions for a limiting case $X = 0$. For the incomplete cylindrical function of order *n*, the Ueda's expansion series can be written as follows[77, 78]:

$$B_n = \int_{-\infty}^{X} \frac{\cos k u}{\left(r^2 + u^2\right)^{n+1/2}}\, du + i \int_{-\infty}^{X} \frac{\sin k u}{\left(r^2 + u^2\right)^{n+1/2}}\, du = B_{n,\,real} + i\, B_{n,\,imag} \qquad (4.15)$$

where

$$B_{v,real} = \sum_{n=0}^{\infty} (-1)^n \, U_{v,2n} + \frac{(-k^2/2)^v}{(2v-1)!!} \sum_{n=0}^{\infty} p_n \frac{(k\,r/2)^{2n}}{n!\,(n+v)!}$$

$$B_{v,imag} = \sum_{n=0}^{\infty} (-1)^n \, U_{v,2n+1} - \frac{p}{2} \frac{(-k^2/2)^v}{(2v-1)!!} \sum_{n=0}^{\infty} \frac{(k\,r/2)^{2n}}{n!\,(n+v)!} \tag{4.16}$$

$$p_n = -g - \ln\frac{k}{2} + \sum_{m=1}^{n} \frac{1}{m} + \sum_{m=n+1}^{n+v} \frac{1}{2m}$$

γ = Euler's constant = 0.57721566490153286060606512…

and the U terms are based on the following recursion formulas :

$$U_{v,\,m\neq 2v} = \frac{k\,(kX)^{m-1}}{(m-2v)\,m\,X_1^{2v-1}} - \frac{(kr)^2}{(m-2v)\,m} U_{v,m-2}$$

$$U_{v,\,2v} = -\frac{k^{2v}}{2v!}\left\{ \ln(X_1 - X) + \sum_{m=1}^{v} \frac{1}{2m-1}\left(\frac{X}{X_1}\right)^{2m-1} \right\} \tag{4.17}$$

$$U_{v,\,2n<2v} = \frac{(v-n-1)!\,k^{2n}}{(2n)!\,r^{2(v-n)}} \left\{ 2^{v-n-1} \frac{(2n-1)!!}{(2v-1)!!} + \sum_{m=0}^{v-n-1} \frac{(-1)^m \, X^{m-1} \, (X/X_1)^{2m+2n+1}}{(2m+2n+1)\,m!\,(v-m-n-1)!} \right\}$$

$$U_{v,1} = -\frac{k}{(2v-1)\,X_1^{2v-1}}$$

and the symbol of double-factorials *!!* is used to define

$$(2n-1)!! = 1 \cdot 3 \cdot 5 \cdot 7 \ldots (2n-1) \tag{4.18}$$

The analytical solution of the improper integral given in Eqs. (4.15) – (4.18) above was proposed by Ueda in Refs. 77 and 78, but no derivation of the formulas is published anywhere except in Ref. 135 where the present author derived the analytical solution applicable for M < 1 (subsonic) flow.

One of the draw backs of the series given in Eqs. (4.15)-(4.18) is that the singularity functions for $r \to 0$ and $X > 0$ are not easily identified. In the present work, a further

analytical procedure to identify and separate the singular and regular parts is conducted. A new alternate series proposed in the present work offers the possibility to unify the treatment for the doublet-lattice and doublet point methods, the two well-known methods for predicting the unsteady aerodynamic loads. More detailed derivations of the doublet-lattice (DLM) and doublet point (DPM) methods are given in Sections 4.2.7 and 4.2.8 respectively. The present DLM and DPM methods are presented in Section 4.5 and 4.6 respectively.

4.2.5 Evaluation of the aerodynamic operator

The aerodynamic operator is a function relating the motion of the surface and the change of the aerodynamic load produced by the surface deformation[57]. The definition of the operator in the present work is similar to that used by Bisplinghoff and Ashley in Ref. 57 as follows

$$\Im = \frac{1}{8p} \iint_S D\,p \;\; K\left(x_{0,}\, y_{0\,,}\, z_0, k, M\right)\, dx\, dh \tag{4.19}$$

where S is the lifting surface area.

There are many types of aeroelastic analyses which make use of this aerodynamic operator. Among these are flutter, gust, and static aeroelastic analyses. The classical approach to evaluate this operator has been through the use of the so-called lifting surface methods. A vast literature on the methods to calculate the aerodynamic operator shows a gradual improvement in the accuracy, capability and efficiency of the methods, as is pointed out in the survey papers in References 52, 55, 68, and 69. The methods can be divided into two broad categories, the mode function method (or the kernel function method) and the discrete element method[66]. The mode function methods use an assumption that the pressure distribution may be approximated by a series of orthogonal polynomial functions with unknown coefficients. These coefficients are then determined by satisfying

the flow tangency boundary conditions at a set of collocation points.[52, 69] For a wing with control surfaces or other complex configurations, a careful treatment for the pressure discontinuity is needed which makes this procedure sensitive to the manner of representing the additional singularities associated with such geometry.

A usual procedure for the second method is to divide the lifting surfaces into small trapezoidal panel elements which permit discrete approximation of Eq. (4.19) to give

$$\Im = \frac{1}{8p} \sum_{n=1}^{N} \left\{ Dp_n \iint_S K_n\left(x_{0,} y_{0,} z_0, k, M\right)\, dx\, dh \right\} \tag{4.20}$$

If the normal wash can be calculated from the given oscillatory mode shape $h_m(x_n, y_n)$ by

$$\overline{w} = \left(\frac{\partial}{\partial x} + i k \right) \overline{h}_m (x_n, y_n) \tag{4.20}$$

then the unknown pressure load, assumed to be constant within each element, may be determined by satisfying the flow tangency condition at the control point of each panel to give a set of linear algebraic equations :

$$\{D\, \overline{p}\} = [\Im]^{-1} \{\overline{w}\} \tag{4.21}$$

In the discrete element method, the treatment for complex wing planforms is similar to regular planforms, *i.e.* by dividing the planform into a number of small piecewise trapezoidal panel elements, assuming an unknown constant Δp for each panel, and finding the unknown by satisfying the boundary condition on each panel. This discrete element approach is used in the present work.

4.2.6 Discrete Element Lifting Surface Methods

Several variations of the discrete element method have been proposed. For steady subsonic flow, one of the well known discrete element method is the vortex lattice method (VLM), such as the method of Weissinger[121], Falkner[141], Campbell[142], Hedman[137], Belotserkovskii[140], Rubbert[189], Dulmovits[190], Margason and Lamar[90], and Lan[88,100]. For unsteady subsonic flow, these include the works of Stark[52], Albano and Rodden[70], Jordan[71], and Giesing *et al.*[62, 67, 72], Houbolt[73], Ueda and Dowell[66], Ichikawa *et al.*[74], Rodden *et al.*[143-145], and van Zyl [146-148]. Application of the vortex lattice method to a high-angle-of-attack subsonic aerodynamics has been proposed by Mook and Nayfeh.[81]

For a subsonic aeroelasticity analysis, the widely-used version of the unsteady aerodynamics method is the doublet lattice method of Rodden *et al.*[80] because of its ready applicability to complex nonplanar configurations. NASTRAN[53, 80] uses the DLM version developed in Refs. 12, 17 and 22 where a quadratic approximation (DLM-quadratic) is used for integrating the kernel function. Despite the wide acceptance of the method, however, the DLM-quadratic version contains inaccuracy in the integration of the elemental kernel function[146, 147]. For this reason, recently, Rodden *et al.* [143-145] attempted to improve the accuracy by proposing a DLM-quartic version, where the integration of the kernel function is based on a quartic function approximation. The DLM-quartic version[143, 144] allows the use of the element aspect ratio of up to 10, a considerable improvement compare to the maximum aspect ratio of 3 for the DLM-quadratic. The DLM-quartic version , however, still requires a large number of chordwise boxes per wavelength[144]. Reference 147 investigated the convergence of the DLM-quartic version and concluded that the limitation of the DLM is as a result of the integration error introduced by the approximations to the kernel numerators. In the present work, a more accurate DLM scheme using an analytical integration of the singular kernel function is proposed. The details of the scheme are given in Sections 4.3 – 4.8.

4.2.7 Doublet-Lattice Method (DLM) of Rodden *et al.*

There are four basic assumptions made in the application of the DLM-quadratic version for subsonic flow:

First, the lifting pressure with an unknown constant strength is assumed to be concentrated along the quarter chord line of each element surface as shown in Fig. 4.2. The flow tangency boundary condition is satisfied at a control point placed at the three-quarter chord along the center line of each element. Based on this assumption, if the control point is at element j and the doublet line is at element i, then the aerodynamic operator in Equation (4.16) may be replaced by

$$\Im_{ij} = \frac{\Delta x_s}{8\pi} \int_{-e}^{+e} K\left(x_i - \xi_j, y_i - \eta_j, z_i - \zeta_j, k, M\right) d\hat{\eta} \tag{4.23}$$

where e is a semiwidth of the chordwise strip of each element

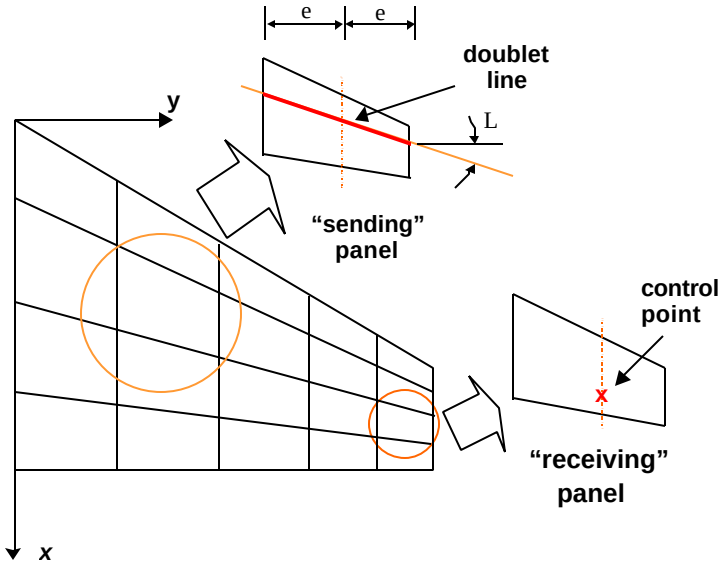


Figure 4.2. Lifting surface idealization in the doublet lattice method

Second, the lifting load line is represented by a horseshoe vortex for its steady effects, and by a line of doublets for its incremental oscillatory effects. This assumption is used by

Albano *et al.*[70] and Giesing *et al.* [62] to simplify the exact integration of the kernel for steady part.

Therefore, for the steady part, the aerodynamic operator becomes

$$\Im_0 = \frac{\Delta x_s}{8\pi} \int_{-e}^{e} \left(\frac{K_{10} T_1 + K_{20} T_2}{r^2} \right) d\hat{\eta} = \Im_{VLM} \tag{4.24}$$

where $\Im_{VLM}$ is calculated based on the VLM of Hedman[62]. The symbol ^ indicates that the local coordinates applied by Albano *et al.* in Reference 70 are to be used.

Third, for the planar part of the kernel, the spanwise integration is performed by approximating the numerator of the kernel using a parabolic function.

$$\Im_1 = \frac{\Delta x_s}{8\,\pi} \int_{-e}^{e} \left(\frac{A_1 \hat{\eta}^2 + B_1 \hat{\eta} + C_1}{r^2} \right) d\hat{\eta} \tag{4.25}$$

where

$$A_1 = \frac{P_1(-e) - 2P_1(0) + P_1(e)}{2e^2}$$

$$B_1 = \frac{P_1(-e) - P_1(e)}{2e} \tag{4.26}$$

$$C_1 = P_1(0)$$

and

$$P_1(\hat{\eta}) = \left(\frac{K_1}{\exp(i k x_m + i k \hat{\eta} \tan\Lambda)} - K_{10} \right) T_1 \tag{4.27}$$

Fourth, for the nonplanar part of the kernel, Albano *et al.* [70] used the same procedure as for the planar part, *i.e.*

$$\Im_2 = \frac{\Delta x_s}{8\pi} \int_{-e}^{e} \left(\frac{A_2 \hat{\eta}^2 + B_2 \hat{\eta} + C_2}{r^2} \right) d\hat{\eta} \tag{4.28}$$

The method gives a reasonable result for any arbitrary nonplanar interfering surfaces, except for a near-coplanar wing-tail combination, such as the Cornell and AGARD wing-horizontal tail combination [62, 67, 72]. The refinement of the formula has been achieved by Giesing *et al.* [62, 67, 72] by presenting a new dihedral angle correction factor

$$T_2^* = T_2 \; r^2 \tag{4.29}$$

such that Equation (4.28) is replaced by

$$\Im_2 = \frac{\Delta x_s}{8\pi} \int_{-e}^{e} \left(\frac{A_2 \hat{\eta}^2 + B_2 \hat{\eta} + C_2}{r^4} \right) d\hat{\eta} \tag{4.30}$$

where the parabolic function for the nonplanar part is

$$P_2(\hat{\eta}) = \left[K_2 \exp\{ -ik(x_m + \hat{\eta} \tan \Lambda) \} - K_{20} \right] T_2^* \tag{4.31}$$

The values of the kernel for $k = 0$ in Equations (4.27) and (4.31) are

$$\begin{aligned} K_{10} &= 1 - x_0 \, R^{-1} \\ K_{20} &= -2 - x_0 \left(2 + \beta^2 r^2 \right) R^{-1} \end{aligned} \tag{4.32}$$

The formula of the kernel for unsteady motion have been given in Equation (4.9), where the improper integrals are calculated by utilizing Laschka's approximation series as follows:

$$\begin{aligned} I_1 &\cong \left\{ 1 + \frac{X}{X_1} - ikr \, I_0 \right\} e^{ikx} \\ 3I_2 &\cong \left\{ (2 - ikX) \left(1 + \frac{X}{X_1} \right) + \frac{Xr^2}{X_1^3} + ikX \, I_0 + kr^2 \, J_0 \, e^{ikx} \right\} \end{aligned} \tag{4.33}$$

$$I_0 = \sum_{n=1}^{11} \frac{a_n \, e^{+ncx/r}}{(nc + ikr)} \left\{ \frac{1}{nc + ikr} + \frac{X}{r} \right\}$$

$$J_0 = \sum_{n=1}^{11} \frac{a_n e^{0.372 n X / r}}{(nc + ikr)} \left\{ \frac{1}{nc + ikr} + \frac{X}{r} \right\}$$

where the coefficients a_n are given in Table 4.1.

The solution of the integral of planar part in Equation (4.21) is

$$\Im_1 = \frac{\Delta x_s}{8\pi} \left\{ \left[\left(\hat{y}_m^2 - z^{-2} \right) A_1 + \hat{y} B_1 + C_1 \right] F + 2eA_1 + \left(\hat{y}_m A_1 + \frac{B_1}{2} \right) \ln \left(\frac{y_a^2 + z^{-2}}{y_b^2 + z^{-2}} \right) \right\} \tag{4.34}$$

where

$$F_p = \int_{-e}^{e} \frac{d\hat{\eta}}{(\hat{y} - \hat{\eta})^2 + \hat{z}^2} = \frac{1}{|\hat{z}|} \tan^{-1} \mu \tag{4.35}$$

$$\mu = \frac{2e|\hat{z}|}{y_a y_b + \hat{z}^2} \tag{4.36}$$

$$y_a = \hat{y} - e$$

$$y_b = \hat{y} + e$$

Table 4.1. The coefficients a_I in Laschka approximation series

i	a_i	i	a_i
1	0.24186198	7	-41.183630
2	-2.7918027	8	545.98537
3	24.991079	9	-644.78155
4	-111.59196	10	328.72755
5	271.43549	11	-64.279511
6	-305.75288		

For planar surfaces, where $\bar{z} = 0$, the Mangler principal part should be used, *i.e.*

$$F_p = \int_{-e}^{e} \frac{d\hat{\eta}}{(\hat{y}-\hat{\eta})^2} = \frac{1}{y_a} - \frac{1}{y_b} \tag{4.37}$$

In order to place the inverse tangent in the range $[0,p]$, the working form of the F term is written as:

$$F = \delta_1 \frac{\mu(1-\varepsilon)}{|\hat{z}|} + \delta_2 \frac{\pi}{|\hat{z}|} \tag{4.38}$$

where

$$\begin{aligned} &\delta = 1 \quad , \quad \delta_2 = 0 && \text{for} \quad 2e|\hat{z}|/\mu > 0 \\ &\delta = 0 \quad , \quad \delta_2 = 1/2 && \text{for} \quad 2e|\hat{z}|/\mu = 0 \\ &\delta = 1 \quad , \quad \delta_2 = 1 && \text{for} \quad 2e|\hat{z}|/\mu < 0 \end{aligned} \tag{4.39}$$

and

$$\varepsilon = \begin{cases} 1 - \dfrac{\tan^{-1}\mu}{\mu} & \text{for } \mu > 0.3 \\ \mu^2 \displaystyle\sum_{n=2}^{7} \frac{(-1)^n}{2n-1} [\mu \, sign(\hat{z})]^{2n-4} & \text{for } \mu < 0.3 \end{cases} \tag{4.40}$$

The solution for the integral of the non-planar part in Eq. (4.28) is

$$\begin{aligned} D_2 &= \frac{\Delta x_s}{16\pi\hat{z}^2} \left[\left(\hat{y}^2 + \hat{z}^2\right) A_2 + \hat{y} B_2 + C_2 \right] F + \frac{F_b}{\hat{y}_b{}^2 + \hat{z}^2} - \frac{F_a}{\hat{y}^2 + \hat{z}^2} \qquad \text{for } \frac{1}{\mu} < 0.1 \\ D_2 &= \frac{\Delta x_s \mu}{16\pi|\hat{z}|} \left[\frac{F_c}{\left(\hat{y}_a^2 + \hat{z}^2\right)\left(\hat{y}_b^2 + \hat{z}^2\right)} - \frac{\delta_1 \varepsilon - \Delta}{\hat{z}^2} \left[\left(\hat{y}^2 + \hat{z}^2\right) A_2 + \hat{y} B_2 + C_2 \right] \right] \quad \text{for } \frac{1}{\mu} > 0.1 \end{aligned} \tag{4.41}$$

where

$$\begin{aligned} F_a &= \left\{ \left(\hat{y}^2 + \hat{z}^2\right)\hat{y} - \left(\hat{y}^2 - \hat{z}^2\right)e \right\} A_2 + \left(\hat{y}\,\hat{y}_a + \hat{z}^2\right) B_2 + \hat{y}_a C_2 \\ F_b &= \left\{ \left(\hat{y}^2 + \hat{z}^2\right)\hat{y} + \left(\hat{y}^2 - \hat{z}^2\right)e \right\} A_2 + \left(\hat{y}\,\hat{y}_b + \hat{z}^2\right) B_2 + \hat{y}_b C_2 \end{aligned} \tag{4.42}$$

$$F_c = 2\left(\hat{y}^2 + \hat{z}^2 + e^2\right)\left(e^2 A_2 + C_2\right) + 4\hat{y}\, e^2\, B_2$$

Applications of the numerical algorithm described above for complex configurations have given good results compared to those of other methods and experimental data[62,67]. There are, however, some limitations in the applications of the method. Rodden *et al.* reported that the convergence of the method is slow for the real part of the lift coefficient, and found that the computation converges if the strip-width of the panel is approximately $l/25$, where $l = 2p/k$, and if the aspect ratio of each element is approximately one. Therefore the method needs a large number of panels to give an accurate result, and needs an appropriate numerical elimination procedure to handle a large system of simultaneous equations.

In their analysis, Giesing *et al.*[62] mentioned that the near-coplanar configuration problem is not completely solved. The procedure fails, for example, if the separation $|\bar{z}|$ is less than 0.001 e for a single precision code. For practical use, such configurations may be assumed to be planar since the value of e itself is usually small. However, this indicates that an effort to improve and optimize the method is still needed.

An effort to improve the accuracy of the method has been proposed by Jordan in Ref. 71. In his DLM formulation, an exact integration of the kernel at a quarter chord of the element has been done. However, this technique is limited to rectangular planar surfaces in incompressible flow (M = 0). In the present work, several numerical improvements are proposed, including an application of the exact solution of the improper integral, a proper separation of the regular and singular functions of the kernel, and an improve integration quadrature of the kernel.

The improper integral I_n in the DLM is solved using Laschka's series to approximate the integrand of the integral. There are two disadvantages to this scheme. *First*, the accuracy of Laschka's series is limited to the order of three digits. *Second*, the series approximates the integrand, and not the integral itself. Gazzini *et al.* [82] described that an approach to solve the integration by approximating the integrand may not be equivalent

to the approach to solve the integral itself. Therefore, it is believed that the application of the exact solution to solve the improper integral directly will increase the accuracy of the previous works.

The kernel function in Equation (4.12) contains regular and singular functions as the values of r approaches zero and $X > 0$. There is no separation between these functions in the DLM as shown in Equation (4.26), (4.27), (4.34) and (4.37). Therefore the Mangler procedure is also applied to the regular function, which is not a proper way to solve the problem. In the present work, the regular and singular functions will be identified and treated separately.

The DLM uses a quadratic approximation for the numerator of the kernel to simplify the integration procedure as shown in Equations (4.25) and (4.30). A further approximation is also needed to evaluate the inverse tangent of the result as shown in Equations (4.35) and (4.38) – (4.40) to give accurate results for small values of z. The scheme clearly needs three integration points to form a quadratic approximation function for every evaluation of the integral. This procedure may be improved if one uses a Gaussian quadrature technique as is suggested by some authors [83-86]. The Gaussian technique does not need a fixed number of integration points. Less than three points may be used if the sending/receiving panel pairs are distant. If the sending and receiving panels are close, such that the kernel function may vary rapidly, one may have to use more than three integration points. The improvements outlined above will be implemented in Section 4.7 of the present work.

4.2.8 Doublet Point Method (DPM) of Ueda and Dowell

The idea of the DPM was first proposed by Houbolt[81] based on the pressure-velocity potential concept, and independently by Ueda and Dowell[66] based on the pressure-normal wash concept. Houbolt (1969), however, did not give numerical results for three-dimensional flows since a direct evaluation of the type B integral in Equation (4.11) was

not available at that time. The exact solution of this type integral was given in 1981, and the first version of DPM was developed in 1982 for planar surfaces[66].

There are two basic assumptions used in the original DPM[66]. First, the lifting pressure is assumed to be concentrated at a single point located at the three-quarter chord along the center line of each element as shown in Fig. 4.3. The point is called a doublet point. Similar to the DLM, the control point is placed on the three-quarter chord at mid-span of each panel. Second, if the receiving point is located on the wake of the sending element, *i.e.* $X > 0$ and $r = 0$, then the Mangler integration procedure should be used by utilizing an average value of the modified Bessel function to treat the singularity problem.

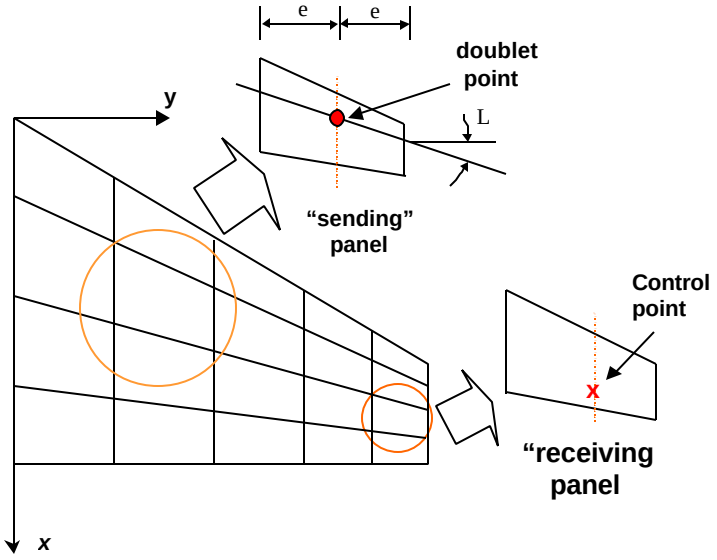


Figure 4.3. The lifting surface idealization in the doublet point method

Based on the first assumption, if the doublet point and the control point are located at elements i and j respectively, then the aerodynamic operator in Equation (4.16) may be written as

$$\Im_{ij}=\frac{\Delta S_i}{8\pi}K\left(x_i-\xi_j, y_i-\eta_j, z_i-\zeta_j, k, M\right) \tag{4.43}$$

where

$\Delta S_i = 2e_s \Delta x_s$ = the area of sending element

The kernel function is calculated from Equations (4.8), (4.9), (4.10) and (4.12) for planar surfaces

$$K = e^{-ikx_0}\left(\frac{M e^{ikX}}{R X_1} + B_{1r} + i B_{1i}\right) \tag{4.44}$$

and the improper integral B_1 is calculated from Equations (4.13) and (4.14) for *v = 1*

$$B_{1r} = \sum_{n=0}^{\infty}(-1)^n U_{1,2n} - \frac{k^2}{2}\sum_{n=0}^{\infty}\frac{(kr/2)^{2n}}{n!(n+1)}\left(\sum_{m=1}^{n}\frac{1}{m} + \frac{1}{2(n+1)} - \gamma - 1n\frac{k}{2}\right)$$

$$B_{1i} = \sum_{n=0}^{\infty}(-1)^n U_{1,2n+1} + \frac{\pi k^2}{4}\sum_{n=0}^{\infty}\frac{(kr/2)^{2n}}{n!(n+1)!} \tag{4.45}$$

$$U_{1,m\geq 3} = \frac{k(kX)^{m-1}}{(m-2)m!X_1} - \frac{(kr)^2}{(m-2)m}U_{1,m-2}$$

$$U_{1,2} = -\frac{k^2}{2}\left\{1n\left(X_1 - X\right) + \frac{X}{X_1}\right\} \tag{4.46}$$

$$U_{1,1} = -\frac{k}{X_1}$$

$$U_{1,0} = \frac{1}{X_1(X_1 - X)}$$

and

$$X_1 = \sqrt{X^2 + r^2} \tag{4.47}$$

Equations (4.44)- (4.47) give an exact value of the kernel for any value of *X* and *r* with one well known exception. Consider the case where the control point is downstream

of the doublet point, or $X > 0$ and $r = 0$. The kernel becomes infinite because of the r^{-2} singularity in the part of $B_{1,r}$ or, more specifically, in the $U_{1,0}$ term. This problem was solved by Ueda and Dowell using the second assumption, which utilizes the Mangler formula to integrate the $B_{1,r}$ term, and uses only the average value of the singular part.

$$\int_{-e}^{e} B_{1,r}(X>0)\, d\eta = -\frac{4}{e} + \int_{-e}^{e} B_{1,r}(-X)\, d\eta + \sum_{n=1}^{\infty} \frac{(k\ e/2)^{2n}}{n!(n+1)!(2n+1)} \left(\sum_{m=1}^{n} \frac{1}{m} + \frac{4n+3}{2(n+1)(2n+1)} - \ln\frac{k\,e}{2} - \gamma \right) \tag{4.48}$$

If $k\,e \ll 1$, Eq. (4.48) can be simplified by

$$\int_{-e}^{e} B_{1,r}(X>0)\, d\eta = \int_{-e}^{e} \left[B_{1,r}(-X) - \frac{2}{e^2} + k^2 \left(\ln\frac{k\,e}{2} + \gamma - \frac{3}{2} \right) \right] d\eta$$

such that the value of the integrand $B_{1,r}$ may be replaced by

$$B_{1,r}(X>0) \approx -B_{1,r}(-X) - \frac{2}{e^2} + k^2 \left(\ln\frac{k\,e}{2} + \gamma - \frac{3}{2} \right) \tag{4.49}$$

Ueda and Dowell further improved the last equation to read

$$B_{1,r}(X>0) \approx -B_{1,r}(-X) - \frac{\pi^2}{6e^2} + k^2 \left(\ln\frac{k\,e}{2} + \gamma - \frac{3}{2} \right) \tag{4.50}$$

Eversman and Pitt (1991) found that the averaging procedure used to give Equation (4.46) is accurate only for element surfaces with uniform strip widths, *e*, as shown in Fig. 2.1a. In the case of unequal strip widths they suggested to include the strip width effect as follows

$$B_{1,r}(X>0) \approx -B_{1,r}(-X) - \frac{S_1 + S_2}{e_i} + k^2 \left(\ln\frac{ke}{2} + \gamma - \frac{3}{2} \right) \tag{4.51}$$

where

$$S_1 = \sum_{n=1}^{i-1} \frac{2e_n}{(y-\eta)^2} + \sum_{n=i+1}^{\infty} \frac{2e_n}{(y-\eta)^2}$$

$$S_2 = \sum_{n=1}^{\infty} \frac{2e_n}{(y_n+\eta_1)^2} \qquad (4.52)$$

Improvements to the DPM proposed in the present study includes a treatment of the $1/r^4$ term for nonplanar configurations which is not considered in the previous work, and an evaluation of the sweep angle of elements for planar configurations which is neglected in the DPM of Ueda and Dowell.

An appropriate treatment will be proposed to solve the ill conditioned problem of the nonplanar $1/r^4$ term based on a separation of singular and regular functions of the kernel. Ueda and Dowell[66] have already made a separation of the kernel function in the B_{1r} term. However their approach did not completely separate the regular/singular functions in the kernel function. If the separation is applied entirely to the singular kernel functions, then it can be shown that the T_1/r^2 term of the planar term of the kernel function will cancel the $3T_2^*/r^4$ term of the nonplanar term. This treatment clearly will improve the accuracy of the nonplanar DPM.

The original DPM used the Mangler procedure to evaluate the singular B_{1r} term as shown in Equation (4.44). This approach obviously evaluates only one part of the kernel since the exponential term, exp ($i\ k\ x_0$), is not included in the evaluation. In the present DPM, the kernel will be evaluated completely through the use of the following equation

$$\overline{K} = \int_{-e}^{e} e^{-ikx_0} B_{1r}\, d\eta \qquad (4.53)$$

where

$$x_0 = x_m - (y-\eta)\tan\Lambda \qquad (4.54)$$

and Λ and x_m are a sweep angle at the quarter chord of each panel and the distance between the doublet point and the control point respectively. Since x_0 is a function of the panel sweep angle, this approach gives a sweep angle correction factor to the previous method.

4.2.9 Doublet Hybrid Method (DHM) of Eversman and Pitt

An extension of the DPM for nonplanar interfering surfaces has been made by Eversman and Pitt[75] based on the nonplanar kernel function of Landahl. In their work, however, a treatment for the $1/r^4$ term of the nonplanar part of the kernel function was not well established. The results have been reported to be less accurate than the DLM results. For this reason, they concluded that the best approach is to utilize the nonplanar DPM only for sending/receiving pairs which are distant. If the sending and receiving points are close, they suggest using the nonplanar DLM. This combined technique is the basis of their doublet hybrid method (DHM).

No further treatment for the limitation of DPM and DLM, was conducted in the DHM method of the Eversman and Pitt. Therefore some singularity problems associated with the DPM and DLM may be found in their DHM. In the present DHM, described in Section. 4.7, the singularity problem is identified and solved in each of the present DPM and DLM procedures. The present DHM also unifies the present DLM and DPM procedures such that the present DPM is nothing more than just a special case of the present DLM.

4.3. Contribution of the Present Work

The advantages and disadvantages of some the discrete element methods have been described in the previous section. Most of the methods can handle complicated lifting surface configurations. However, some mathematical integration and singularity problems

are not completely solved in the previous discrete element methods that may limit the accuracy and applicability of the procedures. In the present work, three discrete element methods are proposed: the DPM, DLM and DHM. Comparisons between the present and previous methods are addressed in the following sections.

4.3.1 The doublet lattice method (DLM)

In the original DLM, the following problems have been identified:

1) The improper cylindrical function occurred in the kernel function is approximated using the Laschka series which is third-order accurate (see Eq. (4.33))
2) No distinction is made between the regular and the singular parts of the kernel (see Eqs. (4.24) and (4.30)).
3) The kernel is integrated based on a quadratic function approximation to the numerator of the kernel (see Eqs. (4.24) and (4.30)). Recently Rodden *et al.* tried to improve the solution of this part by using a quartic function approximation instead of the quadratic function.
4) The non-planar kernel is integrated such that the denominator term is artificially set as r^{-4} instead of r^{-2} (see Eq. 4.30). As pointed out by Nissim and Lottati[93], such a procedure may violate the behavior of the doublet singularity which should be r^{-2}.
5) The scheme has a near singularity problem for two panels having small vertical gaps z.

In the present DLM, some improvement have been developed that cures the problems above. The proposed DLM has the following features:

1) The improper cylindrical function is solved using an analytical expansion series solution.
2) The kernel function is analytically separated into regular and singular functions.
3) The kernel singular part is integrated analytically. The kernel regular part is integrated using a Gauss quadrature technique, where the accuracy can be improved simply by increasing the number of integration points without the need to modify the formula.

4) The non-planar kernel is integrated without any artificial treatment for the denominator, *i.e.* by retaining the r^{-2} term.
5) The singularity parts of the planar and non-planar kernel cancel each other in the present formulation such that the kernel integration is continuous for any arbitrary distance *z* of the vertical gap between two non-planar surfaces.

4.3.2 The doublet point method (DPM)

In the original DPM of Ueda and Dowell[66], the following problems were described:

1) The method is applicable for planar lifting surface only.
2) The improper cylindrical function is solved using the analytical expansion series of Ueda. However, it is difficult to isolate the singularity terms in the series since the terms are implicitly embedded in the series.
3) No *local* sweep angle correction in the series.
4) It may not be accurate for non-uniform discretization of the surface planforms.

In the present DPM, some improvements have been made which alleviate the problems associated with the original DPM.

The proposed DPM has the following features:

1) The DPM is extended to non-planar configurations.
2) The present solution series for the improper cylindrical function separately treats the singular and regular functions. Therefore the singular part is explicitly isolated.
3) The sweep angle correction is included in the singular kernel.
4) Eversman and Pitt formula for the non-uniform spacing discretization is adopted.

4.3.3 The doublet hybrid method

In the original DHM of Eversman and Pitt[75] , the following problems have been identified:

1) The method utilizes the original DPM and DLM with the limitations described above.
2) For a steady flow, the VLM (for a small *r*) and DPM (for a large *r*) are used.

In the present DHM, some improvements have been made which alleviate the problems faced by the original DHM.

The proposed DHM has the following features:

1) The present method utilizes the present DPM and DLM.
2) For a steady flow only the VLM is used for any value of *r*.
3) The DLM and DPM are unified such that the DPM becomes a special case of the DLM.

It should be noted that an effort to perform the present procedure has been initiated by the present author in Ref. 135. The present work may be considered as an improvement to the discrete element methods proposed in Ref. 135. The difference between the present work and Ref. 135 are as follows:

1) The regular and singular kernel functions are separated using a different approach. Reference 135 follows the approach proposed by Ueda and Dowel using the modified Bessel functions. In the present work, the separation is performed analytically based on an expansion series to the exponential function of the kernel function.
2) The procedure to separate the regular and singular kernel functions of the present work can be performed to the incomplete cylindrical functions in both the frequency and Laplace domains. The procedure in Ref. 135 is applicable for the frequency domain only.
3) The regular kernel function of the present work is simpler since no additional term of modified Bessel functions are included.
4) The discrete element methods of Ref. 135 may not be accurate for a high reduced frequency since there is no treatment for the evaluation of the kernel function having large arguments. In the present work, the treatment for a large argument is included using an asymptotic expansion of the kernel function proposed in Ref. 78.

5) Reference 135 does not consider the influence of the reduced frequency k in the Gauss integration of the regular function. In the present work, the number of integration point is set as a function of the reduced frequency.
6) Reference 135 does not consider the effect of the lifting surface camber in the formulation of the VLM. In the present formulation, the effect of the camber is included.
7) The present work uses an alternate representation of the expansion series which is simpler than the original series proposed by Ueda.

A schematic chart of the proposed treatment to the integration of the kernel function, which is the key improvement of the present work, is given in Fig.E.1. and described in Appendix A.

As a summary of the proposed discrete element methods, the following are the steps conducted in the present work:

1) The kernel function is formulated based on the Landahl's formula
2) The improper cylindrical function is solved using an expansion series described in Appendix A.2.
3) The kernel function is divided into regular and singular functions as described in Appendix A.3.
4) For the DPM, the kernel function is evaluated directly except for the singular case where the singular kernel is integrated along the quarter chord using the Mangler formula as given in Section 4.5. The method is applicable for steady or unsteady flows.
5) For the DLM, the singular kernel is integrated analytically and the regular kernel is integrated using a Gauss quadrature formula as given in Section 4.6. The method is applicable for steady or unsteady flows.
6) For the DHM, the treatment for steady and unsteady flow are separated as follows
   a) For a steady flow, the present VLM is developed by considering the Prandtl-Glauert compressibility correction in the governing equation as given in Section 4.4.

b) For the unsteady flow, the incremental unsteady portions of the present DLM and DPM are employed as given in section 4.7.

7) Validation for the present discrete element methods are performed in Section 4.9.

4.4. Alternate Expansion Series for the Incomplete Cylindrical Function

It has been described in Section 4.2 that the analytical solution to the incomplete cylindrical function of order *n* has been given by Ueda [77, 78] as follows:

$$B_v = B_{v,real} + i\, B_{v,\,imag} \tag{4.15}$$

where

$$B_{v,real} = \sum_{n=0}^{\infty} (-1)^n\, U_{v,2n} + \frac{(-k^2/2)^v}{(2v-1)!!} \sum_{n=0}^{\infty} p_n \frac{(k\,r/2)^{2n}}{n!\,(n+v)!}$$

$$B_{v,imag} = \sum_{n=0}^{\infty} (-1)^n\, U_{v,2n+1} - \frac{p}{2} \frac{(-k^2/2)^v}{(2v-1)!!} \sum_{n=0}^{\infty} \frac{(k\,r/2)^{2n}}{n!\,(n+v)!} \tag{4.16}$$

$$p_n = -\left(\gamma + \ln\frac{k}{2}\right) + \sum_{m=1}^{n} \frac{1}{m} + \sum_{m=n+1}^{n+v} \frac{1}{2m}$$

and the recursive term U_m is defined in Eq. (4.17).

It is possible to further simplify the expression of the expansion series in Eqs. (4.15) and (4.16) by combining the real and imaginary parts as follows:

$$B_v = \sum_{n=0}^{\infty} i^n\, U_{v,n} + \frac{(-k^2/2)^v}{(2v-1)!!} \sum_{n=0}^{\infty} p_n^{*} \frac{(k\,r/2)^{2n}}{n!\,(n+v)!} \tag{4.58}$$

where

$$p_n^{*} = -\left(\gamma + \ln\frac{k}{2} + \frac{i\pi}{2}\right) + \sum_{m=1}^{n} \frac{1}{m} + \sum_{m=n+1}^{n+v} \frac{1}{2m} \tag{4.59}$$

and the recursive term U_m is the same as the one defined in Eq. (4.17).

A more useful representation of the incomplete cylindrical function is by expressing the function in terms of singular and regular parts as follows:

$$B_v = B_{v,regular} + B_{v,singular} \tag{4.60a}$$

where

$$B_{v,singular}(X) = \begin{cases} -2(g_a + g_b) & \text{if } X > 0 \text{ and } r \to 0 \\ 0 & \text{otherwise} \end{cases} \tag{4.60b}$$

$$B_{v,regular}(X) = \begin{cases} +B_v(-X) - 2\sum_{n=0}^{\infty}(-1)^n U_{2n}(-X) & \text{if } X > 0 \text{ and } r \to 0 \\ +B_v(X) & \text{otherwise} \end{cases}$$

where the singular functions g_a and g_b are

$$g_a = \left(\frac{-k^2}{2}\right)^h \ln r \, \frac{h!}{(2h-1)!!} \tag{4.61a}$$

$$g_b = \frac{1}{2(2h-1)!!}\left(\frac{2}{r^2}\right)^h \sum_{n=0}^{h-1}(-1)^n \frac{(h-n-1)!}{n!}\left(\frac{kr}{2}\right)^{2n} \tag{4.61b}$$

Equation (4.60) is used in the present work to develop the present lifting surface method. A detailed derivation of Eq. (4.60) is given in Appendix A. It should be noted that the expression for the alternate expansion series presented in Ref. 135 is more complicated than the present expansion series. The alternate expansion series in Ref. 135 can be written in the present notation as follows:

$$B_{v,singular}(X) = \begin{cases} -2(g_a + g_b) & \text{if } X > 0 \text{ and } r \to 0 \\ 0 & \text{otherwise} \end{cases} \tag{4.62a}$$

$$B_{v,regular}(X) = \begin{cases} -B_v(-X) + 2f_R & \text{if } X > 0 \text{ and } r \to 0 \\ +B_v(X) & \text{otherwise} \end{cases}$$

where

$$f_R = \frac{1}{(2v-1)!!}\left(\frac{k}{r}\right)^v \mathbf{K_v}(kr) - (g_a + g_b) \tag{4.62b}$$

and $\mathbf{K_v}$ is the modified Bessel function of the second kind and order v defined as follows:

$$\begin{aligned}\mathbf{K_h}(kr) = (-1)^{h+1}\left\{\ln\frac{kr}{2}+\gamma\right\}\mathbf{I_h}(x) + \frac{1}{2}\sum_{n=0}^{h-1}(-1)^n\frac{(h-n-1)!}{n!}\left(\frac{kr}{2}\right)^{2n-h} \\ + \frac{(-1)^h}{2}\sum_{n=0}^{\infty}\left(\varphi(n)+\varphi(n+h)\right)\frac{(kr/2)^{h+2n}}{n!\,(n+h)!}\end{aligned} \tag{4.62c}$$

$\mathbf{I_h}$ is the modified Bessel function of the first kind:

$$\mathbf{I_h}(kr) = \sum_{n=0}^{\infty}\frac{(kr/2)^{h+2n}}{n!\,(n+h)!} \tag{4.62d}$$

and φ is the Digamma function: $\varphi(n) = \sum_{m=1}^{n}\frac{1}{m}$; $\varphi(0) = 0$ (4.62e)

Therefore the present expansion series given in Eq. (4.61) can be considered to be as a simplification of the expansion series given in Ref. 135. It should be noted also that the alternate expansion series given in Ref. 135 is based on the assumption that the argument of the modified Bessel functions in Eqs. (4.62c) aand (4.62d) is a real number, *i.e.* it is applicable for the lifting surface method in the frequency domain only. On the other hand, the present expansion series given in Eq. (4.61) is derived using a direct expansion series to the exponential function in the incomplete cylindrical function without any assumption on the argument of the modified Bessel function as shown in Appendix A. Therefore the present formulation is applicable to the lifting surface method in the Laplace domain where the argument of the incomplete cylindrical function is presented as a complex variable. More detailed description on the Laplace domain approach is presented in Section 4.9.

4.5 Present Vortex Lattice Method

In this section, the integration of the steady part of the kernel function is evaluated. It has been known that an integration of the doublet line of the kernel is difficult to evaluate directly, even for steady case. The integration has been accomplished by Jordan only for a rectangular wing in an incompressible flow[71]. On the other hand, an integration of a similar vortex distribution using a horseshoe vortex, the well-known vortex lattice method (VLM), has been successfully completed for steady complex planforms[100, 109, 110]. The result for steady rectangular surfaces has been proved to have the same form as those of Jordan[71]. For this reason Albano and Rodden used the concept of the VLM to represent the steady effects in their DLM[70]. Several versions of the VLM have been used including the version of Weissinger[121], Falkner[141], Campbell[142], Hedman[137], Belotserkovskii[140], Margason and Lamar[90], Rubbert[189], Dulmovits[190], Mook and Nayfeh[81], and Lan[88,100]. The Hedman's version is used by Albano *et al.*[70] and Giesing *et al.*[62] to formulate the steady portion of their DLM. In the present method, the VLM for non planar configuration is derived based on the vector formulation given by Lan in the Appendix of Ref. 100. The formulation has been initiated in the previous work of the author in Ref. 135 and is extended in the present work by additional backwash velocity evaluation for a more general lifting surface with camber.

In this approach, the surface is divided into trapezoidal panel element. Each panel is represented by one horseshoe vortex. The vortex is composed of three vortex lines: a bound vortex and two trailing vortices. The bound vortex is placed at the quarter chord of each panel. The trailing vortices are places at the end of the bound vortex and are trailing downstream in the free-stream direction to infinity. The control point is placed at the mid-span of the three-quarter chord of each element. Figure 4.4. shows a typical chordwise row of horseshoe vortices on an arbitrary planform.

Consider a vortex element Γ with an arbitrary direction $\vec{l}$ as shown in Figure 4.5. The induced velocity field due to this vortex element in the linearized compressible flow

has been formulated by Lan[100] based on the vector formulation given by Ward[109]. The induced velocity is formulated as follows:

$$\vec{q} = \frac{\beta^2 \Gamma}{4\pi} \frac{\vec{a} \wedge \vec{l}}{\left| \vec{a}_\beta \wedge \vec{l}_\beta \right|^2} \left\{ \frac{\vec{b}_\beta}{\left| \vec{b}_\beta \right|} - \frac{\vec{a}_\beta}{\left| \vec{a}_\beta \right|} \right\} \bullet \vec{l}_\beta \tag{4.63}$$

where

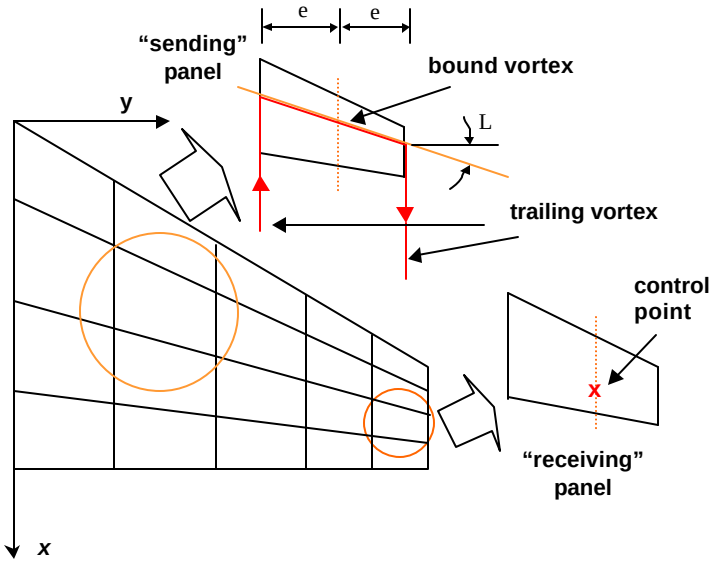


Figure 4.4 Lifting surface idealization in the vortex lattice method

$$\vec{a} = \begin{pmatrix} x_a - x_c \\ y_a - y_c \\ z_a - z_c \end{pmatrix} = \begin{pmatrix} x_{ac} \\ y_{ac} \\ z_{ac} \end{pmatrix} = x_{ac}\,\hat{i} + y_{ac}\,\hat{j} + z_{ac}\,\hat{k}$$

$$\vec{b} = x_{bc}\,\hat{i} + y_{bc}\,\hat{j} + z_{bc}\,\hat{k}$$

$$\vec{l} = \vec{b} - \vec{a} = x_{ba}\,\hat{i} + y_{ba}\,\hat{j} + z_{ba}\,\hat{k}$$

$$\vec{a}_\beta = x_{ac}\,\hat{i} + \beta\, y_{ac}\,\hat{j} + \beta\, z_{ac}\,\hat{k} \tag{4.64}$$

$$\vec{b}_\beta = x_{bc}\,\hat{i} + \beta\, y_{bc}\,\hat{j} + \beta\, z_{bc}\,\hat{k}$$

$$\vec{l}_\beta = \vec{b} - \vec{a} = x_{ba}\,\hat{i} + \beta\, y_{ba}\,\hat{j} + \beta\, z_{ba}\,\hat{k}$$

$$\beta = \sqrt{1 - M^2}\,,\ \mathrm{M} < 1$$

and the symbols Ù and · are used to define vector cross and dot products respectively. The formula has been applied to planar configurations by Lan and is extended to construct his quasi-vortex lattice method[100].

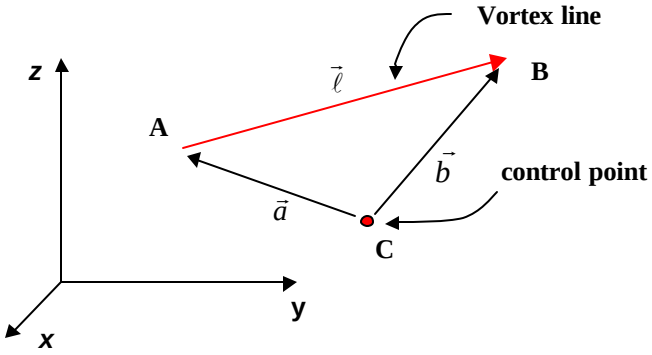


Figure 4.5. Vortex segment geometry

The application of the formulation to a non-planar configuration surface with a dihedral angle γ and camber surface angle δ should consider not only the downwash velocity *w* but also the sidewash velocity *v* and the backwash velocity *u*[110]. These induced velocities are related to the free-stream velocity from the surface boundary condition at each control point as[110]

$$U_¥ \sin(\alpha - \delta)\cos\gamma = w\cos\gamma\cos\delta + v\sin\gamma\cos\delta - u\cos\gamma\sin\delta \qquad (4.65)$$

The formulation to evaluate the downwash velocity *w* and sidewash *v* has been described in Ref. 135. Reference 135 assumes that the camber angle δ = 0 such that there is no need to evaluate the back wash velocity *u*. In the present work, the camber angle is not zero, and therefore the formulation of the backwash velocity is needed.

The backwash *u* can be evaluated from Eq. (4.64)

$$u = \vec{q} \cdot \vec{i} \tag{4.66}$$

Substitution of Eqs. (4.63) and (4.64) into Eq. (4.66) gives

$$\left(\vec{a} \times \vec{l}\right) \cdot \vec{i} = y_{ac} z_{ba} - y_{ba} z_{ac} \tag{4.67}$$

$$\left|\vec{a}_\beta \wedge \vec{l}_\beta\right| = \beta \sqrt{\left(x_{ac} y_{ba} - x_{ba} y_{ac}\right) + \left(x_{ac} z_{ba} - x_{ba} z_{ac}\right) + \beta^2 \left(y_{ac} z_{ba} - y_{ba} z_{ac}\right)}$$

$$\left|\vec{a}_\beta \bullet \vec{l}_\beta\right| = x_{ac} x_{ba} + \beta^2 y_{ac} y_{ba} + \beta^2 z_{ac} z_{ba}$$

$$\vec{b}_\beta \vec{l}_\beta = x_{bc} x_{ba} + \beta^2 y_{bc} y_{ba} + \beta^2 z_{bc} z_{ba} \tag{4.68}$$

$$\left|\vec{a}_\beta\right| = \sqrt{x^2_{ac} + \beta^2 y^2_{ac} z^2_{ac}} \tag{4.69a}$$

$$\left|\vec{b}_\beta\right| = \sqrt{x^2_{bc} + \beta^2 y^2_{bc} z^2_{bc}} \tag{4.69b}$$

Therefore the backwash velocity can be formulated as

$$u \left(\frac{G}{4p}\right)^{-1} = \frac{- y_{ac} z_{ab} + y_{ab} z_{ac}}{\left(x_{ac} y_{ab} - x_{ab} y_{ac}\right) + \left(x_{ac} z_{ab} - x_{ab} z_{ac}\right) + ß^2 \left(y_{ac} z_{ab} - y_{ab} z_{ac}\right)} \cdot \left[\frac{x_{bc} x_{ab} + ß^2 \left(y_{bc} y_{ab} + z_{ab} z_{bc}\right)}{\sqrt{x^2_{bc} + ß^2 \left(y^2_{bc} + z^2_{bc}\right)}} - \frac{x_{ac} x_{ab} + ß^2 \left(y_{ac} y_{ab} + z_{ab} z_{ac}\right)}{\sqrt{x^2_{bc} + ß^2 \left(y^2_{ac} + z^2_{ab}\right)}}\right] \tag{4.70}$$

Similar procedure may be applied for the downwash w and sidewash v[135] :

$$w \left(\frac{G}{4p}\right)^{-1} = \frac{x_{ac} y_{ab} - x_{ab} y_{ac}}{\left(x_{ac} y_{ab} - x_{ab} y_{ac}\right) + \left(x_{ac} z_{ab} - x_{ab} z_{ac}\right) + ß^2 \left(y_{ac} z_{ab} - y_{ab} z_{ac}\right)} \cdot \left[\frac{x_{bc} x_{ab} + ß^2 \left(y_{bc} y_{ab} + z_{ab} z_{bc}\right)}{\sqrt{x^2_{bc} + ß^2 \left(y^2_{bc} + z^2_{bc}\right)}} - \frac{x_{ac} x_{ab} + ß^2 \left(y_{ac} y_{ab} + z_{ab} z_{ac}\right)}{\sqrt{x^2_{bc} + ß^2 \left(y^2_{ac} + z^2_{ab}\right)}}\right] + \frac{y_{ac}}{y^2_{ac} + z^2_{ac}} \left[1 - \frac{x_{ac}}{\sqrt{x^2_{ac} + ß^2 \left(y^2_{ac} + z^2_{ac}\right)}}\right] + \frac{y_{bc}}{y^2_{bc} + z^2_{bc}} \left[1 - \frac{x_{bc}}{\sqrt{x^2_{bc} + ß^2 \left(y^2_{bc} + z^2_{bc}\right)}}\right] \tag{4.71}$$

$$
\nu\left(\frac{G}{4p}\right)^{-1} = \frac{-x_{ac}z_{ab} + x_{ab}z_{ac}}{\left(x_{ac}y_{ab} - x_{ab}y_{ac}\right) + \left(x_{ac}z_{ab} - x_{ab}z_{ac}\right) + \beta^2\left(y_{ac}z_{ab} - y_{ab}z_{ac}\right)} \cdot
$$

$$
\left[\frac{x_{bc}x_{ab} + \beta^2\left(y_{bc}y_{ab} + z_{ab}z_{bc}\right)}{\sqrt{x^2_{bc} + \beta^2\left(y^2_{bc} + z^2_{bc}\right)}} - \frac{x_{ac}x_{ab} + \beta^2\left(y_{ac}y_{ab} + z_{ab}z_{ac}\right)}{\sqrt{x^2_{bc} + \beta^2\left(y^2_{ac} + z^2_{ab}\right)}}\right]
$$

$$
+ \frac{z_{ac}}{y^2_{ac} + z^2_{ac}}\left(1 - \frac{x_{ac}}{\sqrt{x^2_{ac} + \beta^2\left(y^2_{ac} + z^2_{ac}\right)}}\right) \tag{4.72}
$$

$$
- \frac{z_{bc}}{y^2_{bc} + z^2_{bc}}\left(1 - \frac{x_{bc}}{\sqrt{x^2_{bc} + \beta^2\left(y^2_{bc} + z^2_{bc}\right)}}\right)
$$

One may prove that the present non-planar VLM formulation is the same as the trigonometric expression used by Giesing *et al.*[62] based on the VLM of Hedman. For $M = 0$ and $z = 0$, or a planar incompressible case, the present formulation will reduce to the expression given in Bertin and Smith[110]. For $M = 0$, or an incompressible case, the present formulation will reduce to the expression given in Plotkin and Katz[117]. The present VLM does not need any numerical integration procedure, and therefore does not add a significant computational time to the unsteady aerodynamic calculation.

4.6 Present Doublet Point Method

Numerical improvements of the double point method (DPM) are presented in this Section. The improvement is applied to the planar lifting surface configuration, and is extended to the non-planar configurations. The numerical singularity problems of both configurations are first identified, and then the solution procedures are described and compared with the original solution of Ueda and Dowell[66]. The numerical results are given in Section 4.9 and comparisons with other methods are discussed.

4.6.1 Present DPM for Planar Lifting Surfaces

The basic concepts of the original DPM are used here. The surfaces are divided into small trapezoidal elements as shown in Fig. 4.3. The lifting pressure is assumed to be concentrated at the doublet point located at the quarter chord along the midspan of each panel. The control point is placed on the three-quarter chord at midspan of each element.

If the doublet point and the control point are located at elements i and j respectively, then the aerodynamic operator may be written as

$$\Im_{ij} = \frac{\Delta S_i}{8\pi} K\left(x_i - \xi_j, y_i - \eta_j, z_i - \zeta_j, k, M\right) \tag{4.73}$$

where the kernel function is based on Landahl's formula[64]:

$$K = e^{-ikx_0}\left(\frac{M e^{ikX}}{R X_1} + B_{1r} + i B_{1i}\right) \tag{4.74}$$

The improper integral B_1 in Eq. (4.74) is evaluated for the following two cases:

Case 1.

For the control point at a point (x, y, z) located outside the down stream panel of the doublet point at a point (x, h, z), *i.e.* for $X < 0$ or $r > e$, no singularity problem arises, and therefore Eqs. (4.45) – (4.47) can be used directly.

Case 2

If the control point (x, y, z) is located at the center of the down stream panel of the doublet point (x, h, z), *i.e.* for $X > 0$ and $r = 0$, then the singularity problem arises. This can be easily seen if the first two terms of the even series above is rewritten as follows:

$$U_{1,0} = \frac{1}{r^2}\left(1 + \frac{X}{\sqrt{X^2 + r^2}}\right) \tag{4.75a}$$

$$U_{1,2} = -\frac{k^2}{2}\left\{\frac{X}{\sqrt{X^2 + r^2}} + \ln\left(\sqrt{X^2 + r^2} - X\right)\right\} \tag{4.75b}$$

If $r \to 0$, then $X_1 \to X$, and the kernel becomes infinite because of the strong dipole singularity in Eq. (4.75a) and a weak logarithmic singularity in Eq. (4.75b). Ueda and Dowell solved the problem by utilizing the Mangler formula to integrate the $B_{1,r}$ term, and using the average value to the modified Bessel function as shown in Equation (4.44). In the present work, a different approach is employed in the following two solution steps:
First, the *basic* form of the singularity part is identified and separated from the regular part. *Secondly*, the Mangler procedure and the averaging rule is applied to the singular part only.

Based on a detailed derivation of the solution given in Appendix A.2 and E.4, the final term of the formulation for the $B_{1,r}$ is rewritten as follows:

$$B_1\ (X > 0) = + B_{1,regular}(X) - \frac{2}{e^2} + k^2 \left[\ln \frac{k e}{2} + \gamma - \frac{3}{2} \right] - k^2 \tan^2 \Lambda \tag{4.76}$$

where $B_{v,\ regular}$ is given in Eq. (4.62). This result is slightly different than the formulation given in Ref. 135 as follows:

$$B_1\ (X > 0) = - B_{1,real}(- X) + i B_{1,imag}(X) - \frac{2}{e^2} + k^2 \left[\ln \frac{k e}{2} + \gamma - \frac{3}{2} \right] - k^2 \tan^2 \Lambda$$

Compared to the result of Ueda and Dowell in Eq. (4.49), which is rewritten in the following:

$$B_1\ (X > 0) = - B_{1,real}(- X) + i B_{1,imag}(X) - \frac{2}{e^2} + k^2 \left[\ln \frac{k e}{2} + \gamma - \frac{3}{2} \right] \tag{4.49}$$

the present solution clearly gives a correction associated with the element sweep angle Λ. The correction has a significant effect if the reduced frequency or the sweep angle is large. The improvement proposed in Eq. (4.76) can be regarded as the answer to the question arises in the technical comment by Rodden *et al.* to Ref. 66. Rodden *et al.* pointed out that the DPM in Ref. 66 does not have the element sweep angle term. In their reply, Ueda and Dowell[66] acknowledged that their DPM indeed does not have an explicit sweep angle

correction but they suggested that the geometric arrangements of the doublet point may implicitly give the sweep angle effect.

In the present formulation, the explicit sweep angle correction for each element is taken into account as shown in Eq. (4.76). It should be noted that the term f_U in Eq. (4.76) may not add a significant computational time since we can use f_U to evaluate $B_{1,r}$ in the same time.

4.6.2 Present DPM for Nonplanar Lifting Surfaces

The method proposed in this section may be considered as an extension of the planar DPM of Ueda and Dowell to nonplanar lifting surface configurations. In Ref. 75, Eversman and Pitt have proposed the non-planar DPM. However, their method did not specifically address a treatment for the $1/r^4$ near singularity problem in the nonplanar part of the kernel. In the present work, an evaluation of the $1/r^4$ singularity problem will be introduced and treated analytically.

Some basic concepts of the planar DPM are still used in the non-planar DPM formulation. The lifting surface is idealized by dividing the surfaces into small trapezoidal elements arranged in strips parallel to the free stream. The lifting pressure is assumed to be concentrated at the doublet point located on the quarter chord at the midspan of each panel. The control point is placed on the three-quarter chord at midspan of each element. There are, however, at least three differences between the treatments for the planar and nonplanar cases:

1. The fundamental difference is that, if the sending doublet lattice and receiving control point are not in the same plane, the well-known singularity at $r = 0$ no longer appears.
2. For the non-planar configuration, there is an additional term, in the kernel function, associated with the non-planar surfaces. The formulation becomes more complicated because of two problems:

(i) the integration should be performed over both the planar and non-planar surfaces,

(ii) the non planar kernel function involves a higher order of the incomplete cylindrical function B_v, *i.e.* the order is $v = 2$.

3. The non-planar configuration has a three dimensional geometry. It is necessary to perform a coordinate transformation from the global coordinate system into local coordinate of each sending element in order to simplify the integration of the kernel function.

The system coordinate is centered at the midpoint of the doublet lifting line and rotating into the plane of sending element. The relations between the global coordinates $(x, y, z, \xi, \eta, \zeta)$ and the local coordinates $(\hat{x}, \hat{y}, \hat{z}, \hat{\xi}, \hat{\eta}, \hat{\zeta})$ are the same as the expressions used in Appendix A.

If the doublet point and the control points are located at element i and j respectively, then the aerodynamic operator may be written as

$$\Im_{ij} = \frac{\Delta S_j}{8\pi} K\left(x_i - \xi_{j,}\, y_1 - \eta_{j,}\, z_i - \zeta_j,\, k,\, M\right) \tag{4.73}$$

where the kernel is based on the formulation of Landahl in the following notation

$$K = e^{-i\,k\,x_0}\left(K_1^*\, T_1 - K_2^*\, T_2^*\right) \tag{4.77}$$

where

$$K_1 = \frac{M\, e^{ikX}}{R\, X_1} + B_{1r} + i\, B_{1i}$$

$$K_2 = \frac{M\, e^{ikX}}{R^2\, X_1}\left(i\,k\,M + \frac{\beta^2}{R} + \frac{2R - M\, X}{X_1}\right) + 3\, B_{2r} + 3i\, B_{2i} \tag{4.78}$$

$$T_2^* = \left(z_{\,0}\cos\gamma_s - y_0 \sin\,\gamma_z\right)\left(z_{\,0}\cos\gamma_r - y_0 \sin\,\gamma_r\right)$$

Note that the lateral distance, r is now for a three-dimensional coordinate defined as

$$r = \sqrt{y_0^2 + z_0^2} \tag{4.79}$$

Since $z_0 \neq 0$ for nonplanar surfaces then consequently $r \neq 0$, or the singularities no longer appear. However, if the control point is at the center of the sending element wake, *i.e.* $y_0 = 0$ *and* $X > 0$, the value r becomes $r = |z_0|$ and therefore is sensitive to the variations of z_0. If $z_0 << 1$ this leads numerically to the near-singular problem, the solution of which was not well established in the previous works.

The function B_1 has been given in Equations (4.41) – (4.43). The functions B_2 may be obtained from Equations (4.15) – (4.17) for v=2.

$$B_{2r} = \sum_{n=0}^{\infty} (-1)^n U_{2,2n} + \frac{k^4}{12} \sum_{n=0}^{\infty} \frac{(kr/2)}{n!(n+2)!} \times \left(\sum_{m=1}^{n} \frac{1}{m} + \frac{2n+3}{2(n+1)(n+2)} - \gamma - 1n\frac{k}{2} \right)$$

$$B_{2i} = \sum_{n=0}^{\infty} (-1)^n U_{2,2n+1} - \frac{\pi k^4}{24} \sum_{n=0}^{\infty} \frac{(k\ r/2)^{2n}}{n!(n+2)!} \tag{4.80}$$

where

$$U_{2,m\neq 4} = \frac{k(kX)^{m-1}}{(m-4)\, m!\, X_1^3} - \frac{(kr)^2}{(m-4)m}\, U_{2,m-2}$$

$$U_{2,4} = -\frac{k^4}{6} \left\{ \ln(X_1 - X) + \frac{X}{X_1} \left(1 + \frac{X^2}{3X_1^2} \right) \right\}$$

$$U_{2,2} = \frac{k^2}{6} \left\{ \frac{X^2}{X_1^3\ (X_1 - x)} + \frac{1}{X_1} \right\} \tag{4.81}$$

$$U_{2,1} = -\frac{k}{3\ X_1^3}$$

$$U_{2,0} = \frac{2\,X_1 - X}{3\,X_i^3\,(X_1 - X)^2}$$

and

$$X_1 = \sqrt{X^2 + r^2} \tag{4.47}$$

For the case of $X > 0$ and $r << 1$, the value of X_1 approaches X and a nearly – singular problem can be seen in the zeroth, second, and fourth order terms of the U series. Analytical solution to this problem is described in Appendices E.2 to E.4. Therefore, two different treatments are employed for the kernel. The final forms for each case is as follows:

Case 1

Case 1 is for most of the cases of the sending and receiving point pairs, *i.e.* for the control point not directly located in downstream of the doublet point, or more specifically, for

- $X < 0$ and arbitrary r
- $X > 0$ and $r > e$

In this case Eqs. (4.78) – (4.81) can be used directly since no singularity arises.

Case 2

For the control point directly behind the control point, the kernel is evaluated as follows

$$K = e^{-ikx_0}\left(K^*_{1,reg}\,T_1 - K^*_{2,reg}\,T^*_{2,reg}\right) + \frac{c_1}{2e}\sum_{n=0}^{\infty}\frac{\lambda^n}{n!}\left(n\,V_n - \frac{k^2\,V_{n+2}}{2(n+1)} - f_n\right) \tag{4.82}$$

where

$$V_{n>1} = \frac{y_b^{n-1} - y_a^{n-1}}{n-1} - \hat{z}^2\,V_{n-2}$$

$$V_1 = \ln\frac{r_b}{r_a} \tag{4.83}$$

$$V_0 = \frac{1}{|\hat{z}|}\left(\pi - \tan^{-1}\frac{2e|\hat{z}|}{e^2 + r_m^2}\right)$$

$$f_n = y_j^{n+1}\left(\frac{1}{r_j} - \frac{k^2 \ln r_j}{2\,(n+1)}\right)\Bigg|_{j=a}^{j=b} \tag{4.84}$$

$$\lambda = -\,i\,k\,\tan\Lambda$$
$$c_1 = 2\cos(\gamma_r - \gamma_s)\; e^{-ikx_m} \tag{4.85}$$

$$y_a = \hat{y} - e \qquad ; \qquad y_b = \hat{y} + e$$
$$r_a^2 = y_a^2 + \hat{z}^2 \qquad ; \qquad r_b^2 = y_b^2 + \hat{z}^2 \qquad ; \qquad r_m^2 = \hat{y}^2 + \hat{z}^2 \tag{4.86}$$

The regular part of the kernel function is evaluated as follows:

$$K_{1,reg} = \frac{M\,e^{ikX}}{R\,X_1} + B_{1,\,regular} \tag{4.87a}$$

$$K_{2,reg} = \frac{M\,e^{ikX}}{R^2\,X_1}\left(ikM + \frac{\beta^2}{R} + \frac{2R - M\,X}{X_1}\right) + 3B_{2,regular} \tag{4.87b}$$

where $B_{v,\,regular}$ is given in Eq. (4.62).

It should be noted that the present regular kernel function is simpler than the one given in Ref. 135. The regular kernel function used in Ref. 135 can be written in Eqs. (4.88) – (4.90) as follows:

$$K_{1,reg} = \frac{M\,e^{ikX}}{R\,X_1} + B^*_{1,real}(-|X|) + i\,B^*_{1,imag}(|X|) \tag{4.88a}$$

$$K_{2,reg} = \frac{M\,e^{ikX}}{R^2\,X_1}\left(ikM + \frac{\beta^2}{R} + \frac{2R - M\,X}{X_1}\right) + 3B^*_{2,real}(-|X|) + i\,3B^*_{2,imag}(|X|) \tag{4.88b}$$

where the second expansion series is slightly different than the Ueda series as follows:

$$B^*_{1,real} = \sum_{n=0}^{\infty}(-1)^n U^*_{1,2n} - \frac{k^2}{2}\sum_{n=1}^{\infty}\frac{(k\,r/2)^{2n}}{n!(n+1)!}\left(\sum_{m=1}^{n}\frac{1}{m} + \frac{1}{2(n+1)} - \gamma - \ln\frac{k}{2} - 2\ln r\right)$$

$$B^{*}_{2,real} = \sum_{n=0}^{\infty} (-1)^2 U^{*}_{2,2n} - \frac{k^4}{12} \sum_{n=0}^{\infty} \frac{(k\,r/2)^{2n}}{n!(n+2)!} \left[\sum_{m=1}^{n} \frac{1}{m} + \frac{2n+3}{2(n+1)(n+2)} - \gamma \ln \frac{k}{2} - \frac{2}{1} \ln r \right]$$

$$B^{*}_{1,imag} = B_{1,imag}$$

$$B^{*}_{2\,imag} = B_{2,imag}$$

The recursive series U^{*}_{n} for the first order $n = 1$ are

$$U^{*}_{1,m\geq 3} = \frac{k(kX)^{m-1}}{(m-2)m!\,X_1} - \frac{(k\,r)^2}{(m-2)m} U^{*}_{1,m-2}$$

$$U^{*}_{1,2} = +\frac{k^2}{2} \left\{ \ln (X_1 - X) + \frac{X}{X_1} \right\} \tag{4.89}$$

and for the second order $n = 2$, are as follows:

$$U^{*}_{2,m\neq 4} = \frac{k(kX)^{m-1}}{(m-4)m!\,X_1^3} - \frac{(k\,r)^2}{(m-4)m} U^{*}_{2,m-2}$$

$$U^{*}_{2,4} = \frac{k^4}{6} \left[\ln (X_1 + X) + \frac{X}{X_1} \left(1 + \frac{X^2}{3X_1^2} \right) \right]$$

$$U^{*}_{2,2} = -\frac{k^2}{6} \left\{ \frac{X^2}{X_1^3 (X_1 + X)} + \frac{1}{X_1} \right\}$$

$$U^{*}_{2,0} = \frac{2X_1 + X}{3X_1^3 (X_1 + X)^2} + \frac{k^4}{12} \left(\ln \frac{k}{2} + \gamma - \frac{3}{4} \right) \tag{4.90}$$

Equations (4.82) – (4.87) are the final expression used to evaluate the kernel for nonplanar configurations. In contrast to the solution given by Rodden *et al.* in their second version of the DLM [72], the result presented here is finite for any arbitrary value of *z*. In their work, the singular parts of the planar and nonplanar terms functions cancel out each other only for limiting values of the kernel, and the cancellation of these singularities

numerically will lead to difficulties for sufficiently small values of z. In the present work, the singular parts are eliminated not only for the limiting case, but also for any value of r.

4.7 Present Doublet Lattice Method

Numerical improvements of the double lattice method (DLM) are presented in this chapter. The improvements are applied to two types of lifting surface configurations, including the planar lifting surface and the non-planar lifting surface configurations. The numerical singularity problem of both configurations are first identified, and the solution procedures are described and compared with the original solution of Albano and Rodden[70] and with it's refinement solution proposed by Rodden, Giesing and Kalman[72]. The numerical results are given in Section 4.8 and comparisons with other methods are discussed.

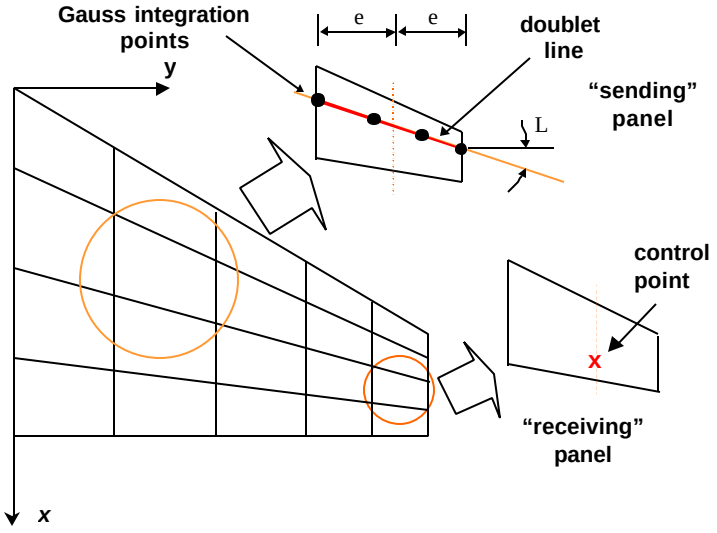


Figure 4.6. Lifting surface discritezation in the present doublet lattice method

4.7.1 Present DLM for Planar Lifting Surfaces

The basic concepts of the original DLM are used here. The surfaces are divided into small trapezoidal elements as shown in Fig. 4.6. The lifting pressure is assumed to be concentrated at the doublet lifting line located at the quarter chord of each panel. The control point is placed on the three-quarter chord at mid-span of each element.

If the doublet lifting line and the control point are located at elements i and j respectively, then the aerodynamic operator may be written as:

$$\Im_{ij}=\frac{\Delta x_s}{8\pi}\int_{-e}^{e} K\left(x_i-\xi_j, y_i-\eta_j, z_i-\zeta_j, k, M\right)d\eta \tag{4.91}$$

In the original DLM, the numerical integration of the kernel function K is based on the quadratic approximation of the numerator as shown in Equation (4.25). In the present work, the integration procedures are based on the following procedure:

1) The improper cylindrical function contained in the kernel function is solved analytically by using an expansion series. This step is described in Appendix A.3.
2) Analytically separate the kernel function into two parts: the regular and singular parts
3) Perform an exact integration solution for the singular part of the kernel, and
4) Perform a Gaussian quadrature integration for the regular part of the kernel

Based on the steps outlined above, the aerodynamic operator can be derived as follows:

$$\Im_{ij}=\frac{\Delta x_s}{8\pi}\left[\int K_{sing}\, d\,\bar{\eta} \quad + \sum_{n=2}^{N}\left(K_{reg}\right)_n W_n\right] \tag{4.92}$$

where W_n is the Gauss-Legendre weighting factor, and N is the number of integration points. This number is not fixed and may be increased to improve the accuracy. In the present work, N is selected based on the distance r, the wing root chord c_{root}, the reduced frequency k, and X as shown in Table 4.1. The weighting factor, W_n can be obtained in Ref. 166.

Table 4.1. The number of Gauss integration points *N*

$r_g = 2r / c_{root} k$	$X < 0$	$X > 0$
$0 < r_g < 0.1$	4	7
$0.1 < r_g < 0.25$	4	6
$0.25 < r_g < 0.5$	3	5
$0.5 < r_g < 1.0$	3	4
$1.0 < r_g < 2.0$	2	3
$r_g > 3.0$	2	2

The Gauss-Legendre technique uses the expression of the integrand directly, without any additional weighting function. Therefore a direct evaluation of the kernel, such as the type *B* integral in Equation (4.11), can be applied directly. For this reason, the present method uses the new expansion series, described in detail in Appendix A.3, to evaluate the improper integral. Compared to the Laschka's approximation used in the previous DLM, the present series is an exact representation of the incomplete cylindrical function. The present expansion series is almost similar to the Ueda's expansion series except that the present series explicitly separates the singular and regular kernel functions such that the kernel function integration can be performed more easily.

Based on the derivation described in Appendix A.4, the final form for the present DLM are as follows:

The regular part of the kernel function can be obtained as follows:

$$K_{reg}(\eta=\eta_n) = f_1 \; e^{ik x_0}\Big|_{\eta=\eta_n} \tag{4.93}$$

where

$$f_1 = \frac{M\ e^{ikX}}{RX_1} + B_{1,\,regular} + k^2 \left\{ \ln \frac{k}{2} + \gamma - \frac{1}{2} \right\} \tag{4.94}$$

and the improper cylindrical function B_1 is given by Eqs. (4.45)-(4.47). It is important that the absolute value of X in the third term of the right-hand side of Eq. (4.94) is intended to set the series into a regular function for every value of X.

Equation (4.94) is almost similar to the formulation given in Ref. 135 given as follows:

$$f_1 = \frac{M\ e^{ikX}}{RX_1} + i\,B_{1,i}(X) + B_{1,r}\left(-|X|\right) + k^2 \left\{ \ln \frac{k}{2} + \gamma - \frac{1}{2} \right\}$$

The singular part of the kernel function is integrated using the Mangler's technique as shown in Appendix A.4. The closed form solution of the integration is

$$\int_{-e}^{e} K_{sing}\, d\hat{\eta} = 2e^{-ik x_m} \times \left\{ \frac{\sin(ke\tan\Lambda)}{\tan\Lambda}\, k \ln e + \sum_{n=0}^{\infty} \frac{(ike\tan\Lambda)}{(2n)!} \left(\frac{2}{e(2n-1)} - \frac{k^2 e}{(2n+1)^2} \right) \right\} \tag{4.95}$$

One may prove that there is no singular term in this final equation. Therefore it eliminates the need to apply a special treatment for the near singularity problem.

4.7.2 The present DLM for Nonplanar Lifting Surface Configurations

Some basic concepts of the planar DLM are still used in the non-planar DLM formulation. The lifting surface is idealized by dividing the surfaces into small trapezoidal elements arranged in strips parallel to the free stream. The lifting pressure is assumed to be concentrated at the doublet lifting line located at the quarter chord of each panel. The control point is placed on the three-quarter chord at midspan of each element.

If the doublet lifting line and the control point are located in panels i and j respectively, then the aerodynamic operator may be written as:

$$\Im_{ij} = \frac{\Delta x_s}{8\pi} \int_{-e}^{e} K\left(x_i - \xi_j, y_i - \eta_j, z_i - \zeta_j, k, M\right) d\bar{\eta} \tag{4.96}$$

Analytical solution to this problem is described in Appendices E.2 to E.4. Two different treatments are employed for the kernel. The final forms for each case is as follows:

Case 1

Case 1 is for most of the cases of the sending and receiving point pairs, *i.e.* for the control point not directly located in downstream of the doublet point, or more specifically, for

- $X < 0$ and arbitrary r
- $X > 0$ and $r > e$

In this case Eqs. (4.78) – (4.81) can be used directly since no singularity arises, *i.e.*

$$\Im_{ij} = \frac{\Delta x_s}{8\pi} \sum_{n=2}^{N} K_n W_n \tag{4.97}$$

Case 2

The integral procedure of the kernel is similar to those of the planar method in the previous section which employed an exact integration procedure to the singular part, and Gauss-Legendre integration technique to the regular part.

$$\text{Á}_{ij} = \frac{\Delta x_s}{8\pi} \left[\int_{-e}^{e} K_{\textbf{\textit{singular}}} \, d\bar{\eta} + \sum_{n=2}^{N} \left(K_{regular}\right)_n W_n \right] \tag{4.98}$$

where W_n is the Gauss-Legendre weighting factor, and N is the number of integration points as shown in Table 4.1.

The regular part of the kernel function in Eq. (4.98) is evaluated as follows:

$$K_{regular} = e^{-ikx_0} \left(K_1^* T_1 - K_2^* T_2 \right) \tag{4.99}$$

where

$$K_{1,reg} = \frac{M\, e^{ikX}}{R\, X_1} + B_1^*$$
$$K_{2,reg} = \frac{M\, e^{ikX}}{R^2\, X_1}\left(ik\, M + \frac{\beta^2}{R} + \frac{2R - M\, X}{X_1} \right) + 3B_2^* + \frac{k^4}{4} r^2 \ln r - k^2 \tag{4.100}$$

and the B^* function is given by Eqs. (4.88) – (4.90).

The singular part of the kernel function in Eq. (4.98) is evaluated as follows:

$$\int_{-e}^{+e} K_{\sin g}\; d\bar{\eta} = c_1 \sum_{n=0}^{\infty} \frac{\lambda^n}{n!} W_n \tag{4.101}$$

where

$$W_n \;=\; nV_n \;- V_{n+2} + n\,\hat{z}\tan\hat{\gamma} V_{n-1} \;+\; f_5(b) \;-\; f_5(a) \tag{4.102}$$

$$f_5(t) \;=\; \frac{k^2}{2(n+1)}\, y_t^{n+1} \ln r_t \;+\; \left(\hat{z}\,\tan\hat{\gamma} - 1\right) \frac{y_t^{n+1}}{r_t^2} \tag{4.103}$$

One may find that the non-planar formulation above gives a finite result for any value of *r*, including for the case X > 0 and $r \to 0$, *i.e.* when the control point is near the center of the wake. Since the singularity problem is identified and separated analytically, the near singularity problem vanishes and the results are continuous and finite for any arbitrary value of *z*.

4.8 Present Doublet Hybrid Method

In the present doublet hybrid method (DHM), the aerodynamic load is calculated based on a hybrid of three different methods: the vortex lattice method (VLM), the doublet lattice method (DLM), and the doublet point method (DPM). The vortex lattice method is used for the steady part since the method performs exact integration of all terms of the kernel function. For the incremental unsteady part of the kernel, both doublet methods are used. The DPM is used if the kernel function is nearly constant across the element. The

DLM is used if the kernel function varies considerably across the element. Since the function is closely related to lateral distance r of sending and receiving points, the doublet methods chosen are based on r as shown in Table 4.3.

Table 4.3

List of procedures used in the doublet hybrid method

$r_g = 2r / c_{root} k$	Steady flow ($k = 0$)	Unsteady Flow ($k > 0$)	
		X < 0	X > 0
$0 < r_g < 0.1$	VLM	DLM with N = 4	DLM with N = 7
$0.1 < r_g < 0.25$	VLM	DLM with N = 4	DLM with N = 6
$0.25 < r_g < 0.5$	VLM	DLM with N = 3	DLM with N = 5
$0.5 < r_g < 1.0$	VLM	DLM with N = 2	DLM with N = 4
$1.0 < r_g < 2.0$	VLM	DLM with N = 2	
$r_g > 3.0$	VLM	DPM	

Based on Table 4.3., the aerodynamic operator is formulated as follows:

$$\Im_{ij} = \frac{\Delta x_i}{8\pi} K\left(x_i - \xi_j, y_i - \eta_j, z_i - \zeta_j, k, M\right) \tag{4.104}$$

where the kernel function K is formulated in the following equation

$$K = \begin{cases} K_{VLM} + \left(K - K(k=0) \right)_{DPM} & \text{for } r > 3 \text{ and any } X \\ K_{VLM} + \left(K^* - K^*(k=0) \right)_{DLM} & \text{for } r < e/2 \text{ and } X > 0 \\ K_{VLM} + \left(K - K(k=0) \right)_{DLM} & \text{for all other cases} \end{cases} \tag{4.105}$$

The Vortex Lattice Method

The kernel function K_{VLM} in Eq. (4.105) is the same as the kernel function for the present vortex lattice method described in Section 4.4. The formula is not rewritten here since it can be used directly for the present DHM.

The Doublet Point Method

The kernel function K_{DPM} in Eq. (4.105) is the same as the kernel function for the present DPM Case 1 (no singularity case) described in Sections 4.6.1. and 4.6.2. The kernel function $K_{DPM}\ (k=0)$ is the steady part of the kernel by setting $k = 0$. The results for planar configuration is as follows:

$$K(k=0)=\frac{M}{R X_1}-\frac{1}{X_1\left(X_1+\left|X\right|\right)}-\frac{2}{e^2} \tag{4.106}$$

For nonplanar configurations the steady part of the kernel is given as:

$$K\left(k=0\right) = K_{1,reg}\left(k=0\right)\mathrm{T}_1 - K_{2,reg}\left(k=0\right)T_2 - \frac{\cos\gamma}{e}\left(\frac{y_b}{r_b^2}-\frac{y_a}{r_a^2}\right) \tag{4.107}$$

$$K_{1,reg}\left(k=0\right) = \frac{M}{R X_1}-\frac{1}{X_1\ (X_1+\left|X\right|)} \tag{4.108}$$

$$K_{2,reg}\left(k=0\right) = \frac{M}{R^2 X_1}\left(\frac{\beta^2}{R}+\frac{2R-M X}{X_1}\right)-\frac{2X_1+\left|X\right|}{X_1^3\ (X_1+\left|X\right|)^2} \tag{4.109}$$

The Doublet Lattice Method

The kernel function K_{DLM} in Eq. (4.105) is the same as the kernel function for the present DLM Case 1 (no singularity case) and Case 2 (singularity case) described in Sections 4.7.1. and 4.7.2. The kernel function $K_{DLM}\ (k=0)$ is the steady part of the kernel by setting $k = 0$. The integration of the kernel is performed as follows:

$$\Im_{ij} = \frac{\Delta x_s}{8\pi}\left[\int_{-e}^{e}\left(K_{\sin g} - K_{\sin g}(k=0)\right)d\,\overline{\eta} \;+\; \sum_{n=2}^{N}\left(K_{reg} - K_{reg}(k=0)\right)_n W_n\right] \tag{4.110}$$

where the steady part for the kernel in planar configuration are

$$\int_{-e}^{e} K_{\sin g}\,(k=0)\; d\eta \;=\; -\frac{4}{e} \tag{4.111}$$

$$K_{reg}\,(k=0) \;=\; \frac{M}{R\,X_1} - \frac{1}{X_1\;(X_1 + |X|)} \tag{4.112}$$

The steady part for the kernel in non-planar configuration are

$$\int_{-e}^{e} K_{\sin g}\,(k=0)\; d\eta \;=\; -\,2\,\cos\hat{\gamma}\left(\frac{y_b}{r_b^2} - \frac{y_a}{r_a^2}\right) \tag{4.113}$$

$$K_{reg}\,(k=0) = K_{1,reg}(k=0)\,\mathrm{T}_1 \;-\; K_{2,reg}(k=0)\,T_2 \tag{4.114}$$

where

$$K_{1,reg}\,(k=0) \;=\; \frac{M}{R\,X_1} - \frac{1}{X_1\;(X_1 + |X|)} \tag{4.115}$$

$$K_{2,reg}\,(k=0) \;=\; \frac{M}{R^2\,X_1}\left(\frac{\beta^2}{R} + \frac{2R - M\,X}{X_1}\right) - \frac{2\,X_1 + |X|}{X_1^3\;(X_1 + |X|)^2} \tag{4.116}$$

4.9 Unsteady Aerodynamic Load in Laplace Domain

The basic lifting surface theory and numerical solution methods described in previous sections are derived based on the so-called frequency domain approach, where the velocity potential j (t) is assumed to oscillate following the lifting surface harmonic motion about its equilibrium as shown in Eqs. (4.3) and (4.6). Attempts to predict unsteady aerodynamic loads for a more general type of motion have also been initiated since six

decades ago[179]. The procedures for constructing aerodynamic loads for general motions can be divided into two different approach: the aerodynamic transfer function method[179 - 182], and the Laplace domain aerodynamic method[136, 183, 184]. A typical technique in the aerodynamic transfer function method is to utilize the aerodynamic loads obtained in the frequency domain. If the general motion is represented in the Laplace domain, then the harmonic unsteady aerodynamic load can be interpreted as the loads on the imaginary axis in the complex *s*-plane. The aerodynamic transfer function can be constructed such that the approximation curve fits the harmonic load data in the imaginary axis[180, 181]. This approach is obviously limited to the proximity of the imaginary axis and needs a number of aerodynamic frequency domain results to give accurate approximation.

The other approach formulates the unsteady aerodynamic loads directly in the Laplace domain[136, 183, 184]. This approach gives an analytical expression of the aerodynamic load in the complex *s*-plane without any curve fitting approximation, and, therefore, reduces the computational time without degrading the accuracy. The possibility of implementing this approach to the present lifting surface methods is shown in the next two Sections.

4.9.1 Kernel Function Formulation

Similar to the Kussner normal wash-pressure equation in frequency domain given by Eq. (4.8), the integral equation in the Laplace domain, that relates the normal wash $\overline{w}$ at a point (x, y, z) to a pressure difference $\Delta \overline{p}$ on an infinitesimal area $d\xi\, d\eta$ centered at a point (x, h, z), can be formulated as follows:

$$\overline{w} = \frac{1}{8\pi} \iint_S \Delta \overline{p}\, K\left(x_o, y_o, z_0, h, M\right) d\xi\, d\eta \tag{4.117}$$

where h is the non-dimensional Laplace transform variable defined as:

$$h = a + ik = \frac{sb}{U_\infty} \tag{4.118}$$

and *s*, *a* and *k* are the dimensional variable of the Laplace transform, its non-dimensional real part and imaginary part, respectively. The function *K* represents the kernel function in Laplace domain which has been formulated by Ueda[184] as follows:

$$K = e^{-hx_o}\left(\frac{K_1 T_1 + K_2 T_2}{r^2}\right) \tag{4.119}$$

where

$$\begin{aligned}
x_o &= x - \xi \\
y_o &= y - \eta \\
z_o &= z - \zeta \\
r &= \sqrt{{y_o}^2 + {z_o}^2} \\
R &= \sqrt{x^2 + \beta^2 r^2} \\
X &= (x_o - M R)\,\beta^{-2} \\
X_1 &= \sqrt{X^2 + r^2} \\
b &= \sqrt{1 - M^2} \\
K_1 &= \frac{M r^2}{R X_1} e^{hx} + I_1 \\
K_2 &= -\frac{M r^4 e^{hx}}{R^2 X_1}\left(hM + \frac{\beta^2}{R} + \frac{2R - MX}{X_1}\right) - 3 I_2 \\
I_v &= \int_{-X/r}^{\infty} \frac{e^{hu}}{\left(1 + u^2\right)^{v+1/2}}\, du \\
T_1 &= \cos(g_s - g_r) \\
T_2 &= \frac{(z_o \cos\gamma_s - y_o \sin\gamma_s)(z_o \cos\gamma_r - y_0 \sin\gamma_r)}{r^2}
\end{aligned} \tag{4.120}$$

and γ_r and γ_s are dihedral angles at the points (x, y, z) and (x, h, z), respectively.

One may find that this kernel function formulation in the Laplace domain given by Eq. (4.119) will reduce to the kernel function formulation in frequency domain given by Eq. (4.12) if the real part of the Laplace domain a approaches zero. In other words, the pressure distribution calculated based on Eq. (4.119) will fit the pressure distribution based on Eq. (4.12) in the imaginary axis of the complex s-plane.

4.9.2 Incomplete Cylindrical Function

Similar to the kernel function formulation for the frequency domain, the incomplete cylindrical function I_1 and I_2 occur in Eq. (4.120) with a complex variable h. In the present formulation, the type-B integral is written as:

$$B_v = \int_{-\infty}^{X} \frac{e^{h\,u}}{\left(r^2 + u^2\right)^{v+1/2}}\, du \tag{4.121}$$

where the integral B_v and I_v are related as follows:

$$B_v = \frac{I_v}{r^{2v}} = \frac{1}{r^{2v}} \int_{-X/r}^{\infty} \frac{e^{hu}}{\left(1 + u^2\right)^{v+1/2}}\, du \tag{4.122}$$

The analytical solution of the type B integral has been given by Ueda [184] in the following infinite series:

$$B_v(h, r, X) = \sum_{n=0}^{\infty} U_{v,n} + \frac{(h/2)^{2v}}{(2v-1)!!} \sum_{n=0}^{\infty} (-1)^n\, p_n\, \frac{(hr/2)^{2n}}{n!\,(n+v)!} \tag{4.123}$$

where

$$p_n = -\gamma^* - \ln\frac{h}{2} + \sum_{m=1}^{n} \frac{1}{m} + \sum_{m=n+1}^{n+v} \frac{1}{2m}$$

γ^* = Euler's constant = 0.57721566490153286060651 2…

$$U_{v,\, n\neq 2v} = \frac{h\,(hX)^{n-1}}{(n-2v)\,n!\,X_1^{2v-1}} - \frac{(hr)^2}{(n-2v)\,n}\, U_{v,n-2}$$

$$U_{v,n=2v} = -\frac{h^{2v}}{2v!}\left\{ \ln(X_1 - X) + \sum_{m=1}^{v} \frac{1}{2m-1}\left(\frac{X}{X_1}\right)^{2m-1} \right\} \tag{4.124}$$

$$U_{v,\,2n<2v} = \frac{(v-n-1)!\,h^{2n}}{(2n)!\,r^{2(v-n)}}\left\{ 2^{v-n-1}\,\frac{(2n-1)!!}{(2v-1)!!} + \sum_{m=0}^{v-n-1} \frac{(-1)^m\,X^{m-1}\,(X/X_1)^{2m+2n+1}}{(2m+2n+1)\,m!\,(v-m-n-1)!} \right\}$$

$$U_{v,1} = -\frac{h}{(2v-1)\,X_1^{2v-1}}$$

and the symbol of double-factorials *!!* is used to define

$$\begin{aligned} (2n-1)!! &= 1 \bullet 3 \bullet 5 \bullet \ldots (2n-1) \\ (-1-2n)\,!! &= \frac{(-1)^n}{(2n-1)\,!!} \end{aligned} \tag{4.125}$$

The expansion series of the incomplete cylindrical function in Laplace domain given by Eqs. (4.123)-(4.125) is similar to the expansion series in frequency domain given by Eqs. (4.15)-(4.16). Therefore the treatment to identify and separate the regular and singular parts of the kernel function is also similar to the treatment for the frequency domain, but with one exception: the logarithmic function with a complex argument *ln*(*h*) appearing in Eq. (4.124) should be evaluated as

$$\ln(a + i\,k) = \ln\sqrt{a^2 + k^2} + i\,\tan^{-1}\left(\frac{k}{a}\right) \tag{4.126}$$

To prove that the expansion series of the Laplace domain in the imaginary axis will give the same expansion series of the frequency domain, we can set the real part of the Laplace domain *a* in Eq. (4.126) to zero:

$$h = i\,k \qquad \text{for } a = 0 \tag{4.127}$$

such that Eq. (4.126) becomes

$$\ln(a + i\,k) = \ln k + i\,\frac{\pi}{2} \qquad \text{for } a = 0 \tag{4.128}$$

Substitution of Eq. (4.128) into Eq. (4.124) will yield the same expression as Eqs. (4.15) and (4.16). This similarity offers the same treatment for the application of the kernel function in the Laplace domain to the present lifting surface methods, *i.e.* the same procedures can be used: identification and separation of the regular and singular parts of the kernel function, exact integration to the singular part of the kernel function, and Gauss quadrature integration to the regular part of the kernel function.

4.9.3 Application to the Strut-Braced Wing Aeroelastic Analysis

The unsteady aerodynamic load prediction in the Laplace domain is important in the strut-braced wing analysis to study its nonlinear aeroelastic response. It has been explained in Chapters 1 and 2 that, because of the compressive force effect, the aeroelastic response of the strut braced wing is more complicated than the conventional cantilever wing. By considering the other aerodynamic loads such as the wind gust, the aeroelastic equation for the strut braced wing can be written as:

$$\mathbf{M}\,\ddot{x}(t) + \left(\mathbf{K} - \mathbf{P}(x,\ddot{x})\,\mathbf{K_g}\right) x(t) - \mathbf{F_a}\,x(t) = \mathbf{F_e}(t) \tag{4.129}$$

where $\mathbf{P}$ is the compressive force generated by the strut, $\mathbf{M}$, $\mathbf{K}$ and $\mathbf{K_g}$ are the mass, stiffness and geometric stiffness matrices respectively, and $\mathbf{F_a}$ and $\mathbf{F_e}$ are the self-excited and external aerodynamic forces respectively.

The compressive force $\mathbf{P}$ in Eq. (4.129) is a function of displacement of motion since the strut-braced wing is an indeterminate structure. $\mathbf{P}$ is also a function of the acceleration of motion since, in the present strut braced wing, the strut is activated if the flight load factor is greater than 0.8 *g*. If the external aerodynamic force $\mathbf{F_e}$, such as a gust load, excites the structure with a considerable positive and negative load factor, the strut will be engaged and disengaged during the motion to prevent the strut buckling. Therefore, Eq.(4.129) becomes a nonlinear equation where it is unlikely that the wing vibrates harmonically.

To calculate the aeroelastic response of the system, the present lifting surface method in the frequency domain can be used to construct the self-excited force $\mathbf{F_e}$. However, to generate a non-harmonic force, the frequency domain approach needs a considerable amount of calculation to approximate the load. On the other hand, the present lifting surface method in the Laplace domain offers the possibility to directly calculate the non-harmonic force $\mathbf{F_e}$ and calculate the response in Laplace or time domain. This aeroelastic response analysis deserve further intense investigation, and is not conducted in the present work.

4.10 Validation

To implement the theoretical development of the present lifting surface methods, a FORTRAN computer code was developed and presented in Appendix A. To evaluate the accuracy of the present methods, a number of wing planforms are used and the results are compared with experimentation data or other lifting surface method results.

4.10.1 Delta Wing with AR=2

Table 4.4. Lift coefficient C_L of a delta wing with AR=2 and α= 4.3°

N_x x N_y aerodynamic panel	Present DPM	Present DLM	Present DHM
1 x 20	0.1662	0.1635	0.1636
2 x 20	0.1678	0.1653	0.1651
3 x 20	0.1681	0.1655	0.1652
4 x 20	0.1682	0.1657	0.1655
5 x 20	0.1683	0.1657	0.1655
Experiment[124]		0.159	
Margason and Lamar[90] (6 x 20)		0.1654	
Lan[100] (3 x 35)		0.1649	
Lamar[119] (4 x 11)		0.168	
Nissim and Lottati[92] (3 x 3)		0.1626	
Dulmovits[119]		0.165	
Wagner[120]		0.1663	

The first example is a delta wing with AR = 2 shown in Fig. 4.7. This wing planform has been selected by many to demonstrate their numerical procedures as shown in Table 4.4. Experimentation data is based on Wick[124]. The experimentation was performed in a steady flow with Mach number 0.13, Reynolds number 2.4 million. The results obtained using the present methods, shown in Table 4.4 and Figure 4.7, are in a good agreement with other lifting surface methods and experiments results. Note that the convergence rate of the present DPM result with respect to the number of panel element is slower than the present DLM and DHM.

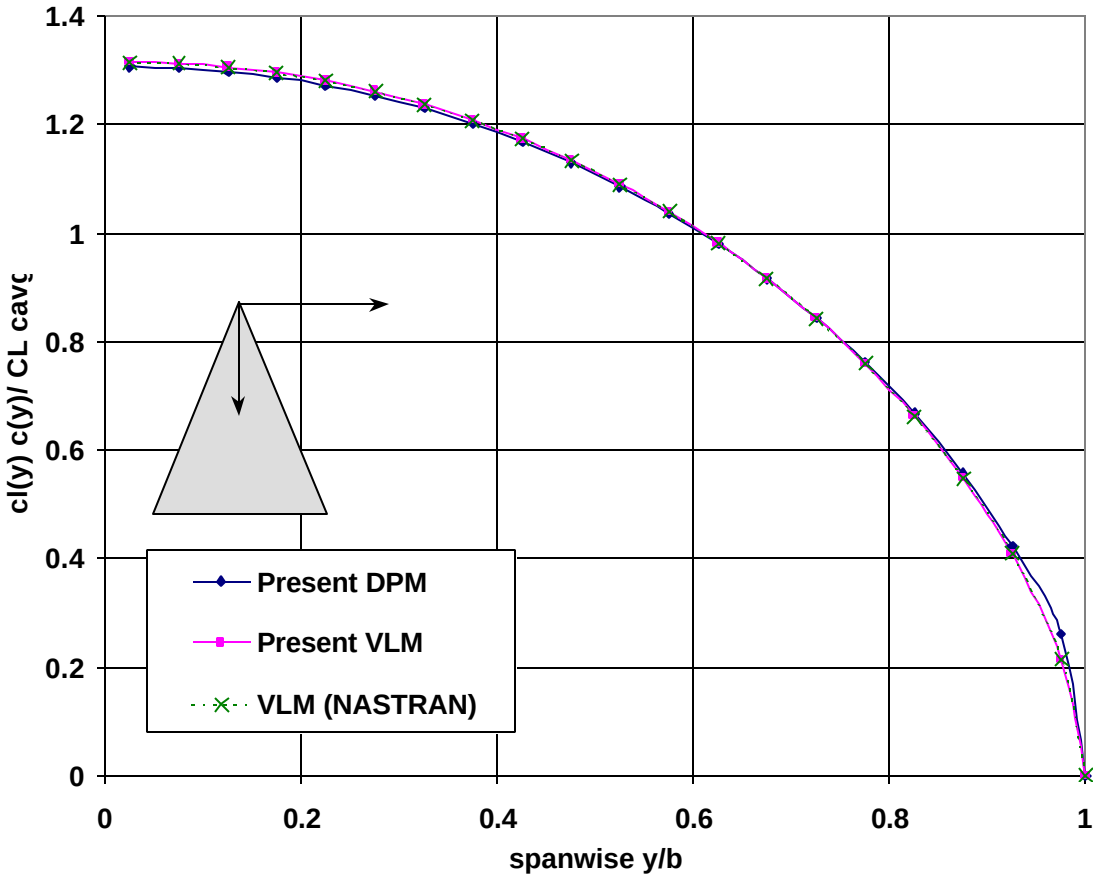


Figure 4.7 Spanwise lift distribution of a delta wing with AR=2 and *M*=0.13

4.10.2. Double-Delta Wing

To demonstrate the accuracy of the present VLM for evaluating a more complicated planform, a cropped double-delta wing is selected. The aerodynamic pressure distribution are calculated using two numerical schemes: the Gauss elimination method with total pivoting, and the LU decomposition method. Both schemes give a good correlation with the modified Multhopp's method of Lamar[119] as shown in Table 4.5.

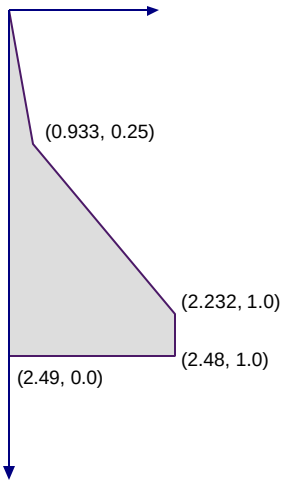


Figure 4.8. A double delta wing planform with AR=1.7.

Table 4.5. The lift coefficient of a double delta wing with AR=1.7 and α=1°

Methods	Paneling*	C_L
Present VLM (with Gauss elimination)	2 x 5 (i/b), 2 x 15 (o/b)	0.036419686
Present VLM (with LU decomposition)	2 x 5 (i/b), 2 x 15 (o/b)	0.036419649
Lamar[119]	2 x 5	0.03740
Lamar[119]	8 x 27	0.03640

* (i/b) : inboard part, (i/b) : outboard part

4.10.3. Sweptback Wing with Partial Flap

Calculations have been carried out on a swept-back wing with an outboard flap as shown in Fig. 4.9. The flap is oscillating with an amplitude of 0.66° and reduced frequency 0.372. Fig. 4.10 shows comparison with the experimental data obtained by Forsching *et al*[125]. It shows that the present results are capable of capturing the pressure singularity region near the flap hinge. Table 4.6 shows comparison with the results of the DPM of Ueda and Dowell[56]. Note that the result of the present DPM using 36 elements is similar to the result of the DPM of Ueda and Dowel using 50 elements.

Table 4.6. The lift coefficient CL of the wing with partial flap

AR=2.94, $\alpha = 0°$, $\delta = 0.66°$, k = 0.372

Aerodynamic Panel	Present DPM	Present DLM	Present DHM
(4 x 7) wing (2 x 4) flap	0.009273 + 0.001719 *i*	0.009348 + 0.001757 *i*	0.008905 + 0.001631 *i*
(5 x 7) wing (2 x 4) flap	0.009469 + 0.001763 *i*	0.009522 + 0.001782 *i*	0.009065 + 0.001655 *i*
(6 x 7) wing (2 x 4) flap	0.009624 + 0.001785 *i*	0.009611 + 0.001789 *I*	0.009144 + 0.001661 *I*
DPM of Ueda-Dowell[66] (6 x 7) wing and (2 x 4) flap		0.0095 + 0.0018 *i*	

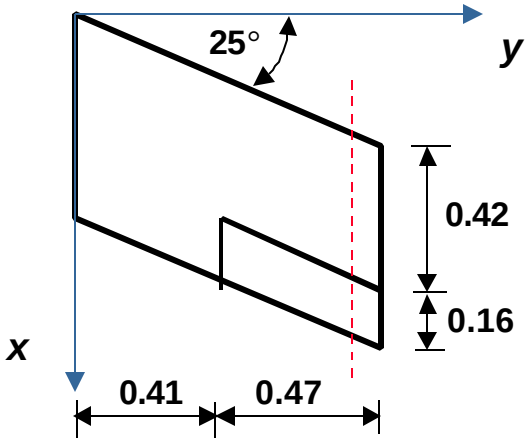


Figure 4.9. A sweptback wing with partial flap

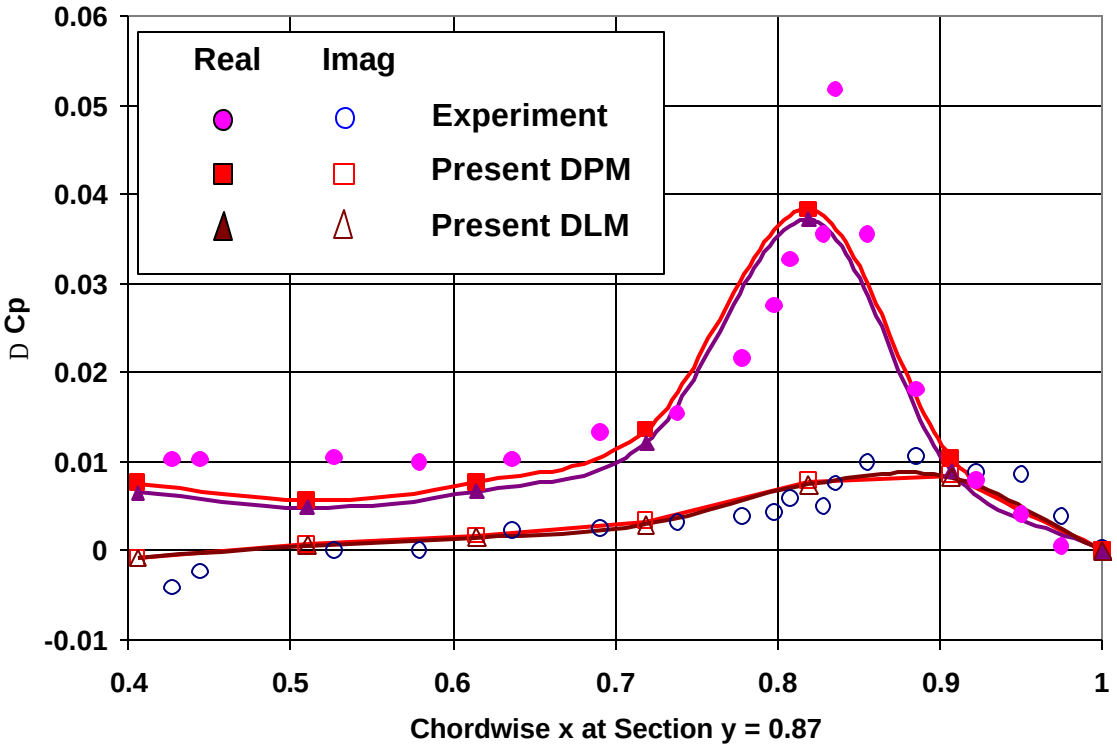


Figure 4.10. Pressure distribution at y = 1.95 of the swept-back wing with flap

4.10.4. AGARD Wing-Horizontal Tail

To illustrate the results of the present methods for nonplanar lifting surface configurations, an AGARD coplanar wing-horizontal tail shown in Fig. 4.11a is selected. The horizontal tail of the configuration is placed at different heights and distances from the wing as shown in Fig. 4.11a and Table 4.7. Note that the x and z coordinates shown in Table 4.7 are presented in non-dimensional forms with respect to the wing half span. Figure 4.11b shows variation of the lift curve slope C_{La} with respect to the vertical gap z between the wing and horizontal tail calculated using the present methods and the piecewise continuos kernel function method (PCKFM) of Lottati and Nissim[93]. The results of the present DLM and DHM are almost identical. All methods give the same trend of the results. Note that for the same configuration with $z = 0$

Table 4.7. The non-dimensional x-coordinate of the AGARD wing-tail planform

		z = 0	z = 0.6	z = 1.2
Wing	a	0	0	0
	b	2.25	2.25	2.25
	c	2.75	2.75	2.75
	d	3.70	3.70	3.70
Horizontal Tail	e	2.70	3.10	3.55
	f	4.00	4.40	4.85
	g	3.90	4.30	4.75
	f	4.25	4.65	5.10

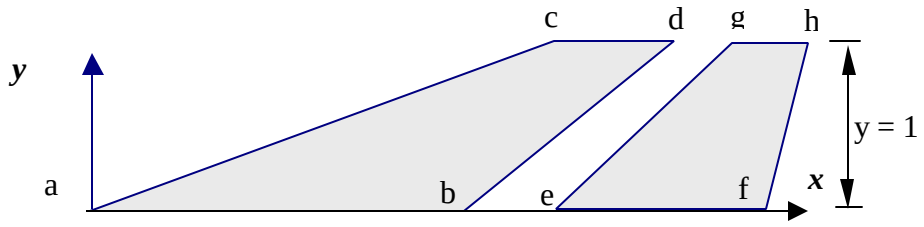


Figure 4.11a. Schematic of AGARD coplanar wing-horizontal tail configuration

(coplanar), Rodden[67] reported that the lift curve slope is 1.9794. The present DPM, DLM and DHM results for the coplanar configuration are 2.0435, 1.9739 and 1.9741, respectively. The PCKFM result[93] for the coplanar configuration is 1.9021. These results are in good agreements.

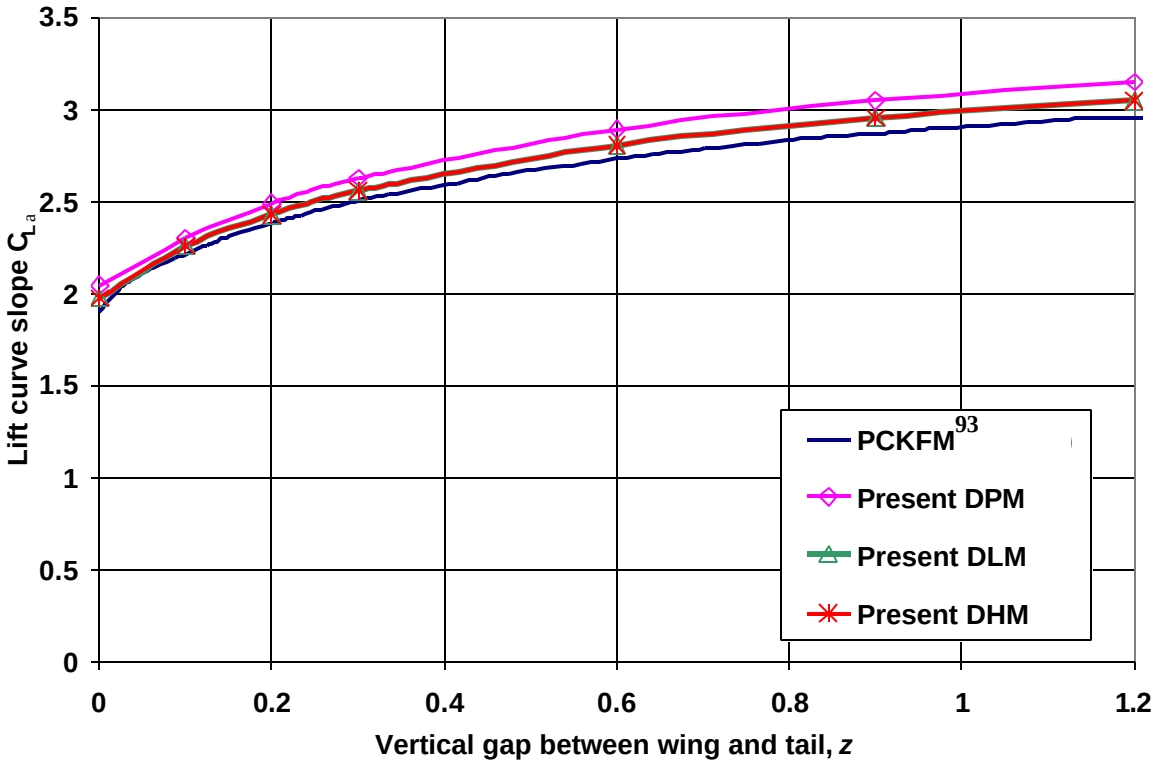


Figure 4.11b. The lift curve slope C_{La} of AGARD wing-horizontal tail as a function of the vertical gap between the wing and horizontal tail. M=0.8, Nx = 7, Ny=12.

4.10.5. Strut-Braced Wing with Camber and Twist Angle

To check the capability of the present lifting surface methods to predict the lift distribution of wing having camber and twist angle distribution, a wing planform of the present SBW configuration with AR = 12.17, taper ratio of 0.21, and swept angle at a quarter chord of 29.9° is used. The spanwise distribution of the wing camber and twist angle, shown in Fig. 4.12, is calculated using LAMDES code[168]. The upstream Mach number is 0.85. To check the accuracy, a calculation was performed using the present VLM method with two schemes: the scheme with and without the back-wash velocity component. Both schemes consider the downwash and sidewash velocity components to take into account the influence of the camber and twist angle distributions.

The results, presented in Fig. 4.13, show excellent agreement with the LAMDES result. The result shows also that the influence of the back wash velocity component is not significant in the present case. Therefore, for the aerodynamic load prediction of the strut-braced wing, only the down wash and side wash velocity components are included in the calculation. The present VLM has been used to calculate the aerodynamic load redistribution on flexible wing, where the results are useful for predicting wing bending weight and jig shape[9, 20-22].

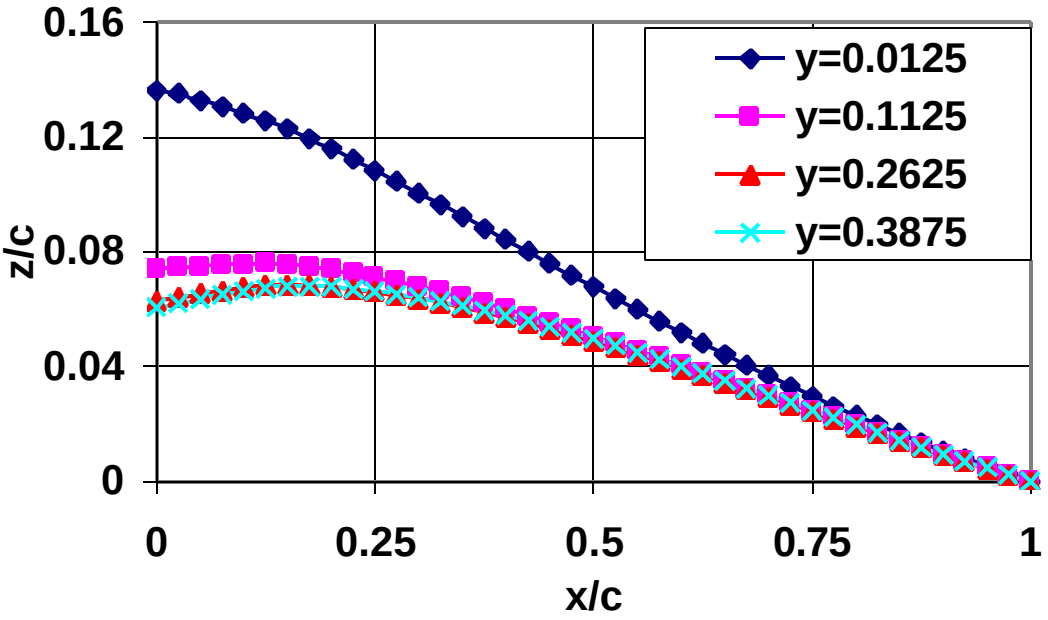


Figure 4.12a. Strut-braced wing camber and twist angle for y < 0.4

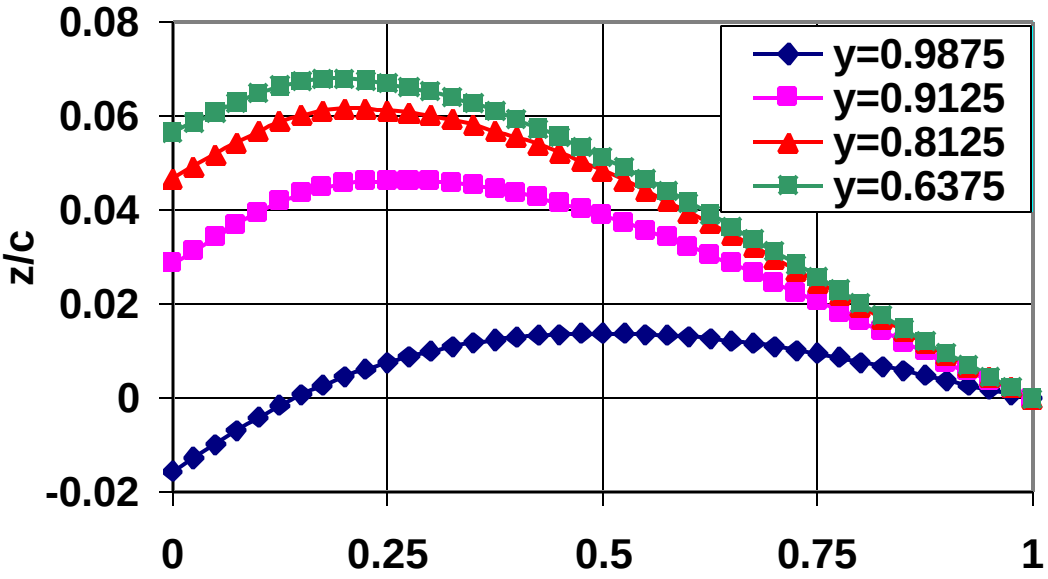


Figure 4.12b. Strut Braced wing camber and twist angle distribution for y > 0.63

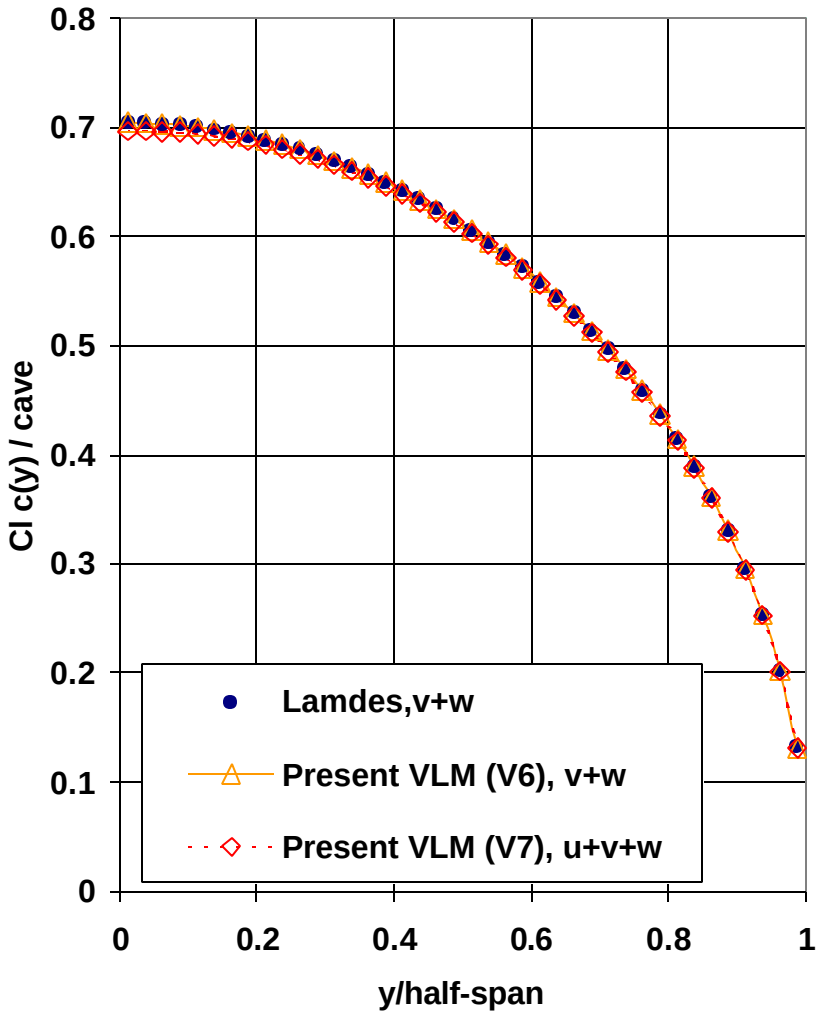


Figure 4.13. Lift distribution of the strut braced wing with camber and twist angle distribution. The symbol *u*, *v* and *w* are the back wash, sidewash and downwash of the air velocity components, respectively..

4.11. Unsteady Transonic Aerodynamics

The lifting surface methods described in the previous sections are derived based on linear aerodynamic theory[54]. The linear aerodynamic theory neglects the influence of viscosity and the lifting surface thickness and assumes no pressure jump due to the shock over the surface. In a transonic flow, where the thickness effect is important and shock wave are present over the surface, linear aerodynamic theory may give inaccurate predictions. The interest in unsteady transonic aerodynamic study arises mainly because of two reasons. The first reason is because the critical flutter speed of many transonic transport aircraft is more likely to occur in the transonic range[198]. The second reason is because the nonlinear transonic aerodynamics theory gives a more conservative flutter prediction than the linear aerodynamic theory. Previous experimental[192-194] and numerical[195-197] investigations on transonic aeroelasticity revealed the so-called transonic-dip effect showing that the aeroelastic calculation based on a nonlinear transonic aerodynamic method gives a lower flutter speed than the calculation based on the linear aerodynamic method. A sketch of a typical transonic flutter boundary plot illustrated in Fig. 4.14 shows that the flutter speed is very sensitive to the variation of Mach number near the transonic dip region[191]. Figure 4.14, adapted from Figs. 1 and 11 of Ref. 191, shows also that a thinner wing may have a lower critical flutter speed. The transonic dip of the thinner wing is shifted to a higher Mach number.

Research on the unsteady transonic aerodynamics has been initiated since 1970's, *c.f.* Ref. 191. Most of numerical predictions of the unsteady transonic aerodynamics are based on computational fluid dynamic (CFD) methods. The aerodynamic governing equation used in the CFD methods can be divided into several categories including 1) time-linearized transonic small disturbance (TSD) equation, *e.g.* Ref. 201, 2) TSD, *e.g.* Ref. 200, 3) full potential equation, *e.g.* Ref. 202, 4) Euler equation, *e.g.* Ref. 203 and 5) Navier-Stokes equation, *e.g.* Ref. 204. In the solution of these equations, numerous methods use

time-domain[204, 217], frequency domain[215] and indicial methods[199]. A more detailed discussion of the CFD-based methods can be found in Ref. 199.

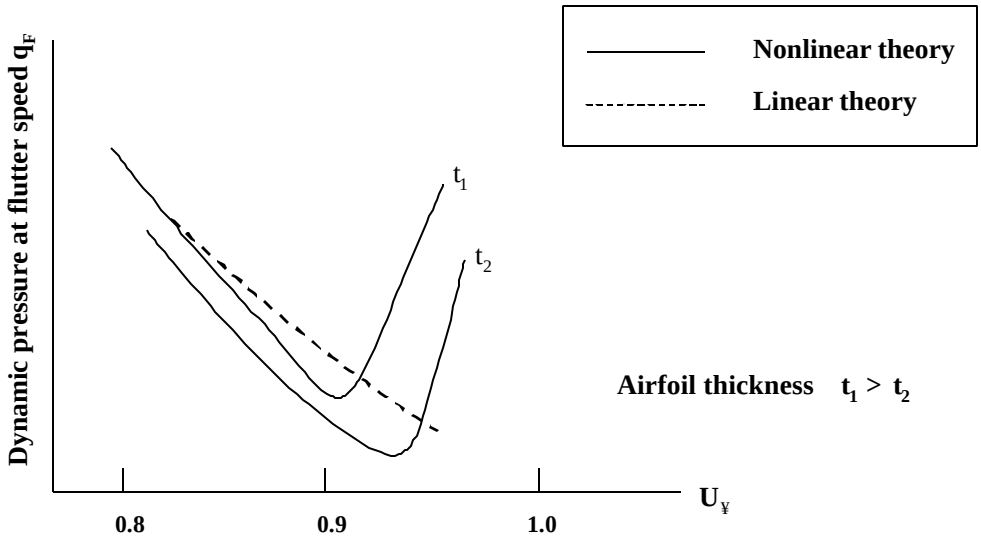


Fig. 4.14. Typical transonic dip plots near the sonic Mach number.

With major advances in parallel computers, CFD-based methods have been used extensively for the transonic aeroelastic simulation. However, their acceptance by the aerospace industry for rapid analysis and design is still hampered by problems in grid generation, CFD/CSD interfacing, and computing time. Note that the order of magnitude of flutter runs that are needed in aircraft certification process of a modern transport aircraft may be larger than ten thousand. On the other hand, most flutter computations in the aerospace industry use commercial finite element codes with aeroelastic modeling capability such as NASTRAN. These codes, however, are usually based on linear aerodynamic methods and thus limited to subsonic or supersonic flows. Therefore, some efforts have been made to overcome this problem by performing some corrections to the aerodynamic influence coefficient (AIC) obtained using unsteady linear aerodynamic methods. Those corrections are carried out by means of data obtained using wind-tunnel

results or CFD methods. The wind tunnel or CFD data needed for these correction factor methods is usually in terms of steady aerodynamic pressure distributions. These correction factor methods offer a more accurate prediction of the unsteady transonic aerodynamic influence coefficient than linear aerodynamic methods. The correction factor methods need less computational time than the CFD methods since the database needed to perform the correction is in the form of the steady pressure distribution.

Several correction factor methods of the AIC can be found in the literature. Yates and Bennet[205] proposed a simple correction factor based on a modified strip theory. Giesing *et al.*[206] suggested using pre-multiplication of the AIC matrix by a diagonal matrix to match the experimental data. Pitt and Goodman[207] suggested using pre-and post multiplication of the AIC matrix. Jadic *et al.*[209] proposed using a full matrix to substitute the diagonal correction matrix. Brink-Spalink and Bruns[210] used an optimization scheme to minimize the error of the correction matrix.

Another technique to extent the applicability of the linear aerodynamic theory is by performing the correction to the pressure difference ΔC_p. Dau and Garner[211] proposed the correction factor based on an assumption that the ratio of the unsteady velocity potential of the transonic and subsonic flow is insensitive to the variation of the reduced frequency k. Therefore, the unsteady transonic velocity potential can be approximated as:

$$\varphi(k)\Big|_{transonic} \approx \left(\frac{\varphi(k)}{\varphi(k=0)}\right)\Bigg|_{subsonic} * \varphi(k=0)\ \Big|_{transonic} \tag{4.130}$$

where $\varphi\ (k=0)_{transonic}$ is the velocity potential for a steady transonic flow.

Luber and Schmid[212] introduced two correction factor techniques that are applied directly to the pressure difference as follows:

Multiplicative correction:

$$\Delta C_p(k)\Big|_{transonic} \approx \left(\frac{\Delta C_p(k)}{\Delta C_p(k=0)}\right)\Bigg|_{subsonic} * \Delta C_p(k=0)\ \Big|_{transonic} \tag{4.131}$$

Additive Correction:

$$\Delta C_p(k)\Big|_{transonic} \approx \Delta C_p(k)\Big|_{subsonic} + \left(\Delta C_p(k=0)\Big|_{subsonic} - \Delta C_p(k=0)\Big|_{subsonic}\right)^* \alpha(k)\Big|_{mode\,i} \tag{4.132}$$

where α is the local angle of attack of each mode.

Chen *et al.*[213] developed another procedure called ZTAIC (ZONA transonic AIC) method that has been successfully applied in an MDO software, such as ASTROS[167]. The correction factor in ZTAIC was derived based on the time-linearized TSD equation.

Another correction technique derived based on the time-linearized TSD was proposed by Lu and Voss for a planar wing[215]. Extension of their method to non-planar configurations and complete aircraft configuration was reported recently in Ref. 201. The method uses the DLM of Rodden to calculate the AIC in subsonic flow. The AIC for subsonic and transonic flow is calculated as follows:

Subsonic : $$[\,AIC\,] = [\,A\,] \tag{4.133}$$

Transonic : $$[\,AIC\,] = [A + B\,(I-D)^{-1}\,C\,] \tag{4.134}$$

where A,B,C and D are derived based on the following kernel function formulation:

$$\begin{aligned} w &= \frac{1}{8\pi}\iint_S \Delta C_p K_A\, dS + \beta e^{i\varepsilon x}\iiint_V \sigma\left(G_{xy} - i\varepsilon G_y\right)dV \\ \varphi &= \frac{e^{i\varepsilon x}}{8\pi}\iint_S \Delta C_p K_B\, dS - \iiint_V \sigma\left(G_y - i\varepsilon G\right)dV \end{aligned} \tag{4.135}$$

where

$$G = \frac{e^{-i\lambda R}}{4\pi R}$$

$$\sigma = k\phi_x^0\left(\varphi_x + i\varepsilon\varphi\right) \tag{4.136}$$

$$\varepsilon = \frac{k M^2}{\beta^2} \; ; \; \lambda = \frac{k M}{\beta^2}$$

$$\varphi = \phi^1(x, y, z)\, e^{i\varepsilon x}$$

and other variables are defined in Eq. (4.12).

The kernel function formulation of Lu and Voss[215] is based on the time-linearized formulation of the velocity potential given as follows:

$$\phi(x, y, z, t) = \phi^0(x, y, z) + \text{Re}\left(\phi^1(x, y, z)\, e^{ikt}\right) \tag{4.137}$$

where ϕ^o is the steady velocity potential that can be obtained using experimental data or CFD method.

The kernel functions K_A and K_B appearing in Eq. (4.135) are similar to the subsonic kernel function given in Eqs. (4.11) and (4.13) as follows:

$$K_A = e^{-ikxo}\left(\frac{M}{R X_1} e^{ikx} + \int_{-X/r}^{\infty} \frac{e^{iku}}{\left(r^2 + u^2\right)^{3/2}}\, du\right) \tag{4.138}$$

$$K_B = e^{-ikxo}\left(\frac{M z}{R X_1} e^{ikx} + z \int_{-X/r}^{\infty} \frac{e^{iku}}{\left(r^2 + u^2\right)^{3/2}}\, du\right) \tag{4.139}$$

where the improper cylindrical function occurring in Eqs. (4.138) and (4.139) was solved in Ref. 215 based on the original DLM of Rodden. Similar to the improvement of the subsonic DLM described in Sections 4.3 – 4.7, the present treatment for the improper cylindrical function can be used to improve the transonic DLM, *i.e.* by separating the singular and regular parts of the kernel function, integrating analytically the singular part and integrating the regular part using Gauss-Legendre quadrature. To reduce the

computational time of the transonic DLM, however, a further study is needed to simplify numerical evaluation of the integral operators C and D given in Eqs. (4.134) and (4.135).

Chapter 5
Effect of Compressive Force on Strut-Braced Wing Aeroelastic Analysis

5.1 Introduction

Classical wing aeroelastic analysis usually deals with the interaction between structural stiffness, structural (and non-structural) inertia and aerodynamic load. The effect of compressive force on wing stiffness is usually ignored in the flutter analysis since, for a conventional wing, the compressive force is relatively small. The aerodynamic load during cruise flight may not induce a compressive force for a wing having a positive dihedral angle. Even for an anhedral wing, the compressive force is small since the upward wing bending deflection during the cruise flight reduces the negative dihedral angle.

For the strut braced wing (SBW) aircraft design, however, the compressive force may have a significant influence on the flutter analysis due to the unconventional nature of the wing as described in Chapter 2. Previous investigations [19] of a strut-braced wing aircraft show that at high positive load factors, a large tensile force in the strut leads to a considerable compressive axial force in the inner wing, resulting in a reduced bending stiffness and even

buckling of the wing. Studying the influence of this compressive force on the structural response of the strut-braced wing is thus of paramount importance.

In the present chapter the effect of the compressive force on the flutter speed of the strut braced wing is investigated. All of the structural finite element and aerodynamic lifting surface formulations described in the last chapters are implemented in the present chapter to solve the flutter problem. In addition, a theoretical derivation of the K method for the flutter solution is described in the second section of this chapter. The K-method adopted in the present work is based on the work developed by ZONA Technology in Refs. 171 and 172. The unsteady aerodynamics is based on the present doublet lattice method described in Chapter 4. Validation of the present flutter procedure is presented in the last part of the second section.

In order to take into account the compressive force effect, the third section focuses on the procedure to modify the flutter equation of the K method by including the additional term related to the compressive force. A schematic procedure is presented that relates all of the structural and aerodynamic codes needed to solve the flutter problem.

In the fourth section, a trim analysis procedure of the strut-braced wing is described. This section is important to predict the internal compressive force. The trim analysis is performed as an iterative process since the equilibrium equation is non linear due to the presence of the compressive force.

In the fifth section, the natural frequencies and mode shape of the strut braced wing is calculated by including the compressive force calculated in the fourth section. Finally, in the last two sections of the present chapter, the flutter analysis for the final design of the strut braced wing and its sensitivity with respect to several parameters are presented.

5.2 The Flutter K-Method

5.2.1 Theoretical Background

Aeroelasticity has been known as a mutual interaction of inertial and elastic structural forces and aerodynamic forces. The aerodynamic forces can be in the form of self-excited aerodynamic forces induced by structural deformation, or in the form of external disturbance forces. In terms of a discrete system, the equation of motion of the aeroelastic system can be derived based on the equilibrium condition of the aforementioned forces, i.e.:

$$\mathbf{M}\,\ddot{x}(t) + \mathbf{K}\,x(t) - \mathbf{F_a}(x) = \mathbf{F_e}(t) \tag{5.1}$$

where $\mathbf{M}$ and $\mathbf{K}$ are the mass and stiffness matrices respectively, and $\mathbf{F_a}$ and $\mathbf{F_e}$ are the self-excited and external aerodynamic forces respectively. In the present work the mass and stiffness matrices are generated by the structural finite element method as described in Chapter 3, and the self excited aerodynamic force is generated by the lifting surface method as described in Chapter 4. The external aerodynamic force, such as the aerodynamic gust load, is usually provided.

For the aeroelastic stability problem, such as flutter and divergence, the right hand side of Eq. (5.1) is set to zero to give:

$$\mathbf{M}\,\ddot{x}(t) + \mathbf{K}\,x(t) - \mathbf{F_a}(x) = 0 \tag{5.2}$$

If the self-excited aerodynamic force is a nonlinear function of the structural deformation x(t), the growth or the decay of the structural response can be predicted by a time-marching procedure. This time-marching approach requires a nonlinear time-domain unsteady aerodynamics prediction usually generated using the computational fluid dynamics (CFD) method. This approach is computationally expensive, and therefore is not widely used as a flutter analysis tool in industry.

The most widely used approach to solve the flutter problem is to recast Eq. (5.2) into a set of linear systems and solve the (complex) eigenvalue problem. This approach is based on the assumption that the aerodynamics response varies linearly with respect to amplitude of the structural deformation provided the amplitude is sufficiently small. In this approach, the aerodynamic function is related to the structural deformation by means of the convolution integral:

$$\mathbf{F_a}(x) = \int_0^t q_\infty \; \boldsymbol{H}\left(\frac{V}{L}(t-\tau)\right) x(\tau)\, d\tau \tag{5.3}$$

where

$q_\infty \; \boldsymbol{H}\left(\frac{V}{L}(t-\tau)\right)$ = the aerodynamic transfer function

and V and L are the velocity of undisturbed flow and the reference length, respectively. The Laplace domain counterpart of Eq. (5.3) is simply:

$$\mathbf{F}\left(x(s)\right) = q_\infty \, \mathbf{H}\left(\frac{sL}{V}\right) x(s) \tag{5.4}$$

where $\mathbf{H}$ is the Laplace domain counterpart of $\boldsymbol{H}$.

Based on Eqs. (5.3) and (5.4), the Laplace domain counterpart of Eq. (5.2) can be written as:

$$\left[s^2 \mathbf{M} + \mathbf{K} - q_\infty \, \mathbf{H}\left(\frac{sL}{V}\right)\right] x(s) = 0 \tag{5.5}$$

Equation (5.5) is usually not solved directly since the size of the mass and stiffness matrices of the aircraft model are very large. Instead one uses the so called modal approach where the structural deformation x is transformed to the generalized coordinate q based on the following relation:

$$x = \Phi\, q \tag{5.6}$$

where Φ is the modal matrix whose columns contains the lower order natural modes. The rationale of the modal approach is based on the premises that the critical flutter modes are usually due to the coupling of lower order structural modes. Normally, no more than ten numbers of the lowest natural modes are sufficient for the flutter analysis of a wing structure.

Substituting Eq. (5.6) into Eq. (5.5) and pre-multiplying the result with Φ^T yield the following flutter equation in Laplace domain:

$$\left[s^2 \boldsymbol{M} + \boldsymbol{K} - q_\infty \boldsymbol{A}\left(\frac{s\,L}{V}\right)\right] q = 0 \tag{5.7}$$

where

$\boldsymbol{M} = \Phi^T \mathbf{M} \Phi$ = generalized mass matrix

$\boldsymbol{K} = \Phi^T \mathbf{K} \Phi$ = generalized stiffness matrix

$\boldsymbol{A} = \Phi^T \mathbf{H} \Phi$ = generalized aerodynamic force matrix

A common approach to solve the flutter equation is to further reduce the transient motion in Laplace domain in Eq. (5.7) to a simple harmonic equation in frequency domain by simply replacing the parameter s by $i\omega$ to give the following flutter equation in frequency domain:

$$\left[-\omega^2 \boldsymbol{M} + \boldsymbol{K} - q_\infty \boldsymbol{A}(ik)\right] q = 0 \tag{5.8}$$

where

ω = harmonic oscillatory frequency

$k = \dfrac{\omega L}{V}$ = reduced frequency

In the present work, the so-called K method is used to solve the flutter problem. In this method, an artificial structural damping g is added to Eq. (5.8) as a tool to measure the stability of the flutter equation[170]. By setting the complex structural damping $i\,g$ to be proportional to the stiffness matrix, the flutter equation in the K-method can be written as:

$$\left[-\omega^2 \boldsymbol{M} + (1+i\,g)\,\boldsymbol{K} - q_\infty \boldsymbol{A}(ik) \right] q = 0 \tag{5.9}$$

In the present work, the flutter analysis is performed to the wing and strut only, i.e. no rigid body modes are considered. In this case Eq. (5.9) can be simplified as follows:

$$\left[\boldsymbol{M}^* - \lambda \boldsymbol{K} \right] q = 0 \tag{5.10}$$

where

$$\boldsymbol{M}^* = \boldsymbol{M} + \frac{\rho}{2}\left(\frac{L}{k}\right)^2 \boldsymbol{A}(ik) \tag{5.11}$$

$$\lambda = \frac{1 + i\,g}{\omega^2} \tag{5.12}$$

Equation (5.10) is solved as an eigenvalue problem for a series of values for parameters k and r. Since $\boldsymbol{M}^*$ is a general complex matrix, the eigenvalues λ are also complex numbers. For n structural modes, there are n eigenvalues corresponding to n modes at each k. The air speed, frequency and structural damping are recovered from the eigenvalue λ as follows:

$$f = \frac{1}{2\pi\sqrt{\mathrm{Re}\,(\lambda)}} \tag{5.13a}$$

$$V = \frac{\omega_f L}{k} \tag{5.13b}$$

$$g = \omega_f^2 \, \mathrm{Im}(\lambda) \tag{5.13c}$$

To evaluate the flutter speed the so-called *V–g* and *V-f* diagrams are constructed. The V-g diagram is the plot of structural damping vs velocity, and the V-f diagram is the plot of frequency vs velocity. The flutter critical speeds is obtained from the *V-g* plot as the lowest velocity *V* at which the *g* curve crosses the *V* axis from negative structural damping *g* (stable region) to positive *g* (unstable region), i.e when $g = 0$.

5.2.2 Validation of the present flutter procedure

In the present work, the K-method procedure described in Section 5.2.1 was performed by using the ZAERO code developed by ZONA Technology, Inc[171]. The unsteady aerodynamics used to generate the generalized matrix ***A*** is calculated based on the present doublet lattice method described in Chapter 4. To validate the present procedure, a flutter calculation was performed to the so-called AGARD Standard 445.6 wing (Figure 5.2) at Mach numbers 0.678, 0.9 and 0.95 with four structural modes and 15 sets of A(*ik*) ranging from $k = 0.05$ to $k=0.2$. The number of aerodynamic panels used in the present method in the spanwise and the chordwise directions are 20 and 10 respectively.

The *V-g* and *V-f* plots for Mach number 0.90 are presented in Fig. 5.2a and 5.2b respectively. The plots indicate that the flutter speed occurs at $V_f = 938.1$ fps and frequency 16.273 Hz. This predicted flutter speed is slightly lower than the onset flutter speed predicted by the transonic wind tunnel at $V_f = 973.4$ fps and frequency 16.09 Hz. Comparison with other methods are shown in Table 5.2.

For Mach number 0.678 the flutter speed is, as expected, close to the wind tunnel test since the influence of the transonic flow non-linearity is small. However, the flutter frequency calculated by the present procedure is considerably higher than the wind tunnel

result. This difference may be attributed to the inaccuracy in the structural model since other numerical prediction methods also give a higher prediction for the flutter frequency.

For Mach number 0.95, where the nonlinear transonic flow effect is very strong, the present procedure fails to predict an accurate result. This is due to the limitation of the present linear unsteady aerodynamic method where the transonic shock and viscous effects are not included in the formulation. The result of the linear method for this Mach number is undesirable since it is not conservative, i.e. gives a higher flutter prediction.

Table 5.1. Comparison of flutter speed and frequency
of the AGARD 445.6 flexible wing

Method	**Case 1** **Mach 0.678** ρ = 0.000404 slug/ft3		**Case 2** **Mach 0.90** ρ = 0.000193 slug/ft3		**Case 3** **Mach 0.95** ρ = 0.000123 slug/ft3	
	V_f (fps)	f (Hz)	V_f (fps)	f (Hz)	V_f (fps)	f (Hz)
Wind Tunnel Test	759.1	17.98	973.4	16.09	1008.4	14.50
Present DLM (Linear)*)	758.0	19.98	938.1	16.27	1158.2	15.79
ZONA6 (Linear)[172]	766	19.81	984	16.31	1192	16.18
ZTAIC (Nonlinear)[172]	761	19.30	965.2	16.38	944.0	13.46
CAPTSD (Nonlinear)[172]	768	19.2	952	15.8	956	12.8

*) The unsteady aerodynamics is calculated based on the present DLM method. The flutter K method used is based on the code developed by ZONA Tech.

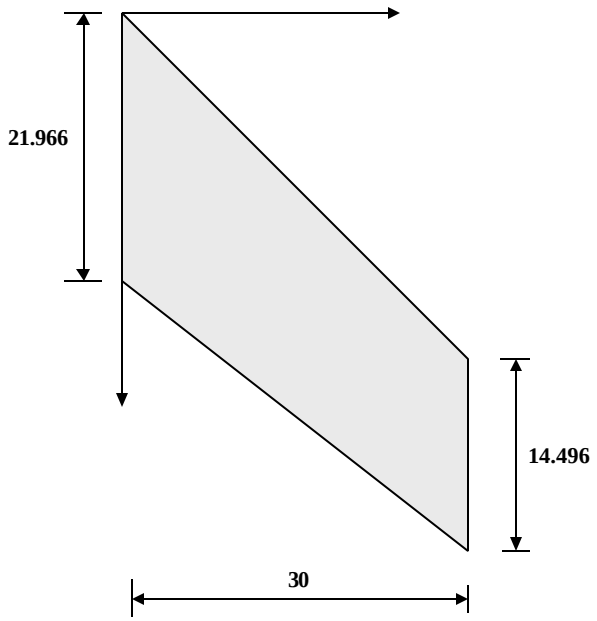


Figure 5.1. The AGARD Standard 445.6 wing planform

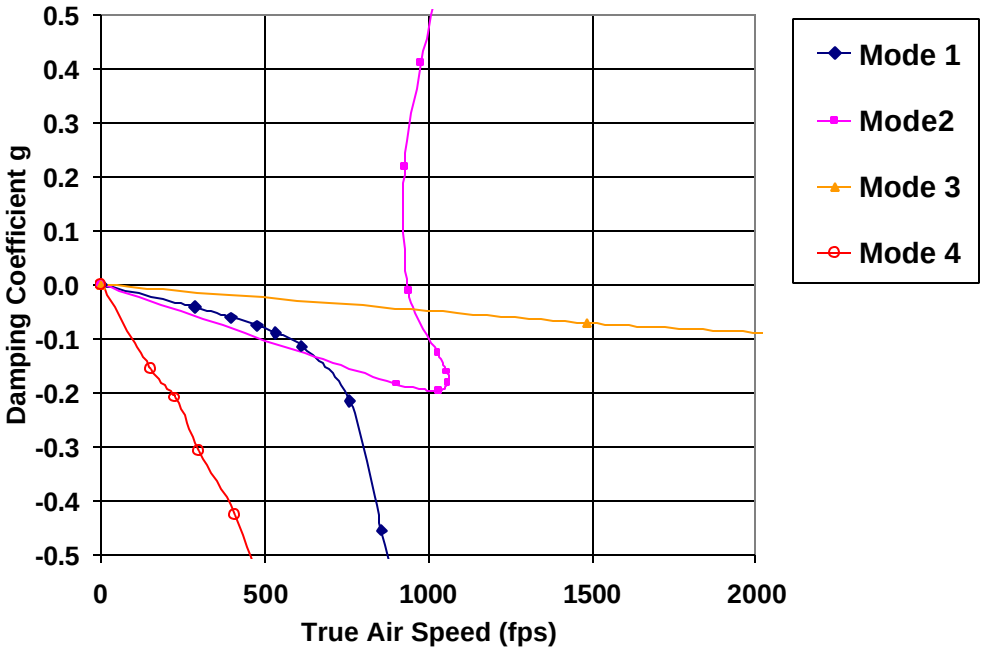


Figure 5.2. The *V-g* plot of the AGARD 445.6 wing at M = 0.90

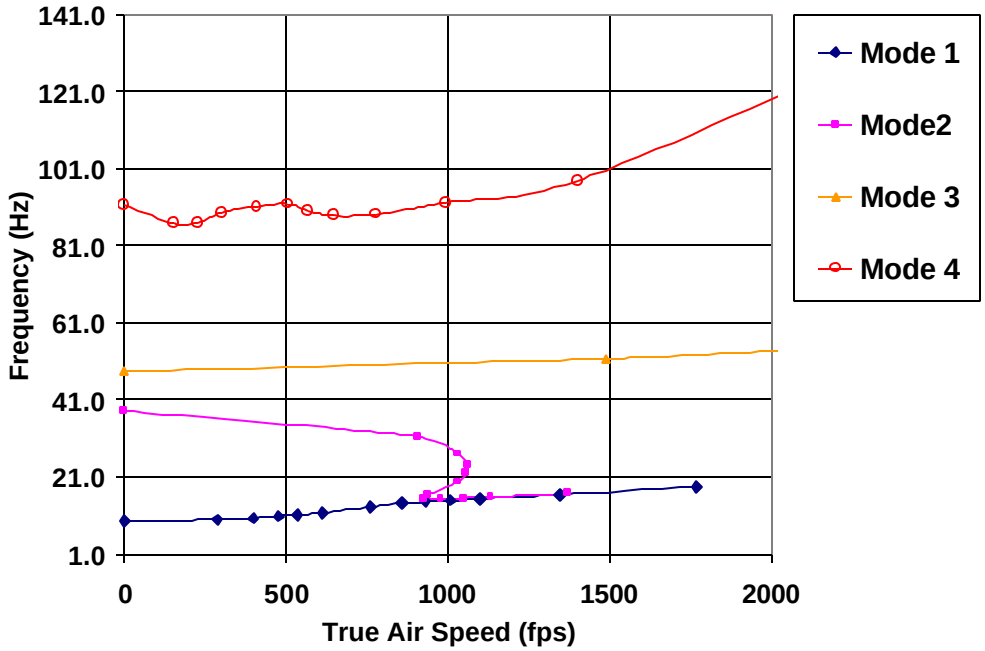


Figure 5.3. The *V-f* plots of the AGARD 445.6 wing at M = 0.90

5.3 The Compressive Force Effect

It has been introduced in Section 5.1. that the effect of compressive force on the strut braced wing stiffness is larger than that of the conventional wing due to the presence of the strut support. To consider the effect of the compressive force, a slight modification of the flutter K-method is suggested in the present work by rewriting Eq. (5.10) as follows:

$$\left[\boldsymbol{M}^{*} - \lambda \boldsymbol{K}^{*} \right] q = 0 \tag{5.14}$$

where the modified stiffness matrix $\boldsymbol{K}^{*}$ is

$$\boldsymbol{K}^{*} = \boldsymbol{K} - \boldsymbol{P}\, \boldsymbol{K}_{g} \tag{5.15}$$

and $\boldsymbol{K_g}$ and $\boldsymbol{P}$ are the geometric stiffness matrix and the internal force and moment of the structure, respectively. For the present flutter calculation, the internal force $\boldsymbol{P}$ is calculated from the force equilibrium of the wing-strut structure at 1.0 g cruise flight condition. This internal force P is used also in the calculation of the natural frequencies and mode shapes of the wing-strut structure.

Therefore, the flutter speed procedure adopted in the present work is as follow:

1. Find the wing and strut stiffness and mass distribution by using *ehexa.f* code described in Chapter 2. The input data necessary for the code is the wing thickness distribution given by the *wing.f* of the double plate model described in detail in Ref. 12..
2. Perform a trim analysis of the strut-braced wing at 1.0 g cruise flight condition to obtain the internal force $\boldsymbol{P}$. The wing flexibility and aerodynamic load redistribution is taken into account in the analysis. The strut slack mechanism is also considered in the analysis, i.e. the strut starts to engage when the load factor n_s = 0.8 g in the present case.
3. Perform a modal analysis of the strut braced wing by including the effect of the compressive force.
4. Calculate the generalized unsteady aerodynamics force based on the present doublet lattice method. The mode shapes to generalize the aerodynamic matrix are taken from the result of Step 2.
5. Calculate the flutter speed using the K-method. The stiffness matrix is modified by including the compressive force effect. The generalized mass and aerodynamic force matrices are taken from Steps 2 and 3 that has already taken into account the effect of the compressive force.

Figure 5.4 shows the flow chart of the present flutter analysis procedure. A more detailed description of Steps 1 and 2 are given in the next two sections.

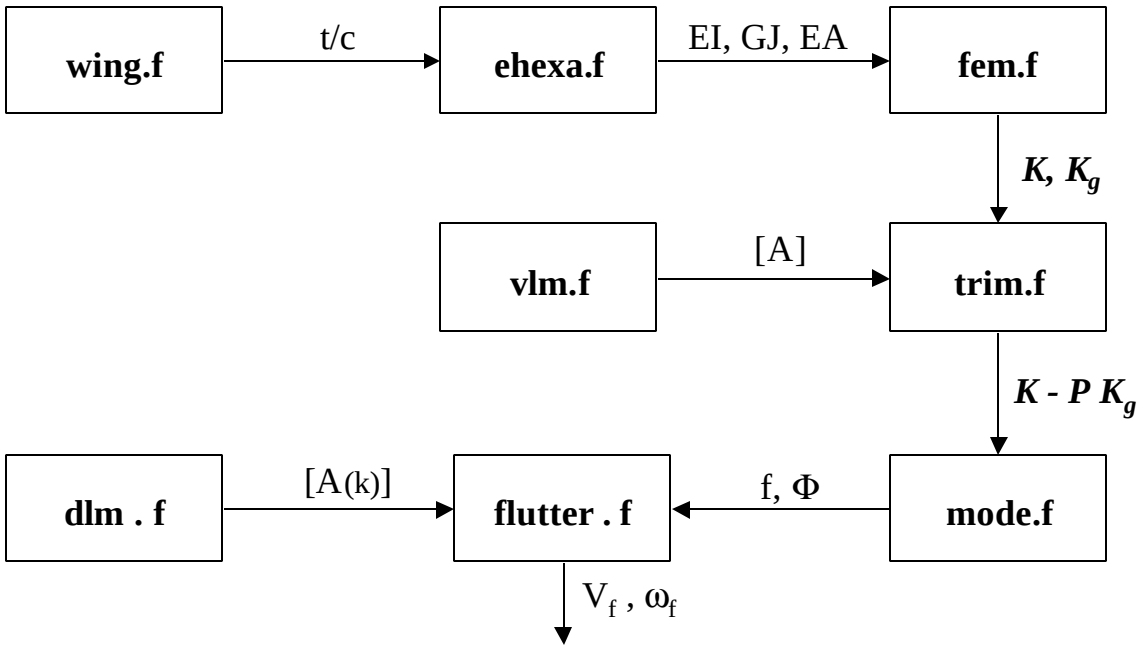


Figure 5.4. Flowchart for the flutter analysis of the strut braced wing

5.4 Trim Analysis Of The Strut Braced Wing

The present trim analysis procedure is applied to the strut-braced wing aircraft with fuselage-mounted engine. The aircraft configuration is obtained from an MDO code developed at Virginia Tech described in Refs. 9 and 10. The MDO code includes influence from several fields including aerodynamics, structures, performance, weights, and stability and control. The aircraft take-off gross weight TOGW is minimized with the design optimization package DOT.[174] For the present strut-braced wing aircraft optimization, 19 design variables of the aircraft parameters including the location of the wing-strut junction y_s

and strut force load P_s (Figs. 2.2 and 2.3) are used. The aircraft configuration data after final MDO design are summarized in Table 5.2

Table 5.2. Strut-braced wing aircraft parameters

Wing half-span	108.44 ft
Wing - strut junction point	74.52 ft
Wing sweep (3/4 chord)	25.98°
Strut sweep (3/4 chord)	19.01°
Strut offset length	2.74 ft
Wing root chord	32.31 ft
Wing tip chord	6.77 ft
Strut force at 1 g load	215 387 lb
Strut chord (constant)	6.62 ft
Wing root t/c	13.75%
Wing tip t/c	6.44%
Strut t/c	8.0%
Fuselage diameter	20.33 ft
Wing flap area	1411.02 ft^2
Wing reference area	4237.30 ft^2
Take-off gross weight	504833 lb

For calculating the wing weight in the SBW optimization, a hexagonal wing-box model representing the wing sections parameters including wing skin, spar caps, spar webs and stringer is used (Fig. 2.4). This model is provided by Lockheed Martin Aeronautical Systems (LMAS) in Marietta, Georgia.[22] Based upon LMAS experience in wing sizing, the wing-box geometry varies in the spanwise direction with optimized area and thickness ratios

for each of the wing section parameters. The bending and torsional stiffness of each wing section computed based on this model is used further for flexible wing aeroelastic stability analysis.

Several load cases are used to determine the SBW wing structural weight in the optimization including *2.5 g* pull-up maneuver, *-1.0 g* pushover and *–2.0 g* taxi bump. To avoid strut buckling, a telescoping sleeve mechanism proposed by Virginia Tech for the SBW design disengages strut during the negative-*g* maneuvers. For a positive-*g* maneuver the strut first engages in tension at some positive load factor n_g by providing a slack in the wing-strut mechanism. If we define a slack load factor (SLF) as the load factor at which the strut initially engages, the wing performs as a cantilever beam for n_g < SLF and performs as a strut-braced beam for n_g > SLF. To prevent the strut from engaging and disengaging during cruise due to gust loads, the slack load factor used in the present SBW configuration is set to 0.8 during the optimization.

If the wing deformation and aerodynamic load redistribution are used to investigate passive load alleviation due to aeroelastic effects, the present procedure includes additional terms related to aerodynamic loading in the governing equation as follows:

$$\left[K - P(x)\,K_g\right]\{x\} + q\,[A]\,\{x\} \;=\; \{0\} \tag{5.16}$$

where A is aerodynamic influence coefficient (AIC) matrix. In the present case, AIC is calculated based on the vortex lattice method (VLM). A more detailed description of the VLM procedure is described in Chapter 4.

Equation (5.16) shows that the axial force P is a function of the deformation x since the wing-strut structure is statically indeterminate. However, the axial force is related also to the wing-strut mechanism adopted in the present work. For a negative-*g* maneuver the strut is disengaged to avoid strut buckling. For a positive-*g* maneuver the strut would first engage at a load factor n_g equals to the slack load factor, SLF, by providing a slack in the wing-strut mechanism. Therefore two different structure configurations should be considered in order to accurately calculate the wing deformation. The first configuration is the wing when the

strut is disengaged for n_g < SLF where in this case P = 0 in Eq. (5.16). The second configuration is the wing when the strut is engaged for n_g > SLF where the geometric stiffness of the wing and strut is used in the calculation. The stress-strain relationship for the strut material is therefore idealized as shown in Fig. 5.5 where the strain ε_s is related to the condition n_g = SLF.

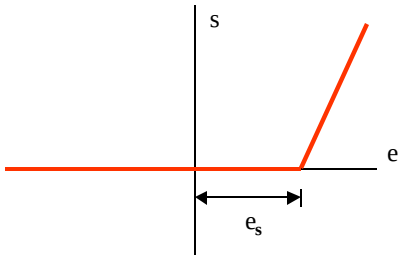


Figure 5.5. A bilinear stress-strain relationship of the strut for calculation of wing response under aerodynamic loading. The strain ε_s is related to the strut slack load factor.

Another important aspect related to the solution of Eq. (5.16) is the fact that the problem involves two different eigenvalues, namely the structural buckling load P and the aeroelastic divergence speed $q_{¥}$. To ensure the continuity from the first to the second configurations of the wing deformation described previously, Eq. (5.16) is solved as a boundary value problem, where P and $q_{¥}$ are updated for each iteration as shown schematically in Fig. 5.6. In the present work, $q_{¥}$ is given as the dynamic pressure related to the design cruise speed V_c, and the aircraft incidence is adjusted such that total lift is the same as the take-off gross weight (TOGW) of the aircraft for each iteration.

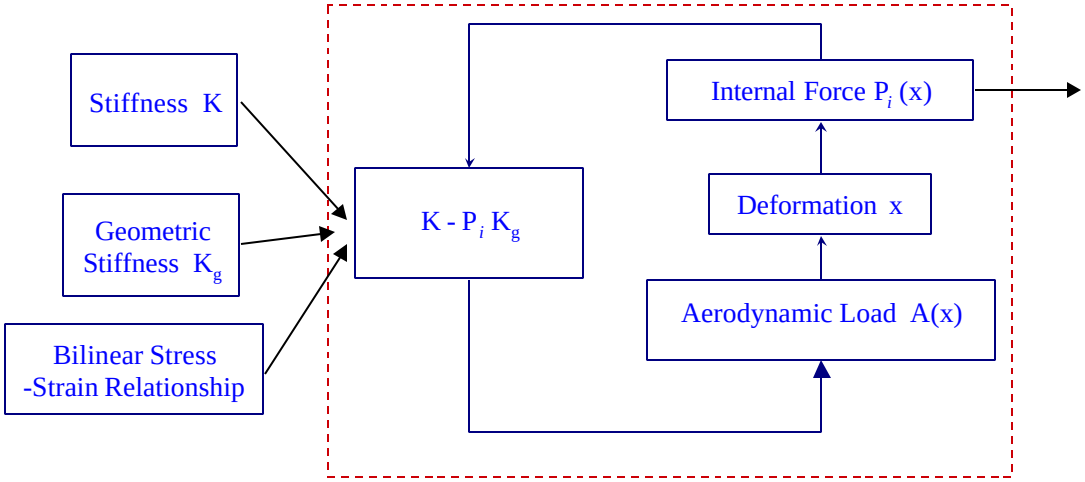


Figure 5.6. Flow chart for the trim analysis of the SBW wing under aerodynamic loads

5.5 Modal Analysis

Based on the present finite element code *mode.f*, a structural dynamic analysis was performed to calculate the natural frequencies and modes of the strut-braced wing. For all the cases considered in the present work, the connection between the fuselage and wing strut and between the fuselage and strut are assumed to be rigid, i.e there are no relative displacements and rotations at the wing-fuselage and strut-fuselage junctions. The free-vibration analysis was performed to the half wing model using the LAPACK eigen solver[169]. The natural frequencies and mode shapes for the first seven modes are presented in Table 5.3 and Fig. 5.7. Table 5.3 also shows comparison between the results of the detailed wing model used in Chapter 2 and the simplified wing beam model used in the present chapter. The results show that the frequencies of the simplified beam model are close to the associated

frequencies of the detailed model. This simplified beam model is used further in the present chapter for calculating the flutter speed.

Table 5.3.

Natural frequencies of the strut-braced wing

i	**Mode Shape**	**Simplified Wing Beam Model (Present Chapter) f (Hz)**	**Detailed Wing Model (Chapter 2) f (Hz)**
1	First vertical bending	2.233	2.332
2	Second vertical bending	3.073	2.971
3	First aft bending	3.720	3.742
4	Third vertical bending	4.784	4.371
5	Fourth vertical bending	6.656	6.765
6	Fith vertical bending	8.538	7.708
7	First torsion	9.170	9.091

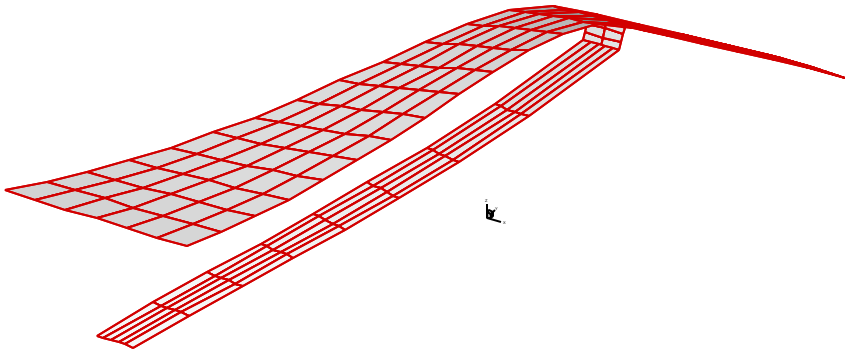


Fig 5.7a. Mode 1 (2.23 Hz)

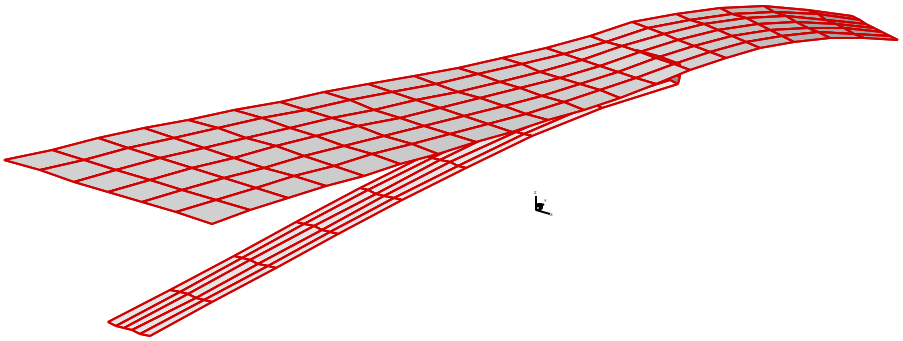


Fig 5.7b. Mode 2 (3.07 Hz)

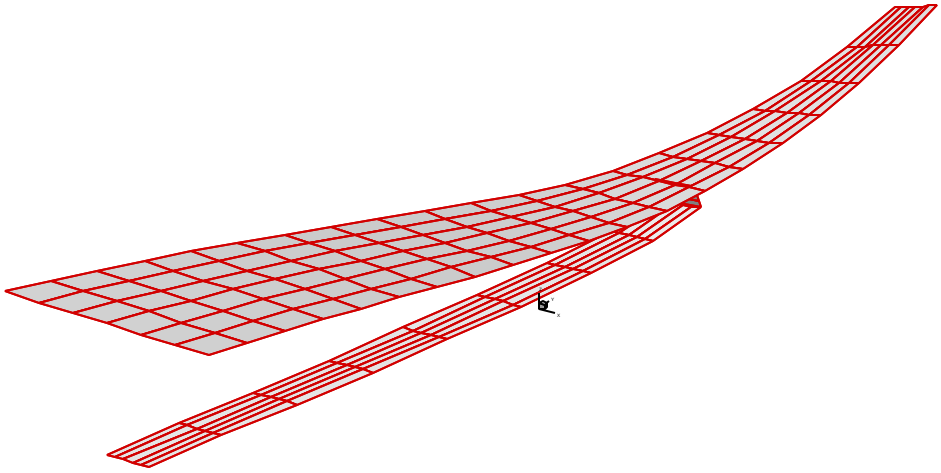


Fig 5.7c. Mode 3 (3.72 Hz)

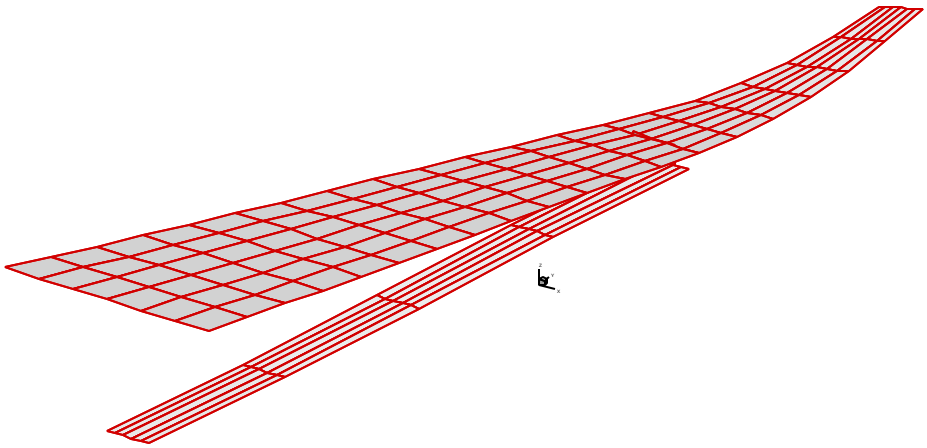


Fig 5.7d. Mode 4 (4.78 Hz)

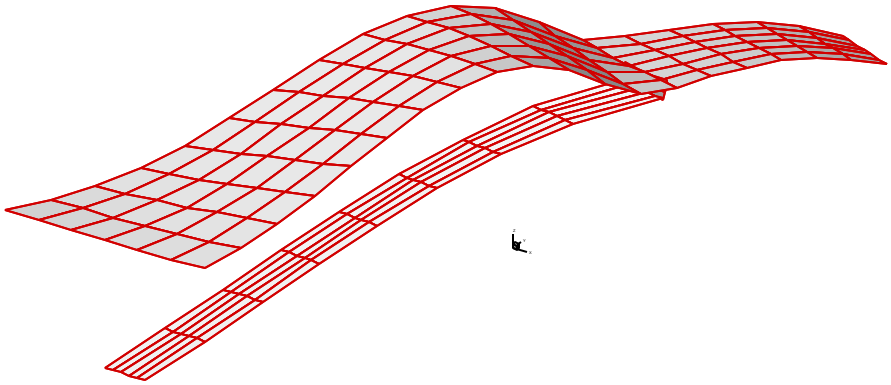


Fig 5.7e. Mode 5 (6.65 Hz)

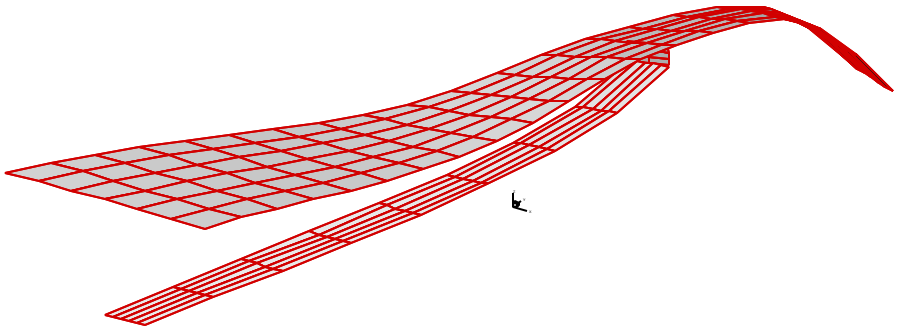


Fig 5.7f. Mode 6 (8.54 Hz)

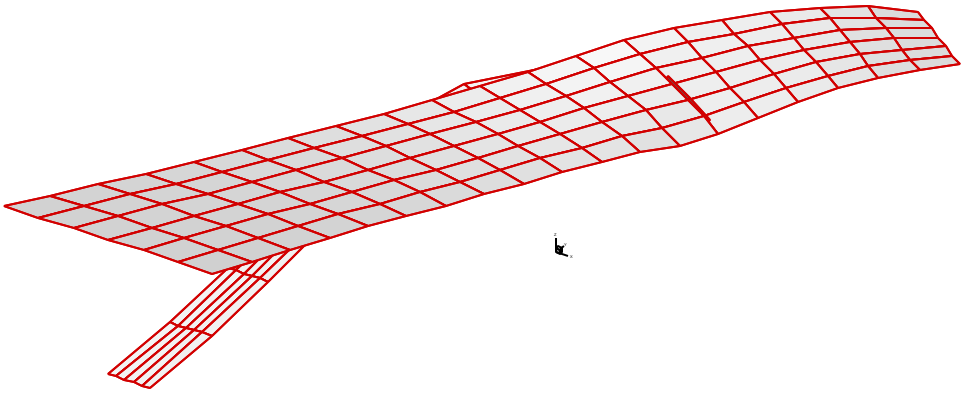


Fig 5.7g. Mode 7 (9.17 Hz)

5.6 Flutter Calculation at Reference Condition

In the present work, the flutter speed is calculated first for the reference condition, and then followed by the flutter calculation for a number of parameter variations including strut locations and flight altitudes. The reference condition for the present flutter calculation is defined as follows:

- The wing and strut structural data are based on the final iteration result of the MDO study
- The wing strut junction location is at y = 0.69 of the wing half span.
- The computations are performed for sea level condition.
- Zero fuel distribution in the wing.
- The compressive force effect is fully included.

In the present flutter analysis, all of the first ten vibration modes are used and the structural damping is assumed to be equal to 0%. The *V-g* and *V-f* plots of the flutter results for the reference condition are shown in Figure 5.8. The flutter speed is found at V_f = 843.6 fps with the flutter frequency of f = 3.859 Hz. No divergence speeds was found for the reference condition.

Comparison is also made to other methods as shown in Table 5.4. The first row is the present flutter speed and frequency for a simplified beam model using the present doublet lattice method. The second row is the results for the detailed wing-strut model with ZONA6 of ZAERO is used for the unsteady aerodynamic method and the g-method of ZAERO is used for the flutter solution. Note that the *g*-method is a generalized PK method which is more robust than the K-method. ZONA6 is derived based on a constant pressure method, which is more accurate than the doublet lattice method.[81] The constant pressure method uses an assumption that the acceleration potential is distributed with a constant strength on the surface of each element. The doublet lattice method uses a more restricted assumption, *i.e.* it assumes that the acceleration potential is lumped with a constant strength on a line of each element.[81]

The third row is the result for the detailed SBW model taken from Section 2.4. of the present work. It was calculated using the PK method of NASTRAN. No compressive force effect was included in the calculation for the detailed SBW model. Finally, the last row is the Lockheed Martin calculation result for their detailed SBW model which is slightly different than the present SBW model. Their wing final model has an anhedral angle. Their strut is rigidly connected to the fuselage and wing, *i.e.* no strut slack mechanism is used. Their offset beam is modeled as a curve beam. Comparing to these results, the present flutter procedure for the simplified beam model gives a conservative result, i.e. the lowest flutter speed among others. However, it will be shown in the next section that this flutter speed is still beyond the flight speed envelope of the strut-braced wing design.

Table 5.4. Comparison of the flutter speed and frequency of the strut braced wing

Method	Structure Model	Flutter Solver	Flutter Speed (fps)	Flutter frequency (Hz)
Present DLM	Beam model	K-method	834.6	3.859
ZONA6	Detailed model*	g-method	873.2	3.109
NASTRAN	Detailed model*	PK-method	902.0	3.93
LMAS	Detailed model*	N/A	1005	N/A

*) No compressive force effect

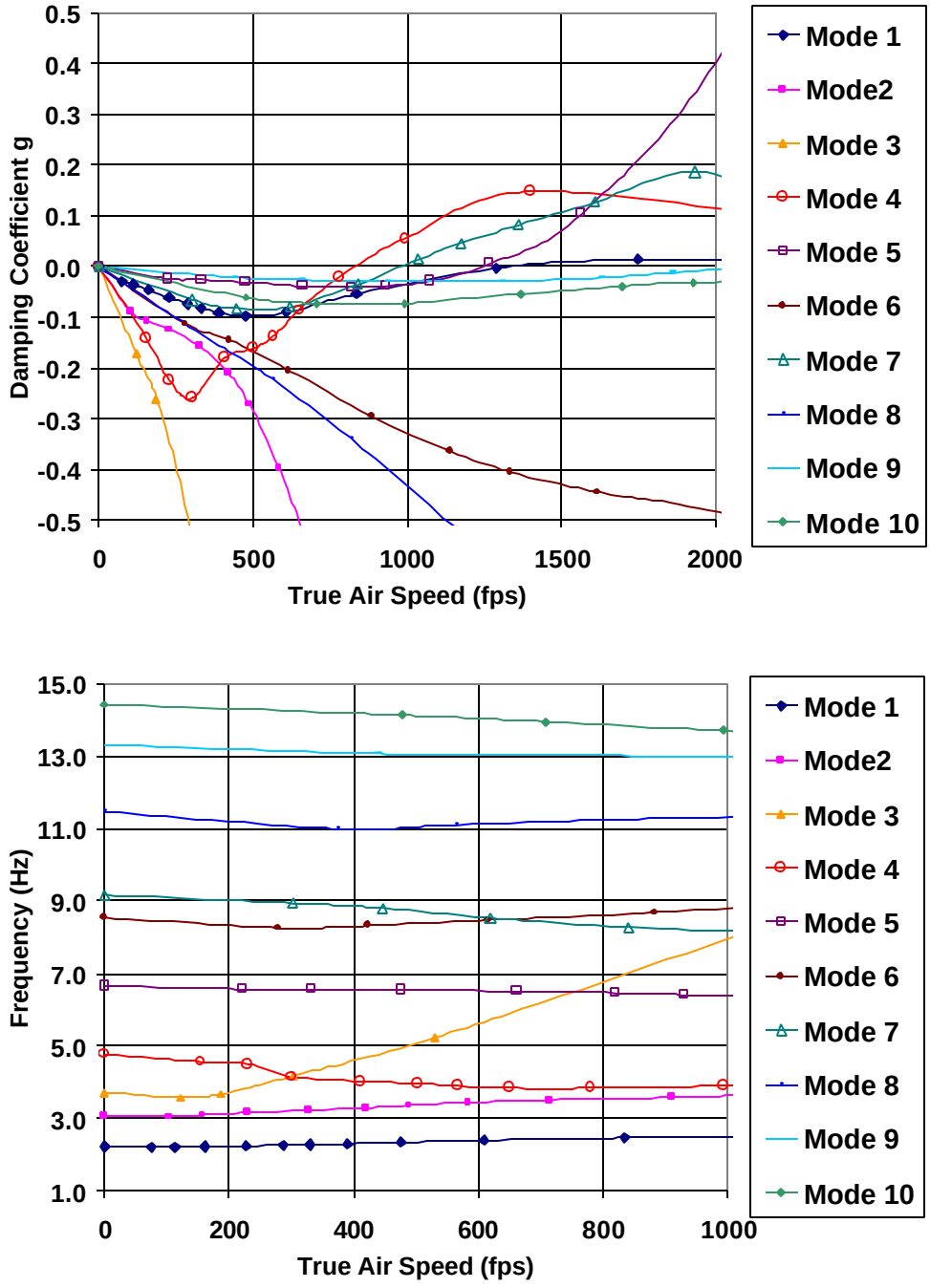


Figure 5.8. The *V-g* and *V-f* plots of the strut braced wing at the reference condition

5.7. Sensitivity Analysis

A sensitivity study was performed to study the behavior of the aeroelastic response near the reference condition described in the previous section. Variation of several parameters are selected including the changes of:

- spanwise position of the wing-strut junction
- offset beam length in the wing-strut junction
- altitude

It is assumed that the stiffness and dimension of the wing and strut are fixed at the reference condition as the aforementioned parameters are made to vary.

The first variation is to investigate the variation of the flutter speed if the wing-strut junction position changes along the spanwise direction. Two different flutter results for the strut braced wing are shown in Figure 5.9. The first result, shown in Fig. 5.9 by a line with triangular symbols, is for the strut braced wing but ignoring the compressive force effect, i.e. the wing strut is statically indeterminate but the stiffness matrix of the system is not modified by the $\boldsymbol{P}\,\boldsymbol{K_g}$ term. The second result, shown by a line with rectangular symbols, is for the same strut-braced wing but with the compressive effect included. Comparison between these two results are important to investigate the trend of the compressive force along the spanwise direction. Several conclusion that can be drawn from the results are as follow:

- The compressive force tends to give a lower flutter speed. Figure 5.9 shows that the second plot, the one with compressive effect, is almost always below the first plot.
- The influence of the compressive force is not significant if the wing-strut junction is near the wing root. Figure 5.9 shows that if the wing-strut location $\boldsymbol{y_s}$ is less than 0.3 than the two plots are identical, i.e. we can ignore the influence of the compressive force for this case.

- The influence of the compressive force is significant if the wing strut junction is placed near the wing tip. Figure 5.9 shows that for $y_s > 0.8$, the flutter speed of the second plot drops faster than the first plot.
- The flutter speed is reduced significantly when the wing-strut junction is moved toward the wing tip from $y_s = 0.5$ to 1.0. Note that, for the second plot, the flutter speed at $y_s = 1.0$ is almost one third of the flutter speed at $y_s = 0.5$. This trend is related to the decrease of the strut stiffness as its length increases. The strut cross sectional area and moment of inertia are kept constant in this sensitivity study.
- Note that the second plot has a dip near $y_s = 0.4$. The reduction of the flutter speed here is related to the switch of the flutter mode from the bending mode to the torsion mode.

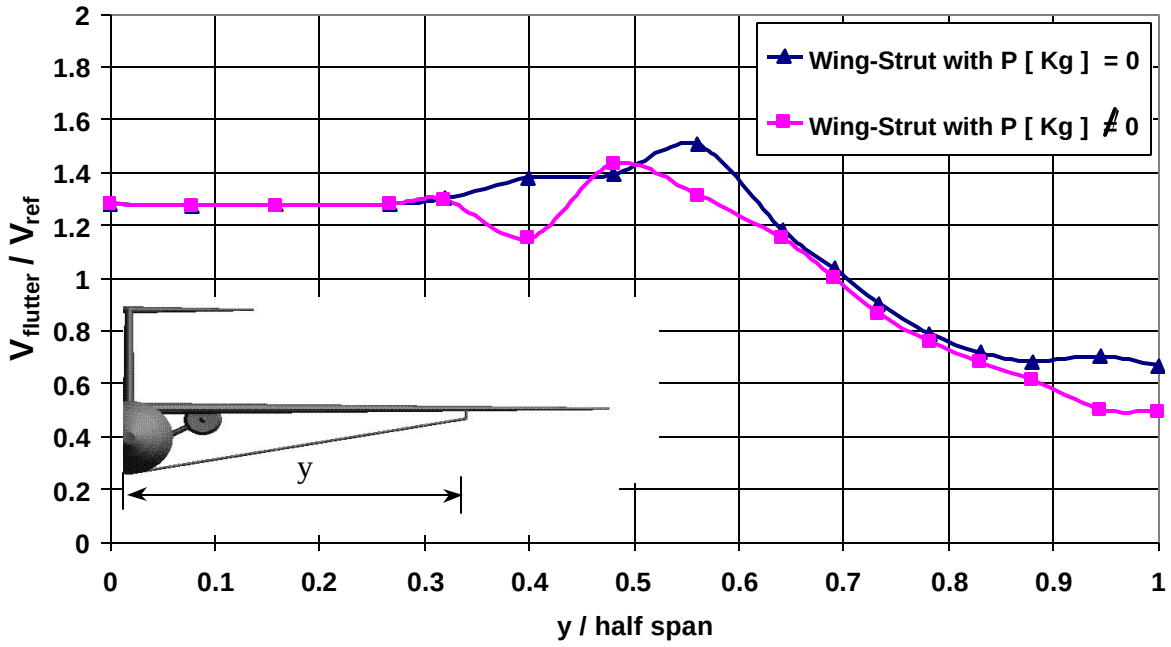


Figure 5.9. Flutter speed as a function of the spanwise position of the strut junction at the wing. V_{ref} = 834.6 fps.

The second sensitivity study is performed to investigate the variation of the flutter speed if the length of the offset beam changes. Figure 5.10 shows the results for three different spanwise location of the wing-strut junction, i.e at y_s = 0.56, 0.69 and 1.0. Figure 5.10 indicates that the flutter speed decreases as the length of the offset beam increases. This trend is the same for the three different spanwise locations of the wing strut junction. These results are expected since the increase of the offset beam length will reduce the wing-strut stiffness, and thus reduce the flutter speed. All of the calculations were performed by including the effect of the compressive force.

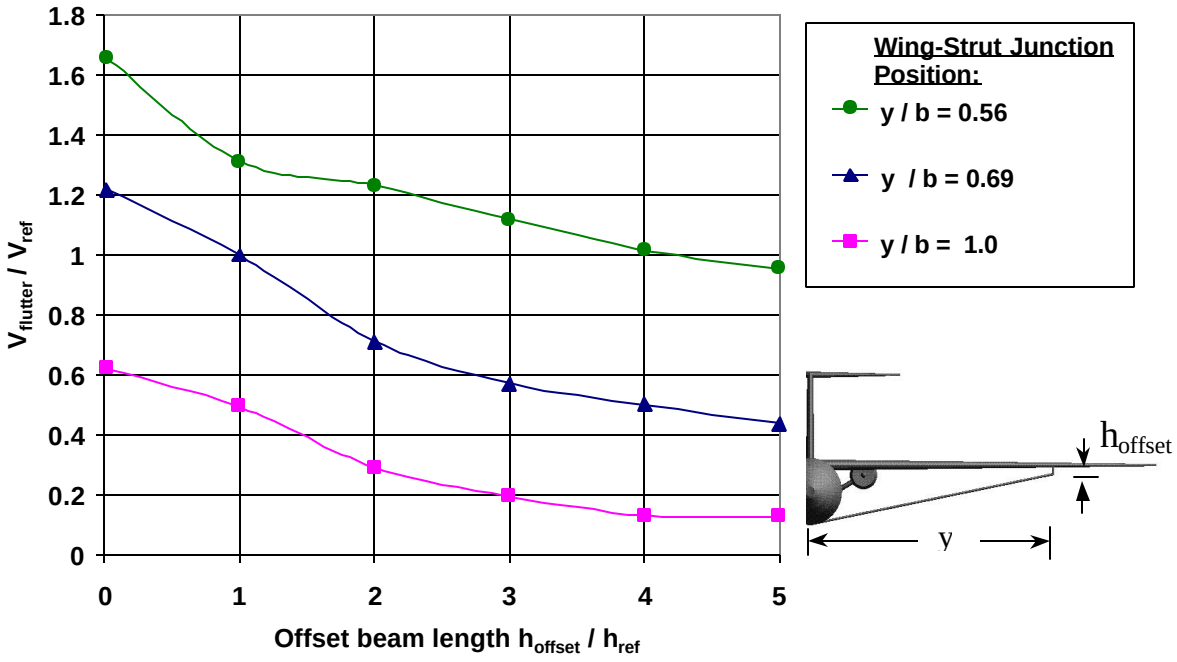


Figure 5.10. Flutter speed as function of the length of the offset beam at the wing-strut junction. V_{ref} = 834.6 fps.

Finally, the flutter speed was calculated for the wing with and without strut for every altitude. Related to the FAA regulation,[25] this condition is required to check the flutter speed of an aircraft not only for a nominal/healthy condition but also for a failure condition. The flutter speed for a nominal aircraft should be greater than 1.2 of $V_{D,}$ and for a failure condition should be greater than V_D, where V_D is a dive speed which is greater than the design cruise speed. A brief description of the aeroelastic stability envelope is given in Appendix B.

Figure 5.11 presents the results and comparison with the flight envelope. The wing without strut in the present case gives higher flutter speed than that of the wing with strut. The lower flutter speed for the wing with strut is related to the effect of the compressive force that reduces the stiffness of the inboard part of the wing. Aerodynamic interference between the strut and wing may also contribute to the reduction of the flutter speed. This trend is different than the flutter solution of the Keldysh problem given in Refs. 27 and 28 where the flutter speed for the wing with strut is higher than the wing without strut. In the Keldysh problem, the strut is assumed to have an infinite stiffness such that the wing does not move in lateral directions at the wing-strut junction location. The effect of the strut compressive force is also ignored in the Keldysh problem, *i.e.* the inner wing stiffness does not decrease. Therefore, the structural stiffness for the wing with strut in the Keldysh problem is stronger than the wing without strut, and thus the flutter speed is higher for the wing with strut than the wing without strut.

Figure 5.11 also shows that the present design of the strut-braced wing aircraft is free from flutter within its flight envelope. This important conclusion is in agreement with the finding by LMAS in Ref. 26. The strut braced wing aircraft version of LMAS is derived from the present configuration with a more refined aerodynamic and structural design of the wing. After performing a flutter analysis using a more detailed aircraft structure, LMAS concluded, in their final report to NASA-Langley, that their strut-braced wing is free from flutter.

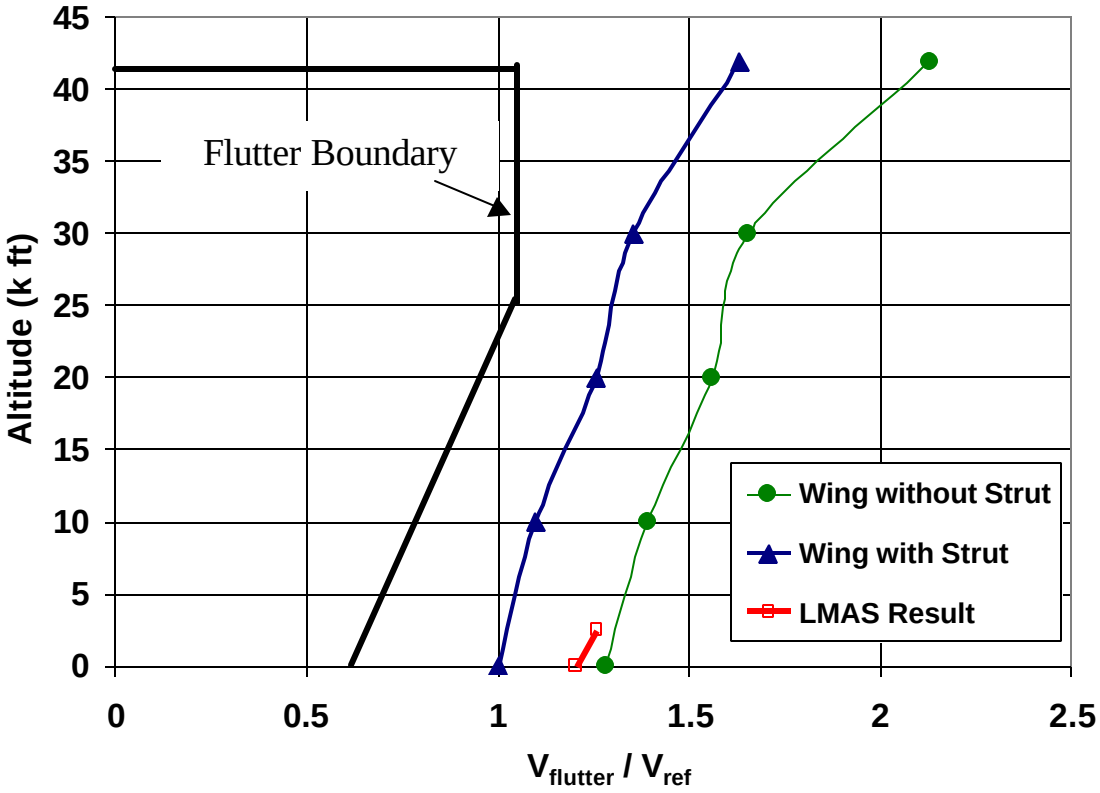


Figure 5.11. Flutter speed boundary of the strut braced wing. V_{ref} = 834.6 fps.

CHAPTER 6

Conclusions

The focus of the present work was to investigate the effect of compressive force on aeroelastic stability analysis of a strut-braced wing by using efficient structural finite element and aerodynamic lifting surface methods. The main goal is to develop an aeroelastic analysis code that is accurate but fast enough to be implemented as a tool in a multidisciplinary optimization environment.

A study to reduce the aeroelastic computational time has been conducted by reducing the number of elements of wing structure and aerodynamic models. To minimize the number of wing structural elements, an accurate finite element formulation for non-uniform beam is developed. For a static problem, the present formulation yields an exact stiffness matrix of the beam with arbitrary polynomial variation of the beam stiffness. For a buckling problem, a new procedure was introduced to improve the accuracy by using a quadratically convergent iteration technique. The results shows that the number of the beam element can be reduced significantly without degrading the accuracy.

To minimize the number of aerodynamic panel models, an efficient unsteady aerodynamic formulation for multiple lifting surfaces was developed. The present formulation improves the accuracy of existing lifting surface methods by implementing a more rigorous treatment of the aerodynamic kernel integration. The singularity of the kernel function is identified and isolated by implementing an exact expansion series to solve a modified cylindrical function problem. An exact integration is performed to the singular part

of the kernel. A Gaussian quadrature is used to integrate the regular part of the kernel that allows to increase the accuracy of the integration without changing the formulation scheme. A hybrid doublet lattice/doublet point scheme is devised to further reduce the total number of integration points by increasing the integration points near a rapid variation of the kernel function and reducing the integration points near a gradual variation of the kernel. Validation has been performed to a number of wing planforms and the results are in good agreements with those obtained using other methods.

In order to include the compressive force in the aeroelastic solution, a static aeroelastic analysis procedure was developed to calculate the internal forces and moment of the structural element during the 1.0 g cruise flight. The wing structural flexibility and the compressive force effect are considered in the analysis. The strut is allowed to deform following the bilinear stress-strain relationship to model the slack mechanism of the strut to engage and disengage during the vehicle maneuver, including the 2.5 g and – 1.0 g load maneuvers .

The flutter solution module combines all of the structural stiffness, inertia and geometric stiffness matrices, the aerodynamic influence coefficient matrix, and the internal compressive load data to perform aeroelastic stability analysis. The flutter K method is selected as the flutter solver since it is one of the fastest among other techniques. Validation of the procedure to a standard AGARD 445.6 wing at several Mach numbers shows that the results are in good agreement with those of wind tunnel test and other methods, except for Mach number near 1.0 where the nonlinear transonic flow effect should be taken into account.

The aeroelastic procedure above has been implemented to investigate the influence of the compressive force on the flutter speed of the strut-braced wing. The aircraft configuration selected is the strut-braced wing aircraft with fuselage-mounted engine with the technical data given in Table 5.1. Flutter analysis was performed to the final MDO design and parametric studies with respect to several design studies were conducted to study the effect of the compressive force. The flutter boundary was constructed based on the Federal

Aviation Regulation §25.629 and § 25.333. Several conclusions that can be drawn are as follows:

- *No* flutter occurs within the flight envelope of the present strut-braced wing configuration.
- The compressive force tends to decrease the flutter speed
- Flutter speed *reduces* as the following parameters changes:
  - The wing-strut junction position moves outward toward the wing tip
  - The wing strut junction position moves along chordwise direction from wing front spar to rear spar.
  - The length of the offset beam connecting the wing and strut increases
  - The flight altitude decreases
- The best location of the wing-strut junction is located between 50% - 80% of the wing half-span measured from the wing root. (Note that the location of the wing-strut junction of the present design is at 69%).
- The compressive force effect is significant to decrease the inner wing buckling capacity and the flutter speed if the wing-strut junction is placed near the wing tip.

CHAPTER 7

Future Work

Although this research represents the latest in a long line of work that has been performed in an effort to investigate the advantage and disadvantage of the strut-braced wing design, there is still much work to be done. Among topics that warrant further study in the area presented in this research are as follows:

- The aeroelastic procedure in the present work was developed in a modular form that can be applied to other wing designs by turning off the compressive force effect. However more work is needed to improve the efficiency of the eigen solver code. Currently, the eigen solver used is *dsbgv.f* of LAPACK where all eigenvalues of the generalized eigen problem are computed. On the other hand only a few eigenvalues are needed for the flutter analysis. In the present work, the order of the structural finite element equations are between 400 to 500, but, typically, only the first ten modes are needed for wing flutter analysis. One of possible best candidates to replace the current eigen solver is the sub-space iteration technique described in Ref. 195.
- Static and dynamic aeroelastic stability analysis were investigated in the present work, but no aeroelastic response analysis due to gust loads was performed. If the acceleration amplitude of the wind gust oscillates beyond 1.0 *g* load, than it would be necessary to include the geometrically non-linear analysis in the time domain aeroelastic simulation. The present formulation for the unsteady aerodynamic was derived in Laplace domain, therefore it is still suitable to be implemented for the transient type motion.

- The strut-braced wing configuration selected in the present work was the final design of the SBW fuselage-mounted engine. A similar aeroelastic procedure can be performed to other configurations including the SBW under-wing engine and the SBW tip-engine configurations.
- The present study was based on a linear unsteady aerodynamic theory that may not be accurate near sonic Mach number. Application of higher order aerodynamic prediction would be necessary to capture the so-called transonic dip effect in aeroelastic stability analysis.

References

1. Pfenninger, W., “Design Considerations of Large Subsonic Long Range Transport Airplanes with Low Drag Boundary Layer Suction,” Northrop Aircraft, Inc., Report NAI-54-800 (BLC-67), November 1954.
2. Jobe, C.E., Kulfan, R.M., and Vachal, J.D., “Wing Planforms for Large Military Transports,” AIAA-78-1470, 1978.
3. Kulfan, R.M., and Vachal, J.D., "Wing Planform Geometry Effects on Large Subsonic Military Transport Airplanes," Boeing Commercial Airplane Company, AFFDL-TR-78-16, February 1978.
4. Park, H. P., "The Effect on Block Fuel Consumption of a Strutted vs. Cantilever Wing for a Short Haul Transport Including Strut Aeroelastic Considerations," AIAA-78-1454-CP, Los Angeles, California, Aug. 21-23, 1978.
5. Turriziani, R.V., Lovell, W.A., Martin, G.L., Price, J.E., Swanson, E.E., and Washburn, G.F., "Preliminary Design Characteristics of a Subsonic Business Jet Concept Employing an Aspect Ratio 25 Strut Braced Wing," *NASA CR*-159361, October 1980.
6. Smith, P.M., DeYoung, J., Lovell, W.A., Price, J.E., and Washburn, G.F., “A Study of High-Altitude Manned Research Aircraft Employing Strut-Braced Wings of High-Aspect Ratio,” *NASA CR*-159262, February, 1981.
7. Grasmeyer, J.M., Naghshineh-Pour, A.H., Tetrault, P.A., Grossman, B., Haftka, R.T., Kapania, R.K., Mason, and W.H., Schetz, "Multidisciplinary Design Optimization of a

Strut-Braced Wing Aircraft with Tip-Mounted Engines," MAD Center Report 98-01-01, Virginia Tech, January 1998.

8. Grasmeyer, J.M., “Multidisciplinary Design Optimization of a Strut-Braced Wing Aircraft,” MS Thesis, Virginia Tech, April 1998.
9. Gern, F.H., Ko, A., Sulaeman, E., Gundlach, J.F., Kapania, R.K., and Haftka, R.T., “Multidisciplinary Design Optimization of a Transonic Commercial Transport with a Strut-Braced Wing,” *Journal of Aircraft*, Vol. 38, No. 6, 2001, pp. 1006-1014.
10. Gundlach, J.F., Gern, F.H., Tetrault, P, Naghshineh-Pour, A.H., Ko, A., Schetz, J.A., Mason, W.H., Grossman, B., Kapania, R.K., and Haftka, R.T., “Multidisciplinary Design Optimization of a Strut-Braced Wing Transonic Transport,” AIAA Paper 2000-0420, Jan. 2000.
11. Tretault, P.A., “Numerical Prediction of the Interference Drag of a streamlined Strut Intersecting a Surface in Transonic Flow,” Ph.D Dissertation, Virginia Tech, January 2000.
12. Tretault, P.A. , Schetz, J.A., and Grossman, B., “Numerical Prediction of Interference Drag of Strut-Surface Intersection in Transonic Flow,” *AIAA Journal*, Vol. 39, No. 5, May 2001, pp. 857-864.
13. Naghshineh-Pour, A.H.,” Structural Optimization and Design of a Strut-Braced Wing Aircraft,” MS Thesis, Virginia Tech, November 1998.
14. Grossman, B., Strauch, G.J., Eppard, W.M., Gurdal, Z., and Haftka, R.T., "Integrated Aerodynamic/Structural Design of a Sailplane Wing," AIAA-86-2623, Dayton, Ohio, October 20-22, 1986.
15. Giunta, A.A., Balabanov, V., Haim, D., Grossman, B., Mason, W.H., Watson, L.T., and Haftka, R.T., "Multidisciplinary Optimization of a Supersonic Transport Using Design of Experiments Theory and Response Surface Modeling," *The Aeronautical Journal*, pp. 347-356, October 1997.

16. Hutchison, M.G., Unger, E.R., Mason, W.H., Grossman, B., Haftka, R.T., "Variable Complexity Aerodynamic Optimization of a High Speed Civil Transport Wing," *Journal of Aircraft*, Vol. 31, No. 1, pp. 110-116, 1994.

17. Ko, Y.A.," The Role of Constraints and Vehicle Concepts in Transport Design: A Comparison of Cantilever and Strut-Braced Wing Airplane Concepts," MS Thesis, Virginia Tech, April 2000.

18. Ko, Y.A., Grossman, B., Mason, W.H., and Haftka, R.T., "The Role of Constraints in the MDO of a Cantilever and Strut-Braced Wing Transonic Commercial Transport Aircraft, AIAA Paper 2000-5609, SAE Paper 2000-01-5609, *World Aviation Conference*, San Diego, CA, Oct. 10-12, 2000.

19. Gern, F.H., Sulaeman, E., Naghshineh-Pour, A., Kapania, R.K., and Haftka, R.T., "Flexible Wing Model for Structural Wing Sizing and Multidisciplinary Design Optimization of a Strut-Braced Wing," AIAA Paper 2000-1427, *41st AIAA/ASME/ASCE/AHS/ASC Structures, Structural Dynamics, and Materials Conference and Exhibit*, Atlanta, GA, April 3-6, 2000.

20. Gern, F.H., Ko, A., Sulaeman, E., Kapania, R.K., Mason, W.H., Grossman, B., and Haftka, R.T., "Passive load alleviation in the design of a strut-braced wing transonic transport aircraft," AIAA Paper 2000-4826, *8th AIAA/USAF/NASA/ISSMO Symposium on Multidisciplinary Analysis and Optimization*, Long Beach, CA, Sept. 6-8, 2000.

21. Gern, F.H., Naghshineh-Pour, A., Sulaeman, E., Kapania, R.K., and Haftka, R.T., "Structural Wing Sizing for Multidisciplinary Design Optimization of a Strut-Braced Wing," *Journal of Aircraft*, Vol. 38, No. 1, 2001.

22. Sulaeman, E., Kapania, R.K., and Haftka, R.T, "Effect of Compressive Force on a Strut-Braced Wing Response," AIAA Paper 2001-1611, *42nd AIAA/ASME/ASCE/AHS/ASC Structures, Structural Dynamics, and Materials Conference and Exhibit*, Seatle, WA, April 16-19, 2001.

23. McCullers, L.A., FLOPS User's Guide, Release 5.81, NASA Langley Research Center.

24. Kroo, I., Gallman, J.W., and Smith, S.C., "Aerodynamic and Structural Studies of Joined-Wing Aircraft", *Journal of Aircraft*, Vol. 28, No.1, 1991, pp. 74-81.
25. Miura, H., Shyu, A., and Wolkovitch, J., "Parametric Weight Evaluation of Joined Wings by Structural Optimization", *Journal of Aircraft*, Vol. 25, No. 12, 1988, pp. 1142-1149.
26. Oliffe, B., *Private Communications with R.K. Kapania,* May - June 1998.
27. Mailybaev, A.A., and Seiranyan, A.P. "The Keldysh Problem on Aeroelastic Stability of a Strut-braced Wing," *Physics-Doklady*, Vol. 41, No. 10, 1996, pp. 484-487 (Translated from original Russian text in *Doklady Akademii Nauk*, Vol. 350, No.4, 1996).
28. Keldysh, M.V., Izbrannye trudy: Mekanika, Moscow, Nauca, 1985, pp. 304 – 341.
29. Gern, F.H., Weekly Presentation of the Strut Braced Wing, MAD Center, AOE Department, Virginia Tech, 1998 – 2000.
30. Anon., "Structural and Aerodynamic Investigation of a Strut-Braced Wing Transport Aircraft", Lockheed Martin Aeronautical Systems Phase 2 Final Report, Dec. 8, 1999.
31. de Lagrange, J.L., "Sur la Figure des Colonnes," *Miscellanea Taurinesia*, Vol. 5, 1770-1773, p. 173.
32. Taylor, J.E., and Liu, C.Y., "Optimal Design of Columns," *AIAA Journal*, Vol. 6, No. 8, 1968, pp. 1497-1502.
33. Bisplinghoff, R.L., Ashley, H., and Halfman, R.L., *Aeroelasticity,* Addison-Wesley, 1955.
34. Rodden,W.P., and Johnson, E.H., *MSC/NASTRAN Aeroelastic Analysis User's Manual*, Version 68, 1994, pp. 237-257.
35. Heard,W.L., Bush, H.G., Wallsom, R.E., and Jensen, J.K., "A mobile work station concept for mechanically aided astronaut assembly of large space trusses," *NASA Technical Paper 2108,* 1983, pp. 1-35.

36. Banerjee, J.R., and Williams, F.W., "Exact Bernoulli-Euler Static Stiffness Matrix for a Range of Tapered Beam-Columns," *International Journal for Numerical Methods in Engineering*," Vol. 23, 1986, pp. 1615-1628.
37. Weaver, W., and Gere, J.M., *Matrix Analysis of Framed Structures*, 3rd ed., Van Nostrand Reinhold, New York, 1990.
38. Yang, T.Y., *Finite Element Structural Analysis*, Prentice Hall, 1986.
39. Lee, S.Y., Ke, H.Y., and Kuo, Y.H., "Exact Static Deflections of a Non-Uniform Bernoulli-Euler Beam with General Elastic End Strains, " *Computers and Structures*, Vol. 36, No. 1, 1990, pp. 91-97.
40. Friedman, Z., and Kosmatka, J.B., "Exact Stiffness Matrix of a Non-Uniform Beam", *Computers and Structures*, Vol. 42, 1992, pp. 671-682.
41. Baker, G., "Exact Deflections in Non-prismatic Members," *Computer and Structures*, Vol. 61, No. 3, 1996, pp. 515-528.
42. Baker, G.,"A Numerical Parametric Study of Nonlinear Behavior in Variable Depth Beams," Ph.D. Dissertation, Heriot-Watt University, Edinburgh, 1987.
43. Lamb, R.S., "Stress Distributions in Tapered Concrete Beams," Ph.D. Dissertation, University of Nottingham, 1971.
44. Eisenberger, M., "An Exact Element Methods", *International Journal for Numerical Methods in Engineering*," Vol. 30, No. 2, 1990, pp. 363-370.
45. Eisenberger, M., "Explicit Stiffness Matrices for Non-prismatic Members", *Computers and Structures*, Vol. 20, 1985, pp. 715-720.
46. Karabalis, D.L., and Beskos, D.E., "Static, Dynamic and Stability Analysis of Structures Composed of Tapered Beams," *Computers and Structures*, Vol. 16, No. 6, 1983, pp. 731-748.
47. Iremonger, M.J., "Finite Difference Buckling Analysis of Non-Uniform Columns," *Computers and Structures*, Vol. 12, 1980, pp. 741-748.

48. Gallagher, R.H., and Lee, C.H., "Matrix Dynamic and Instability Analysis with Non-uniform Elements", *International Journal for Numerical Methods in Engineering*," Vol. 20, No. 2, 1970.

49. Dube, G.P. and Dumir, P.C., "Tapered Thin Open Section Beams on Elastic Foundation-I. Buckling Analysis," *Computers and Structures*, Vol. 61, 1996, pp. 845-857.

50. Rajasekaran, S., "Instability of Tapered Thin Walled Beams of Generic Section," *J. Engineering Mechanics*, Vol. 120, 1994, pp. 1630-1640.

51. Bisplinghoff, R.L., Ashley, H., and Halfman, R.L., *Aeroelasticity*, Addison-Wesley, 1955.

52. Landahl, M.T., and Stark, V.J.E., "Numerical Lifting Surface Theory – Problems and Progress," *AIAA Journal*, Vol. 6, No. 11, Nov. 1968, pp. 2049 – 2000.

53. Rodden, W.P., Harder, R.L., and Bellinger, E.D., "Aeroelastic Addition to NASTRAN," *NASA CR 3094*, March 1979.

54. Dowell, E.H., Curtiss, H.C.Jr., Scanlan, R.H., Sisto, F., *A Modern Course in Aeroelasticity*, 2nd ed., Kluwer Academic Pub., 1989.

55. Ashley, H., Widnall, S.E., and Landahl, M.T., "New Directions in Lifting Surface Theory," *AIAA Journal*, Vol. 3, No. 1, Jan . 1965, pp. 3 – 16.

56. Ashley, H., and Rodden, W.P., "Wing – Body Aerodynamic Interaction," *Annual Review of Fluid Mechanic*s, Vol. 4, 1972, pp. 431 – 472.

57. Bisplinghoff, R.L., and Ashley, H., *Principles of Aeroelasticity*, Dover Pub., New York, 1962.

58. Rodden, W.P., "A Comparison of Methods Used in Interfering Lifting Surface Theory, "*AGARD R. 643*., Feb. 1976.

59. Hildebrand, F.B., *Advanced Calculus for Applications*, 3rd ed., Prentice Hall, Tokyo, 1963.

60. Watkins, C.E., Runyan, H.L., and Woolston, D.S., "On the Kernel Function of the Integral Equation Relating the Lift and Downwash Distribution of Oscillating Finite Wings in Subsonic Flow, " *NACA Rept. 1234*, 1955.

61. Kussner, H.G., "General Airfoil Theory," *NACA TM 979*, 1941.

62. Giesing, J.P., Kalaman, T.P., and Rodden, W.P., "Subsonic Unsteady Aerodynamic for General Configurations," *AFFDL-TR 71-5*, 1971.

63. Yates, E.C., Jr., " A Kernel Function for Nonplanar Oscillating Surfaces in Subsonic Flow, " *AIAA Journal*, Vol. 5, No. 4, Aug. 1966, pp. 1486-1488.

64. Landahl, M.T., "Kernel Function for Nonplanar Oscillating Surfaces in a Subsonic Flow," *AIAA Journal*, Vol. 4, No. 4, May 1967, pp. 1045-1046.

65. Laschka, B., "Das Potential und das Geschwindigkeitsfeld der Harmonisch schwingenden tragenden Flache bei Unterschallanstromung," *Z. Angew. Math. Mech.*, Vol. 43, 1963, pp. 325-333.

66. Ueda, T., and Dowell, E.H., "A New Subsonic Method for Lifting Surfaces in Subsonic Flow," *AIAA Journal*, Vol. 20, No. 3, March 1982, pp. 348 – 355.; Technical Comment by Rodden, W.P., Vol. 22, No.1, p. 160.; Reply by Ueda, T. and Dowell, E.H., Vol. 22, No.4, p.575.

67. Rodden, W.P., Giesing., J.P., and Kalman, T.P., "New Developments and Applications of the Subsonic Doublet Lattice Method for Nonplanar Configurations," Symposium on Unsteady Aerodynamics for Aeroelastic Analyses of Interfering Surfaces, *AGARD* CP 90-71, April 1971.

68. Jones, R.T., and Cohn, D., "High Speed Wing Theory," General Theory of High Speed Aerodynamics, Vol. VI, Sec. A., Princeton Univ. Press., New Jersey, 1954.

69. DeYoung, J.(ed.), "Vortex Lattice Utilization," *NASA SP-405*, 1976.

70. Albano, E. and Rodden, W.P., "A Doublet Lattice Method for Calculating Lift Distribution on Oscillating Surfaces in Subsonic Flow," *AIAA Journal*, Vol 7, No. 2, Feb. 1969, pp. 279-285; Errata, *AIAA Journal*, Vol. 7, No. 11, Nov. 1969, p. 2192.

71. Jordan, P.F., 'Reliable Lifting Surface Solutions for Unsteady Flow," *Journal of Aircraft*, Vol. 15, Sept. 1978, pp. 626-633.
72. Rodden, W.P., Giesing, J.P., and Kalman, T.P., "Refinement of the Nonplanar Aspects of the Subsonic Doublet Lattice Lifting Surface Method," *Journal of Aircraft*, Vol. 9, Jan 1972, pp. 69 – 73.
73. Houbolt, J.C., "Some New Concepts in Oscillatory Lifting Surface Theory, " *AFFDL-TR*-68-2, 1969.
74. Ichikawa, I., "Doublet Strip Method for Oscillating Swept Tapered wings in Incompressible Flow," *Journal of Aircraft*, Vol. 22, No. 11, Nov. 1985, pp. 1008 – 1012.
75. Eversman, W., and Pitt, D.M., "Hybrid Doublet Lattice/Doublet Point Method for Lifting Surfaces in Subsonic Flow, " *Journal of Aircraft*, Vol. 28, No. 9, Sept. 1991, pp. 572 – 578.
76. Kalman, T.P., Rodden, W.P., and Giesing, J.P., "Application of the Doublet Lattice Method to Nonplanar Configurations in Subsonic Flow," *Journal of Aircraft*, Vol. 8, No. 6, June 1971, pp. 406 – 413.
77. Ueda, T., "Asymptotic Expansion of the Kernel Function in Subsonic Unsteady Lifting Surface Theory," *Journal of the Japan Society for Aeronautical Space Sciences*, Vol 20, No. 326, 1981, pp. 169 – 174.
78. Ueda, t., "Expansion Series of Integral Functions in Unsteady Aerodynamics," *Journal of Aircraft*, Vol. 19, No. 7, April 1982, pp. 345 – 347.
79. Bismarck – Nasr, M.N., "Kernel Function Occuring in Subsonic Unsteady Potential Flow," *AIAA Journal*, Vol 29, No. 6, June 1991, pp. 878 – 879.
80. Rodden, W.P., *MSC NASTRAN Handbook for Aeroelastic Analysis*, Rept. MSR-57, The MacNeal-Schwendler Corp., Los Angeles, Nov. 1987.
81. Mook, D.T. and Nayfeh, A.H., "Application of the Vortex Lattice Method to High Angle of Attack Subsonic Aerodynamics," SAE Paper No. 851817, Oct. 1985.

82. Ando, S. and Ichikawa, A., "Quadratic Formulas for Chordwise Integrals of Lifting Surface Theories," *AIAA Journal*, Vol. 21, No. 3, March 1983.
83. Stark, V.J.E., "A Generalized Quadrature Formula for Cauchy Integrals," *AIAA Journal*, Vol. 9, No. 9, Sept. 1971, pp. 1854 – 1855.
84. Bera, R.K., "Quadrature Formula for a Double Pole Singular Integral, *AIAA Journal*, Vol. 26, No.6, June 1988.
85. Song, C.C.S., "Numerical Integration of a Double Integral with Cauchy-Type Singularity," *AIAA Journal*, Vol. 7, No. 7, July 1960, pp. 1389 – 1390.
86. Brandao, M.P., "Improper Integrals in Theoretical Aerodynamics: The Problem Revisited," *AIAA Journal*, Vol. 25, No. 9, 1987, pp. 1258 – 1260.
87. Van Niekerk, B., "Integration of Singular Functions Associated with Lifting Surface Theory," *AIAA Journal*, Vol. 24, No. 7, July 1986, pp. 1194 – 1196.
88. Lan, C.E., "Some Applications of the Quasi-Vortex Lattice Method in Steady and Unsteady Aerodynamics", *NASA SP*-405, 1976, pp. 385 – 406.
89. Graham, J.M.R., "A Lifting Surface Theory for the Rectangular Wing in Non-Stationary Flow," *Aeronautical Quarterly*, Vol 12, Feb. 1971, p. 83.
90. Margason, R.J., and Lamar, J.E., "Vortex Lattice Fortran Program for Estimating Subsonic Aerodynamic Characteristics of Complex Planform," *NASA TN D*-6142, Feb. 1971.
91. Lottati, I., and Nissim, E., "Oscillatory Piecewise Continuous Kernel Function Method," *Journal of Aircraft*, Vol. 14, No. 6, June 1977, pp. 515 – 516.
92. Lottati, I., and Nissim, E., "Three-Dimensional Oscillatory Piecewise Continuous Kernel Function Method. Part I, II and III," *Journal of Aircraft*, Vol. 18, No. 5, May 1981, pp. 346 - 363.
93. Lottati, I., and Nissim, E., "Nonplanar, Subsonic, Three-Dimensional Oscillatory Piecewise Continuous Kernel Function Method," *Journal of Aircraft*, Vol. 22, No. 12, Dec 1985, pp. 1043 - 1048.

94. Hough, G.R., “Remarks on Vortex Lattice Methods,” *Journal of Aircraft*, Vol. 10, No. 5, May 1973, pp. 314 – 317.
95. Hewitt, B.L., “Unsteady Airforces for wings with Control Surfaces,” Symposium on Unsteady Aerodynamics for Aeroelastic Analyses of Interfering Surfaces, *AGARD* CP-80-71, April 1971.
96. Rowe, W.S., Redman, M.C., Ehlers, F.E., and Sebastian, J.D., “Prediction of Unsteady Aerodynamic Loading Caused by Leading Edge and Trailing Edge Control Surface Motion in Subsonic Flows, *NASA CR-2543*, 1975.
97. Bohm, G., and Schmid, H., “Subsonic Unsteady Airloads on Multiple Lifting Surfaces,“ Symposium on Unsteady Aerodynamics for Aeroelastic Analyses of Interfering Surfaces, *AGARD CP-80-71*, April 1971.
98. Davies, D.E., “Calculation Methods for Unsteady Airforces of Tandem Surfaces and T-Tails in Subsonic Flow,” Symposium on Unsteady Aerodynamics for Aeroelastic Analyses of Interfering Surfaces, *AGARD* CP-80-71, April 1971.
99. Dat, R., and Akamatsu, Y., Representation d’Une Aile par des Lignes Portantes: Application au Calcul de l’Interaction de Deux Ailes en Tandem,“ Symposium on Unsteady Aerodynamics for Aeroelastic Analyses of Interfering Surfaces, *AGARD* CP-80-71, April 1971.
100. Lan, C.E., “A Quasi Vortex Lattice Method in Thin Wing Theory,” *Journal of Aircraft*, Vol. 11, No. 9, Sept. 1974, pp.518 – 527.
101. Watkins, C.E., Woolston, D.S., and Cunningham, H.J., “A Systematic Procedure for determining Aerodynamic Forces on Oscillating or Steady Finite Wings at Subsonic Speed,” *NASA R-48*, 1959.
102. Laschka, B., “Zur Theorie der Harmonisch Schwingenden Tragenden Flache bei Unterschallanstromung,” *Z. Flugwissenschaften*, Vol. 11, No. 7, 1963, pp. 265 – 292.
103. Dat, R. and Malfois, J.P., “Sur le Calcul du Noyau de l’Equation Integrale de la Surface Postante en Ecoulement Subsonique Instationnaire,” *La Recherche Aerospatiale*, No. 5, 1970, pp. 251 – 259.

104. Desmarais, R.N., "Accurate Numerical Evaluation of Modified Struve Functions Occurring in Unsteady Aerodynamics," *Journal of Aircraft*, Vol. 16, No. 7, July 1979, pp. 441 - 447.

105. Berman, H.J., Shyprykevich, P., and Smedfjeld, J.B., "A Subsonic Nonplanar Kernel Function for Surfaces Inclined to the Freestream," *Journal of Aircraft*, Vol. 7, No. 2, Feb. 1970, pp. 188 – 190.

106. Lance, G.N., "The Kernel Function of the Integral Equation Relating the Lift and Downwash Distributions of Oscillating Finite Wings in Subsonic Flow," *Journal of Aeronautical Sciences*, Vol. , 1954, pp. 635 – 636.

107. Ando, S. and Kato, M., "Evaluation of the Desmarais's Method Computing Subsonic Kernel Function," *Journal of the Japan Aeronautical Space Sciences*, Vol. 36, No. 418, 1988, pp. 529 – 534.

108. DeYoung, J., "Convergence-Proof of Discrete-Panel Wing Loading Theories," *Journal of Aircraft*, Vol. 8, No. 10, Oct. 1971, pp. 837 – 839.

109. Ward, G.N., *Linearized Theory of Steady High Speed Flow*, Cambridge Univ. Press., New York, 1955.

110. Bertin, J.J. and Smith, M.L., *Aerodynamics for Engineers*, Prentice-Hall, New Jersey, 1979.

111. Abramowitz, M., and Stegun, I.A. (eds.), *Handbook of Mathematical Functions*, National Bureau of Standards, 1965.

112. Fogiel, M. (ed.), *Handbook of Mathematical Scientific and Engineering Formulas, Tables, Functions, Graphs, and Transforms*, REA, New Jersey., 1991.

113. Prudnikov, A.P., Brychkov, Y.A., Marichev, O.I., *Integrals and Series*, Gordon and Breach Science Pub., N.Y., 1986.

114. Allen, E.E., "Polynomial Approximations to Some Modified Bessel Functions," *Math. Tables Aids Comp*., Vol. 10, 1956, pp. 162 – 164.

115. Ghizzetti, A., and Oscini, A., *Quadrature Formulae*, Academic Press, New York, 1970.

116. Stroud, A.H., and Secrest, D., *Gaussian Quadrature Formulas*, Prentice Hall, New York, 1983.
117. Katz, P., and Plotkin, A., *Low-Speed Aerodynamics*, McGraw-Hill, Inc., New York, 1991.
118. Singh, B.K., and Basu, B.C., "A Numerical Model for Analysis of Thin wings in Inviscid Incompressible Flow," *Aeronautical Journal*, Vol. 91, August-Sept. 1987, pp. 333 – 337.
119. Lamar, J.E., "A Modified Multhopp Approach for Predicting Lifting Pressures and Camber Shape for Composite Planforms in Subsonic Flow," *NASA TN-D 427*, July 1968.
120. Wagner, S., "On the Singularity Method of Subsonic Lifting Surface Method," *Journal of Aircraft*, Vol. 7, No. 6, 1969, pp. 549 – 558.
121. Thiel, A., Weissinger, J., "Pressure Distribution Measurement on a Straight and on a 35^0 Swept-Back Tapered Wings, *NACA TM-1126*, 1948.
122. Fischel, J., Naseth, R.L., Hagerman, J.R., O'Hara, W.M., "Effect of Aspect Ratio on the Low Speed Lateral Control Characteristics of Untapered Low Aspect Ratio Wings Equipped with Flap and with Retractable Ailerons," *NACA Rep. 1091*, 1952.
123. Graham, R.R., "Low Speed Characteristics of a 45^0 Sweptback Wing of Aspect Ratio 8 from Pressure Distributions and Force Tests at Reynolds Numbers from 1,500,000 to 4,800,000," *NACA RM L51H13*, 1951.
124. Wick, B.H., "Chordwise and Spanwise Loadings Measured at Low Speed on a Triangular Wing Having an Aspect Ratio of Two and NACA 0012 Airfoil Section," *NACA TN 1650*, 1948.
125. Forsching, H., Triebstien, H., and Wagener, J., "Pressure Measurement on a Harmonically Oscillating Swept Wing with Two Control Surfaces in Incompressible Flow," Symposium on Unsteady Aerodynamics for Aeroelastic Analyses of Interfering Surfaces, *AGARD CP-80-71*, April 1971.

126. DeJarnette, F.R., "Arrangement of Vortex Lattics on Subsonic Wings," *NASA SP* 405, 1976, pp. 301 – 323.
127. Cunningham, A.M.,Jr., "An Efficient Steady, Subsonic, Collocation Method for Solving Lifting Surface Problems," *Journal of Aircraft*, Vol. 8, No. 3, Mar. 1971, pp. 168 – 192.
128. Hough, G.R., "Lattice Arrangements for Rapid Convergence," *NASA SP 40*5, 1976, pp. 325-342.
129. Rowe, W.S., and Cunningham, H.J., "On the Convergence of Unsteady Generalized Aerodynamic Forces," *Journal of Aircraft*, Vol. 21, No. 6, June 1984, pp. 420 – 427.
130. Harder, R.L., and Rodden, W.P., "Kernel Function for Nonplanar Oscillating Surfaces in Supersonic Flow," *Journal of Aircraft*, Vol. 8, No. 8, Aug. 1971, pp. 677 – 679.
131. Ueda, T. and Dowell, E.H., "Doublet Point Method for Supersonic Unsteady Lifting Surfaces," *AIAA Journal*, Vol. 20, No. 3, Mar. 1982, pp. 348 - 335.
132. Giesing, J.P., and Kalman, T.P., "Oscillatory Supersonic Lifting Surface Theoru using a Finite element Doublet Representation," *AIAA Paper 75-761*, May 1975.
133. Brock, B.J., and Griffin, J.A., Jr., "The Supersonic Doublet Lattice Method – A Comparison of Two Approaches," *AIAA Paper 75-760*, May 1975.
134. Ando, S., and Kato, M., "Evaluation of the Desmarais Method for Computing Subsonic Kernel Function," *Journal of Japan Society for Aeronautical Space Sc*iences, Vol. 36, No. 418, 1988, pp. 529 – 534.
135. Sulaeman, E., *"Discrete Element Methods for Calculating Aerodynamic Loadings on Lifting Surfaces in Unsteady Subsonic Flows*," MS. Thesis, University of Dayton, Ohio, 1993.
136. Ueda, T., "Lifting Surface Calculations in the Laplace Domain with Application to Root Loci," *AIAA Journal*, Vol 25, No. 5, May 1987, pp. 698 – 704.
137. Hedman, S.G., "Vortex Lattice Method for Calculation of Quasi Steady State Loadings on Thin Elastic Wings," *Aeronautical Research Institute of Sweden Rept. 105*, Oct. 1965.

138. Blair, M., “A Compilation of the Mathematics Leading to the Doublet Lattice Method,” *WPAFB Air Force Wright Laboratory WL-TR-95-3022*, November 1994.
139. Mason, W.H, *Applied Computational Aerodynamics*, Virginia Tech. AOE Class Note, Blacksburg, 1999.
140. Belotserkovskii, S.M., *The Theory of Thin Wings in Subsonic Flow*, Plenum Press, New York, 1967.
141. Falkner, V.M, “The Calculation of Aerodynamic Loading on Surfaces of any Shape,” *British Aeronautical Research Council R & M 1910*, 1943.
142. Campbell, G.S., “A Finite Step Method for the Calculation of Span Loadings of Unusual Plan Forms,” *NACA RM L50L13*, July 1951.
143. Rodden, W.P., Taylor, P.F., and McIntosh, S.C., Jr., “Further Refinement of the Nonplanar Aspects of the Subsonic Doublet Lattice Lifting Surface Method,” *International Council of the Aeronautical Sciences (ICAS)*, Paper 96-2.8.2, 1996.
144. Rodden, W.P., Taylor, P.F., and McIntosh, S.C., Jr., “Further Refinement of the Subsonic Doublet Lattice Method,” *Journal of Aircraft*, Vol. 35, No. 5, 1998, pp. 720–727.
145. Rodden, W.P., Taylor, P.F., McIntosh, S.C., Jr., and Baker, M.L, “Further Convergence Studies of the Enhanced Subsonic Doublet Lattice Oscillatory Lifting Surface Method,” *Proceedings of the International Forum on Aeroelasticity and Structural Dynamics*, Vol. III, Rome, Italy, 1997, pp. 401-408.
146. Van Zyl, L.H., “Arbitrary Accuracy Integration scheme for the Subsonic Doublet Lattice Method,” *Journal of Aircraft*, Vol. 35, No. 6, pp. 975-977.
147. Van Zyl, L.H., “Convergence of the Subsonic Doublet Lattice Method,” *Journal of Aircraft*, Vol. 35, No. 6, pp. 977-979.
148. Van Zyl, L.H., “Application of the Subsonic Doublet Lattice Method to Delta Wings,” *Journal of Aircraft*, Vol. 36, No. 3, pp. 609-611.

149. Chen, P.C., Lee, H.W., and Liu, D.D., "Unsteady Subsonic Aerodynamics for Bodies and Wings with External Stores including Wake Effect," *Journal of Aircraft*, Vol. 30, No. 5, Sept.-Oct. 1993, pp. 618 – 628.
150. Liu, D.D., Chen, P.C., Yao, Z.X., and Sarhaddi, D., "Recent Advances in Lifting Surface Methods," *The Royal Aeronautical Journal,* Vol. 100, No. 998, Oct. 1996, pp. 327 – 339.
151. Epstein, R.J., and Bliss, D.B., "Alternative Solution of the Kernel Function in Subsonic Unsteady Lifting Surface Theory," *AIAA Journal,* Vo. 33, No. 11, 1995, pp. 2228-2230.
152. Abrate, S., "Vibration of Non-Uniform Rods and Beams," *Journal of Sound and Vibration*, Vol. 185, No. 4, 1995, pp. 703-716.
153. Kumar, B.M., and Sujith, R.I., "Exact Solutions for Longitudinal Vibration of Non-Uniform Rods, " *Journal of Sound and Vibration*, Vol. 206, No. 5, 1997, pp. 721-729.
154. Eisenberger, M., "Exact Longitudinal Vibration Frequency of a Variable Cross-section Rods", *Applied Acoustics*, Vol. 34, No. 2, 1991, pp. 123-130.
155. Chehil, D.S., "Determination of Natural Frequencies of a Beam with Varying Section Properties," *J. Sound and Vibration*, Vol. 115, 1987, pp. 423-436.
156. Chen, Y.Z., and Xie, J.R., " Evaluation of Natural Frequencies of Non-Uniform Beams by Numerical Integration," *Computers and Structures*, Vol. 29, 1988, pp. 693-697.
157. Plaut, R.H., Johnson, L.W. and Olhoff, N., "Bimodal Optimization of Compressed Columns on Elastic Foundations," *J. Applied Mechanics*, Vol. 53, 1986, pp. 130-134.
158. Bendsoe, M.P., Olhoff, N., and Taylor, J.E., "A Variational Formulation for Multicriteria Structural Optimization," *J. Structural Mechanics*, Vol 11, No. 4, 1983, pp. 523-544.
159. Washizu, K., *Variational Methods in Elasticity and Plasticity*, second edition, Pergamon Pers, 1975.
160. Haftka, R.T., and Gurdal, Z., *Elements of Structural Optimization*, Third edition, Kluwer Academic, 1996.

161. Cox, S.J. and McCarthy, C.M., "The Shape of the Tallest Column," *Siam J. Mathematical Analysis*, Vol. 29, No. 3, 1998, pp. 547-554.
162. Masur, E.F., "Optimal Structural Design Under Multiple Eigenvalue Constraints," *International Journal of Solid Structures*, Vol. 20, No. 3, 1984, pp. 211-231.
163. Barnes, E.R., "The Shape of the Strongest Column and Some Related Extremal Eigenvalue Problems," *Quarterly of Applied Mathematics*, 1977.
164. Frauenthal, J.C., "Constrained Optimal Design of Columns Against Buckling," *J. Structural Mechanics*, Vol. 1, 1972, pp. 79-89.
165. Olhoff, N., and Rasmussen, S.H., "Bimodal Optimum Buckling Loads of Clamped Columns," *International Journal of Solid Structures*, Vol. 13, 1977, pp. 605-614.
166. Caffrey, J.P., and Lee, J.M., *MSC/NASTRAN Linear Static Analysis. User's Guide*, Version 68, 1994.
167. Johnson, E.H., and Venkayya, V.B., "Automated Structural Optimization System (ASTROS)," *AFWAL-TR*-88-3028, Flight Dynamic Laboratory WPAFB, Ohio, 1988.
168. Lamar, J.E., "A Vortex Lattice Method for the Mean Camber Shapes of Trimmed Non-Coplanar Planforms with Minimum Vortex Drag," *NASA TN D*-8090, June 1976.
169. Anderson, E., *LAPACK User Guide (Version 3.0)*, *SIAM*, Philadelphia, 2nd Ed., 1994.
170. Theodorsen, T., "General Theory of Aerodynamic Instability and the Mechanism of Flutter," *NACA Report 496*, 1935.
171. ZONA Technology,. Inc., *ZAERO User's Manual*, Version 4.3, ZONA 00-24.1, Scottsdale, AZ, August 2000.
172. ZONA Technology,. Inc., *ZAERO Theoretical Manual*, Version 5.0, ZONA 01-24.4, Scottsdale, AZ, February 2001.
173. Yates, E.C., Jr., Land, N.S., and Foughner, J.T., Jr., "Measured and Calculated Subsonic and Transonic Flutter Characteristics of a 45° Sweptback Wing Planform in Air and in Freon-12 in the Langley Transonic Dynamics Tunnel," *NASA TN-D-1616*, Mar. 1963.

174. Vanderplaats Research and Development, Inc., *DOT User's Manual*, Version 4.20, Colorado Springs, CO, 1995.
175. Lomax, T.L., *Structural Loads Analysis for Commercial Transport Aircraft: Theory and Practice*, AIAA Education Series, Washington, D.C., 1996.
176. Raymer, D.P., *Aircraft Design: A Conceptual Approach*, AIAA Education Series, Washington, D.C., 1989.
177. Chen, P.C. and Liu, D.D., "A Harmonic Gradient Method for Unsteady Supersonic Flow Calculations," *Journal of Aircraft*, Vol. 22, 1985, pp. 371-379.
178. *MSC/NASTRAN Numerical Methods User's Manual*, Version 68, Section 4.2.4, 1994.
179. Edwards, J.W., "Unsteady Aerodynamic Modeling and Active Aeroelastic Control," *SUDAAR 504*, Feb. 1977.
180. Vepa, R., "Finite State Modeling of Aeroelastic Systems," *NASA CR* 2779, Feb. 1977.
181. Roger, K.L., "Airplane Math Modeling Methods fir Active Control Design," *AGARD CP* 228, Aug. 1977.
182. Stark, V.J.E., "General Equations of Motion for an Elastic Wing and Method of Solution," *AIAA Journal*, Vol. 22, Aug. 1984, pp. 1146-1153.
183. Cho, J. and Williams, M.C., "S-Plane Aerodynamics of Nonplanar Lifting Surfaces," *J. Aircraft*, Vol. 30, No. 4, 1993, pp 433-438.
184. Ueda, T., "Continuity of Lifting Surface Theory in Subsonic and Supersonic Flow," *AIAA Journal*, Vol. 36, No. 10, 1998, pp. 1788-1791.
185. Von Karman, T., Biot, M.A., *Mathematical Method in Engineering*, McGraw-Hill, New York, 1940, pp. 306-309.
186. Liu,D.D., Chen, P.C., Yao, Z.X., and Sarhaddi, D.,"Recent Advances in Lifting Surface Methods," *International Forum on Aerolasticity and Structural Dynamics*, 1995, pp. 4.1 - 4.14.
187. Barsoum, R.S. and Gallagher, R.H.,"Finite Element Analysis of Torsional and Lateral Stability Problems," *International Journal for Numerical Method in Engineering*, Vol. 2, No. 3, 1979, pp. 335-352.

188. Gallagher, R.H., *Finite Element Analysis: Fundamentals*, 4th Edition, Prentice-Hall, New Jersey, 1975.
189. Rubbert, P.E., "Theoretical Characteristics of Arbitrary Wings by a Nonplanar Vortex Lattice Method", Rept. D6-9244, 1964, The Boeing Co., Seattle, WA.
190. Dulmovits, J.,"A Lifting Surface Method for Calculating Load Distributions and the Aerodynamic Influence Coefficient Matrix for Wings in Subsonic Flow," Report ADR 01-02-64.1, 1964, Grumman Aircraft Engineering Corp., Bethpage, NY.
191. Bendiksen, O.O., "Transonic Flutter and the Nature of the Transonic Dip," *Proc. International Forum on Aeroelasticity and Structural Dynamics*, Madrid, Spain, June, 2001, pp. 273- 286.
192. Dogget, R.V., Jr., Rainey, A.G., and Morgan, H.G., "An Experimental Investigation of Aerodynamic Effects of Airfoil Thickness on Transonic Flutter Characteristics," NASA TM X-79, 1959.
193. Farmer, M.G., and Hanson, P.W., "Comparison of Supercritical and Conventional Wing Flutter Characteristics," NASA TM X-72837, 1976.
194. Houwink, R., Kraan, A.N. and Zwaan, R.J., "A Wind Tunnel Study of the Flutter Characteristics of a Supercritical Wing," AIAA Paper 81-0651, 1981.
195. Ashley, H., "Role of Shocks in the Sub-Transonic Flutter Phenomenon," *Journal of Aircraft*, Vol. 17, 1980, pp. 187-197.
196. Edwards, J.W. *et al.*, "Time-Marching Transonic Flutter Solutions Including Angle-of-Attack Effects," *Journal of Aircraft*, Vol. 20, 1983, pp. 899-906.
197. Bendiksen, O.O., "Nonunique Solutions in Transonic Aeroelasticity," *Proc. International Forum on Aeroelasticity and Structural Dynamics*, Rome, Italy, 1997, pp. 425-435.
198. Landahl, M.T., *Unsteady Transonic Flow*, Cambridge Science Classic, Cambridge, UK, 1989.
199. Nixon, D., *Unsteady Transonic Aerodynamics*, AIAA Progress in Astronautics and Aeronautics, Vol. 120, 1997.

200. Bennett, R.M., Batina, J.T., and Cunningham, H.J., "Wing Flutter Calculations with CAP-TSD Unsteady Transonic Small-Disturbance Program," *Journal of Aircraft*, Vol. 26, No. 9, 1989, pp. 876-882.

201. Brendes, G., and Voss, R., "Transonic Flutter Calculations for a Low Wing Transport Aircraft Using the Transonic Doublet Lattice Method," *Proc. International Forum on Aeroelasticity and Structural Dynamics*, Madrid, Spain, June, 2001, pp. 295-305.

202. Isogai, K. "Development of Unsteady Transonic 3D Full Potential Code and its Aeroelastic Application," *AGARD CP*-374, Jan. 1985.

203. Salmond, D.J. "Calculation of Harmonic Aerodynamic Forces on Aerofoils and Wings from the Euler Equation," *AGARD CP*-374, 1985.

204. Guruswamy, G.P. and Obayashi, S., "Transonic Aeroelastic Computations on Wings Using Navier-Stokes Equation," *AGARD CP*-507, 1991.

205. Yates, E.C., and Bennet, R.M., "Analysis of Supersonic – Hypersonic Flutter of Lifting Surfaces at Angle of Attack," *Journal of Aircraft*, Vol. 9, No. 7, 1972.

206. Giesing, J.P., Kalman, T.P., and Rodden, W.P., "Correction Factor Techniques for Improving Aerodynamic Prediction Methods," *NASA CR*-144967, May 1976.

207. Pitt, D.M., and Goodman, C.E., "Flutter Calculations Using Doublet Lattice Aerodynamics Modified by the Full Potentil Equations," *41st AIAA/ASME/ASCE/AHS Structures, Structural Dynamics, and Materials Conference*, AIAA-87-0882-CP, 1987.

208. Silva, R., Mello, O., and Azevedo, J., "Transonic Flutter Calculations Based on Assumed Mode Shape Corrections," *International Forum on Aeroelasticity and Structural Dynamics*, Madrid, Spain, 2001, pp. 183-194.

209. Jadic, I., Hartley, D., and Giri, J., "An Enhanced Correction Factor Technique for Aerodynamic Influence Coefficient Methods," *Proc. 1999 MSC User's Conference, 1999.*

210. Brink-Spalink, J., and Bruns, J.M., "Correction of Unsteady Aerodynamic Influence Coefficients Using Experimental or CFD Data," *International Forum on Aeroelasticity and Structural Dynamics*, Madrid, Spain, 2001, pp. 175-182.

211. Garner, H.C., “A Practical Framework for Evaluation of Oscillating Aerodynamic Loading on Wings in Supercritical Flows,” *AGARD CP*-226, April, 1977.
212. Luber, W., and Schmid, H., “Flutter Investigations in the Transonic Flow Regime for a Fighter Type Aircraft,” *AGARD RN*-703, September, 1982.
213. Chen, P.C., Sarhaddio, D., and Liu, D.D., “Transonic AIC Approach for Aeroelastic and MDO Applications,” *The Euromech Colloquium* 349, Gottingen, Germany, Sept. 16-18, 1996.
214. Edwards, J.W., “Transonic Shock Oscillations and Wing Flutter Calculated with an Interactive Boundary Layer Coupling Method,” *NASA TM* 110284, Aug. 1996.
215. Lu, S and Voss, R., “TDLM – A Transonic Doublet-Lattice Method for 3D Potential Unsteady Transonic Flow Calculation and Its Application to Transonic Flutter Prediction,” *International Forum on Aeroelasticity and Structural Dynamics*, Strasbourg, France, 1993.
216. Anon., *Airworthiness Standards: Transport Category Airplanes*, Federal Aviation Administration, Department of Transportation, Part 25, Last Updated Date: Dec 1, 2001.
217. Tjatra, I.W., Kapania, R. K., and Grossman, B., "Structural Nonlinearity Effects on Flutter of a Swept Wing," *International Journal of Computational Systems in Engineering*, Vol., 3, 1992, pp. 131-138.

Appendix A.

Detailed Derivation Of The Kernel Function Integration

A.1. Introduction

A detailed derivation of the hybrid doublet-lattice/doublet-point method is described in the following four sections of this Appendix. To simplify the derivation, a summary of the relationship between each section is shown schematically in Fig. A.1. Section A.2 describes the procedure to identify the singular part of the kernel function. Section A.3 proposes a procedure to separate explicitly the singular and regular parts of the kernel function solution. Section A.4 describes an exact integration to the singular part of the kernel function and a numerical Gauss quadrature integration to the regular part. In summary, the scheme introduced in the present work are all involved exact integration of the kernel function along the doublet lattice of each panel element, except the numerical Gauss integration. However, the accuracy of the Gauss integration procedure can be significantly increased simply by increasing the number of integration points without the need to change any other formulation scheme. More detailed derivation of the scheme are described in the following sections.

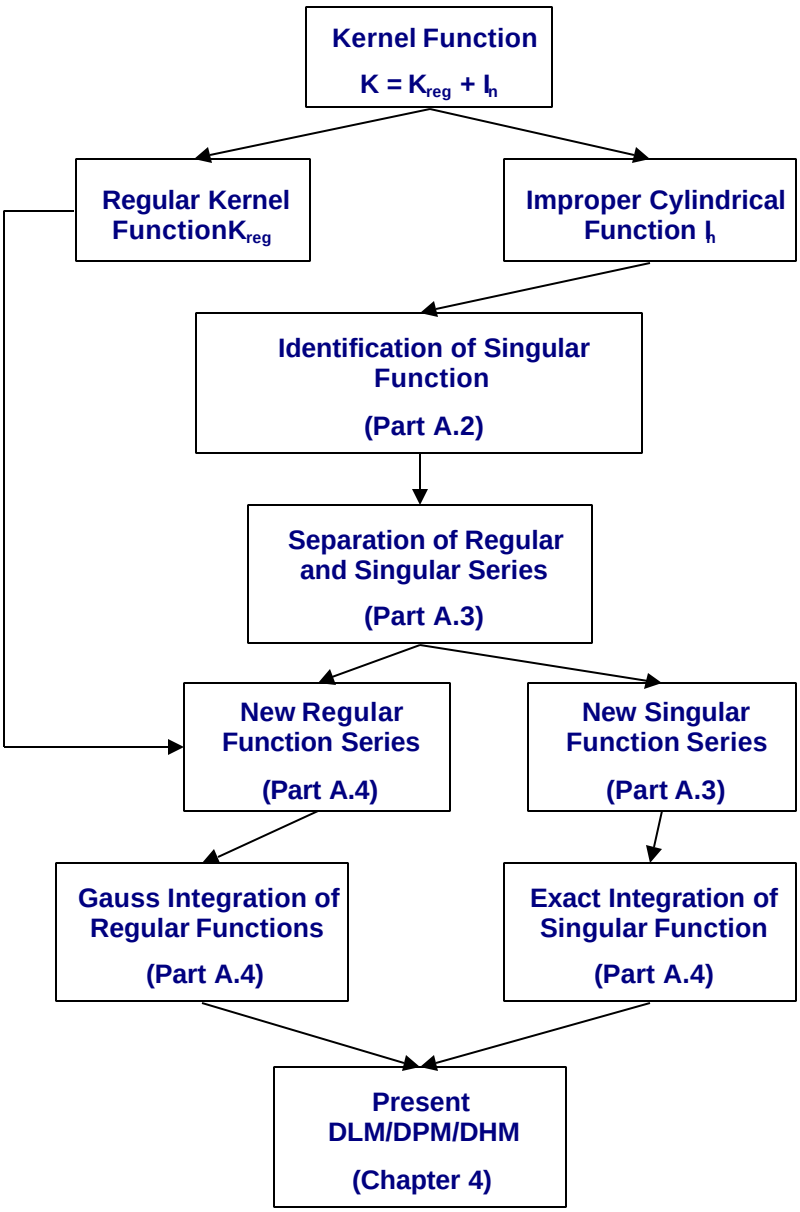


Figure A.1 Flow chart diagram describes the relationship between sections in Appendix E

A.2. Identification of the Singular Part of the Kernel Function

It has been described in Chapter 4 that the singular part of the lifting surface kernel function is embedded in the incomplete cylindrical functions B_n of the Landahl's kernel formulation. The incomplete cylindrical function given in Equation (4.10) has been solved in an exact closed form by Ueda based on an expansion series [77, 78]. A procedure is presented in this Appendix to identify and isolate this singular function.

Recall the definition of the incomplete cylindrical function in Eq. (4.14)

$$B_v = \int_{-\infty}^{X} \frac{e^{iku}}{\left(r^2 + u^2\right)^{v+1/2}}\, du \tag{4.14}$$

It is more convenient to divide the function B_v into two parts:

$$B_v = B_{v,real} + i\, B_{v,\,imag} = \int_{-\infty}^{X} \frac{\cos(ku)\, du}{\left(r^2 + u^2\right)^{v+1/2}} + i \int_{-\infty}^{X} \frac{\sin(ku)\, du}{\left(r^2 + u^2\right)^{v+1/2}} \tag{4.15}$$

where Ueda has already solved this cylindrical function in Refs. 77 and 78 as

$$B_{v,real} = \sum_{n=0}^{\infty} (-1)^n\, U_{v,2n} + \frac{(-k^2/2)^v}{(2v-1)!!} \sum_{n=0}^{\infty} p_n \frac{(k\,r/2)^{2n}}{n!\,(n+v)!} \tag{4.16a}$$

$$B_{v,imag} = \sum_{n=0}^{\infty} (-1)^n\, U_{v,2n+1} - \frac{p}{2} \frac{(-k^2/2)^v}{(2v-1)!!} \sum_{n=0}^{\infty} \frac{(k\,r/2)^{2n}}{n!\,(n+v)!} \tag{4.16b}$$

and

$$p_n = -\gamma - \ln\frac{k}{2} + \sum_{m=1}^{n} \frac{1}{m} + \sum_{m=n+1}^{n+v} \frac{1}{2m}$$

γ = Euler's constant = 0.57721566490153286060651 2…

and the U terms in Eq. (4.16) are based on the following recursion formulas :

$$U_{v,\,m>2v} = \frac{k\,(kX)^{m-1}}{(m-2v)\,m\,X_1^{2v-1}} \;-\; \frac{(kr)^2}{(m-2v)\,m}\,U_{v,m-2}$$

$$U_{v,\,2v} = -\frac{k^{2v}}{2v!}\left\{\ln(X_1 - X) + \sum_{m=1}^{v}\frac{1}{2m-1}\left(\frac{X}{X_1}\right)^{2m-1}\right\}$$

$$U_{v,\,2n<2v} = \frac{(v-n-1)!\,k^{2n}}{(2n)!\,r^{2(v-n)}}\left\{2^{v-n-1}\,\frac{(2n-1)!!}{(2v-1)!!} + \sum_{m=0}^{v-n-1}\frac{(-1)^m\,X^{m-1}\,(X/X_1)^{2m+2n+1}}{(2m+2n+1)\,m!\,(v-m-n-1)!}\right\}$$

$$U_{v,1} = -\frac{k}{(2v-1)\,X_1^{2v-1}} \tag{4.17}$$

where

$$r = \sqrt{y_o^{\,2} + z_o^{\,2}}$$

$$R = \sqrt{x^2 + \beta^2 r^2}$$

$$X = (x_o - M\,R)\,\beta^{-2} \tag{4.12}$$

$$X_1 = \sqrt{X^2 + r^2}$$

$$b = \sqrt{1 - M^2}$$

$$M < 1 \quad \text{(subsonic)}$$

The symbol of double-factorials *!!* is used to define

$$(2n-1)\,!!\;\; = 1 \bullet 3. \bullet 5 \bullet 7 \ldots (2n-1)$$

It has been described in Chapter 4 that the incomplete cylindrical function B_h is numerically singular when $r = 0$ and $X > 0$, *i.e.* when the control point is located at the center of the downstream panel of the doublet point or doublet line. This can be easily observed for the case of $h = 1$, where the singularity is located in the 0^{th} and 2^{nd} terms of the recurrence series as follows:

$$U_{1,0} = \frac{1}{r^2}\left(1 + \frac{X}{\sqrt{X^2 + r^2}}\right) \tag{A.1}$$

$$U_{1,2} = -\frac{k^2}{2}\left\{\frac{X}{\sqrt{X^2 + r^2}} + \ln\left(\sqrt{X^2 + r^2} - X\right)\right\} \tag{A.2}$$

If $r \to 0$ and X > 0, the kernel becomes infinite because of the strong dipole singularity in Eq. (A.1) and a weak logarithmic singularity in Eq. (A.2). Note that Eqs. (A.1) and (A.2) are the Ueda's expansion series for planar lifting surfaces. Note also that the singularity occurs only on the real part of the incomplete cylindrical function, or $B_{h,real}$.

A direct approach to separate the singular and regular parts in Ueda's expansion series may not be simple since the singularity occurs in the recurrence series, *i.e.* higher order terms of $U_{1,2n}$ are affected by $U_{1,2}$ according to the following recursion formula:

$$U_{1,\,m>2} = \frac{k\,(kX)^{m-1}}{(m-2)\,m\,!\,X_1} - \frac{(kr)^2}{(m-2)\,m}\,U_{1,m-2} \tag{A.3}$$

An attempt to isolate the singularity has been initiated by the present author in Ref. 135 by using the modified Bessel function as follows:

$$B_{h,real}(|X|) + B_{h,real}(-|X|) = \int_{-\infty}^{|X|} \frac{\cos(ku)\,du}{\left(r^2 + u^2\right)^{\nu+1/2}} + \int_{-\infty}^{-|X|} \frac{\cos(ku)\,du}{\left(r^2 + u^2\right)^{\nu+1/2}}$$

$$= \int_{-\infty}^{0} \frac{\cos(ku)\,du}{\left(r^2 + u^2\right)^{\nu+1/2}} + \int_{0}^{|X|} \frac{\cos(ku)\,du}{\left(r^2 + u^2\right)^{\nu+1/2}} + \int_{-\infty}^{0} \frac{\cos(ku)\,du}{\left(r^2 + u^2\right)^{\nu+1/2}} + \int_{0}^{-|X|} \frac{\cos(ku)\,du}{\left(r^2 + u^2\right)^{\nu+1/2}} \tag{A.4}$$

Since the integrand is an even function, we can simplify Eq. (A.4) as follows:

$$B_{h,real}(|X|) + B_{h,real}(-|X|) = 2\int_0^{\infty} \frac{\cos(ku)\,du}{\left(r^2 + u^2\right)^{\nu+1/2}}$$

or,

$$B_{h,real}(|X|) = B_{h,real}(-|X|) + 2\int_0^{\infty} \frac{\cos ku}{\left(r^2 + u^2\right)^{h+1/2}}\,du \qquad (A.5)$$

Since no singularity occurs in $B_{h,real}(-|X|)$ even for $r \to 0$ and X > 0, then the singularity has been extracted to the second integral in the right hand side of Eq. (A.5). This second integral in the sub-interval [-∞, 0] has been known to be a complete cylindrical function which consists of the modified Bessel function of the second kind $\mathbf{K_h}$ or MacDonald function as follows[113, 114]:

$$\int_0^{\infty} \frac{\cos ku}{\left(r^2 + u^2\right)^{h+1/2}}\,du = \frac{1}{(2h-1)!!}\left(\frac{k}{r}\right)^h \mathbf{K_h}(kr) \qquad (A.6)$$

where

$$\mathbf{K_h}(kr) = (-1)^{h+1}\left\{\ln\frac{kr}{2} + \gamma\right\}\mathbf{I_h}(x) + \frac{1}{2}\sum_{n=0}^{h-1}(-1)^n\,\frac{(h-n-1)!}{n!}\left(\frac{kr}{2}\right)^{2n-h} + \frac{(-1)^h}{2}\sum_{n=0}^{\infty}\left(\varphi(n) + \varphi(n+h)\right)\frac{(kr/2)^{h+2n}}{n!\,(n+h)!} \qquad (A.7)$$

$\mathbf{I_h}$ is the modified Bessel function of the first kind:

$$\mathbf{I_h}(kr) = \sum_{n=0}^{\infty}\frac{(kr/2)^{h+2n}}{n!\,(n+h)!}$$

and φ is the Digamma function: $\varphi(n) = \sum_{m=1}^{n}\frac{1}{m}$; $\varphi(0) = 0$

The singularity of $\mathbf{K_h}$ in the right hand side of Eq. (A.6) is shown for $r = 0$ where the logarithmic singular functions occurs in the first part and the multipole singular functions

appears in the second part. This procedure may complicate the computation of the incomplete cylindrical function for $X > 0$ and r is small since it needs a special function subroutine to evaluate numerically the modified Bessel function. The other disadvantage of the procedure is the limitation to treat the kernel function in the frequency domain only.

In the present work another approach is presented to identify the singular part of the singular function. The procedure is based on the following identity relation:

$$
\begin{aligned}
B_h(|X|) &= \int_{-\infty}^{|X|} \frac{e^{iku}}{\left(r^2+u^2\right)^{h+1/2}}\,du \qquad du \\
&= \int_{-\infty}^{-|X|} \frac{e^{iku}}{\left(r^2+u^2\right)^{h+1/2}}\,du + \int_{-|X|}^{|X|} \frac{e^{iku}}{\left(r^2+u^2\right)^{h+1/2}}\,du \\
&= \int_{-\infty}^{-|X|} \frac{e^{iku}}{\left(r^2+u^2\right)^{h+1/2}}\,du - 2\int_{0}^{-|X|} \frac{\cos ku}{\left(r^2+u^2\right)^{h+1/2}}\,du \\
&= B_h(-|X|) - 2\int_{0}^{-|X|} \frac{\cos ku}{\left(r^2+u^2\right)^{h+1/2}}\,du
\end{aligned}
\tag{A.8}
$$

Note that the integration of the present approach was performed to both even and odd series terms of B_h. Therefore the approach is more general than the previous work[135], where only the real part is treated. Since no singularity occurs in $B_h(-|X|)$ even for $r \to 0$ and X > 0, then the singularity has been extracted to the second integral in the right hand side of Eq. (A.54).

To solve the second integral in the right hand side of Eq. (A.54), one may use an expansion series to the cosine function as follows:

$$\cos\, k\,u \;=\; \sum_{n=0}^{\infty}(-1)^n\,\frac{(k\,u)^{2n}}{(2\,n)\,!} \tag{A.9}$$

Substitution of Eq. (A.9) into the second part of Eq. (A.8) gives

$$\int_0^X \frac{\cos\;k\,u}{\left(r^2+u^2\right)^{h+1/2}}\,du \;=\; \sum_{n=0}^{\infty}(-1)^n\;T_{2n} \tag{A.10}$$

where

$$T_m = \frac{k^m}{m\,!}\int_0^X \frac{u^m}{\left(r^2+u^2\right)^{h+1/2}}\,du \tag{A.11}$$

The evaluation of the integral T_m for each term can be simplified by considering three different cases as follows:

(1) For $m > 2\,h$, T_m can be evaluated using an integration by part technique[113] as follows:

$$\int_0^X \frac{u^m}{\left(r^2+u^2\right)^{h+1/2}}\,du \;=\; \frac{u^{m-1}}{(m-2h)\,(r^2+u^2)^{h-1/2}}\Bigg|_0^X \;-\; \frac{(m-1)\,r^2}{(m-2h)}\int_0^X \frac{u^{m-2}}{\left(r^2+u^2\right)^{h+1/2}}\,du \tag{A.12}$$

or

$$T_m = \frac{k\,(k\,X)^{m-1}}{(m-2h)\;m!\;X_1^{2h-1}} - \frac{(k\,r)^2}{(m-2h)}\,T_{m-2} \qquad for\;\; m > 2h \tag{A.13}$$

(2) For $m = 2h$ the solution for the integral T_m is based on the relation[113]

$$\int_0^X \frac{u^{m-2}}{\left(r^2+u^2\right)^{h+1/2}}\,du \;=\; \frac{-u^{m-1}}{(2\,h-1)\left(r^2+u^2\right)^{h-1/2}}\Bigg|_0^X \;-\; \frac{(m-1)}{(2h-1)}\int_0^X \frac{u^{m-2}}{\left(r^2+u^2\right)^{h-1/2}}\,du \tag{A.14}$$

and for $m = h = 0$

$$\int_0^X \frac{1}{\left(r^2+u^2\right)^{1/2}}\,du \;=\; \ln r \;-\ln\left(X_1 - X\right) \tag{A.15}$$

Substitution $m = 2h$ into Eq. (A.14) gives

$$\int_0^X \frac{u^{2h}}{\left(r^2 + u^2\right)^{h+1/2}}\, du = \frac{-1}{(2h-1)}\left(\frac{X}{X_1}\right)^{2h-1} + \int_0^X \frac{u^{2(h-1)}}{\left(r^2 + u^2\right)^{(h-1)-1/2}}\, du \qquad \text{(A.16)}$$

Note that the exponent of the numerator of the integrand in the left-hand side of Eq. (A.16) is reduced from $2h$ to $2(h\text{-}1)$. If the same procedure is repeated to the integral in the right hand side of Eq. (A.16) and using Equation (A.15) when $m = h = 0$, the integral T_{2h} can be written as

$$T_{2h} = \frac{-k^{2h}}{(2h)!}\left\{\ln(X - X_1) - \sum_{m=1}^{h}\frac{1}{(2m-1)}\left(\frac{X}{X_1}\right)^{2m-1}\right\} + \frac{k^{2h}}{(2h)!}\ln r \qquad \text{(A.17)}$$

It can be easily seen that T_{2h} above has a logarithmic singularity as r approaches 0.

(3) For $m < 2h$, Eq. (1.2.43.5) of Ref. 113 can be used directly as follow

$$\int_0^X \frac{u^{2n}}{\left(r^2 + u^2\right)^{h+1/2}}\, du = \frac{1}{r^{2(h-n)}}\sum_{m=0}^{h-n-1}\frac{(-1)^m}{(2m+2n+1)}\binom{h-n-1}{m}\left(\frac{X}{X_1}\right)^{2m+2n+1} \qquad \text{(A.18)}$$

or

$$T_{2n} = \frac{k^{2n}(h-n-1)!}{r^{2(h-n)}(2n)!}\sum_{m=0}^{h-n-1}\frac{(-1)^m}{(2m+2n+1)(h-m-n-1)!\,m!}\left(\frac{X}{X_1}\right)^{2m+2n+1} \quad \text{for } n < h \qquad \text{(A.19)}$$

It can be noticed that the last equation has a multiple pole singularity $1/r^{2m}$ for $r \to 0$.

Therefore it can be concluded that the integral given in Eq. (A.10) can be solved using Eqs. (A.13), (A.17) and (A.19). For $r = 0$ one may identify that there are two singular functions occurring in the integral of Eq. (A.10): the logarithmic singularity, $ln\ r$ and the multiple pole singularity $1/r^{2h}$. The logarithmic singularity is shown in Eq. (A.17), and the multiple pole singularity is shown in Eq. (A.19). Separation of these singular functions is given in the next Section.

A.3. Separation of Regular and Singular Parts of the Kernel Function

To isolate the logarithmic singular function occurring in Eq. (A.17), one should consider the recurrence function given in Eq. (A.13). If Eq. (A.12) is rewritten as

$$T_{2h} = \frac{-k^{2h}}{(2h)!}\left\{ \ln (X - X_1) \; - \sum_{m=1}^{h} \frac{1}{(2\, m - 1)} \left(\frac{X}{X_1} \right)^{2m-1} \right\} + \; T^*_{2h} \tag{A.20}$$

where the new functions that extract only the singularity function of Eq. (A.17) is

$$T^*_{2h} = \frac{k^{2h}}{(2h)!} \ln r \tag{A.21}$$

and a recursive relation based on Equation (A.13)

$$T^*_m = \; - \; \frac{(k\, r)^2}{(m \; - \; 2h)\; m} \; T^*_{m\,-\,2} \qquad\qquad for \;\; m > \; 2h \tag{A.22}$$

Equation (A.22) can be written for $2n = m > 2h$ in a direct form as follows

$$\begin{aligned} T^*_{2n} &= \; - \; \frac{(k\, r/2)^2}{(n-h)\; n} \; T^*_{2(n-1)} \\ &= \; \frac{-(k\, r/2)^2}{(n-h)\; n} \bullet \frac{-(k\, r/2)^2}{\{(n-1-h)\,(n-1)\}} \bullet \frac{-(k\, r/2)^2}{\{(n-2-h)\,(n-2)\}} \bullet \ldots \bullet \frac{-(k\, r/2)^2}{\{(h+1)1\}} T^*_0 \\ &= (-1)^{n-h} \; \frac{h!}{(2h)!} \; \frac{(k\, r/2)^{2(n-h)}}{(n-h)!\;\; n!} \; k^{2h} \ln r \end{aligned} \tag{A.23}$$

The total summation of T^*_{2n} for $n \; = h$ until ∞ is based on Equation (A.10) and is given as

$$\sum_{n=0}^{\infty} (-1)^n \, T^*_{2n} = (-k^2)^h \; \ln r \; \frac{h!}{(2\,h)!} \; \sum_{n\,=\,h}^{\infty} \frac{(k\, r/2)^{2(n-h)}}{(n-h)!\; n!} \tag{A.24}$$

To simplify Eq. (A.24), one may use the following factorial relations given in Refs. 109 and 112:

$$(2n)! \; = \; 2^{2n} \, n! \, (n-1/2)! \, \pi^{-1.2}$$

$$(2n-1)!! \; = \; 2^n \; \; (n-1/2)! \, \pi^{-1.2}$$

such that

$$(2n)! \;=\; 2^n\, n!\,(2n-1)!! \tag{A.25}$$

Substitution of the last equation into Eq. (A.24) and setting $m = n - h$ gives

$$\sum_{n=h}^{\infty} (-1)^n\, T^*_{2n} = \left(\frac{-k^2}{2}\right)^h \ln r\, \frac{h!}{(2h-1)!!} \sum_{n=h}^{\infty} \frac{(k\,r/2)^{2(n-h)}}{(n-h)!\,n!} \tag{A.26}$$

Equation (A.26) is the total summation for $n = h$ until $n = \infty$ of the logarithmic singular terms occurring in the integral given in Eq. (A.10).

The summation of the multipole singular functions given in Eq. (A.19) can be simplified by the following series T_{2n} for $n = 0$ until $(h - 1)$ as follows

$$T^*_{2n} \;=\; -\frac{k^{2n}\,(h-n-1)!}{r^{2(h-n)}\,(2n)!} \left\{ 2^{h-1-n}\, \frac{(2n-1)!!}{(2h-1)!!} \right\} \qquad \text{for } n < h \tag{A.27}$$

The total summation of T^*_{2n} for $n = 0$ until $(h - 1)$ is

$$\sum_{n=0}^{h-1} (-1)^n\, T^*_{2n} \;=\; \frac{1}{r^{2h}}\, \frac{2^{h-1}}{(2h-1)!!} \sum_{n=h}^{h-1} (-1)^n\, \frac{(h-n-1)!\,(2n-1)!!\,(k\,r/2)^{2n}}{(2n)!\,2^n} \tag{A.28}$$

which can be simplified by using Equation (A.25) to give

$$\sum_{n=0}^{h-1} (-1)^n\, T^*_{2n} = \frac{1}{r^{2h}}\, \frac{2^{h-1}}{(2h-1)!!} \sum_{n=h}^{h-1} (-1)^n\, \frac{(h-n-1)!\;(k\,r/2)^{2n}}{n!} \tag{A.29}$$

Equation (A.26) is the total summation of the multipole singular terms occurring in the integral given in Eq. (A.30).

Therefore it can be concluded that the singular and regular parts of the integral given in Eq. (10) can be written as follows:

$$\int_0^X \frac{\cos\, k\,u}{\left(r^2 + u^2\right)^{h+1/2}}\, du \;=\; \sum_{n=0}^{\infty} (-1)^n\; T_{2n} \tag{A.10}$$

$$= B_{regular}(0, X) \;+\; B_{\text{sin}\,gular}(0, X)$$

$$= \sum_{n=0}^{\infty} (-1)^n\; U_{2n} \;+\; \sum_{n=0}^{\infty} (-1)^n\; T^*_{2n} \tag{A.30}$$

where the U_n term is the T_n term subtracted by the T^*_n term :

$$U_n = T_n - T_n^* \tag{A.31}$$

Substitution of Eqs. (A.19) and (A.27) into Eq. (A.31) for $n < h$ gives

$$U_n = \frac{(h-n-1)!}{(2n)!}\frac{k^{2n}}{r^{2(h-n)}}\left\{2^{h-n-1}\frac{(2n-1)!!}{(2h-1)!!} + \sum_{m=0}^{h-n-1}\frac{(-1)^m X^{m-1}(X/X_1)^{2m+2n+1}}{(2m+2n+1)\,m!\,(h-n-1-m)!}\right\} \quad \text{for } n < h \tag{A.32}$$

Substitution of Eqs. (A.17) and (A.21) into Eq. (A.31) for $n = h$ gives

$$U_{2h} = \frac{-k^{2h}}{(2h)!}\left\{\ln(X_1 - X) - \sum_{m=1}^{h}\frac{1}{2m-1}\left(\frac{X}{X_1}\right)^{2m-1}\right\} \qquad \text{for } n = h \tag{A.33}$$

Substitution of Eqs. (A.13) and (A.22) into Eq. (A.31) for $n > h$ gives

$$U_n = \frac{k(kX)^{n-1}}{(n-h)\,n!\,X_1^{2h-1}} - \frac{(kr)^2}{(n-2h)}U_{n-2} \qquad \text{for } n > 2h \tag{A.34}$$

One may find that the U_n terms given in Eqs. (A.31) – (A.34) are the same as the Ueda series given in Eq. (4.17).

The singular part of the kernel function given in Eq. (A.30) can be evaluated as follows:

$$\begin{aligned} B_{\text{singular}}(0, X) &= \sum_{n=0}^{h-1}(-1)^n T^*_{2n} + \sum_{n=h}^{\infty}(-1)^n T^*_{2n} \\ &= g_b + g_a \end{aligned} \tag{A.35}$$

where, by substituting Eqs. (A.26) and Eq. (A.29) into Eq. (A.35), the two singular functions g_a and g_b are as follows

$$g_a = \left(\frac{-k^2}{2}\right)^h \ln r \,\frac{h!}{(2h-1)!!} \tag{A.36}$$

$$g_b = \frac{1}{2(2h-1)!!}\left(\frac{2}{r^2}\right)^h \sum_{n=0}^{h-1}(-1)^n \frac{(h-n-1)!}{n!}\left(\frac{kr}{2}\right)^{2n} \tag{A.37}$$

where h is the order of the incomplete cylindrical function. In the lifting surface theory, h is equal to 1 and 2 for the planar and non-planar configurations, respectively.

These singular functions g_a and g_b are completely separated from the regular kernel functions. Therefore, the incomplete cylindrical function can be represented by separated regular and singular functions as follows:

$$B_v = B_{v,regular} + B_{v,\mathbf{singular}} \tag{A.38}$$

where

$$B_{v,\mathbf{singular}}(X) = \begin{cases} -2(g_a + g_b) & \text{if } X > 0 \text{ and } r \to 0 \\ 0 & \text{otherwise} \end{cases} \tag{A.39}$$

$$B_{v,\mathbf{regular}}(X) = \begin{cases} +B_v(-X) - 2\sum_{n=0}^{\infty}(-1)^n U_{2n}(-X) & \text{if } X > 0 \text{ and } r \to 0 \\ +B_v(X) & \text{otherwise} \end{cases} \tag{A.40}$$

Equations (A.38) – E (40) are used in the present development of the lifting surface methods. In the lifting surface kernel function for a planar surface configuration, the needed order v of the incomplete cylindrical function is equal to one. Substitution of $v = 1$ into Eqs. (A.38) – E(40) gives

$$B_1 = B_{1,regular} + B_{1,\mathbf{singular}} \tag{A.41}$$

where

$$B_{1,\mathbf{singular}}(X) = \begin{cases} -2(g_a + g_b) & \text{if } X > 0 \text{ and } r \to 0 \\ 0 & \text{otherwise} \end{cases} \tag{A.42}$$

$$B_{1,\mathbf{regular}}(X) = \begin{cases} +B_1(-X) - 2\sum_{n=0}^{\infty}(-1)^n U_{2n}(-X) & \text{if } X > 0 \text{ and } r \to 0 \\ +B_1(X) & \text{otherwise} \end{cases} \tag{A.43}$$

where the singular functions for $v = 1$, $X > 1$ and $r \to 0$ are given as follows:

$$g_a = \frac{-k^2}{2} \ln r \tag{A.44}$$

$$g_b = \frac{-1}{r^2} \tag{A.45}$$

The incomplete cylindrical functions with the order numbers $v = 1$ and $v = 2$ are needed for the formulation of the kernel function of non-planar lifting surfaces. The singular functions for $v = 2$, $X > 1$ and $r \to 0$ can be obtained from Eq. (A.36) and (A.37) as follows:

$$g_a = \frac{k^4}{6} \ln r \tag{A.46}$$

$$g_b = \frac{2}{3\,r^4} - \frac{k^2}{6\,r^2} \tag{A.47}$$

One may find that the singular function consists of elementary function such that it can be evaluated easily. A further application of the singular function in the lifting surface theory is described in Section A.4.

It should be noted that the present procedure to separate the singular and regular parts of the incomplete cylindrical function in frequency domain can be applied also to the one in Laplace domain. On the other hand, the separation procedure based on the previous work of the present author in Ref. 135 is derived for the frequency domain only.

It has been described in Chapter 4 that the incomplete cylindrical function occurring in the formulation of the kernel function in Laplace domain can be written as follows:

$$B_v = \int_{-\infty}^{X} \frac{e^{z\,u}}{\left(r^2 + u^2\right)^{v+1/2}}\, du \tag{A.48}$$

where the non-dimensional Laplace variable z is defined as

$$z = a + i\,k \tag{A.49}$$

One may find that if the real part of z approaches zero than Eq. (48) becomes the incomplete cylindrical function in frequency domain. If a is not zero than the exponential function of the integrand in Eq. (A.48) can be separated into hyperbolic functions as follows:

$$e^{zu} = \sinh(zu) + \cosh(zu) \tag{A.50}$$

The series expansion of the hyperbolic functions are as follows:

$$\cosh\, ku \;=\; \sum_{n=0}^{\infty} \frac{(zu)^{2n}}{(2n)!} \tag{A.51}$$

$$\sinh\, ku \;=\; \sum_{n=0}^{\infty} \frac{(zu)^{2n+1}}{(2n+1)!} \tag{A.52}$$

If we use the procedure similar to Eq. (A.8), the incomplete cylindrical function becomes

$$B_h(|X|) \;=\; \int_0^{-|X|} \frac{e^{zu}}{\left(r^2+u^2\right)^{h+1/2}}\, du \;=\; B_h(-|X|) \;-\; 2\int_0^{-|X|} \frac{\cosh\, zu}{\left(r^2+u^2\right)^{h+1/2}}\, du \tag{A.53}$$

Substitution of Eq. (A.51) into the last integral in Eq. (A.53) gives

$$\int_0^{X} \frac{\cosh\, zu}{\left(r^2+u^2\right)^{h+1/2}}\, du \;=\; \sum_{n=0}^{\infty} T_{2n} \tag{A.54}$$

where

$$T_m \;=\; \frac{z^m}{m!} \int_0^{X} \frac{u^m}{\left(r^2+u^2\right)^{h+1/2}}\, du \tag{A.55}$$

The integral given in Eq. (A.55) is the same as the integral given in Eq. (A.11). Therefore the procedure to separate the singular and regular parts of the incomplete cylindrical function can be performed similarly.

A.4. Integration of Singular and Regular Parts of the Kernel Function

Accurate integration of the kernel function is important in the lifting surface method. It has been described in Chapter 4 that a common approach of the kernel integration in various lifting surface methods is based on the following equation:

$$\Im_{ij}=\frac{\Delta x_s}{8\pi}\int_{-e}^{+e} K\left(x_i-\xi_j, y_i-\eta_j, z_i-\zeta_j, k, M\right) d\hat{y} \tag{A.56}$$

where $\Im$ is the aerodynamic operator, Δx_s, is the panel chord length of element j, e is the panel semi-width of the element j, and K is the kernel function that relates the pressure distribution at point (x_j, y_j, z_j) to the normal-wash at point (x_i, h_i, z_i). Based on Landahl's formulation given in Eq. (4.13), the kernel function for planar multiple lifting surface can be written as follows:

$$K = e^{-ikx_0}\left\{\frac{M e^{ikX}}{R X_1} + B_1\right\} \tag{A.57}$$

and the incomplete cylindrical function B_1 is calculated from Equations (4.13) and (4.14) for $\nu = 1$

$$B_1 = \sum_{n=0}^{\infty} (i)^n U_1 - \frac{k^2}{2}\sum_{n=0}^{\infty} p_n \frac{(k r/2)^{2n}}{n!(n+1)} \tag{A.58}$$

$$p_n = \frac{1}{m} + \frac{1}{2(n+1)} - \gamma - 1n\frac{k}{2} - i\frac{\pi}{2} \tag{A.59}$$

$$U_{1,m\geq 3} = \frac{k(kX)^{m-1}}{(m-2)m!X_1} - \frac{(k r)^2}{(m-2)m} U_{1,m-2} \tag{A.60}$$

$$U_{1,2} = -\frac{k^2}{2}\left\{1n\left(X_1 - X\right) + \frac{X}{X_1}\right\} \tag{A.61}$$

$$U_{1,1} = -\frac{k}{X_1} \tag{A.62}$$

$$U_{1,0} = \frac{1}{X_1(X_1 - X)} \tag{A.63}$$

and

$k = \dfrac{\omega b}{U_\infty}$ = reduced frequency

$$x_o = x - \xi$$
$$y_o = y - \eta \tag{A.64}$$
$$r = | y_o |$$

$$R = \sqrt{x^2 + \beta^2 r^2} \tag{A.65}$$

$$X = (x_o - M R)\beta^{-2}$$

$$b = \sqrt{1 - M^2}$$

$M < 1$ (subsonic)

$$X_1 = \sqrt{X^2 + r^2} \tag{A.66}$$

It has been described in Section A.2. that the singularity problem arises when $r \to 0$ and $X > 0$. The singular part of the function B_{1r} has been separated from the regular part as shown in Eqs. (A.42) - (A.43). Therefore, by substituting Eq. (A.57) with $h = 1$ and $X > 0$ into Eq. (A.63), the kernel function becomes:

$$K = e^{-ikx_0}\left(\frac{M e^{ikX}}{R X_1} + B^*_{1,r} + i B_{1i}\right) + g^*_a + g^*_b \tag{A.67}$$

where

$$g^*_a = g_a * e^{-ikx_0} = e^{-ikx_0} k^2 \ln r \tag{A.68}$$

$$g^*_b = g_a * e^{-ikx_0} = \frac{2}{r^2} e^{-ikx_0} \tag{A.69}$$

In the present work, two integration schemes, *i.e.* for the doublet lattice and doublet point methods, are presented.

A.4.1. Present Doublet Point Method

In the present DPM, the singular functions is integrated with respect to $\hat{y}$ across the sub-interval [-*e*, *e*]. By referring to Fig. (A.2), one may find that x_0 in Eq. (A.69) is also a function of $\hat{y}$ as follows:

$$x_0 = x_m - y_0 \tan \Lambda \tag{A.70}$$

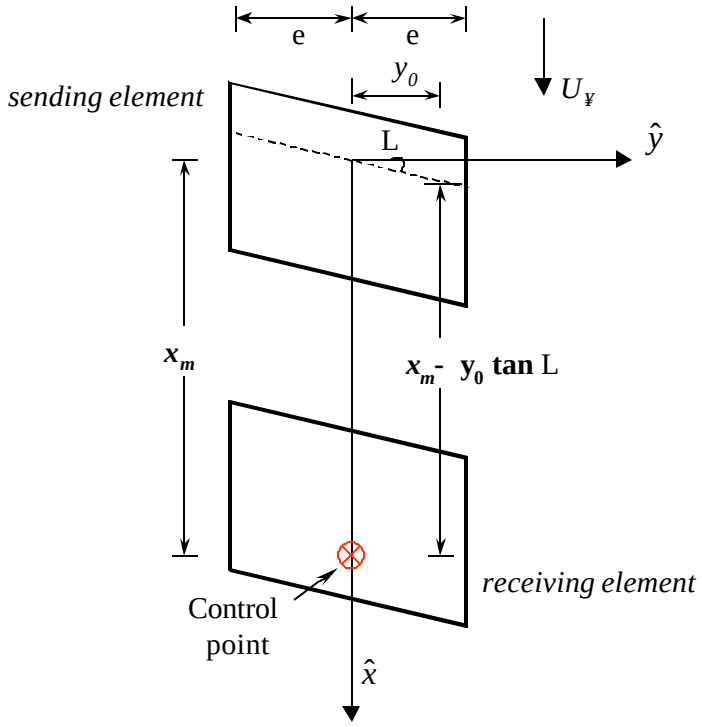


Figure A.2. Control point in the center of downstream panel of the doublet point / doublet-lattice

such that Eqs. (A.68) and (A.69) become

$$g_a^* = e^{-ik(x_m - y_0 \tan \Lambda)} k^2 \ln r \tag{A.71}$$

$$g_b^* = \frac{2}{r^2} e^{-ik(x_m - y_0 \tan \Lambda)} \tag{A.72}$$

Note that g^*_a and g^*_b are no longer ordinary singular functions. Therefore, a procedure should be performed to separate the singular and regular parts of both functions such that the singular part are in terms of ordinary functions.

To separate the singular and regular parts of g^*_b, define a function c_b such that Eq. (A.72) becomes:

$$g_b^* = \frac{2}{r^2} c_b + \frac{2}{r^2}\left(-c_b + e^{-ik(x_m - y_0 \tan\Lambda)}\right) \tag{A.73}$$

and such that the second term in the right hand side of Eq. (A.73) has a finite value or regular for $r \to 0$.:

$$\lim_{r\to 0} \frac{2}{r^2}\left(-c_b + e^{-ik(x_m - y_0 \tan\Lambda)}\right) = g^*_{b,regular} \tag{A.74}$$

By using l'Hospital 's rule to Eq. (A.74), one may find that the function c_b that satisfies the two requirement above is as follows:

$$c_b = (1 + ik\, y_0 \tan\Lambda)\, e^{-ik x_m} \tag{A.75}$$

and the finite value $g^*_{b,regular}$ is

$$g^*_{b,regular} = \lim_{r\to 0} \frac{2}{r^2}\left(-c_b + e^{-ik(x_m - y_0 \tan\Lambda)}\right) = -k^2 \tan^2\Lambda\; e^{ik x_m} \tag{A.76}$$

By using the same steps, define a function c_a to separate the regular and singular parts of g^*_a such that Eq. (A.71) becomes:

$$g_a^* = c_a k^2 \ln r + \left(-c_a + e^{-ik(x_m - y_0 \tan\Lambda)}\right) k^2 \ln r \tag{A.77}$$

and such that the second term in the right hand side of Eq. (A.77) has a finite value or regular for $r \to 0$.:

$$\lim_{r\to 0} \left(-c_a + e^{-ik(x_m - y_0 \tan\Lambda)}\right) k^2 \ln r = g^*_{a,regular} \tag{A.78}$$

By using l'Hospital 's rule to Eq. (A.78), one may find that the function c_a that satisfies the two requirement above is as follows:

$$c_a = e^{-ik x_m} \tag{A.79}$$

and the finite value $g^*_{a,regular}$ is

$$g^{*}_{a,regular} = \lim_{r\to 0} \frac{2}{r^2}\left(-e^{-ikx_m} + e^{-ik(x_m - y_0 \tan\Lambda)}\right) = 0 \qquad \text{(A.80)}$$

Substitution of Eq. (A.71) – (A.80) into Eq. (A.67) gives the expression for the singular and regular parts of the kernel function as follows:

$$K = K_{regular} + K_{singular} \qquad \text{(A.81)}$$

where

$$K_{regular} = e^{-ikx_0}\left(\frac{M\, e^{ikX}}{R\, X_1} + B^{*}_{1,r} + i B_{1\,i} + g^{*}_{b,regular}\right) \qquad \text{(A.82)}$$

$$K_{singular} = e^{-ikx_m}\left(k^2 \ln r + \frac{2(1 + ik\, y_0 \tan\Lambda)}{r^2}\right) \qquad \text{(A.83)}$$

For the regular kernel function, a direct evaluation of the kernel at the center of the panel (Fig. A2), *i.e.* by substitution of $r = 0$ into Eq. (A.82), gives :

$$K_{regular} = \frac{M\, e^{ikX}}{R\, X_1} + i B_{1,i} - B_{1,r}(-X) + k^2\left(\ln\frac{k}{2} + \gamma - \frac{1}{2} - \tan\Lambda\right) \qquad \text{(A.84)}$$

Substitution of Eq. (A.81) into Eq. (A.62) and a Gaussian quadrature technique to integrate the regular function yields

$$\Im_{ij} = \frac{\Delta x_s}{8\pi}\int_{-e}^{+e} K_{\boldsymbol{singular}}\, d\hat{y} + \frac{\Delta x_s}{8\pi}\sum_{n=1}^{N}\left(K_{\boldsymbol{regular}}\right)_n * W_n \qquad \text{(A.84)}$$

where W_n is the Gauss-Legendre weighting factor, and N is the number of integration points.

In the doublet point approach, the number of integration point N is equal to one, *i.e.* only one doublet point at the center of the panel is used. Therefore, the integration of the regular part becomes:

For the singular part, however, a direct evaluation of the kernel function at the center of the panel (Fig. A.2), *i.e.* by substitution of $r = 0$ into Eq. (A.69), will give singularity.

Therefore, the singular kernel function is evaluated as the average of the singular kernel function integrated across the sub-interval [-*e*, *e*] as follows:

$$K_{\boldsymbol{singular}} \approx \frac{1}{2e} \int_{-e}^{+e} K_{\boldsymbol{singular}}(\hat{y})\, d\hat{y} \tag{A.85}$$

Since the integrand is singular, the integration is performed using the Cauchy and Mangler technique where only the principal value of the integration is taken as follows:

$$\int_{-e}^{+e} K_{\boldsymbol{singular}}\, d\hat{y} = -\frac{4}{e} + 2ek^2\left(-1 + \ln e\right) \tag{A.86}$$

Equations (A.84) and (A.86) are the equations used in the present doublet point method. One may combine both equations and divide the results by the panels width *2e* to give:

$$\frac{1}{2e}\int_{-e}^{+e}\left(K_{\boldsymbol{singular}} + K_{regular}\right) d\hat{y} \approx \frac{M e^{ikX}}{R X_1} + B_{1,\,regular} + k^2\left[\ln\frac{ke}{2} + \gamma - \frac{3}{2} - \tan^2\Lambda\right] - \frac{2}{e^2} \tag{A.87}$$

To compare with Ueda and Dowell's DPM formulation[66] , we may write $B_1(X>0)$, based on Eq. (A.87) as follows:

$$B_1(X>0) \approx B_1(-X) + k^2\left[\ln\frac{ke}{2} + \gamma - \frac{3}{2} - \tan^2\Lambda\right] - \frac{2}{e^2} \tag{A.88}$$

On the other hand, Ueda and Dowell formulation[66] is

$$B_1(X>0) \approx -B_{1,real}(-X) + i\,B_{1,imag} + k^2\left[\ln\frac{ke}{2} + \gamma - \frac{3}{2}\right] - \frac{2}{e^2} \tag{A.89}$$

Therefore, the present formulation has additional term associated with the element sweep angle Λ. The correction may be significant if the reduced frequency or the sweep angle is large.

A.4.2. Present Doublet-Lattice Method (DLM)

In the DPM, the pressure load is concentrated at a single doublet point, and therefore it requires a treatment to separate g^*_a and g^*_b functions in Section A.4.1. On the other hand, in the present DLM, the pressure load is concentrated along the doublet-lattice, and therefore no further treatment for g^*_a and g^*_b is needed. Substitution of Eqs. (A.67) – (A.69) into Eq. (A.62) and performing a Gaussian quadrature technique to integrate the regular function yields

$$\Im_{ij}=\frac{\Delta x_s}{8\pi}\int_{-e}^{+e} K_{\textbf{\textit{singular}}}\, d\hat{y} \;+\; \frac{\Delta x_s}{8\pi}\sum_{n=2}^{N}\left(K_{\textbf{\textit{regular}}}\right)_n * W_n \tag{A.90}$$

where the number of integration points N is selected based on Table 4.1. The regular kernel function is

$$K_{regular} \;=\; e^{-ikx_0}\left[\frac{M\, e^{ikX}}{R\, X_1} + B_1\right] \tag{A.91}$$

where the function B_1 can be obtained from Eq. (A.59).

The singular kernel function, based on Eq. (A.68) and (A.69), is

$$K_{\textbf{\textit{singular}}} \;=\; g^*_a \;+\; g^*_b \tag{A.92}$$

The integration of $K_{singular}$ along the sub-interval [- e, e] can be performed based on an expansion series to the exponential function as follows:

$$e^{\lambda x} \;=\; \sum_{n=0}^{\infty}\frac{\lambda^n}{n!}x^n \tag{A.93}$$

Substitution of Eq. (A.93) into the integration of g^*_b gives:

$$\begin{aligned}\int_{-e}^{+e} g^*_b\, d\hat{y} &= 2\, e^{-ik\,x_m}\int_{-e}^{e}\frac{e^{\lambda\hat{y}}}{\hat{y}^2}\, d\hat{y}\\ &= 2\, e^{-ik\,x_m}\sum_{n=0}^{\infty}\frac{\lambda^n}{n!}\int_{-e}^{e}\hat{y}^{n-2}d\,\hat{y}\end{aligned} \tag{A.94}$$

where

$$\lambda = -ik\tan\Lambda \tag{A.95}$$

for n > 2, the solution of the integral in Eq. (A.95) is straight forward, *i.e.*

$$\int_{-e}^{e} \hat{y}^{n-2}\, d\hat{y} = \begin{cases} \dfrac{2(e)^{n-1}}{n-1} & \text{if } n \text{ is even number} \\ 0 & \text{if } n \text{ is odd number} \end{cases} \tag{A.96}$$

For n=0 and 1, the integrals are singular and therefore the Mangler and Cauchy principal values should be taken as follows:

$$\int_{-e}^{e} \frac{1}{\hat{y}^2}\, d\hat{y} = \frac{2}{e}$$
$$\int_{-e}^{e} \frac{1}{\hat{y}}\, d\hat{y} = 0 \tag{A.97}$$

Substitution of Eqs. (A.96) and (A.97) into Eq. (A.94) gives:

$$\int_{-e}^{+e} g_b^*\, d\hat{y} = 4\, e^{-ikx_m} \sum_{n=0}^{\infty} \frac{(ik\,e\tan\Lambda)^{2n}}{n!(2n-1)e} \tag{A.98}$$

The same procedure is performed to integrate the function g^*_a. The integration result is as follows:

$$\int_{-e}^{+e} g_a^*\, d\hat{y} = 2\, e^{-ikx_m} \left\{ \frac{\sin(k\,e\tan\Lambda)}{\tan\Lambda}\, k\ln e - k^2 \sum_{n=0}^{\infty} \frac{(ik\,e\tan\Lambda)^{2n}\, e}{(2n+1)!\,(2n+1)} \right\} \tag{A.99}$$

By combining Eqs. (A.98) and (A.99), the analytical integration of the singular part of the kernel function for the DLM is given as follows:

$$\int_{-e}^{+e} K_{\text{sin}\,gular}\; d\hat{y} = 2\, e^{-i\,k\,x_m} \left\{ \frac{\sin\left(k\, e \tan\Lambda\right)}{\tan\Lambda}\, k \ln e + \sum_{n=0}^{\infty} \frac{\left(i\, k\, e \tan\Lambda\right)^{2n}}{\left(2\, n\right)!} \left(\frac{2}{e\,(2n-1)} - \frac{k^2\, e}{(2n+1)^2} \right) \right\}$$

(A.100)

Appendix B

Aeroelastic Stability Envelope

An airplane must be designed to be free from aeroelastic stability, such as flutter and divergence, within a minimum flight envelope required by the Federal Aviation Administration (FAA). To obtain the minimum flight envelope, one should, at least, refer to two sections of Federal Aviation Regulation (FAR)[216] given as follows:

- FAR § 25.629 that describes the aeroelastic stability requirements
- FAR § 25.335 that describes design air speeds

According to FAR § 25.629, the aeroelastic stability envelope V_E or M_E at each altitude should be obtained as follows:

- For a normal condition (without any failure):

$$\begin{aligned} V_E &\geq 1.15\ V_D \\ M_E &\geq 1.15\ M_D \end{aligned} \tag{B.1}$$

- For a failure condition:

$$\begin{aligned} V_E &\geq V_D \\ M_E &\geq M_D \end{aligned} \tag{B.2}$$

where V_E and M_E are air speed and Mach number for the flight envelope, respectively. V_D and M_D are dive speed and dive Mach number, respectively. The failure condition includes malfunction of flutter damper system and failure of any single element of the frame structure

supporting engine, independently mounted propeller shaft, large auxiliary power unit, or large externally mounted aerodynamic body (such as an external fuel tank).

The dive speed can be obtained from FAR § 25.335 as follows:

$$V_D \geq V_c / 0.8$$
$$M_D \geq M_c / 0.8 \tag{B.3}$$

where V_C and M_C are the design cruising speed and Mach number. In addition, the minimum speed margin between V_C / M_C and V_D / M_D should be enough to provide for atmospheric variations, such as horizontal gusts, and penetration of jet streams and cold fronts. More detailed description of the dive speed and aeroelastic stability requirement may refer to Ref. 216. It should be noted that V_C., V_D and V_E given in Eqs. (B.1) – (B.3) are calculated as equivalence air speeds (EAS). Equations (B.1) – (B.3) are used in the present work to construct the aeroelastic stability envelope of the strut-braced wing presented in Chapters 2 and 5.

Appendix C

Minimum Denominator Rational Function

C.1 Introduction

A minimum denominator rational function (MDRF) is defined in this Appendix as a sum of polynomial functions and rational function terms with minimum denominators, i.e. the denominator is a polynomial function of x having only one root. A general expression of the MDRF function can be written as follow

$$\frac{\sum_{j=0}^{N_e} e_j x^j}{\prod_{j=1}^{N} \left(x - c_j\right)^{m_j}} = \sum_{j=1}^{N} \frac{a_j}{\left(x - c_j\right)^{m_j}} + \sum_{j=1}^{N} \sum_{k=1}^{m_j - 1} \frac{d_{jk}}{\left(x - c_j\right)^{k}} + \sum_{j=0}^{N_e - N_{tot}} b_j x^j \qquad \text{(C.1)}$$

where the right hand side of Eq. (C.1) is a general rational function and the left-hand side the MDRF functions. N_{tot} is the total number of multiple-roots c_j , which is defined as

$$N_{tot} = \sum_{j=1}^{N} m_j \qquad \text{(C.2)}$$

The MDRF function is important in the present work to transform the general rational function, described in Chapter 2 for the Euler Lagrange differential equation of the non-linear beam element, into a sum of simple rational function and/or polynomial function forms. The transformation into simpler forms is an important key in the present finite element codes, since an analytical solution to the differential equation can be performed by direct integration to the MDRF function.

Present derivations of the MDRF function are given gradually from some elementary functions into a more general form. Three cases related to Chapter 2 are described in the following sections.

C.2. Case 1. MDRF with $N_e = 1$, $N = 1$, and $m_1 = 1$

This simplest case is related to the formulation of the flexural stiffness matrix of a beam with a linear variation of the stiffness distribution. Equation (C.1) for this case can be written as

$$\frac{e_0 + e_1 x}{x - c_1} = \frac{a_1}{x - c_1} + b_0 \tag{C.3}$$

The coefficient a_1 can be obtained directly by multiplying both sides of Eq. (C.3) by $(x - c_k)$,

$$e_0 + e_1 x = a_1 + b_0 (x - c_1) \tag{C.4}$$

and substituting $x = c_1$ to give

$$a_1 = e_0 + e_1 c_1 \tag{C.5}$$

For this simple case, the coefficient b_0 can be obtained directly by equating both sides of Eq. (C.4) to give

$$b_0 = e_1 \tag{C.6}$$

However, for more complicated cases (see Case 3), the coefficient b_j may not be easily obtained by direct application of the equality rule above. In the present work, it is proposed to find b_0 from Eq. (C.4) by substituting an arbitrary number x_0 to replace x, and then solving the problem for b_0:

$$b_0 = -\frac{e_0 + e_1 x_0 - a_1}{(x_0 - c_1)} \tag{C.7}$$

where, after substituting a_1 from Eq. (C.5), the result for b_0 is the same as previously obtained in Eq. (C.6). Obviously, from Eq. (C.7), x_0 can be selected arbitrarily but it is required not to be the same as the root c_1

C.3. Case 2. MDRF with $N_e < N_{tot}$ and $m_j = 1$, $1 < j \leq N$

This case is related to the formulation of the flexural stiffness matrix of a beam with a non-linear variation of the stiffness distribution. The stiffness function is an N^{th} order polynomial function with no multiple root. For $N = 3$, the cubic polynomial function of the stiffness distribution is useful for the problem where a cubic spline approximation is used to approximate the beam stiffness distribution. Equation (C.1) for this case can be written as:

$$\frac{\sum_{j=0}^{N_e} e_j x^j}{\prod_{j=1}^{N} (x - c_j)} = \sum_{j=1}^{N} \frac{a_j}{(x - c_j)} \tag{C.8}$$

Note that in Eq. (C.8) there is no b_j terms since $N_e < N_{tot}$, and no d_{jk} terms since $m_j = 1$.

Similar to Case 1, the coefficients a_k, can be obtained directly by multiplying both sides of Eq. (C.8) by $(x - c_k)$ to give

$$\frac{\sum_{j=0}^{N_e} e_j x^j}{\prod_{\substack{j=1 \\ j \neq k}}^{N} (x - c_j)} = a_k + (x - c_k) \sum_{\substack{j=1 \\ j \neq k}}^{N} \frac{a_j}{(x - c_j)} \tag{C.9}$$

and substituting $x = c_k$ into Eq. (C.10) to give

$$a_k = \frac{\sum_{j=0}^{N_e} e_j c_k^j}{\prod_{\substack{j=1 \\ j \neq k}}^{N} (c_k - c_j)} \tag{C.10}$$

C.4. Case 3. MDRF with $N_e < N_{tot}$

This case is related to the formulation of the flexural stiffness matrix of a beam with a non-linear variation of the stiffness distribution. The order of the polynomial function with some multiple roots is N_{tot}. For $N_e = 1$, the solution is used to derive the stiffness matrix of

the nonlinear beam, such as the one presented in Ref. C2. Equation (C.1) for this case can be written as:

$$\frac{\sum_{j=0}^{N_e} e_j x^j}{\prod_{j=1}^{N} (x-c_j)^{m_j}} = \sum_{j=1}^{N} \frac{a_j}{(x-c_j)^{m_j}} + \sum_{j=1}^{N} \sum_{k=1}^{m_j-1} \frac{d_{jk}}{(x-c_j)^k} \tag{C.11}$$

Similar to Case 2, the coefficients a_k, can be obtained directly by multiplying both sides of Eq. (C.11) by $(x - c_k)^{m_k}$ to give

$$\frac{\sum_{j=0}^{N_e} e_j x^j}{\prod_{\substack{j=1 \\ j\neq k}}^{N} (x-c_j)^{m_j}} = a_k + (x-c_k)^{m_k} \left(\sum_{\substack{j=1 \\ j\neq k}}^{N} \frac{a_j}{(x-c_j)^{m_j}} + \sum_{j=1}^{N} \sum_{i=1}^{m_j-1} \frac{d_{ji}}{(x-c_j)^i} \right) \tag{C.12}$$

and substituting $x = c_k$ into Eq. (C.12) to give

$$a_k = \frac{\sum_{j=0}^{N_e} e_j c_k^j}{\prod_{\substack{k=1 \\ k\neq j}}^{N} (c_k - c_j)^{m_j}} \tag{C.13}$$

In the present Case, two procedures to find the coefficient d_{jk} are presented, including a direct differentiation procedure and a substitution procedure.

1. Direct Differentiation Method

The first procedure is a direct procedure where d_{ab}, is calculated one-by-one by direct differentiation. To calculate effectively, the procedure should be started from the highest rank of the second index $\boldsymbol{k}$ of the coefficient $d_{j\boldsymbol{k}}$, i.e. in Eq. (C.11) the highest rank is $m_j - 1$. To start calculation for the coefficient d_{ab}, multiply Eq. (C.11) by $(x - c_a)^{m_a}$ to give

$$\frac{\sum_{j=0}^{N_e} e_j x^j}{\prod_{\substack{j=1 \\ j\neq a}}^{N} (x-c_j)^{m_j}} = a_a + \sum_{k=1}^{m_a-1} d_{ai}(x-c_a)^{m_a-k} + (x-c_a)^{m_a}\left(\sum_{\substack{j=1 \\ j\neq a}}^{N}\frac{a_j}{(x-c_j)^{m_j}} + \sum_{\substack{j=1 \\ j\neq a}}^{N}\sum_{k=1}^{m_j-1}\frac{d_{jk}}{(x-c_j)^k}\right) \tag{C.14}$$

To find d_{ab} for$b = m_a$ - 1, differentiate Eq. (14) once to give

$$\begin{aligned}\frac{d}{dx}\left(\frac{\sum_{j=0}^{N_e} e_j x^j}{\prod_{\substack{j=1 \\ j\neq a}}^{N} (x-c_j)^{m_j}}\right) = {} & 0 + d_{a,m_a-1} + \sum_{k=1}^{m_a-2} d_{ai}(m_a-k)(x-c_a)^{m_a-k-1} + \\ & (x-c_a)^{m_a}\frac{d}{dx}\left(\sum_{\substack{j=1 \\ j\neq a}}^{N}\frac{a_j}{(x-c_j)^{m_j}} + \sum_{\substack{j=1 \\ j\neq a}}^{N}\sum_{k=1}^{m_j-1}\frac{d_{jk}}{(x-c_j)^k}\right) + \\ & m_a(x-c_a)^{m_a-1}\frac{d}{dx}\left(\sum_{\substack{j=1 \\ j\neq a}}^{N}\frac{a_j}{(x-c_j)^{m_j}} + \sum_{\substack{j=1 \\ j\neq a}}^{N}\sum_{k=1}^{m_j-1}\frac{d_{jk}}{(x-c_j)^k}\right)\end{aligned} \tag{C.15}$$

Substitution of $x = c_a$ into Eq. (C.15) gives:

$$d_{a,m_a-1} = \frac{d}{dx}\left(\frac{\sum_{j=0}^{N_e} e_j x^j}{\prod_{\substack{j=1 \\ j\neq a}}^{N} (x-c_j)^{m_j}}\right)\Bigg|_{x=c_a} \tag{C.16}$$

To find the next coefficient d_{ab} for $b = m_a$ - 2, differentiate Eq. (C.15) once and perform the same procedure. Therefore, it can be shown that d_{ab} can be obtained by the following formula:

$$d_{ab} = \frac{1}{(m_a - ß)!} \frac{d^{m_a - b}}{d x^{m_a - b}} \left(\frac{\sum_{j=0}^{N_e} e_j x^j}{\prod_{\substack{j=1 \\ j \neq a}}^{N} (x - c_j)^{m_j}} \right) \Bigg|_{x = c_a} \qquad \text{(C.17)}$$

2. A Substitution Procedure

Equation (C.17) for calculating the coefficients d_{jk} is used when a symbolic package solver such as *Mathematica*[C3] is available. As an alternate formula suitable for FORTRAN or C computer programming languages, the procedure introduced in Case 1 is used. The detail of the procedures to solve Eq. (C.11) for d_{jk} are as follows:

1. The coefficient a_j should be obtained first, i.e. by using Eq. (C.10).
2. Rearrange Eq. (C.11) by moving the set of rational functions containing a_j into the left hand side of Eq. (C.11).

$$\frac{\sum_{j=0}^{N_e} e_j x^j}{\prod_{j=1}^{N} (x - c_j)^{m_j}} - \sum_{j=1}^{N} \frac{a_j}{(x - c_j)^{m_j}} = \sum_{j=1}^{N} \sum_{k=1}^{m_j - 1} \frac{d_{jk}}{(x - c_j)^k} \qquad \text{(C.18)}$$

If the variable x in Eq. (C.18) can be selected arbitrarily, the unknown parameters in Eq. (C.18) are the d_{jk}. The total number of d_{jk} is N_d where

$$N_d = \sum_{j=1}^{N} (m_j - 1) \qquad \text{(C.19)}$$

3. Therefore, to obtain the d_{jk} we need to select as many as N_d number of $x = x_{jk}$. Note that x_{jk}, can be selected arbitrarily but should not be equal to the roots c_j.
4. Substitute each of $x = x_{jk}$ into Eq. (C.18) to form an N_d set of linear equations with the d_{jk} as the unknown.

In a matrix form, the coefficient d_{jk} can be computed as a vector from the following equation:

$$\{ d \} = [D]^{-1} \{ g \} \tag{C.20}$$

where $\{ d \}$ and $\{ g \}$ can be divided into N-submatrices $\{ d^*_j \}$ and $\{ g^*_j \}$ respectively defined as follows

$$\{ d \} = \begin{Bmatrix} \{d^*_1\} \\ \{d^*_2\} \\ \cdot \\ \cdot \\ \{d^*_j\} \\ \cdot \\ \cdot \\ \{d^*_N\} \end{Bmatrix} ; \{ g \} = \begin{Bmatrix} \{g^*_1\} \\ \{g^*_2\} \\ \cdot \\ \cdot \\ \{g^*_j\} \\ \cdot \\ \cdot \\ \{g^*_N\} \end{Bmatrix} \tag{C.21}$$

and $[D]$ is divided into N-by-N submatrices $[D^*_{jk}]$ defined as follows

$$[D] = \begin{bmatrix} [D^*_{11}] & [D^*_{12}] & \cdots & \cdots & [D^*_{1,N}] \\ [D^*_{21}] & [D^*_{22}] & \cdots & \cdots & \vdots \\ [D^*_{j1}] & \cdots & [D^*_{jk}] & \cdots & [D^*_{j,N}] \\ \cdots & \cdots & \cdots & \cdots & \cdots \\ [D^*_{N,1}] & \cdots & \cdots & \cdots & [D^*_{N,N}] \end{bmatrix} \tag{C.22}$$

The sub-matrices $\{ d^*_j \}$, $\{ g^*_j \}$ and $[D^*_{jk}]$, can be obtained as

$$\{d^*_j\} = \begin{Bmatrix} d_{j1} \\ d_{j2} \\ \cdot \\ \cdot \\ d_{jk} \\ \cdot \\ \cdot \\ d_{j,m_j-1} \end{Bmatrix} ; \{g^*_j\} = \begin{Bmatrix} g_{11} \\ g_{12} \\ \cdot \\ \cdot \\ g_{jk} \\ \cdot \\ \cdot \\ g_{j,m_j-1} \end{Bmatrix} \tag{C.23}$$

$$\left[D^{*}_{jk} \right] = \begin{bmatrix} \frac{1}{x_{k,1}-c_j} & \frac{1}{(x_{k,1}-c_j)^2} & \cdots & \frac{1}{(x_{k,1}-c_j)^t} & \cdots & \frac{1}{(x_{k,1}-c_j)^{m_j-1}} \\ \frac{1}{x_{k,2}-c_j} & \frac{1}{(x_{k,2}-c_j)^2} & \cdots & \frac{1}{(x_{k,2}-c_j)^t} & \cdots & \frac{1}{(x_{k,2}-c_j)^{m_j-1}} \\ \cdots & \cdots & \cdots & \cdots & \cdots & \cdots \\ \frac{1}{x_{k,s}-c_j} & \frac{1}{(x_{k,s}-c_j)^2} & \cdots & \frac{1}{(x_{k,s}-c_j)^t} & \cdots & \frac{1}{(x_{k,s}-c_j)^{m_j-1}} \\ \cdots & \cdots & \cdots & \cdots & \cdots & \cdots \\ \frac{1}{x_{k,m_j-1}-c_j} & \frac{1}{(x_{k,m_j-1}-c_j)^2} & \cdots & \frac{1}{(x_{k,m_j-1}-c_j)^t} & \cdots & \frac{1}{(x_{k,m_j-1}-c_j)^{m_j-1}} \end{bmatrix} \quad \text{(C.24)}$$

where the vector element g_{jk} in Eq. (C.21) can be obtained as

$$g_{jk} = \frac{e_0 + e_1 x_j}{\prod_{\substack{i=1 \\ i \neq j}}^{N} (x_{k,j} - c_i)^{m_j}} - \sum_{i=1}^{N} \frac{a_i}{(x_{k,j} - c_i)} \quad \text{(C.25)}$$

C.5. Case 4. MDRF with $N_e > N_{tot}$

This case is not related to the formulation of the stiffness matrix of the beam, but is related to the formulation of a vector load for a nonuniform beam element subjected to nonuniform load distributions. Since the polynomial order of the numerator N_e in Eq. (C.1) is larger than that of the denominator N_{tot}, additional step is required to calculate the b_j coefficients. This step can be performed directly for low numbers of N_e and N_{tot} by using the equality rule as given in Section C2. For high numbers of N_e and N_{tot}, however, the substitution procedure given in Section C4 is easier to use. The detail of the procedure is as follows:

1. The coefficient a_j should be obtained first, i.e. by using Eq. (C.10).
2. Rearrange Eq. (C.1) by moving the set of rational functions containing a_j into the left hand side of Eq. (C.11).

$$\frac{\sum_{j=0}^{N_e} e_j x^j}{\prod_{j=1}^{N} (x-c_j)^{m_j}} - \sum_{j=1}^{N} \frac{a_j}{(x-c_j)^{m_j}} = \sum_{j=1}^{N} \sum_{k=1}^{m_j-1} \frac{d_{jk}}{(x-c_j)^k} + \sum_{j=0}^{N_e-N_{tot}} b_j x^j \qquad \text{(C.26)}$$

If the variable x in Eq. (C.26) can be selected arbitrarily, the unknown parameters are the d_{jk} and bj. The total number of d_{jk} is N_d as given Eq. (19). The total number of b_j is N_b defined as

$$N_b = N_e - N_{tot} + 1 \qquad \text{(C.27)}$$

3. Therefore, to obtain the d_{jk} and b_j we need to select as many as (N_d + N_b - 1) number of x = x_{jk}. Note that $x_{jk,}$ can be selected arbitrarily but should not be equal to the roots c_j.
4. Substitute each of x = x_{jk} into Eq. (C.26) to form a (N_d + N_b) set of linear equations with the d_{jk} and b_j as the unknowns.

In a matrix form, the coefficient d_{jk} and b_j can be computed as a vector from the following equation:

$$\{ d \} = [D]^{-1} \{ g \} \qquad \text{(C.28)}$$

where { d } and { g } can be divided into N-submatrices { d^*_j }and { g^*_j } respectively defined as follows

$$\{ d \} = \begin{Bmatrix} \{d^*_1\} \\ \{d^*_2\} \\ \cdot \\ \cdot \\ \{d^*_j\} \\ \cdot \\ \cdot \\ \{d^*_N\} \\ \{b^*\} \end{Bmatrix} \quad ; \quad \{ g \} = \begin{Bmatrix} \{g^*_1\} \\ \{g^*_2\} \\ \cdot \\ \cdot \\ \{g^*_j\} \\ \cdot \\ \cdot \\ \{g^*_N\} \\ \{g^*_b\} \end{Bmatrix} \qquad \text{(C.29)}$$

and [D] is divided into four sub-matrices as follows

$$[D] = \begin{bmatrix} D_{dd} & D_{db} \\ D_{bd} & D_{bb} \end{bmatrix} \tag{C.30}$$

where

$$[D_{dd}] = \begin{bmatrix} [D^*_{11}] & [D^*_{12}] & \cdots & \cdots & [D^*_{1,N}] \\ [D^*_{21}] & [D^*_{22}] & \cdots & \cdots & \vdots \\ [D^*_{j1}] & \cdots & [D^*_{jk}] & \cdots & [D^*_{j,N}] \\ \cdots & \cdots & \cdots & \cdots & \cdots \\ [D^*_{N,1}] & \cdots & \cdots & \cdots & [D^*_{N,N}] \end{bmatrix} \tag{C.31}$$

$$[D_{db}] = \begin{bmatrix} [D^*_{1b}] \\ [D^*_{2b}] \\ \cdots \\ [D^*_{jb}] \\ \cdots \\ [D^*_{Nb}] \end{bmatrix} \tag{C.32}$$

$$[D_{bd}] = \begin{bmatrix} [D^*_{b1}] & [D^*_{b2}] & \ldots & [D^*_{bj}] & \ldots & [D^*_{bN}] \end{bmatrix} \tag{C.32}$$

$$[D_{bb}] = \begin{bmatrix} 1 & x_{N+1,N+1} & x^2_{N+1,N+2} & \ldots & x^j_{N+1,N+j} & \ldots & x^{N_b-1}_{N+1,N_b-1} \\ 1 & x_{N+2,N+1} & x^2_{N+2,N+2} & \ldots & x^j_{N+2,N+j} & \ldots & x^{N_b-1}_{N+2,N_b-1} \\ \ldots & \ldots & \ldots & \ldots & \ldots & \ldots & \ldots \\ 1 & x_{N+j,N+1} & x^2_{N+j,N+2} & \ldots & x^j_{N+j,N+j} & \ldots & x^{N_b-1}_{N+j,N_b-1} \\ \ldots & \ldots & \ldots & \ldots & \ldots & \ldots & \ldots \\ 1 & x_{N_b-1,N+1} & x^2_{N_b-1,N+2} & \ldots & x^j_{N_b-1,N+j} & \ldots & x^{N_b-1}_{N_b-1,N_b-1} \end{bmatrix} \tag{C.33}$$

The sub-matrices { d^*_j } , { g^*_j } and [D^*_{jk}] , can be obtained as

$$\left\{ d_j^* \right\} = \begin{Bmatrix} d_{j1} \\ d_{j2} \\ . \\ . \\ d_{jk} \\ . \\ . \\ d_{j,m_j-1} \end{Bmatrix} \; ; \left\{ g_j^* \right\} = \begin{Bmatrix} g_{11} \\ g_{12} \\ . \\ . \\ g_{jk} \\ . \\ . \\ g_{j,m_j-1} \end{Bmatrix} \tag{C.34}$$

$$g_{jk} = \frac{e_0 + e_1 \, x_j}{\prod_{\substack{i=1 \\ i \neq j}}^{N} \left(x_{k,j} - c_i \right)^{m_j}} \quad - \quad \sum_{i=1}^{N} \frac{a_i}{\left(x_{k,j} - c_i \right)} \tag{C.35}$$

$$\left[D_{jk}^* \right] = \begin{bmatrix} \frac{1}{x_{k,1} - c_j} & \frac{1}{\left(x_{k,1} - c_j \right)^2} & \cdots & \frac{1}{\left(x_{k,1} - c_j \right)^t} & \cdots & \frac{1}{\left(x_{k,1} - c_j \right)^{m_j - 1}} \\ \frac{1}{x_{k,2} - c_j} & \frac{1}{\left(x_{k,2} - c_j \right)^2} & \cdots & \frac{1}{\left(x_{k,2} - c_j \right)^t} & \cdots & \frac{1}{\left(x_{k,2} - c_j \right)^{m_j - 1}} \\ \cdots & \cdots & \cdots & \cdots & \cdots & \cdots \\ \frac{1}{x_{k,s} - c_j} & \frac{1}{\left(x_{k,s} - c_j \right)^2} & \cdots & \frac{1}{\left(x_{k,s} - c_j \right)^t} & \cdots & \frac{1}{\left(x_{k,s} - c_j \right)^{m_j - 1}} \\ \cdots & \cdots & \cdots & \cdots & \cdots & \cdots \\ \frac{1}{x_{k,m_j - 1} - c_j} & \frac{1}{\left(x_{k,m_j - 1} - c_j \right)^2} & \cdots & \frac{1}{\left(x_{k,m_j - 1} - c_j \right)^t} & \cdots & \frac{1}{\left(x_{k,m_j - 1} - c_j \right)^{m_j - 1}} \end{bmatrix} \tag{C.36}$$

Appendix D

Translation of Axis Procedure

Most of the following translation axis procedure is a summary of the concept described in Ref. 7. The procedure is used in Chapter 2 of the present work to simplify the construction of the stiffness matrix of a beam element from its flexibility matrix. Among other methods, this procedure is suitable for the present work because of the following advantages:

(1) The 12-by-12 element stiffness matrix is constructed by only inverting a 2-by-2 flexibility matrix and performing some simple matrix multiplications. This procedure is derived in Ref. 7.

(2) The procedure (1) of Ref. 7 is further modified and exploited in the present work. Direct matrix inversion and multiplication are avoided such that the 12-by-12 stiffness matrix can be constructed only from 5 independent coeffients, i.e. three of the coefficients are related to flexural stiffness, and two of the rest are related to axial and torsional stiffnesses. The application of the present procedure to formulate the stiffness matrix of the non-uniform beam is described in Chapter 2.

(3) The need to calculate only 5 independent variables is an important step in the present work to reduce the computational time..

D.1. Static Equivalence Translation

Consider a force vector P_a and a moment vector M_a at point a as shown in Fig. D.1. The actions at point a can be computed from their static equivalence P_b and M_b actions at other point b based on the following expressions:

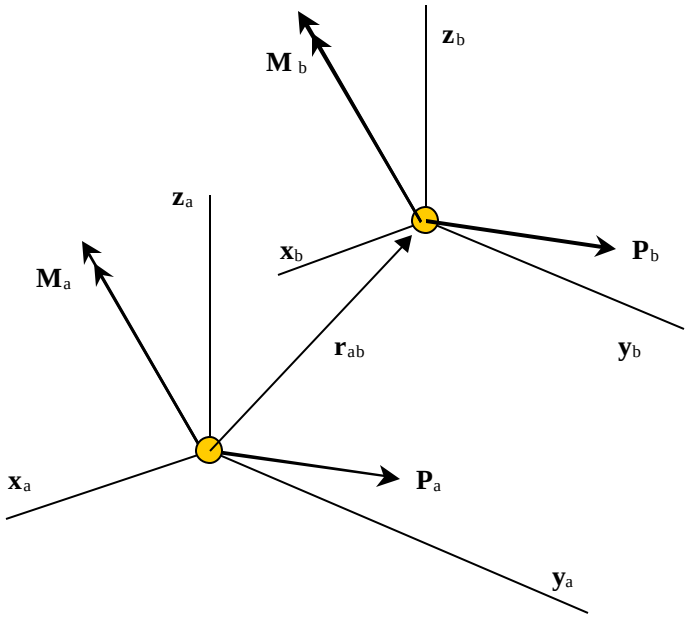


Figure D.1 Translation of axes for (P_a, M_a) and its static equivalence (P_b, M_b)

$$\begin{aligned} P_a &= P_b \\ M_a &= r_{ab} \times P_b + M_b \end{aligned} \tag{D1}$$

or, in matrix notations:

$$\begin{Bmatrix} P_a \\ M_a \end{Bmatrix} = T_{ab} \begin{Bmatrix} P_b \\ M_b \end{Bmatrix} = \begin{bmatrix} I_3 & 0 \\ c_{ab} & I_3 \end{bmatrix} \begin{Bmatrix} P_b \\ M_b \end{Bmatrix} \tag{D2}$$

where I_3 is a 3-by-3 identity matrix, the vector r_{ab} is

$$\overrightarrow{r_{ab}} = x_{ab}\ \hat{i} + y_{ab}\ \hat{j} + x_{ab}\ \hat{k} \tag{D3}$$

and c_{ab} is a skew-symmetric matrix given as:

$$c_{ab} = \begin{bmatrix} 0 & -z_{ab} & y_{ab} \\ z_{ab} & 0 & -x_{ab} \\ -y_{ab} & x_{ab} & 0 \end{bmatrix} \tag{D4}$$

A reverse transformation, i.e. from point b to a, can be written as

$$\begin{Bmatrix} P_b \\ M_b \end{Bmatrix} = T_{ab}^{-1} \begin{Bmatrix} P_b \\ M_b \end{Bmatrix} = \begin{bmatrix} I_3 & 0 \\ c_{ba} & I_3 \end{bmatrix} \begin{Bmatrix} P_a \\ M_a \end{Bmatrix} \tag{D5}$$

where

$$c_{ba} = -c_{ab} \tag{D6}$$

D.2. Kinematic Equivalence Translation

Similar to the above procedure, a kinematic relationship between displacements at two different points on a rigid body can be expressed in a matrix form. Consider a displacement vector u_a and a rotation vector q_a at point a. The displacements at point a can be computed from their kinematic equivalence u_b and q_b displacements at other point b based on the following expressions:

$$\begin{aligned} u_a &= u_b + q_b \times r_{ab} \\ q_a &= q_b \end{aligned} \tag{D7}$$

or, in matrix notations:

$$\begin{Bmatrix} u_a \\ ?_a \end{Bmatrix} = T_{ab}^T \begin{Bmatrix} u_b \\ ?_b \end{Bmatrix} = \begin{bmatrix} I_3 & c_{ab}^T \\ 0 & I_3 \end{bmatrix} \begin{Bmatrix} u_b \\ ?_b \end{Bmatrix} \tag{D8}$$

where

$$c_{ab}^T = -c_{ab} \tag{D9}$$

D.3 Stiffness Matrix Construction

Figure D.2 shows a beam element with six degree of freedom displacements at each end. The relationship between displacements and actions have the following forms:

$$\begin{Bmatrix} R_a \\ R_b \end{Bmatrix} = \begin{bmatrix} S_{jj} & S_{jk} \\ S_{kj} & S_{kk} \end{bmatrix} \begin{Bmatrix} U_a \\ U_b \end{Bmatrix} \tag{D10}$$

$$\begin{Bmatrix} U_a \\ U_b \end{Bmatrix} = \begin{bmatrix} F_{jj} & F_{jk} \\ F_{kj} & F_{kk} \end{bmatrix} \begin{Bmatrix} R_a \\ R_b \end{Bmatrix} \tag{D11}$$

where

$$R_i = \begin{Bmatrix} P_i \\ M_i \end{Bmatrix} \qquad U_i = \begin{Bmatrix} u_i \\ q_i \end{Bmatrix} \tag{D12}$$

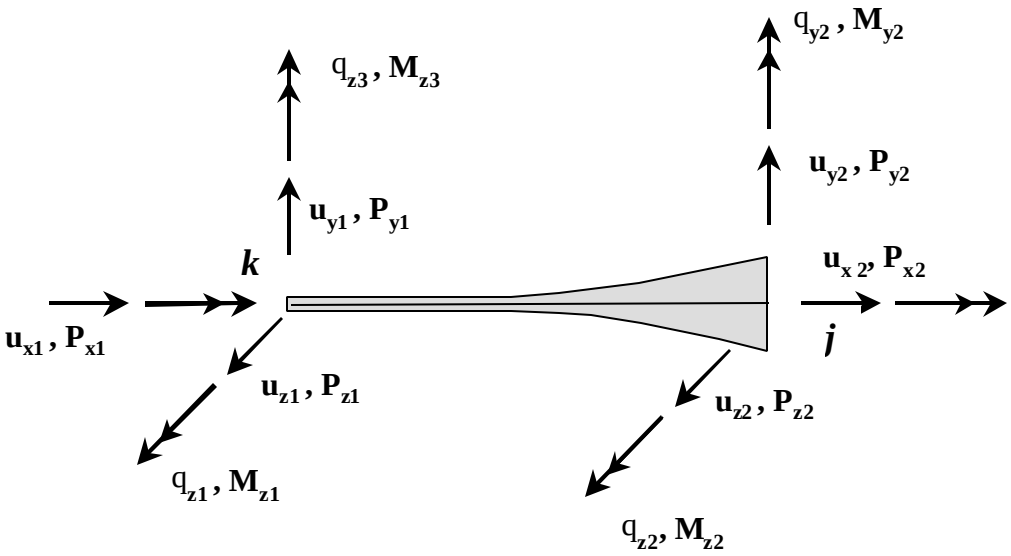


Figure D.2. Beam element with 6 degrees of freedom displacements at each end

The step procedures to construct the 12-by-12 stiffness matrix **S** used in the present work are as follow :

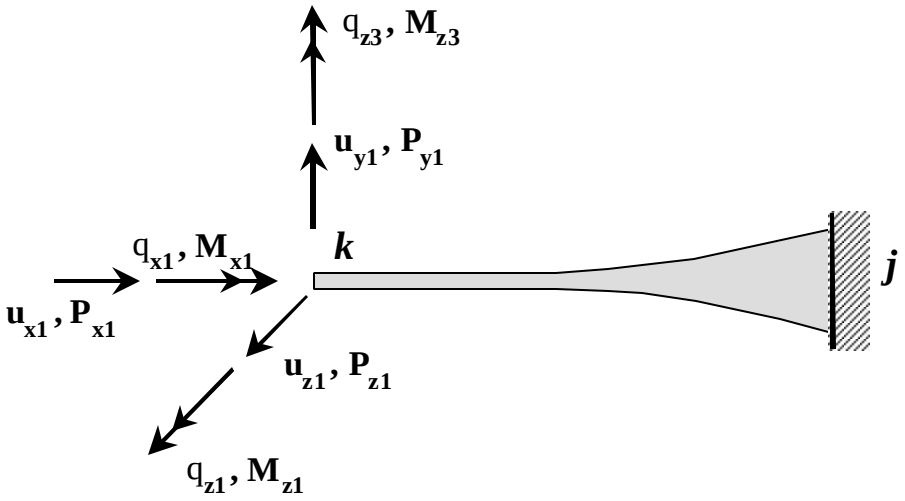


Fig. D.3. A cantilever beam with six degrees of freedom deformations at the tip

(1) Determine $\mathbf{u}_k$ displacements at point k at the tip of a cantilever beam shown in Fig. D.3. A direct integration is used to solve the Euler-Lagrange differential equation.

(2) Form the flexibility sub-matrix $\mathbf{F}_{kk}$ from the displacements $\mathbf{u}_k$

(3) Inversion of $\mathbf{F}_{kk}$ produces the stiffness sub-matrix $\mathbf{S}_{kk}$ as follow

$$S_{kk} = F_{kk}^{-1} \tag{D13}$$

(4) The sub -matrix $\mathbf{S}_{jk}$ can be determined from $\mathbf{S}_{kk}$ based on Eq. (D2)

$$S_{jk} = -T_{jk}\ S_{kk} \tag{D14}$$

where

$$T_{jk} = \begin{bmatrix} I_3 & 0 \\ c_{jk} & I_3 \end{bmatrix} \tag{D15}$$

Based on Fig. D.3. the vector r_{jk} can be obtained as

$$r_{jk} = L\,\hat{i} \tag{D16}$$

Substitution of Eq (D15) into Eq. (D4) gives

$$c_{jk} = \begin{bmatrix} 0 & 0 & 0 \\ 0 & 0 & -L \\ 0 & L & 0 \end{bmatrix} \tag{D17}$$

(5) Since the stiffness matrix **S** is symmetric, the sub-matrix $\mathbf{S}_{kj}$ must be equal to the transpose of $\mathbf{S}_{jk}$

$$S_{kj} = S_{jk}^{T} \tag{D18}$$

(6) Finally the sub -matrix $\mathbf{S}_{jj}$ can be determined from $\mathbf{S}_{kj}$ based on Eq. (D2)

$$S_{jj} = -T_{jk}\ S_{kj} \tag{D19}$$

If there is no coupling among axial, torsional and flexural stiffness terms, a further simplification can be performed by treating the axial, torsional and flexural stiffness terms separately. For the bending problem in an x - y plane, the steps above is repeated with a simpler matrix operation, since the static equivalence relationship in Eq. (D2) becomes

$$\begin{Bmatrix} F_a \\ M_a \end{Bmatrix} = T_{ab} \begin{Bmatrix} F_b \\ M_b \end{Bmatrix} = \begin{bmatrix} 1 & 0 \\ L & 1 \end{bmatrix} \begin{Bmatrix} F_b \\ M_b \end{Bmatrix} \tag{D20}$$

For the axial and torsional problems, Eq. (D2) becomes

$$F_a = T_{ab}\ F_b = 1.\ F_b \tag{D21}$$

such that a direct calculation of the stiffness matrix can be obtained using the six steps above.

Vita

Erwin Sulaeman was born on January 31, 1959 in Bandung, Indonesia. In 1978, he began his Bachelor's degree at Institut Teknologi Bandung in Indonesia. During his studies, he worked for the Atalanta Arupadhatu, a Civil Engineering Consultant, in the field of Soil Mechanics. He graduated in 1986 with B.S. and Engineer degrees in Civil Engineering with a specialty in Structural Dynamics. He started to work in 1987 for the Indonesian Aerospace Industry (IPTN) in the field of Aeroelasticity. In 1991, he began his M.S. degree at University of Dayton, Ohio. He graduated in 1993 with a degree in Aerospace Engineering. He began his Ph.D degree at Virginia Tech in the Fall of 1997. He joined the strut-braced wing (SBW) team of the Multidisciplinary Analysis and Design (MAD) Center of Virginia Tech in 1998. During his time at Virginia Tech, he was involved also in the Uninhabitated Combat Air Vehicle (UCAV) project of the Center for Intelligent Material Systems and Structures (CIMSS) of Virginia Tech for one year. Upon completion of his doctoral studies, he will continue for his academic training in ZONA Tech of Scottsdale, Arizona.